

Parylene-C as a New Piezoelectric Material

Thesis by
Justin Young-Hyun Kim

In Partial Fulfillment of the Requirements for the degree of
Doctor of Philosophy



CALIFORNIA INSTITUTE OF TECHNOLOGY

Pasadena, California

2013

(Defended 2012.06.22)

To my God,

To my parents and parents in law,

To Sujin, Jaeyeon, Nayeon and Hayeon,

To my friends from CALTECH,

To my brothers and brother in law,

And to Dr. Tai

ACKNOWLEDGEMENTS

First, I would like to express my sincere appreciation to Professor Yu-Chong Tai for his academic and personal guidance and support. His enthusiasm and faith in this project has carried me through many hard times and has helped me out of many dead ends.

I would also like to thank the staff and students of the Caltech Micromachining Group for their assistance both inside and outside our lab. I could not have learned so much throughout this Ph.D. program without the support of Dr. Wen Li, Dr. Mike Liu, Dr. Quoc (Brandon) Quach, Dr. Ray Huang, Dr. Luca Giacchino, Dr. Jeffrey Lin, Dr. Nick Lo, Dr. Changlin Pang, Dr. Po-Jui (PJ) Chen, Dr. Jason Shih, Mandheerej (Monty) Nandra, Charles DeBoer, Bo Lu, Penvipha (Yok) Satsanarukkit, Wendian (Leo) Shi, Han-Chieh (Jay) Chang, Yu (Joy) Zhao, Dongyang (Clark) Kang, Xiaoxiao (Shell) Zhang, and Austin Cheng. I would like to thank Yang Liu for his enthusiasm, dedication and perseverance while measuring the piezoelectric coefficient. In addition I would like to thank Nick Scianmarello for his help in determining the mathematical description of a circular diaphragm. My appreciation also extends to Trevor Roper, Christine Garske and Tanya Owen who have done an excellent job in keeping the Caltech Micromachining Lab running smoothly.

Outside of the lab I would like to thank Taesik Oh for teaching me and helping me to use the XRD to analyze the crystallinity of PA-C.

I am deeply grateful to my younger brothers Do Hyun Kim and Soo Hyun Kim and my colleague, Siyang Zheng, for mentorship in the PhD program. Your encouragement, companionship and devotion have been invaluable to me.

Finally, I would like to express my deepest thanks to my wife Sujin and my kids, Jaeyeon, Nayeon and Hayeon for always being there for me, and to my parents and my parents in law for all their sacrifices and support. Their love and patience have made this work possible.

ABSTRACT

The goal of this thesis is to develop a proper microelectromechanical systems (MEMS) process to manufacture piezoelectric Parylene-C (PA-C), which is famous for its chemical inertness, mechanical and thermal properties and electrical insulation. Furthermore, piezoelectric PA-C is used to build miniature, inexpensive, non-biased piezoelectric microphones.

These piezoelectric PA-C MEMS microphones are to be used in any application where a conventional piezoelectric and electret microphone can be used, such as in cell phones and hearing aids. However, they have the advantage of a simplified fabrication process compared with existing technology. In addition, as a piezoelectric polymer, PA-C has varieties of applications due to its low dielectric constant, low elastic stiffness, low density, high voltage sensitivity, high temperature stability and low acoustic and mechanical impedance. Furthermore, PA-C is an FDA approved biocompatible material and is able to maintain operate at a high temperature.

To accomplish piezoelectric PA-C, a MEMS-compatible poling technology has been developed. The PA-C film is poled by applying electrical field during heating. The piezoelectric coefficient, -3.75pC/N , is obtained without film stretching.

The millimeter-scale piezoelectric PA-C microphone is fabricated with an in-plane spiral arrangement of two electrodes. The dynamic range is from less than 30 dB to above 110 dB SPL (referenced $20\ \mu\text{Pa}$) and the open-circuit sensitivities are from $0.001 - 0.11\ \text{mV/Pa}$ over a frequency range of 1 - 10 kHz. The total harmonic distortion of the device is less than 20% at 110 dB SPL and 1 kHz.

TABLE OF CONTENTS

ACKNOWLEDGEMENTS.....	iv
ABSTRACT	v
TABLE OF CONTENTS.....	vi
LIST OF ILLUSTRATIONS	x
LIST OF TABLES	xvii
Chapter 1.....	1-1
Introduction.....	1-1
Motivation.....	1-1
Piezoelectric material.....	1-2
Parylene.....	1-5
Micro Electro Mechanical Systems (MEMS).....	1-6
Thesis Outline.....	1-8
Chapter 2.....	2-1
Piezoelectric Microphone Review	2-1
Piezoelectricity.....	2-1
Definitions of Piezoelectric Coefficients and Directions	2-6
Piezoelectric Polymer	2-8
For being Piezoelectric Polymers.....	2-9
Mechanism of piezoelectricity in semicrystalline polymers.	2-10
Poly-Vinyl DiFluoro (PVDF).....	2-11
Non-MEMS Piezoelectric Microphone	2-15
Rochelle Salt transducer	2-15
Piezo-Ceramic Microphone.....	2-16
Piezoelectric Plastic	2-17
MEMS Piezoelectric Microphones	2-18
A piezoelectric microphone based on PZT thin films[72]	2-19
An AlN MEMS Piezoelectric Microphone for Aeroacoustic Applications[74].....	2-22
ZnO on Si integrated acoustic sensor[81]	2-25

Fabrication and Characterization of Piezoelectric Micromachined Ultrasonic Transducers with Thick Composite PZT Films[87]	2-28
Electroacoustical measurements of silicon microphones on wafer scale[90].....	2-32
Microphone based on Polyvinylidene Fluoride (PVDF) micro-pillars and patterned electrodes[91].....	2-34
Piezoelectric Polyimide MEMS Device[13].....	2-37
MEMS Condenser Microphone	2-39
Summary.....	2-40
Chapter 3.....	3-1
Piezoelectricity of Parylene-C.....	3-1
Parylene-C.....	3-1
Piezoelectricity of Parylene-C film	3-5
Piezoelectric film preparation.....	3-7
Measuring System	3-11
Long Time Constant Charge Integration Amplifier	3-17
d_{33} Dependence on Poling Condition	3-21
piezoelectric coefficient over an electrical field.....	3-21
Piezoelectric coefficient over temperature	3-22
Piezoelectric coefficient over poling time.....	3-23
Ageing effect on Piezoelectric coefficient	3-23
Piezoelectric coefficient over pre-annealing time.....	3-25
Simultaneous Poling and Stretching to Piezoelectric coefficient.....	3-26
Summary.....	3-34
Chapter 4.....	4-1
Microphone Design	4-1
Design of Microphone.....	4-1
Model Description and small deflection theory.....	4-1
Linear Model of Plate with Tension.....	4-3
Free Oscillations of Undamped System.....	4-4
Transition of Plate-membrane Behavior and Results.....	4-8

Plate Model ($T = 0$, i.e. $N_0 = 0$)	4-8
Membrane Model ($D=0$).....	4-8
Plate-membrane Transition	4-9
Residual tension measurement and tension parameter k	4-16
Static pressure deflection experimental setup	4-20
Lumped element model	4-22
Frequency Response	4-28
Low-Frequency Cut-Off[153]	4-29
High-Frequency Cut-Off	4-31
Summary	4-34
Chapter 5.....	5-1
MEMS Piezoelectric Microphones with Piezoelectric Parylene-C Diaphragms	5-1
Preface.....	5-1
Piezoelectric Microphone Process	5-2
Thermal Oxidation.....	5-5
DRIE etching for the backside of wafer.....	5-6
A-174 adhesion promotion for PA-C deposit	5-8
PA-C deposition.....	5-11
Liftoff pattern made out of LOR3B and Az1518	5-14
Metalization	5-20
Lift off	5-22
Parylene-Parylene adhesion improvement step	5-24
2 nd PA-C Layer Deposition.....	5-24
Electrodes Opening by O ₂ Plasma	5-24
Cleaning surface with BHF and chip mounting.....	5-26
XeF ₂ etching.....	5-26
Detach a chip from the slide glass.....	5-31
Poling	5-31
Microphone assembly.....	5-34
Resonance Frequency Measuring setup.....	5-36

Microphone Measuring Setup	5-49
Testing.....	5-49
Performance testing	5-49
Sound pressure Level.....	5-50
Summary	5-53
Chapter 6.....	6-1
Conclusion	6-1
bibliography	6-2

LIST OF ILLUSTRATIONS

<i>Number</i>	<i>Page</i>
Figure 1-1 Rochelle salt transducer, diaphragm type.....	1-3
Figure 1-2 Molecular structures of PA-C Note that only PA-C has an asymmetric structure and polarity.....	1-6
Figure 2-1 Piezoelectric Materials.....	2-2
Figure 2-2 Piezoelectric effect on Quartz.....	2-3
Figure 2-3 Cut of quartz.....	2-3
Figure 2-4 Reversible Piezoelectric effect. a) A generation of electrical charge resulting from an applied mechanical force, b) the generation of a mechanical strain from an applied electrical field.	2-4
Figure 2-5 PZT unit cell: a) Perovskite-type lead zirconate titanate (PZT) unit cell in the symmetric cubic state above the Curie temperature. b) Tetragonally distorted unit cell below the Curie temperature[50].	2-5
Figure 2-6 Electric dipoles in domains; a) unpoled ferroelectric ceramic below curie temperature, b) during the poling (applying electrical bias and heating near below the Curie temperature) and c) after poling[50].	2-6
Figure 2-7 Orthogonal system describing the properties of a poled piezoelectric ceramic. Axis 3 is the poling direction[52].	2-8
Figure 2-8 Schematic illustration showing random stacks of amorphous and crystal lamellae in PVDF polymer.	2-11
Figure 2-9 Piezoelectric coefficients of PVDF depends on, a) electrical bias; b)stretching ratio; c)poling temperature.....	2-14
Figure 2-10 Time stability of optimum d_{31} at various decay temperatures, The line curves are Simultaneous Stretching and corona poling PVDF film; Broken curves are for first stretched and then poled PVDF films.....	2-14
Figure 2-11 Rochelle Salt transducer, diaphragm type.	2-16
Figure 2-12 Piezo-Ceramic Microphone.	2-17

Figure 2-13 Basic PVDF Transducer.....	2-18
Figure 2-14 Fabrication process flow for creating a PZT membrane microphone: (a) Starting wafer, (b) sacrificial titanium, (c) Ar ion mill of Ti/Pt/PZT/Pt, (d) PZT wet etch, (e) oxide passivation deposition, (f) etching of passivation, (g) Ti/Au contact, (h) silicon DRIE, and front view of released PZT membrane.....	2-20
Figure 2-15. Images of the acoustic test chamber used for testing the PZT microphone. (The BNC mounts provide electrical contact to the packaged microphone whereas the acrylic plate on top provides a connection for the acoustic tube.)	2-21
Figure 2-16 Acoustic response of a B&K and a 750- μ m diameter PZT MEMS microphone with 20% sensor coverage for B&K Pistonphone 250-Hz tone at 124 dB and.....	2-21
Figure 2-17 Microphone structure with quarter cutout (not to scale), featuring a circular diaphragm with an annular electrode/piezoelectric/electrode ring.....	2-22
Figure 2-18 Micrograph of a MEMS piezoelectric microphone (design F; refer to Section III-E)....	2-23
Figure 2-19. Outline of fabrication steps. (a) Etch cavity in silicon wafer, and deposit sacrificial oxide. Perform CMP. (b) Deposit and pattern films (structural layer, Mo/AlN/Mo stack, and passivation layer). (c) DRIE through backside, and stop on sacrificial oxide. (d) Release the diaphragm via oxide release etching.....	2-24
Figure 2-20 Cutout diagram of the device (not to scale).....	2-25
Figure 2-21 Structure of the electrodes. Because the center part and outer part is under the different direction of the stress, the bottom electrodes are divided in two sections.	2-26
Figure 2-22 Crossectional view of the device.	2-27
Figure 2-23 Top view of the devvice.....	2-28
Figure 2-24 Cross-section images of two 10 μ m thick composite films. (a) and (b) Loaded with nano-sized powder; concentration of sol-gel solution is 40 wt%; powder-to-solution mass ratio is 1 to 2. (c) and (d) Loaded with submicron-sized powder, concentration of sol-gel solution is 40 wt%; powder-to-solution mass ratio is 2 to 3.....	2-30
Figure 2-25 Cross-section view of ultrasonic radiating device.....	2-31
Figure 2-26 A silicon microphone with a piezoelectric polymer layer.	2-33
Figure 2-27 Measured open-circuit frequency response of a piezoelectric microphone.....	2-34

Figure 2-28 Schematic of PVDF microphone process.....	2-35
Figure 2-29 Pillar structure formed from PVDF and corresponding electrodes	2-35
Figure 2-30 Schematic diagram of PVDF micro-pillar sensor with full electrodes.....	2-36
Figure 2-31 The piezoelectric strain coefficient (actuator response) of polyimides vs. PVDF.....	2-37
Figure 2-32 Piezoelectric polyimide sensor structure.....	2-38
Figure 2-33 Silicon condenser microphone of Hohm and Hess (1986) [93].....	2-39
Figure 3-1 Chemical structures of Parylene N, C and D [1].....	3-2
Figure 3-2 Parylene deposition system and the involved chemical processes	3-4
Figure 3-3 Parylene Conformal Coating Specifications & Properties.....	3-5
Figure 3-4 Molecular structures of various type of Parylene. Note that only PA-C has an asymmetric structure.	3-6
Figure 3-5 Dimensions of the sample of the PA-C film.....	3-7
Figure 3-6 Distances from the edges of electrodes of film sample to the edge of bottom ground plate.	3-8
Figure 3-7 Experimental setup for PA-C poling. To avoid the oxidation of PA-C, the poling process was performed in a nitrogen-filled glove box. A thermocouple is located underneath the bottom mica insulation sheet to control the hot plate. The pressure of the globe box is maintained at 3psi higher than the atmospheric pressure.....	3-10
Figure 3-8 Detailed figure of poling jig.....	3-11
Figure 3-9 The schematic of the pneumatic testing system. The voltage (from the charge amplifier) and the pressure signals are gathered and analyzed by a control PC through NI DAQ USB-6281. The solenoid valve is also controlled by the same PC.	3-12
Figure 3-10 Detailed figure of pressurizing chamber. a) cross section of the chamber. b) top cover is removed. The deformable mesh electrode is translucent to show the relative position to the piezoelectric PA-C film.....	3-13
Figure 3-11 EMI (Electric Magnetic Interference) shielding gasket.....	3-14
Figure 3-12 Picture of the pressuring chamber.....	3-14
Figure 3-13 Charge model of Piezoelectric PA-C film	3-15
Figure 3-14 The charge integrator circuit.....	3-16

Figure 3-15 The recorded temperature, pressure and voltage for one cycle of pneumatic stressing of the piezoelectric PA-C sample. For the pressure (green) curve, the vertical axis is the pressure difference from atmospheric pressure.....	3-19
Figure 3-16 d_{33} vs. applied electrical field (poled at 200°C for 2hrs). This shows that d_{33} increases with the E-field although the significant increase occurs above -40MV/m.	3-21
Figure 3-17 d_{33} vs. poling temperature (for 50um thick PA-C film, poled for 5 minutes with -5.0kVm, i.e. -100MV/m). This shows that d_{33} peaks at 160°C.....	3-22
Figure 3-18 Poling process is finished within 5 minutes.	3-23
Figure 3-19 Ageing effect on Piezoelectric PA-C film.....	3-24
Figure 3-20 Lack of temperature stability of PVDF; polyimide with low d_{31} value.....	3-25
Figure 3-21 Pre-annealing can decrease the piezoelectric coefficient.....	3-26
Figure 3-22 Molecular structures of PVDF. Hydrogen atoms are omitted.	3-27
Figure 3-23 Simultaneous Stretching and Corona poling device.	3-28
Figure 3-24 Continuous rolling stretching device.....	3-28
Figure 3-25 Simultaneous Stretching and poling, the maximum d_{31} is at 4.5X.....	3-29
Figure 3-26 Schematics of stretching setup.....	3-30
Figure 3-27 3D drawing of stretching and corona poling setup.....	3-31
Figure 3-28 Corona charge unit.	3-31
Figure 3-29 Poled at 200°C, with a speed of (2 steps/sec), with 2KV of surface static voltage, with different stretching. Stretching is shown as strain.	3-32
Figure 3-30 Increase of polarity of PA-C film by stretching. 2 times of stretching (100% strain) 3-33	3-33
Figure 4-1 Illustration of a diaphragm clamped along its edge.....	4-2
Figure 4-2 $\alpha_2 * a$ over tension parameter k	4-7
Figure 4-3 Resonance frequency dependency over different radiuses (30um thick PA-C).....	4-9
Figure 4-4 Resonance frequency dependency over different radiuses (5um thick PA-C).....	4-10
Figure 4-5 Resonance frequency dependency over different thickness (3mm in radius).	4-11
Figure 4-6 Mode shape dependency over tension parameter k	4-12
Figure 4-7 Normalized radial stress change over non-dimensional radius.....	4-13
Figure 4-8 Where the radial stress becomes zero ($\sigma_r = 0$). The value is shown as fraction over radius.	4-14
Figure 4-9 Normalized tangential stress change over non-dimensional radius.....	4-15

Figure 4-10 Where the Tangential stress becomes zero ($\sigma_t = 0$). The value is shown as fraction over radius.....	4-16
Figure 4-11 Static pressure inducing the deflection of the diaphragm, after the process.....	4-18
Figure 4-12 Static pressure inducing the deflection of the diaphragm, after a annealing at 160°C, 1hr	4-18
Figure 4-13 Static pressure inducing the deflection of the diaphragm, after a annealing at 200°C, 5m	4-19
Figure 4-14: Experimental setup of the blister test: (a) the cross-section view of the test jig, and (b) schematic diagram of the testing setup	4-21
Figure 4-15 Equivalent circuit representation of a lumped-element model of a piezoelectric microphone.	4-23
Figure 4-16 Layers of the microphone	4-28
Figure 4-17 Structure of the electrodes.....	4-28
Figure 4-18 Typical frequency response of a microphone.....	4-29
Figure 4-19 Pressure equalization hole positions. (a) Hole exposed. (b) Hole unexposed.	4-30
Figure 4-20 Low frequency response vs. location of pressure equalization hole.....	4-31
Figure 4-21 Different degrees of microphone response damping.....	4-32
Figure 5-1 Overall processes.....	5-4
Figure 5-2 Wet thermal oxidation data	5-5
Figure 5-3 DRIE process.....	5-7
Figure 5-4. Molecular structure of A-174, γ -MPS	5-8
Figure 5-5. Silanization on the surface of silicon.	5-9
Figure 5-6. Covalent bond between PA-C and A-174	5-11
Figure 5-7. The deposition process of PA-C	5-12
Figure 5-8. Pressure and temperature profiles of PA-C deposition process.....	5-13
Figure 5-9 Double layer for Liftoff.....	5-14
Figure 5-10. Spin speed vs thickness for LOR B series resists.....	5-15
Figure 5-11 Liftoff pattern delamination from poor LOR3B adhesion, baked at 140oC, 5min.	5-16
Figure 5-12 Standard pattern check with different exposure time in a stepper.	5-19
Figure 5-13 Stepper exposure check.....	5-19
Figure 5-14. Liftoff patterns with 2um of undercut.....	5-20

Figure 5-15. Variation of contact angle with time on polycarbonate substrate after plasma treatment.	5-22
Figure 5-16. A short induced by liftoff metal pattern.	5-22
Figure 5-17 Single acetone system cannot clean all layers of LOR3B and AZ1518	5-23
Figure 5-18. After liftoff process is completed	5-23
Figure 5-19 Weight decreasing of AZ4620 10um by baking time.	5-25
Figure 5-20 Delamination at the interface of PA-C and SiOx after 1hr of XeF ₂ etching.	5-26
Figure 5-25 Ball model of XeF ₂	5-28
Figure 5-26 XeF ₂ sublimation Pressure	5-28
Figure 5-27 Local loading effect and Aperture opening effect	5-29
Figure 5-28 Schematics of XeF ₂ etching system	5-31
Figure 5-29 A setup for poling process.	5-32
Figure 5-30 Microphone chip poling jig	5-33
Figure 5-31 Microphone with assembly	5-34
Figure 5-32 Schematic of microphone assembly	5-35
Figure 5-33 a) Microphone housing, b) with preamplifier	5-35
Figure 5-34 Structure of a DVD/CD pick-up head.	5-37
Figure 5-35 An astigmatic detection scheme. FES signal is represented as a black line. Intensity is represented as a dotted red line.	5-39
Figure 5-36 Sanyo SF-HD62	5-42
Figure 5-37 Measuring setup with DVD pickup. Coarse z stage is composed of a linear motorized stage from Vlemex®. For a fine z stage, piezo stack from Omega® is adopted	5-43
Figure 5-38 A differential amplification circuit to get FES signal	5-44
Figure 5-39 Beam, focused at the center electrode	5-44
Figure 5-40 The measured F-E signal Vs distance. For this case, the proportional constant between the distance change and the measured voltage is 9×10^{-6} m/V.	5-45
Figure 5-41 A reference Automatic Power Control circuit suggested from Sanyo®	5-47
Figure 5-42 Measured data, resonance peak at 24.22kHz for 29um thickness, 6mm in diameter.	5-48
Figure 5-43 Loud human voice record.	5-49
Figure 5-44 Measuring setup.	5-50
Figure 5-45 Input sound pressure level for frequency response measurements	5-51

Figure 5-46 Frequency response of MEMS piezoelectric microphone.5-52

LIST OF TABLES

<i>Number</i>	<i>Page</i>
Table 3-1 Properties of Parylene N, C and D [1].	3-3
Table 4-1 Measured residual tension after process and after poling process. * The maximum temperature which the device experienced during the fabrication is 150°C, 5 minutes.....	4-19
Table 4-2 Table of material properties.....	4-27
Table 5-1 LOR3B baking test (baked on a hot plate).....	5-16
Table 5-4 XeF ₂ Etching depends on Materials.....	5-27
Table 5-5 Specifications of the DVD optical pickup head white paper.	5-36
Table 5-6 Pin connection of Sanyo SF-HD62, A,B,C,D for DVD mode, a,b,c,d for CD mode are used to generate FES signal; Pin 8, RF represents intensity of light used to figure out the maximum reflecting point.....	5-41

Chapter 1

INTRODUCTION

Motivation

The chemical nature of Parylene-C (PA-C); non symmetric, polar and insulating, indicates it could be a piezoelectric material after using the proper process, poling. After demonstrating the piezoelectric nature of polled PA-C for the first time, we investigate devices utilizing PA-C as a piezoelectric material.

As a piezoelectric polymer, PA-C has varieties of applications due to its low dielectric constant, low elastic stiffness, low density, high voltage sensitivity, high temperature stability and low acoustic and mechanical impedance. Furthermore, because PA-C is an FDA approved biocompatible material and is able to maintain operate at a high temperature (piezoelectricity can be kept more than a week at 160oC without decaying), it can withstand the harsh sterilizing process (121oC and 10~20 minutes) in an autoclave. This distinguishes it from other piezoelectric materials because it can be used for biomedical devices including blood flow sensors, heart rate sensors, hydrophones and cochlear implant microphones. In this research, we fabricate a microphone to demonstrate the FIRST piezoelectric PA-C device. This is an ideal application due to the high volume of microphones used in mobile devices, digital cameras, cell phones, and tablet PCs. In all these devices miniature acoustic chip systems, such as microphones, are monolithically integrated with microelectronic circuitry, which is ideal for a MEMS fabricated microphone.

Currently, these devices use electret microphones because of favorable characteristics such as: self-biasing (requires no external power supply), wide-band frequency response, vibration resistance, low noise and stability in the environment. However, the modular nature and primitive manufacturing techniques of today's electret microphones has been a limiting factor in making them smaller, cheaper, more reliable and better performing. MEMS electrets microphones are limited in their ability to separate the electrode and diaphragm, which induces problems of control a gap between electrodes. In addition, nonlinearity due to electrical fields inducing diaphragm

stiffness, and sensitivity to environmental change, dust, moisture and shock also limit performance. Furthermore, wafer bonding or removing of sacrificial layer is necessary and this becomes a limiting factor to the low cost and productivity.

Compared with the electrets microphone, the piezoelectric microphone has only one diaphragm and it brings several advantages including robustness to shock and dust, and producibility. Also, by the nature of the piezoelectric effect, it has a wide bandwidth, high output impedance, large dynamic range, and is robust from electromagnetic interference, even though it has a lower sensitivity than the electret microphone.

Combined with MEMS technology, the piezoelectric microphone has additional advantages including

- high degree of miniaturization with no or minimal loss in performance
- repeatable and precise dimensional control
- high volume manufacturing with a high degree of reproducibility
- ability to array multiple microphones on the same substrate
- ability to integrate with on-chip microelectronics
- freedom to choose from a wide range of materials and processing techniques.

Piezoelectric material

In 1820 Becquerel described and observed piezoelectric effect[1] although a systematic study leading to modern understanding of these effects is credited to the Curies.[2] The two physicists found that the surfaces of certain crystals became electrically charged when the crystal is mechanically loaded.

The Rochelle Salt transducer by Sawyer in 1931 is considered as the first practical invention of the piezoelectric microphone.[3] The microphone uses a thin strip of piezoelectric material attached to a diaphragm. The two sides of the crystal acquire opposite charges when the diaphragm deflects the crystal. This bimorph idea has been widely used in low cost microphones since this invention. However, due to water solubility, low melting temperature and fragile nature, the Rochelle salt bimorph microphone has a poor environmental stability. It is quickly substituted with other piezoelectric ceramic materials, such as Barium Titanate ceramics of Gray[4] and more recently by PZT ceramics of Jaffe.[5]

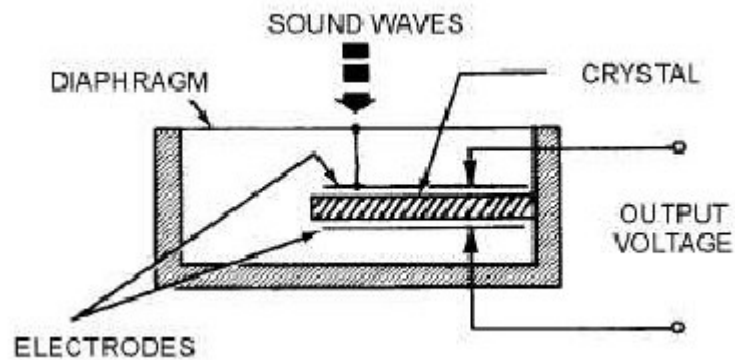


Figure 1-1 Rochelle salt transducer, diaphragm type

Inorganic ceramic piezoelectric materials are characterized by mechanical hardness, high piezoelectric coefficients, thermal and humidity stability. Organic piezoelectric materials have lower piezoelectric coefficients than inorganic ceramic piezoelectric materials. However, they have the advantage of flexibility, low weight, low acoustic and mechanical impedance, and are generally non-toxic.[6] Despite its outstanding piezoelectric property, PZT is currently facing global restrictions due to its lead toxicity.

The piezoelectric strain constant (d_{33}) for the polymers is lower (PVDF(Poly Vinyl DiFluoro), 30pC/N) than that of the ceramic (PZT, 300pC/N). However, due to their low Young's modulus, piezoelectric polymers (PVDF, 240mV-m/N) have much higher piezoelectric stress constants (g_{33}) than ceramics (PZT, 11mV-m/N), which indicates that they can be better sensors than ceramics.

Piezoelectric polymeric sensors and actuators offer the advantage of processing flexibility because they are lightweight, tough, readily manufactured into large areas, and can be cut and formed into complex shapes. Polymers also exhibit high strength and high impact resistance.[7] Other notable features of polymers are low dielectric constant, low elastic stiffness, and low density, which result in a high voltage sensitivity (excellent sensor characteristic), and low acoustic and mechanical impedance (crucial for medical and underwater applications).

Thus, for example, PVDF is widely used as sensor material in applications such as, traffic signal control loop sensor buried under the load, musical instrument pickups, sports scoring, impact printers, bearing wear sensors, fan flow sensor and accelerometers.[8] Polymers also typically possess a high dielectric breakdown and high operating field strength, which means that they can withstand much higher driving fields than ceramics.

Also, polymers offer the ability to become a thin layer, to be patterned and to achieve electrodes on the film surface, and consequently to be poled only selected regions. Based on these features, piezoelectric polymers possess their own established area for technical applications and useful device configurations. In MEMS field, curable polyimide is also used to build a touch sensor array, air flow sensor and vibration sensor [9–13].

However, even though the overwhelming piezoelectric property of PVDF over other piezoelectric polymers, it lacks temperature stability and is limited to less than 80 °C. For high temperature applications, polyimide-based MEMS devices are used [9–15]. However, polyimide is hydrophilic, which induces lower stability in high humidity environments. In addition, these films are cured in convection or diffusion ovens at high enough temperatures (350-400°C)[16] to assure adequate mechanical and electrical properties. These high temperatures can change the electrical properties of the devices. If the cure temperature of these films were lowered there could be a reduction in the film (and wafer) stress as well as a lower thermal budget for the devices. However, curing polyimide films below 250°C has does not provide the mechanical, chemical, and dielectric properties required for the final device operation parameters or mechanical and dielectric protection.[17]

Parylene

Parylene development started in 1947, by Michael Szwarc but the reaction yield was only a few percent, and a more efficient route was developed in the 1950s by William F. Gorham and was commercialized in 1965 by the Union Carbide Corporation [18]. The Parylene film deposition process did not require a solvent and resulted in chemically resistant films free from pinholes [19], [20]. Since the coating process takes place at ambient temperature in a mild vacuum, and because of Parylene's conformal properties, it has a wide variety of applications. Various types of Parylene films have been extensively studied for numerous applications due to its mechanical and electrical properties and chemical resistance [20].

Among the Parylene variants, Parylene-N and -C are currently approved by FDA as a USP class VI polymer [21], which allows them to be used in biomedical devices, and in electronic insulation and environmental passivation. PA-C has higher thermal stability and chemical/moisture resistance than Parylene N, and thus was commonly chosen as an encapsulation material for biomedical devices and for variety of anticorrosion applications. Some applications have included stents, pacemakers, neural probes, and solder joints encapsulation [22], [23].

Furthermore, due to the unique CVD deposition process, Parylene is favorable for use in the fabrication of MEMS process. A conformal, uniform and pinhole free film that can range in thickness from a few hundred nanometers to a few tens of microns is achievable.

The origin of polymer piezoelectricity comes from the molecular polar asymmetry in the unit polymer molecule. For examples, this can be found in PVDF, which is known to enable PVDF piezoelectricity if properly poled [1, 2]. Similarly, other polymer, such as PVC [3] and polyimide [4, 5], also have polarizing groups and, therefore, have been shown to have piezoelectricity after proper poling [2]

PA-C is well known for its mechanical properties and chemical inertness for bioMEMS applications. PA-C, like many piezoelectric materials, also has a single chlorinated benzene ring, which gives an asymmetry and, hence, is a potential piezoelectric material as shown in Figure 1-2. Interestingly, PA-C was reported as a pyroelectric sensor material (United States Patent 4147562) but it has never

been reported as a piezoelectric material before our research. And this work is the first to study methods of poling PA-C and validate that PA-C can be a piezoelectric material.

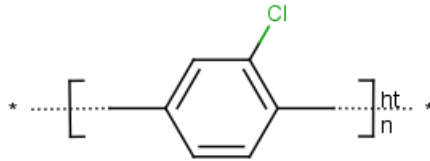


Figure 1-2 Molecular structures of PA-C Note that only PA-C has an asymmetric structure and polarity.

Micro Electro Mechanical Systems (MEMS)

Traditionally, silicon and other semiconductor materials have been used to fabricate electrical devices such as transistors [24] and diodes for use in integrated circuits [25]. In these examples, the semiconductor material is utilized for its *electrical* properties only. Since the 1980s, extensive research has been conducted on utilizing the *mechanical* properties of these same semiconductor materials [26]. This effort has resulted in the birth of a new and rapidly growing technology platform called Micro Electro Mechanical Systems (MEMS).

MEMS allows millimeter- to micron-sized sensors, actuators, mechanical elements and microelectronics to be built on the same semiconductor substrate [27]. While the electronics are fabricated using integrated circuit (IC) process sequences (e.g., CMOS, Bipolar, or BICMOS), the micromechanical components are fabricated using compatible "micromachining" processes that selectively etch away parts of the silicon wafer or add new structural layers to form the mechanical and electromechanical devices. Bulk micromachining [28] describes the process that selectively etches away large pieces of the bulk substrate leaving behind the desired 3-D micromechanical elements. Surface micromachining [29] describes the sequential deposition and selective removal of thin films that can serve as the structural and/or sacrificial layer. These two MEMS process technologies allow for the fabrication of micromechanical structures such as beams [30], cavities [31], channels [32], membranes [33], nozzles [34], posts and tips using materials such as silicon,

silicon dioxide, silicon nitride, polysilicon, various metals and other silicon derivatives. Together with a host of new MEMS technologies such as LIGA [35], plastic injection molding [36], microstereolithography [37], laser micromachining [38], micro electrical discharge machining [39], silicon carbide processes [40] and selective Parylene deposition/etching [41], MEMS promises to revolutionize nearly every product category by bringing together (silicon-based) microelectronics with miniature sensor and actuator technology.

MEMS is truly an enabling technology allowing the development of smart products by augmenting the computational ability of microelectronics with the perception and control capabilities of microsensors and microactuators. For the first time in scientific history, this enables the creation of sophisticated multifunctional microchips that can take input directly from their surrounding environment through a MEMS microsensor (e.g., as sound, heat, moisture, pressure, etc.), process the information through a microelectronic circuit, and relay a response back to the physical environment through a MEMS microactuator (e.g., through force, magnetic field, etc.). The ideal embodiment is for all of this to take place on the same microchip substrate.

Because MEMS devices are built with the same underlying technology and utilize the same infrastructure as that used in the microelectronics industry, they can be effectively miniaturized and mass-produced reliably and cost-efficiently. In the past decade, the United States Defense Advanced Research Project Agency (DARPA) has poured millions of dollars into MEMS research. Since the 1990s, the commercialization of MEMS devices has also developed at a torrid pace. Today, almost all the accelerometers used in car airbag deployment systems are MEMS accelerometers [42]. Many of the most precise pressure sensors used in portable devices are MEMS pressure sensors [43]. Most recently, the biotech industry has embraced MEMS micro-fluidic technology to develop microchip bioassays, gene screening and chemical analysis systems [44]. Booming communication infrastructure companies (such as Lucent Technologies Inc. and Nortel Networks Corp.) are now turning to MEMS technology to develop micro-optical switches [45] that will re-route the packets of light blazing down fiber optic cables around the globe. MEMS devices are beginning to revolutionize the way we interact with our macroscopic and microscopic environments.

THESIS OUTLINE

The aim of this work is to develop miniature, inexpensive, high-quality, self-generating piezoelectric microphones that can be fabricated using piezoelectric PA-C by Micro Electro Mechanical systems (MEMS) technology. These MEMS piezoelectric microphones are to be used in any application where a conventional piezoelectric and electret microphone can be used (such as in cell phones, and hearing aids).

Although a complete piezoelectric PA-C MEMS microphone affords many advantages, there are many components of the technology that need to be developed or refined before a fully functional device was fabricated. With respect to the MEMS microphone history, theory, poling process, design, modeling, fabrication, packaging, testing and performance specs, this thesis is organized as follows:

- Chapter 2 introduces piezoelectric materials and reviews discrete and MEMS piezoelectric microphones.
- Chapter 3 introduces the piezoelectric properties of poled Parylene-C. It includes the poling process and characteristics of piezoelectric Parylene-C.
- Chapter 4 provides the theory and history behind a piezoelectric circular diaphragm and the design aspects of the microphones.
- Chapter 5 details the fabrication, testing and analysis of piezoelectric Parylene-C MEMS microphones.
- Chapter 6 summarizes the entire thesis.

Chapter 2

PIEZOELECTRIC MICROPHONE REVIEW

Piezoelectricity

When the charge is generated in certain solid materials, (such as crystals like quartz topaz, or ceramics, bone, protein, sugar and wood Figure 2-1), by applied mechanical stress, these materials can be called as piezoelectric material. It is derived from the Greek *piezo*, which means to squeeze or press, and *electric*, which stands for amber, an ancient source of electric charge.[46]

In 1820 Becquerel described and observed piezoelectric effects,[1] although a systematic study leading to modern understanding of these effects is credited to the Curies.[2] The two physicists found that the surfaces of certain crystals become electrically charged when the crystal is mechanically loaded.



Figure 2-1 Piezoelectric Materials

When a non-conducting crystal with no inversion symmetry, such as quartz (whose structure is shown in simplified form, Figure 2-2), is cut with the orientation of the axes of the crystal and stretched or pressed, a small charge is generated between opposite faces of the crystal, Figure 2-3. When the tension (T) changes to compression (C), the voltage changes sign.

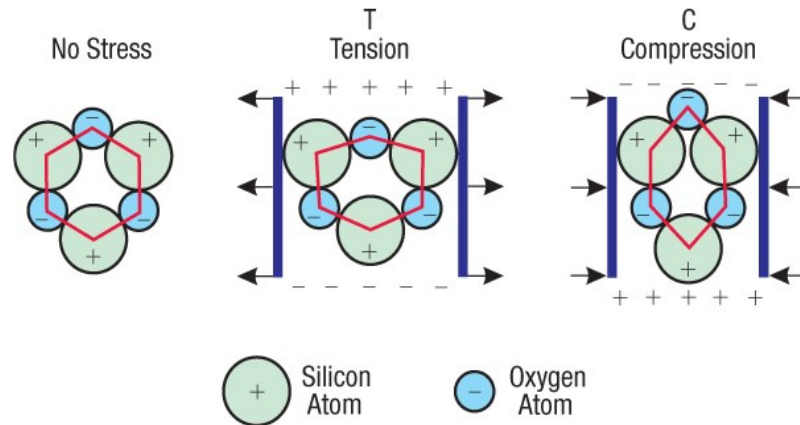


Figure 2-2 Piezoelectric effect on Quartz

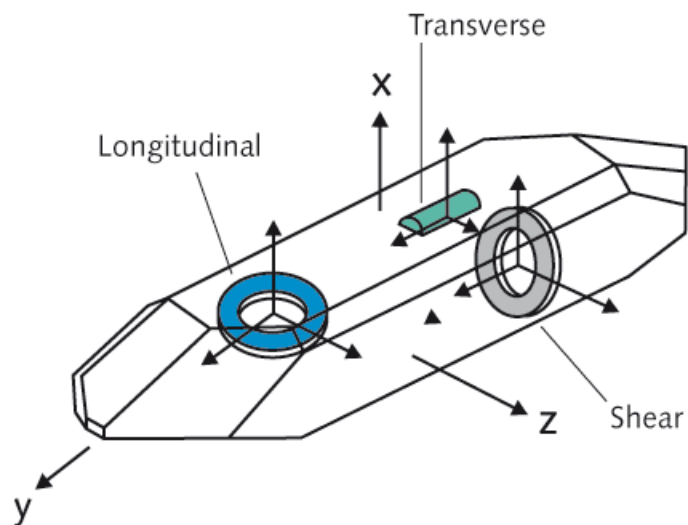


Figure 2-3 Cut of quartz

The piezoelectric effect is reversible in the materials. The generation of electrical charge results from an applied mechanical force, which is known as the direct effect. Also, piezoelectric materials also display the converse effect; the generation of a mechanical strain results from an applied electrical field. For example, quartz crystals will generate measurable piezoelectricity when their static structure is deformed. Conversely, those same crystals will change their static dimension when an external electric field is applied to the material Figure 2-4.

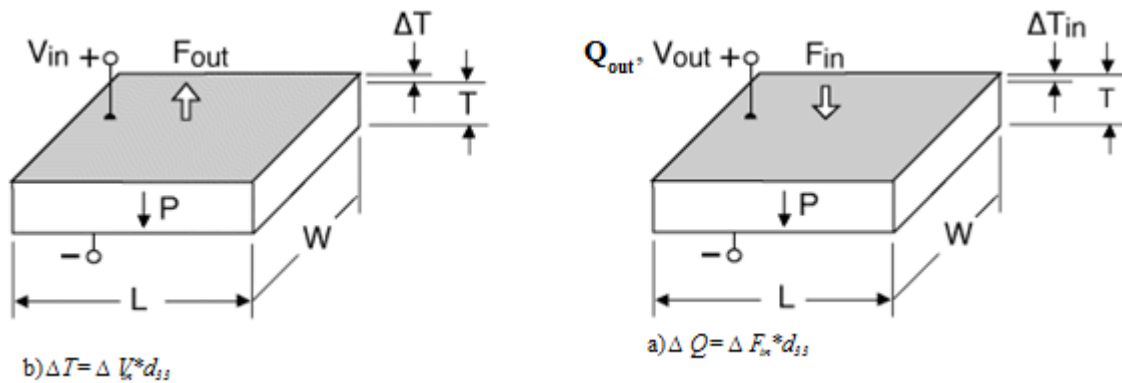


Figure 2-4 Reversible Piezoelectric effect. a) A generation of electrical charge resulting from an applied mechanical force, b) the generation of a mechanical strain from an applied electrical field.

A subset of piezoelectricity is pyroelectricity, whereby the polarization is a function of temperature. Some pyroelectric materials are ferroelectric, although not all ferroelectrics are pyroelectric. Ferroelectricity is a property of certain dielectrics, which exhibit a spontaneous electric polarization (separation of the center of positive and negative electric charge, making one side of the crystal positive and the opposite side negative) that can be reversed in direction by the application of an appropriate electric field.[6]

Piezoelectricity is found in useful applications such as the production and detection of sound, generation of high voltages, electronic frequency generation, microbalances, monitoring the health of airplanes wings, and energy harvesting[47–49]. It is also the basis of a number of scientific instrumental techniques with atomic resolution, the scanning probe microscopies (STM, AFM, etc.), and also, everyday uses for cigarette lighters as the ignition.

However, natural piezoelectric materials such as quartz, tourmaline, Rochelle salt, etc., are very small, polycrystalline ferroelectric ceramic materials such as barium titanate(BaTiO_3) and lead zirconate titanate (PZT, $\text{Pb}[\text{Zr}_x\text{Ti}_{1-x}]\text{O}_3$ $0 \leq x \leq 1$), it was developed by Yutaka Takagi, Gen Shirane and Etsuro Sawaguchi, physicists at the Tokyo Institute of Technology, around 1952) with improved properties have been developed. PZT ceramics are available in many variations and are

still the most widely used materials for actuator applications today. Before applied electrical field, PZT crystallites have symmetric cubic unit cells. At temperatures below the Curie temperature with electrical biasing, the lattice structure becomes deformed and asymmetric. The unit cells exhibit spontaneous polarization (see Figure 2-5), i.e. the individual PZT crystallites are piezoelectric.

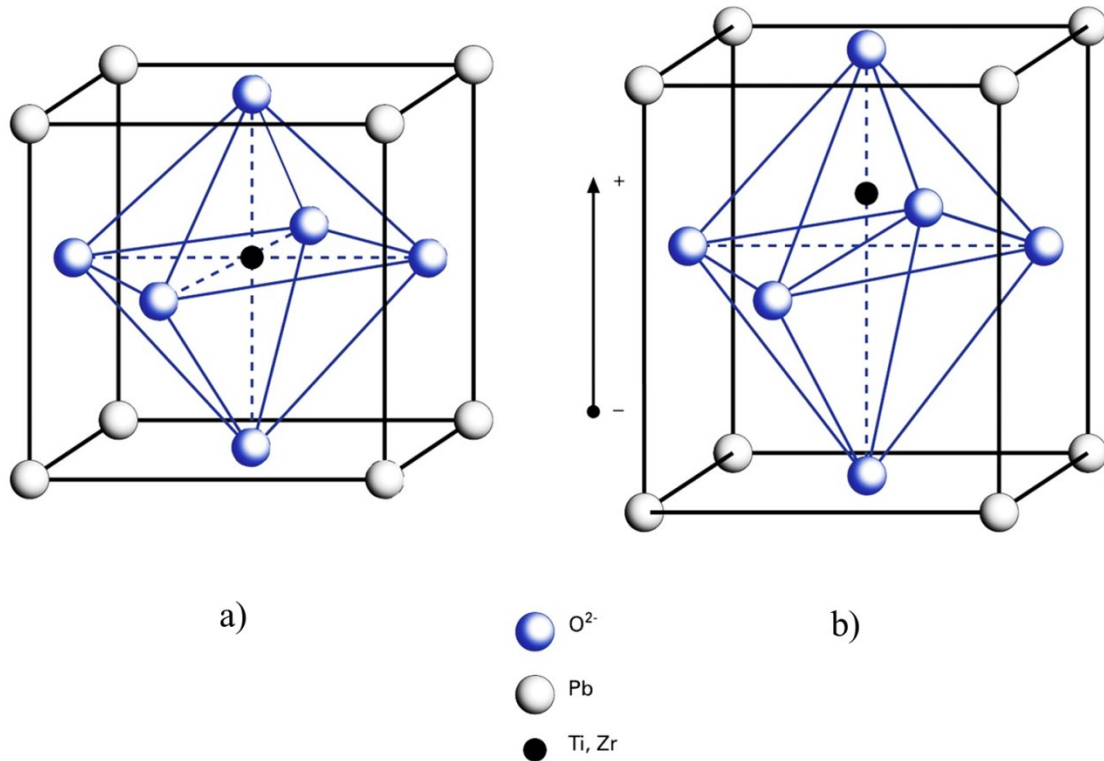


Figure 2-5 PZT unit cell: a) Perovskite-type lead zirconate titanate (PZT) unit cell in the symmetric cubic state above the Curie temperature. b) Tetragonally distorted unit cell below the Curie temperature[50].

Groups of unit cells with the same orientation are called Weiss domains. Because of the random distribution of the domain orientations in the ceramic material no macroscopic piezoelectric behavior is observable.[51] However applying an electrical bias, 1 MV/m, and heating, it is possible to force permanent alignment of the different. The material now has a remnant polarization (which

can be degraded by exceeding the mechanical, thermal and electrical limits of the material) properties as shown in Figure 2-6. Each arrow represents a polarization domain. The ceramic now exhibits piezoelectric[50].

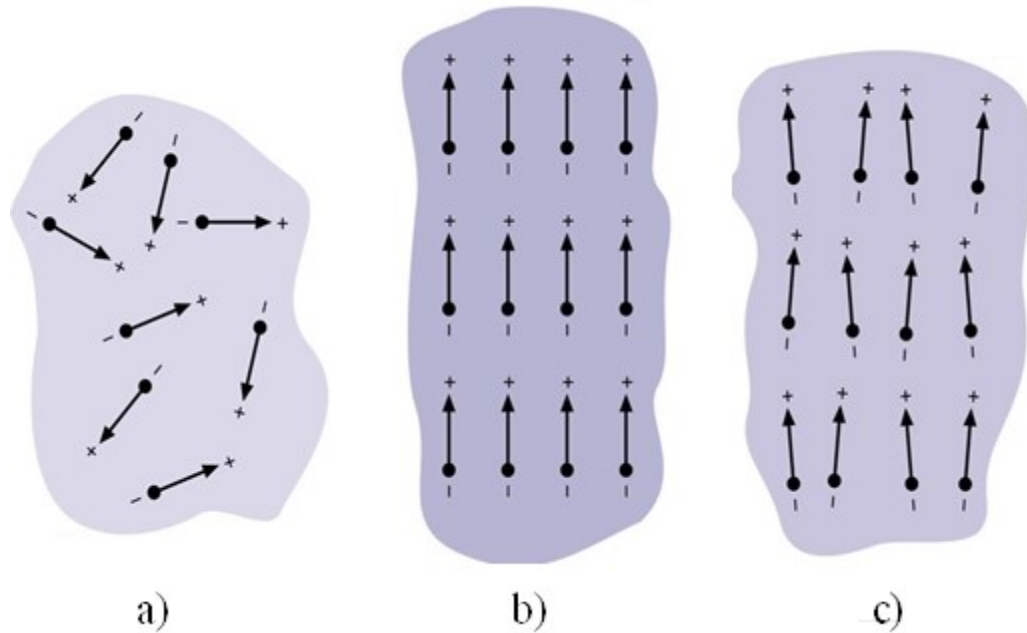


Figure 2-6 Electric dipoles in domains; a) unpoled ferroelectric ceramic below curie temperature, b) during the poling (applying electrical bias and heating near below the Curie temperature) and c) after poling[50].

Definitions of Piezoelectric Coefficients and Directions

Because of the anisotropic nature of PZT ceramics, piezoelectric effects depend on direction. To identify directions, the axes 1, 2, and 3 will be introduced (corresponding to X, Y, Z of the classical right-hand orthogonal axis set). The axes 4, 5 and 6 identify rotations (shear), θ_x , θ_y , θ_z (also known as U, V, W.) The axes and polarization are shown in Figure 2-7.

The direction of polarization (axis 3) is established during the poling process by a strong electrical field applied between two electrodes. For linear actuator (translator) applications, the piezo properties along the poling axis are the most important (largest deflection).

Piezoelectric materials can be characterized by several coefficients: d_{ij} and g_{ij} .

1. Charge mode (d_{ij}), Strain coefficients [m/V] or charge output coefficients [C/N]: A strain developed [m/m] per unit of electric field strength applied [V/m] or charge density developed [C/m²] per given stress [N/m²]. The charge output coefficients [C/N] is used to describe mechanical input and electrical output, such as microphone and vibration sensor. Generally, pC/N (pico-Coulomb per Newton) is widely used. The strain coefficient [m/V] is used for describing electrical input and mechanical output (for example, buzzer element and precise linear stage).
2. Voltage mode; g_{ij} : Voltage coefficients or field output coefficients [Vm/N, (V/m)/(N/m²)]: Open-circuit electric field developed [V/m] per applied mechanical stress [N/m²] or strain developed [m/m] per applied charge density [C/m²].

k_{ij} : Coupling coefficients [dimensionless]. The coefficients are energy ratios describing the conversion from mechanical to electrical energy or vice versa. k^2 is the ratio of energy stored (mechanical or electrical) to energy (mechanical or electrical) applied.

$$k^2 = \frac{\text{electrical energy stored as mechanical energy}}{\text{input electrical energy}}$$

$$k^2 = \frac{\text{mechanical energy stored as electrical energy}}{\text{input mechanical energy}}$$

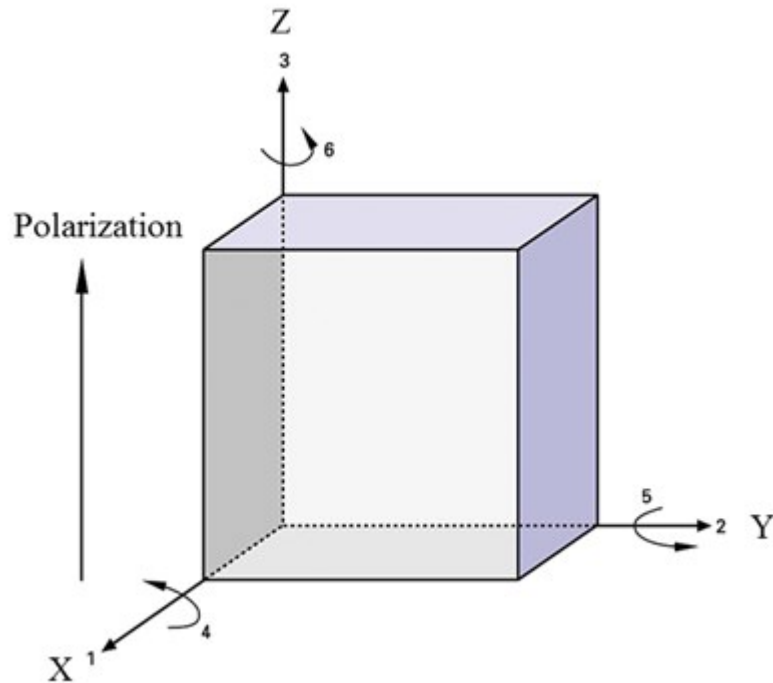


Figure 2-7 Orthogonal system describing the properties of a poled piezoelectric ceramic. Axis 3 is the poling direction[52].

Piezoelectric Polymer

Even though ceramic and crystal piezoelectric material is widely used, there are niche areas where single crystals and ceramics are incapable of performing sufficiently. Comparing to inorganic ceramic piezoelectric material, polymer piezoelectric material has unique advantages: flexible, lightweight, low acoustic and mechanical impedance; while inorganic materials are brittle, heavy [50]and toxic.[6] Despite its outstanding piezoelectric property, PZT is currently facing global restrictions due to its Pb-originated toxicity. The International Agency for Research on Cancer (IARC) classifies Lead Compounds (not metallic lead) as a Category 2A (probably carcinogenic to humans). The National Toxicology Program (NTP) classifies Lead/Lead Compounds as reasonably anticipated to be a human carcinogen based on limited human evidence and laboratory testing of animals.[53]

The piezoelectric strain constant (d_{33}) for the polymer is lower (Poly-Vinyl DiFluoro , PVDF , 30pC/N) than that of the ceramic (PZT, 300 pC/N). However, due to its low Young's modulus, piezoelectric polymers (PVDF, 240 mV-m/N) have much higher piezoelectric stress constants (g_{33}) than ceramic (PZT, 11 mV-m/N), which indicating that they can be better sensor than ceramics. Piezoelectric polymeric sensors and actuators offer the advantage of processing flexibility because they are lightweight, tough, readily manufactured into large areas, and can be cut and reformed into complex shapes. Polymers also exhibit high strength and high impact resistance.[7] Other notable features of polymers are low dielectric constant, low elastic stiffness, and low density, which result in a high voltage sensitivity (excellent sensor characteristic), and low acoustic and mechanical impedance (crucial for medical and underwater applications). Thus, for example, PVDF is widely used as sensor material such as, traffic signal control loop sensor buried under the load, musical instrument pickups, sports scoring, impact printers, bearing wear sensors, fan flow sensor and accelerometers.[8] Polymers also typically possess a high dielectric breakdown and high operating field strength, which means that they can withstand much higher driving fields than ceramics. Polymers offer the ability to pattern electrodes on the film surface, and to pole only selected regions. Based on these features, piezoelectric polymers earned their own area for technical applications and useful device configurations. In MEMS field, curable polyimide is also used to build a touch sensor array, air flow sensor and vibration sensor.[9–13]

For being Piezoelectric Polymers.

For respecting to polarization stability, four critical elements exist for all piezoelectric polymers, regardless for both semicrystalline and amorphous polymers. As summarized by Broadhurst and Davis[54] these four elements are: a) the permanent molecular dipoles; b) the molecular dipoles aligning ability to external electrical field; c) the sustainability of the dipole alignment once it is accomplished; and d) the durability to undergo large strains when mechanically stressed.

Mechanism of piezoelectricity in semicrystalline polymers.

As we mention before, semicrystalline polymers must have a polar crystalline phase to be a piezoelectric material. The crystallites disperse within amorphous regions of polymer as shown in Figure 2-8. The amorphous region is related to a glass transition temperature which dominates the mechanical properties of the polymer while the crystallites are related to a melting temperature that decides the upper limit of the use temperature. The degree of crystallinity in polymers depends on their thermal history and origin of preparation method.

Most semicrystalline polymers have several polymorphic phases, some of which may be polar. Electrical poling is accomplished by applying an electric field across the thickness of the polymer as depicted in Figure 2-8b). Typically an electric field on the order of 50 MV/m is sufficient to effect crystalline orientation at 90~100°C.[52], [55–61] Either a direct contact method or a corona discharge[62], [63] can be applied to Polymer poling. Also, it is reported that the simultaneous stretching of a polymer film while the poling process can increase piezoelectric coefficient roughly 2 times, Figure 2-8c).[64] Depending on whether stretching is uniaxial or biaxial, the electrical and mechanical properties (and therefore the transduction response), are either highly anisotropic ($d_{31} \neq d_{32}$) or isotropic ($d_{31} = d_{32}$) in the plane of the polymer sheet.

The corona charge is favorable for manufacture commercially available poly-vinylidene fluoride (PVDF) film because it doesn't require contacting electrodes and large area samples can be poled in a continuous extrusion. For semicrystalline polymers the amorphous phase supports the crystal orientation and the polarization is stable up to the Curie temperature. This polarization can remain constant for many years if it is not influenced by the spurious effects of moisture uptake or elevated temperatures.

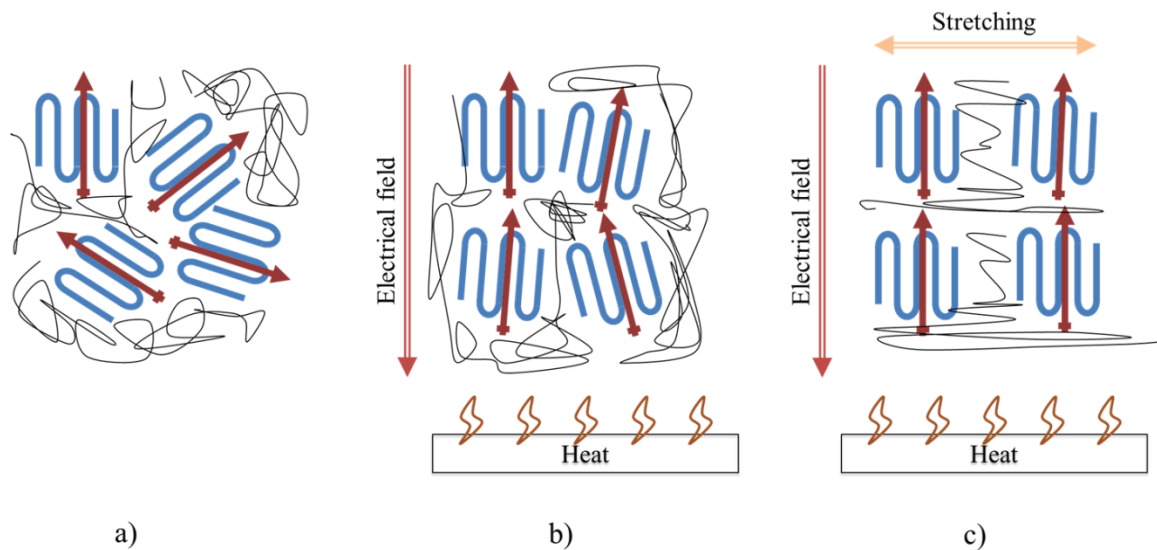


Figure 2-8 Schematic illustration showing random stacks of amorphous and crystal lamellae in PVDF polymer.

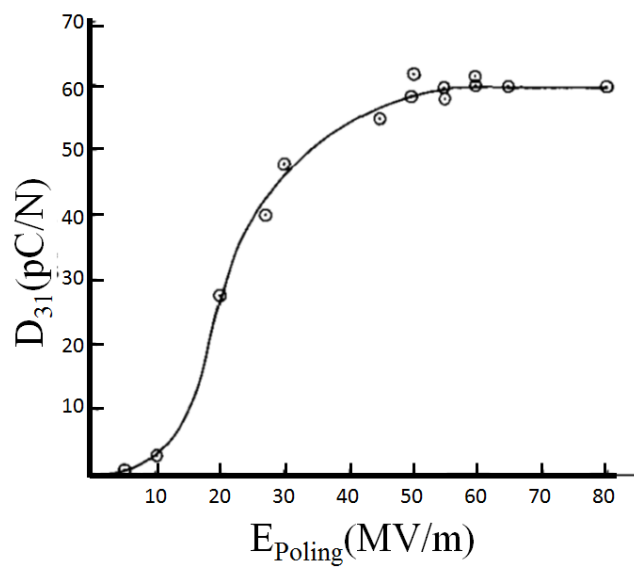
Poly-Vinyl DiFluoro (PVDF).

Interest in the electrical properties of PVDF began in 1969 when Kawai [65] showed that thin films that had been poled exhibited a very large piezoelectric coefficient, 6-7 pC/N, a value which is about ten times larger than had been observed in any other polymer. PVDF is inherently polar. The spatially symmetrical disposition of the hydrogen and fluorine atoms along the polymer chain gives rise to unique polarity effects that influence the electromechanical response, solubility, dielectric properties, crystal morphology and yield an unusually high dielectric constant. The dielectric constant of PVDF is about 12, which is four times greater than most polymers. This makes PVDF attractive for integration into devices as the signal to noise ratio is less for higher dielectric materials. The amorphous phase in PVDF has a glass transition point (-35°C) that is well below room temperature, hence the material is quite flexible and readily strained at room temperature. PVDF is typically 50 to 60% crystalline depending on thermal and processing history and has at least four crystal phases (α , β , γ , and δ), of which at least three are polar.[66–69] The most stable, non-polar phase results upon casting PVDF from the melt and can be transformed into the polar phase by

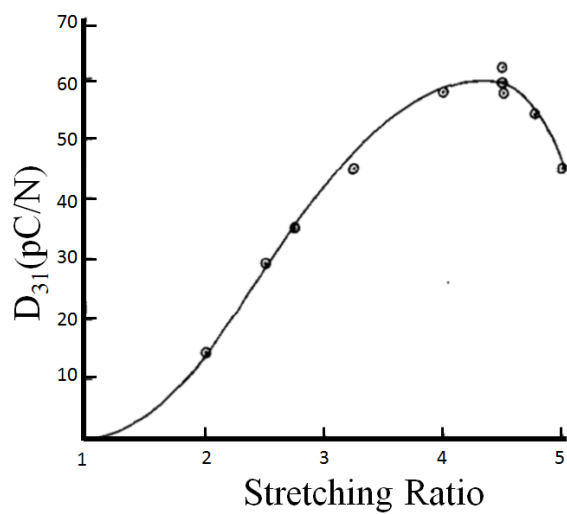
mechanically stretching at elevated temperatures or into the polar phase by rotating the molecular chain axis with a high electric field (~ 130 MV/m) [70]. The phase is most important for piezoelectric considerations and has a dipole moment perpendicular to the chain axis of 2.1 D corresponding to a dipole concentration. After poling PVDF, the room temperature polarization stability is excellent; however polarization and piezoelectricity degrade with increasing temperature and is erased at its Curie temperature. Previously it was believed that polarization stability was defined only by the melting temperature of the PVDF crystals. Recently, some researchers suggest that the polarization stability of PVDF and its co-polymers is associated with Coulomb interactions between injected, trapped charges and oriented dipoles in the crystals.[71] They hypothesize that the thermal decay of the polarization is caused by the thermally activated removal of the trapped charges from the traps at the surface of the crystals. The role of trapped charges in stabilizing orientation in both semicrystalline and amorphous polymers is still a subject that needs further study.[64]

A simultaneous stretching and corona poling process is studied for PVDF.[64] Without the stretching d_{31} is around 30 pC/N. But as we see in Figure 2-9a) it becomes around 60 pC/N. Also, poling condition is studied and it shows saturation over poling electrical field beyond 50 MV/m from Figure 2-9a). This is due to saturation in the number of crystallites and/or dipoles aligned in the field direction. For the stretching ratio as shown in Figure 2-9b), the maximum d_{31} is obtained at the ratio is 4.5. The stretching ratio is defined as the final length over initial length. From Figure 2-9c), we can see the d_{31} against poling temperature T_{poling} . d_{31} increases with poling temperature to a maximum of 60 pC/N in the range 70-85 °C, and decreases to 37 pC/N when poled at 110 °C. The drop in d_{31} may be due to an increase in electrical conductivity, which would reduce the effective poling field. The optimum poling parameters obtained from Figure 2-9 are $E_{\text{poling}} = 55$ MV/m, Stretching Ratio = 4.5 and $T_{\text{poling}} = 80^\circ\text{C}$.

The film at the optimum condition is also tested for its stability against the time and temperature as shown is Figure 2-10.



a)



b)

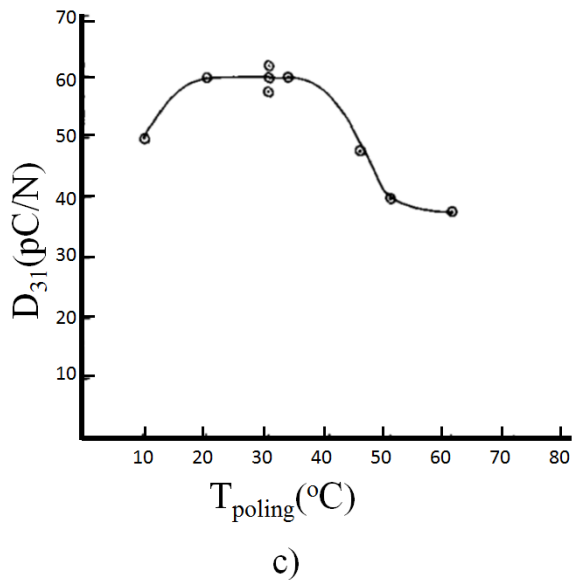


Figure 2-9 Piezoelectric coefficients of PVDF depends on, a) electrical bias; b) stretching ratio; c) poling temperature.

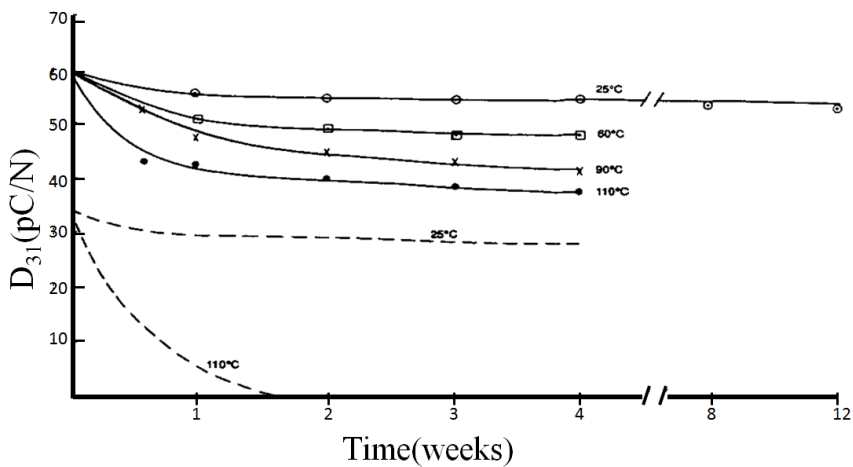


Figure 2-10 Time stability of optimum d_{31} at various decay temperatures, The line curves are Simultaneous Stretching and corona poling PVDF film; Broken curves are for first stretched and then poled PVDF films.

Non-MEMS Piezoelectric Microphone

In 1820 Becquerel described and observed piezoelectric effects[1] although a systematic study leading to modern understanding of these effects is credited to the Curies.[2] Nevertheless, piezoelectric microphones had not become practical until the invention of the "bimorph" Rochelle Salt transducer by Sawyer in 1931.[3] The "bimorph" ushered a quarter of a century era of dominance for Rochelle Salt crystals in low cost microphones. However, because of poor stability to the humidity of Rochelle salt, which there was new challenge from new ceramic material, polycrystalline Barium Titanate ceramics of Gray[4] and more recently by PZT ceramics of Jaffe.[5] Here, we are going to take a brief review for non-MEMS piezoelectric microphone.

Rochelle Salt transducer

The Rochelle Salt (sodium potassium tartrate tetrahydrate, $\text{NaKC}_4\text{H}_4\text{O}_6 \cdot 4\text{H}_2\text{O}$), colorless to blue-white orthorhombic crystalline salt with a saline, cooling taste. It is also called Seignette salt after Pierre Seignette, an apothecary of La Rochelle, France, who was the first to make it (c.1675). It is soluble in water and slightly soluble in alcohol, melts at about 75°C. Crystals of Rochelle salt are easily grown and are used in piezoelectric devices, e.g., crystal microphones and phonograph pickup cartridges

The Rochelle Salt transducer by Sawyer in 1931 is considered as the first practical invention of the piezoelectric microphones.[3] The microphone uses a thin strip of piezoelectric material attached to a diaphragm. The two sides of the crystal acquire opposite charges when the diaphragm deflects the crystal. This bimorph idea is widely used since this invention in low cost microphones. However, its solubility to water, low melting temperature and nature of fragile, it has a poor stability to the humidity and environment. It is quickly substituted with other piezoelectric ceramic materials, such as Barium Titanate ceramics of Gray[4] and more recently by PZT ceramics of Jaffe.[5]

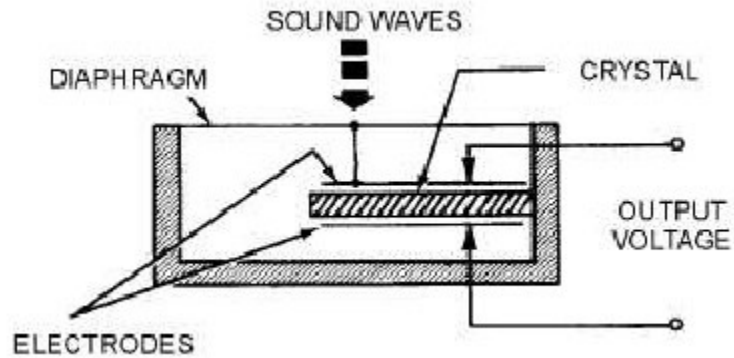


Figure 2-11 Rochelle Salt transducer, diaphragm type.

Piezo-Ceramic Microphone

Microphones using piezoelectric crystals and ceramics were widely used in consumer equipment some years ago but have now been largely superseded by electrets. Figure 2-12 shows a cross section of a ceramic microphone in which a light metal diaphragm is attached to a ceramic bimorph which produces an electrical output when a force is applied to it. These microphones are high-impedance devices, although not as high as capacitor microphones, and are not suited to harsh conditions because of the risk of damage by mechanical shock.

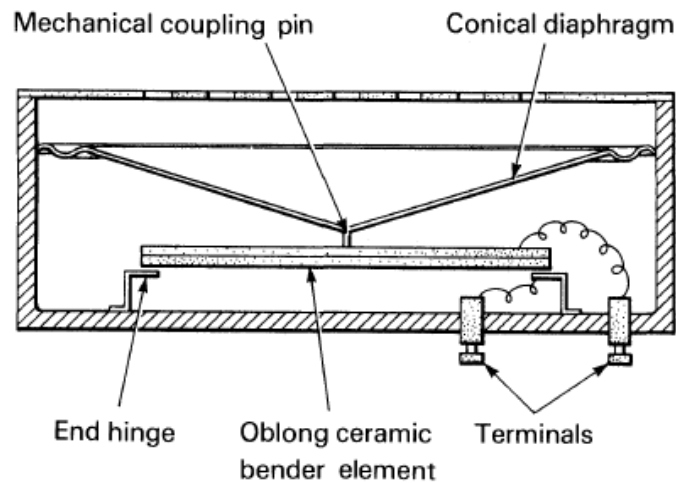


Figure 2-12 Piezo-Ceramic Microphone.

Piezoelectric Plastic

As we reviewed earlier, piezoelectric plastics have been developed and these materials are relatively tough and may be manufactured cheaply as thin flexible sheets. This raises the possibility of making an extremely simple robust microphone in which the diaphragm and transducer assembly consists solely of sheets of plastic and in which there are no small clearances to be set accurately, or fine wires to be manipulated during manufacture. This type of microphone has been under development at ACRC for some years and several prototypes have been produced for different applications.

The transducer assembly in all the PVDF microphones developed at ACRC has the same basic structure and consists of two sheets of PVDF clamped between two supporting plates, Figure 2-13. The two PVDF sheets behave as a bimorph structure in which one sheet is stretched and the other compressed when sound pressure is incident on them. The polarity of the sheets is arranged so that the electrical outputs reinforce.

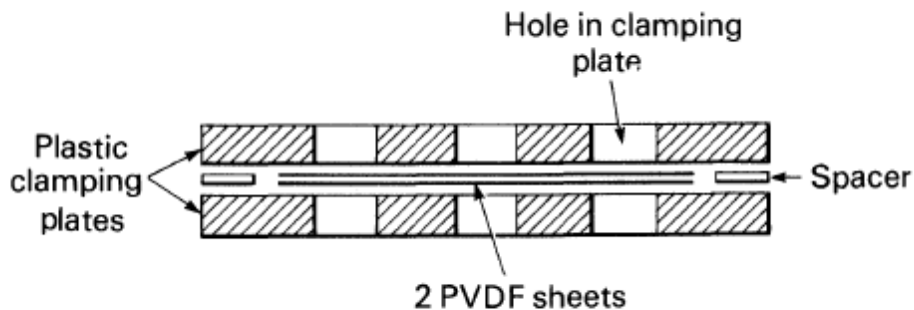


Figure 2-13 Basic PVDF Transducer.

MEMS PIEZOELECTRIC MICROPHONES

A piezoelectric-based microphone can offer two main advantages: no required input power and a wide dynamic range. A passive acoustic sensor is ideal for the low-cost disposable sensors required by the military for remote sensing. Although the piezoelectric sensors may be less sensitive than their capacitive and piezoresistive counterparts, they can be very advantageous in situations not necessarily governed by sensor sensitivity.

For example, in an open environment, low frequency and 1/f noise can dominate the spectrum and provide a noise floor of 30 to 40 dB sound pressure level (SPL) (re 20 μ Pa). Under the same conditions, typical battlefield sounds can be much greater than 100 dB SPL (e.g., a brick of C4 explosive at 30 m is 165 dB and a rifle shot at the shooter’s ear is 156 dB).

	Capacitive	Piezoresistive	Piezoelectric
Sensitivity (V/Pa)	Good 400 to 1000	Low 0.1 to 100	Medium 10 to 500
Input Power	Required	Required	None
Dynamic Range	Narrow	Relatively Wide	Wide

For a passive piezoelectric microphone, there are several options for the thin film sensor material including ZnO, aluminum nitride (AlN), and lead zirconate titanate (PZT).

A piezoelectric microphone based on PZT thin films[72]

Polcawich, Ronald G et. al. developed a piezoelectric microphone based on PZT thin films in order to investigate its potential use as a passive sensing element in a photoacoustic resonant cell.[72] The microphone fabrication process began with a double-side polished silicon wafer and used several different types of deposition systems. A plasma-enhanced chemical vapor-deposited (PECVD) silicon dioxide thin film (1 μm thick) was deposited with a Plasma-Therm 790 reactor using a mixture of SiH_4 , He, and N_2O . The oxide served as the membrane structural layer and was chosen to be 1 μm thick. After the deposition, the film was annealed in an A.G. Associates Heatpulse 610 rapid thermal anneal (RTA) furnace at 700 $^\circ\text{C}$ for 60 seconds in a nitrogen atmosphere to remove the trapped hydrogen within the film. And this annealing caused the film to obtain a slightly tensile stress, for producing a planar membrane.

After the oxide was deposited and annealed, a metal electrode was deposited via sputtering to serve as the bottom electrode and as a growth template for the piezoelectric actuator. Titanium/Platinum (200/800 \AA) was sputtered in a Varian 3190 direct current (DC) magnetron sputter deposition system. Titanium layer is used for improving adhesion. Following the platinum deposition, the wafers were annealed in the RTA furnace at 700 $^\circ\text{C}$ for 60 seconds in a flowing dry air in order to improve the adhesion between the oxide and metal layers and the surface texture of the platinum before deposition of the piezoelectric thin film.

The next fabrication step was to deposit the $\text{PbZr}_{0.52}\text{Ti}_{0.48}\text{O}_3$ thin film. The building process was a sol-gel spin-on process. First, a PZT sol-gel solution was prepared via a modified alkoxide process first introduced by Budd, Dey, and Payne [73]. This process used lead acetate trihydrate, zirconium n-propoxide, and titanium isopropoxide as the precursors and 2-methoxyethanol as the solvent. Once the sol-gel solution was prepared and aged, the repetitive deposition process, as depicted in Figure 2-14 c), began with a portion of the sol dispensed onto a platinized silicon substrate. The wafer was then spun at 2,500 rpm for 30 seconds. Next, the wafers were placed onto a hotplate at

350 °C for 120 seconds causing the film to undergo the pyrolysis, which thereby decomposed all the organics. This process of deposition, spin, and pyrolysis was then repeated a total of four times. After the last pyrolysis, the wafer was annealed in a RTA furnace at 700 °C for 30 seconds in the flowing air in order to crystallize the PZT thin film. The result was approximately a 0.25 μm PZT film, and the entire process was continued in order to achieve the desired thickness of a 1- μm PZT thin film. After the piezoelectric was deposited, a top electrode of platinum (800 Å) was sputter deposited onto the wafer surface. The wafers were then annealed in an RTA at 350 °C for 120 seconds in the flowing air to improve adhesion and reduce any sputtering-induced surface damage.

The resultant wafer stack at this stage was Si/SiO₂/Ti/Pt/PZT/Pt.

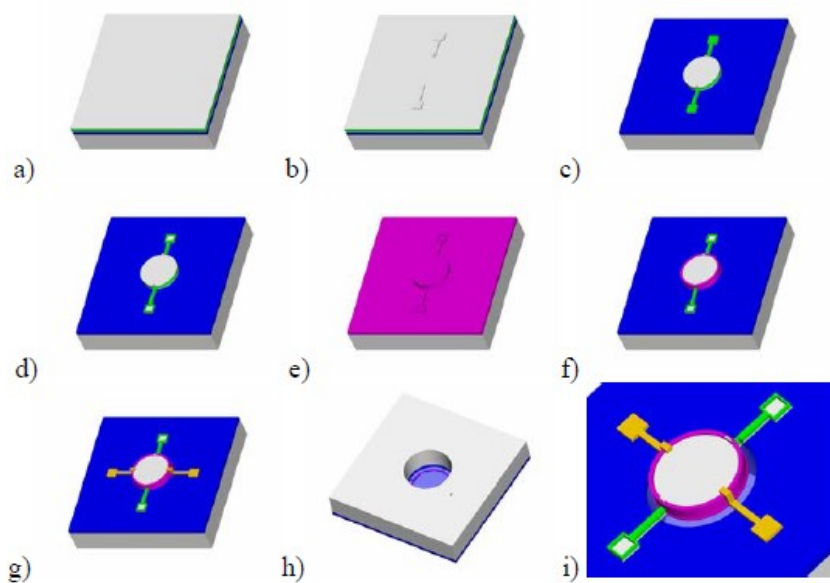


Figure 2-14 Fabrication process flow for creating a PZT membrane microphone: (a) Starting wafer, (b) sacrificial titanium, (c) Ar ion mill of Ti/Pt/PZT/Pt, (d) PZT wet etch, (e) oxide passivation deposition, (f) etching of passivation, (g) Ti/Au contact, (h) silicon DRIE, and front view of released PZT membrane.

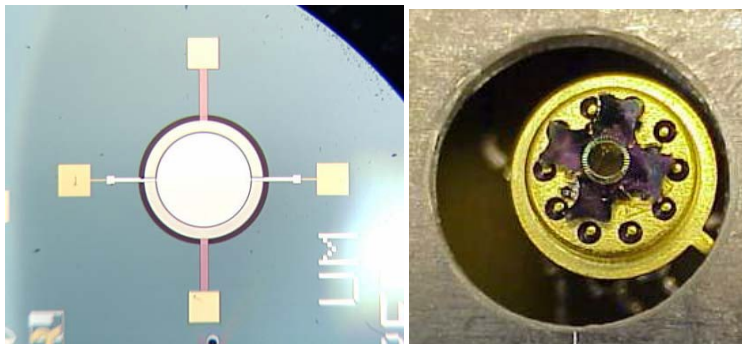


Figure 2-15. Images of the acoustic test chamber used for testing the PZT microphone. (The BNC mounts provide electrical contact to the packaged microphone whereas the acrylic plate on top provides a connection for the acoustic tube.)

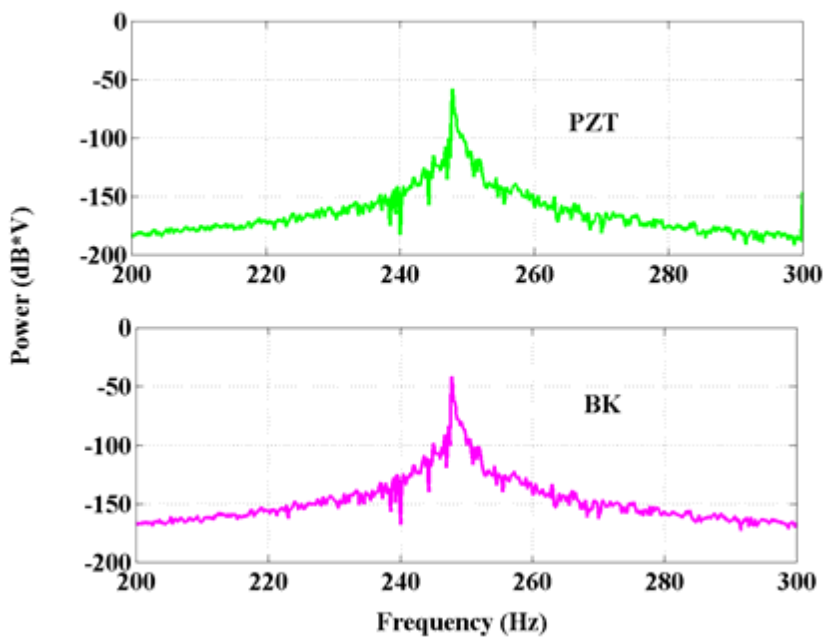


Figure 2-16 Acoustic response of a B&K and a 750- μm diameter PZT MEMS microphone with 20% sensor coverage for B&K Pistonphone 250-Hz tone at 124 dB and

An AlN MEMS Piezoelectric Microphone for Aeroacoustic Applications[74]

Achieving a high-dynamic range, particularly a high p_{\max} , is the most difficult performance challenge for an audio-band aeroacoustic microphone. Until recently, difficulties in fabrication and limited commercial availability of aluminum nitride (AlN) films resulted in very little attention to this material for use in microfabricated microphones[75–77], despite its attractive properties. These include high stiffness, a high material figure of merit for sensitivity (g_{31}), low dielectric loss, and high intrinsic signal-to-noise ratio [78]. For the fuselage array application, the low dielectric loss of AlN is a critical advantage over PZT and ZnO because it translates to an improved low-frequency microphone response.[78] As a result, AlN is utilized in this work.

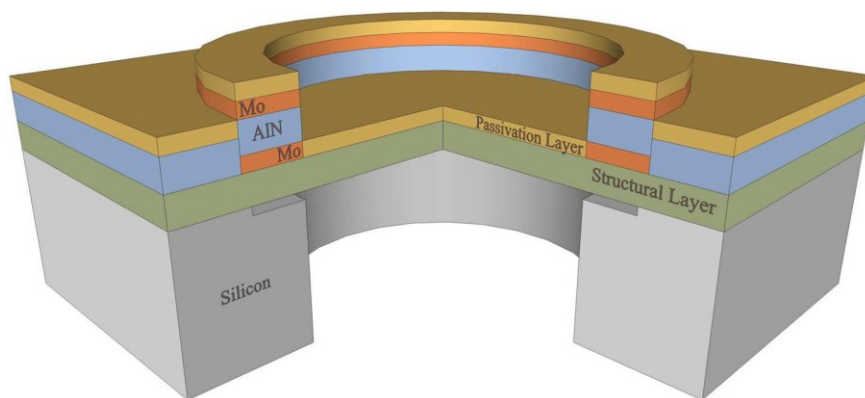


Figure 2-17 Microphone structure with quarter cutout (not to scale), featuring a circular diaphragm with an annular electrode/piezoelectric/electrode ring.

A depiction (not scaled exactly) of the microphone structure enabled by this process is shown in Figure 2-17. The operation of the microphone is based on deflection of the circular diaphragm due to an incident acoustic pressure wave. The annular metal/piezoelectric/metal film stack situated on the high stress/strain region around the outer boundary of the diaphragm produces a proportional output voltage. The diaphragm is composed of passivation, electrode (molybdenum), piezoelectric

(aluminum nitride), and structural layers. As proprietary features of the FBAR-variant process, the materials used in the passivation and structural layers are not disclosed.

Exact FBAR process details are proprietary. However, a general outline of fabrication steps was published by Avago Technologies[75],[79] and is summarized in Fig. 3. The process involved both surface and bulk micromachining, starting with a 675- μm -thick 150-mm (6-in) silicon wafer. First, a shallow cavity was etched and filled with sacrificial material, which served to define the diaphragm diameter and set an etch stop for subsequent backside processing. The wafer surface was thinned to 500 μm and planarized via chemical–mechanical polishing (CMP), as in Figure 2-19a). The structural, metal, piezoelectric, and passivation layers, in addition to the bond pads, were then deposited and patterned in a set of proprietary process steps [Figure 2-19b)]. A deep reactive ion etch (DRIE) from the backside of the wafer formed the back cavity [Figure 2-19c)], and the sacrificial material was etched to release the diaphragm [Figure 2-19d)]. A fabricated and diced microphone is shown in Figure 2-18.

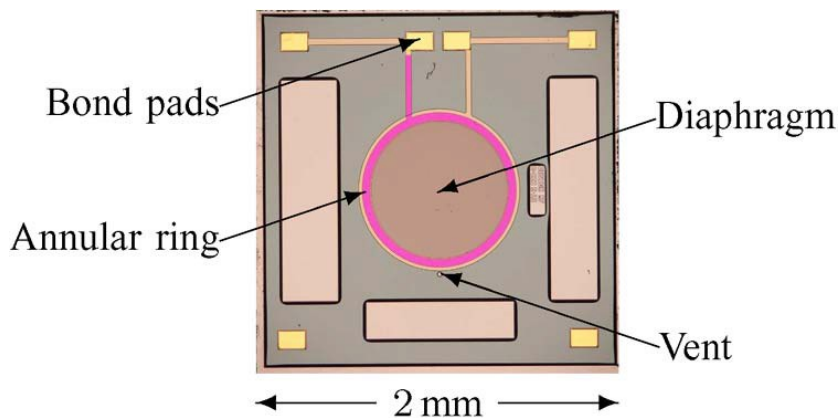


Figure 2-18 Micrograph of a MEMS piezoelectric microphone (design F; refer to Section III-E).

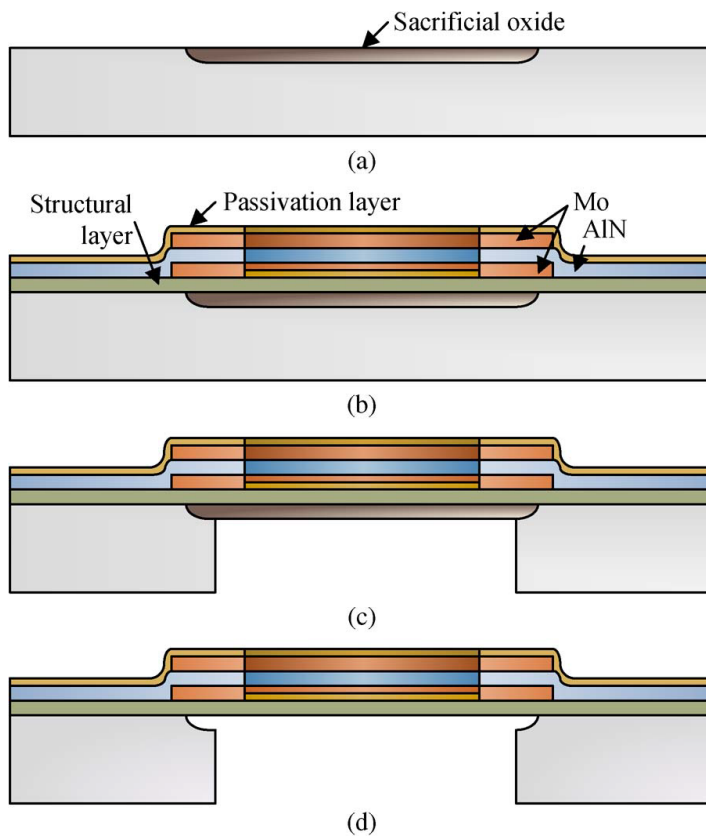


Figure 2-19. Outline of fabrication steps. (a) Etch cavity in silicon wafer, and deposit sacrificial oxide. Perform CMP. (b) Deposit and pattern films (structural layer, Mo/AlN/Mo stack, and passivation layer). (c) DRIE through backside, and stop on sacrificial oxide. (d) Release the diaphragm via oxide release etching.

The performance of microphones with thin-film diaphragms is extremely sensitive to film stress. The amount of stress control varies by process; sputter deposition (common for AlN), for instance, is a complex process that does afford some flexibility to tailor stresses. Customization of the stress state is achieved via adjustment of bias power, argon pressure, sputtering gas mass, temperature, and/or deposition rate.[80] Avago Technologies is able to adjust film deposition parameters to target a large range of film stresses.

ZnO on Si integrated acoustic sensor[81]

The structure of the device is based upon a ZnO PIFET[82]. A thin ZnO piezoelectric film is connected to the gate of an MOS amplifier integrated on the same Si substrate. When a piezoelectric voltage is created across the ZnO layer, it modulates the input signal to the gate of the MOS, varying the channel current. In order to extend the frequency response of the devices to below 1 Hz, insulating layers of SiO_x are used to encapsulate the ZnO film, the sensor electrodes and the connecting leads to the MOS amplifier. This effectively reduces surface and interface charge leakages.[83] The acoustic sensor design is shown in Figure 2-20. A thin diaphragm is formed under the ZnO active film using anisotropic etching techniques, giving the device a high sensitivity to incoming sound waves. The concentric electrode configuration, shown in Figure 2-21, was designed to cancel the sensor response to temperature variations due to the pyroelectric property of the ZnO.[84] This is an important concern, especially for low-frequency applications. The electrode pattern forms two ZnO capacitors, one formed by the center electrode, the other by the outer ring electrode. These two capacitors are connected in series through the top circular electrode and the output signal is taken across the bottom concentric electrodes. The pyroelectrically induced charges being uniform in the whole ZnO film.

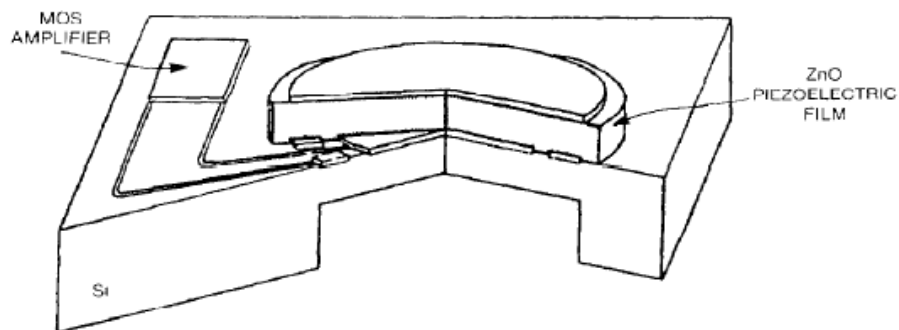


Figure 2-20 Cutout diagram of the device (not to scale).

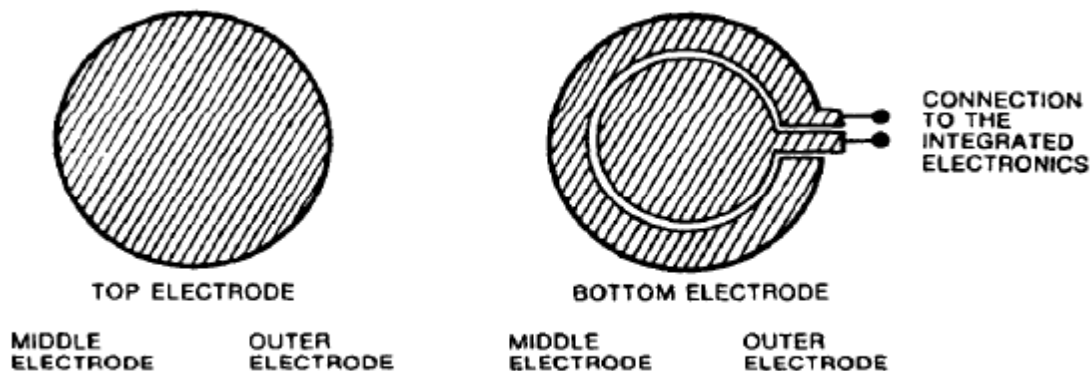


Figure 2-21 Structure of the electrodes. Because the center part and outer part is under the different direction of the stress, the bottom electrodes are divided in two sections.

On the other hand, when the diaphragm is flexed under a uniform pressure, the central part of the diaphragm is under tension while the outer part is under compression, creating piezoelectric voltages of opposite signs in the two capacitors. The piezoelectric signals add to one another, thus increasing the pressure sensitivity of the device. A third advantage of this electrode design is that it allows the connections between sensor and on-chip electronics to be made at the ZnO/Si interface, suppressing step coverage problems. The structure dimensions are shown in Figure 2-22.

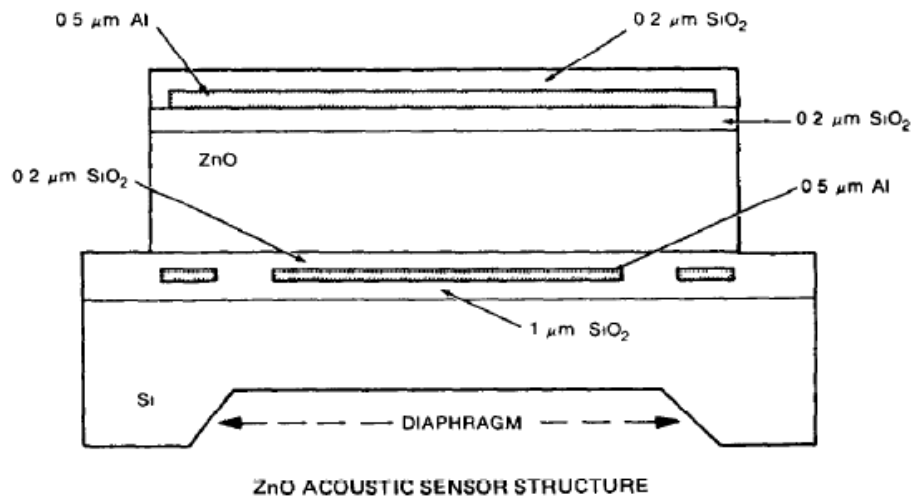


Figure 2-22 Crosssectional view of the device.

Using the stress equations of a circular plate with clamped edges [85], the device performances can be computed. The expected sensitivity for a 3 mm diameter, 30 μm thick diaphragm with a 3 μm thick ZnO layer is 37 $\mu\text{V}/\text{ubar}$. Some noise computations were also conducted using a circuit analysis program and these predicted a signal-to-noise ratio of 8:1 at 2 ubar .

The first step in the sensor fabrication is the processing of the amplifiers. These are PMOS devices with a high input impedance ($>10^{13}$). The expected gain of amplification was 2 and the drain current at standby was 10 pA with a 4 volt supply. After the SiO_2 layers and the bottom electrodes are deposited, the ZnO process takes place. A planar magnetron sputtering system with a ZnO target was used for the ZnO deposition. The film quality is very dependent on the careful adjustment of the sputtering parameters.[86] Extensive development work was conducted to establish a process yielding good quality ZnO layers with high piezoelectric efficiency and low stress levels. This is particularly important in this sensor, since the diaphragm thicknesses are about 30 μm while the ZnO layer thickness is up to 5 μm , any significant amount of thermal mismatch between the ZnO layer and the substrate will result in unacceptable warpage of the diaphragm. After completion of the front side processing, the diaphragms are etched from the back surface of the chips. The present chip size is 6 mm on the side with a diaphragm diameter of 3 mm. The chip is shown in Figure 2-23.

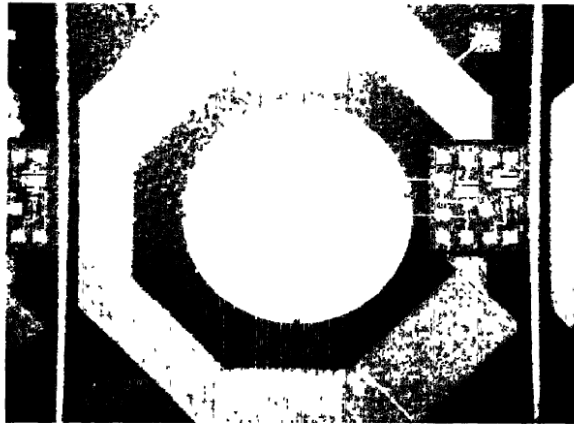


Figure 2-23 Top view of the device.

Fabrication and Characterization of Piezoelectric Micromachined Ultrasonic Transducers with Thick Composite PZT Films[87]

This device is not a microphone but ultrasound-radiating applications. For the sound radiating, thicker PZT films are preferred because generative force and response speed of the diaphragm-type transducers increase with increasing film thickness. However, integration of 4 to 20 μm thick PZT films on silicon wafer, either the deposition or the patterning, is still a bottleneck in the micromachining process.

This research reports on a diaphragm type piezoelectric micromachined ultrasonic transducers. A composite coating technique based on chemical solution deposition and high-energy ball milled powder has been used to fabricate thick PZT films. The fabricated device with crack-free PZT films up to 7 μm thick was evaluated as an ultrasonic transmitter. The generated sound pressure level of up to 120 dB indicates that the fabricated device has very good ultrasound-radiating performance and, therefore, can be used to compose form of arrays for generating ultrasound beam with high directivity in numerous applications.

The key technique of the composite processing is how to prepare uniform slurry by dispersing PZT powder (APC 850 from APC International Ltd., Mackeyville, PA) with desired size into PZT sol-gel precursor solution ($Zr/Ti = 53/47$). The details of the slurry preparation have been described elsewhere[88], [89]. High energy ball milling, which is effective in getting the well-dispersed slurry, was used to perform the mixing procedure. A selected dispersant first was added to the powder during ball milling to get surface-modified powder with desired size.

The smaller the powder is, the more important this procedure is. Afterward, the PZT sol-gel solution was mixed with the surface-modified powders and ball milled till uniform slurry was obtained. The prepared slurry then was deposited on platinized silicon wafer using a spin-coater. The added powder can reduce the stress within the film significantly, thus it is easy to obtain thick films without crack. During spin-coating, the important procedure is that powder-free, sol-gel thin layers and slurry-derived thick layers were deposited alternately.

The first layer of powder-free thin film was deposited on the bottom electrode as a buffer layer to enhance the adhesion between thick film and the substrate. After several thick coatings were deposited, an intermediate pure precursor solution layer was deposited because it can infiltrate into the pores or other defects in the thick film to increase the film density and smooth the film surface. Figure 2-24 shows two typical microstructures of two composite films using nano-sized and submicron-sized PZT powder, respectively.

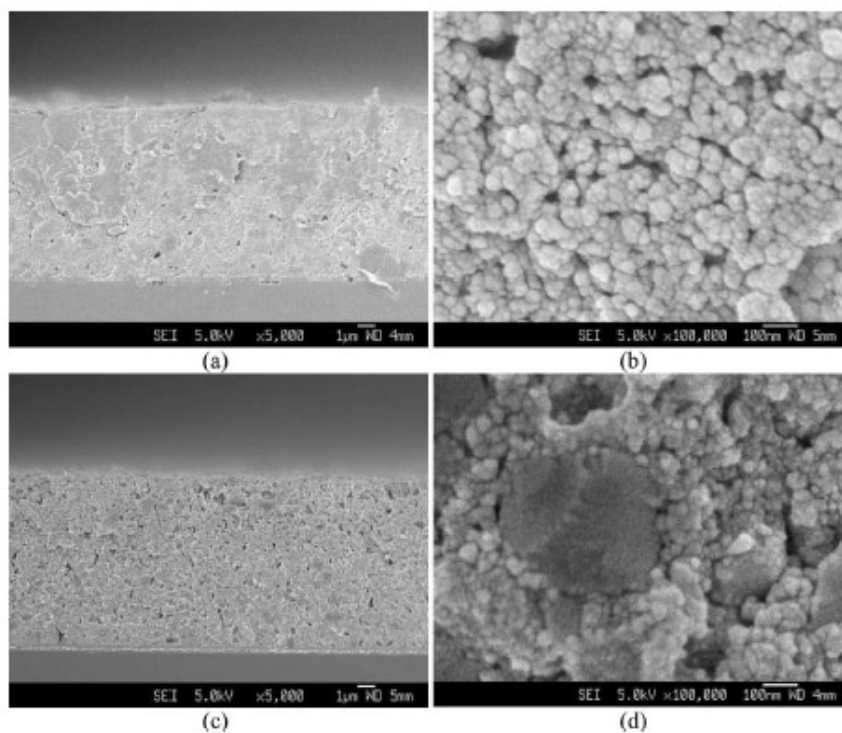


Figure 2-24 Cross-section images of two 10 μ m thick composite films. (a) and (b) Loaded with nano-sized powder; concentration of sol-gel solution is 40 wt%; powder-to-solution mass ratio is 1 to 2. (c) and (d) Loaded with submicron-sized powder, concentration of sol-gel solution is 40 wt%; powder-to-solution mass ratio is 2 to 3.

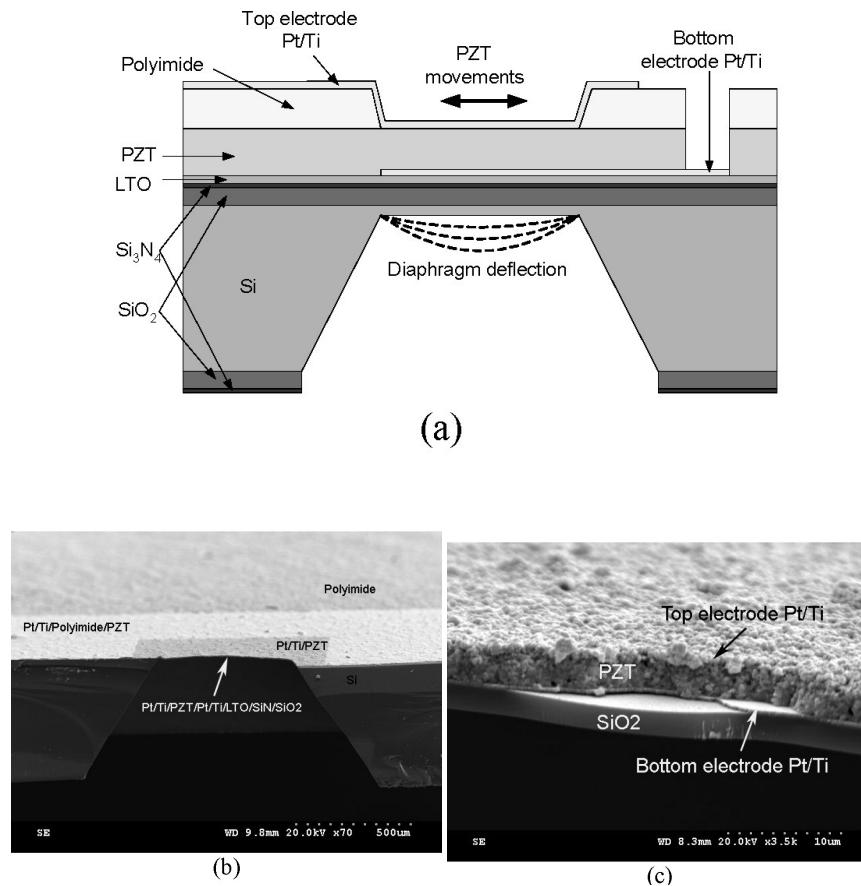


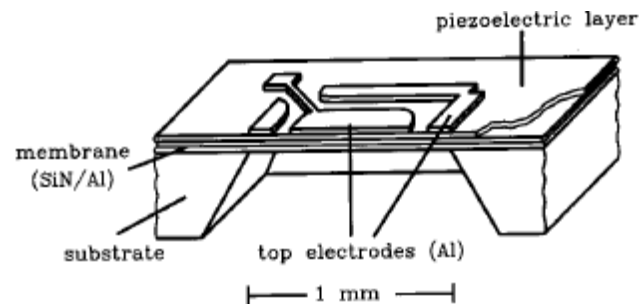
Figure 2-25 Cross-section view of ultrasonic radiating device

First, a 1.8- μm thick layer of thermal silicon oxide, which can be used as a structural layer of the diaphragm, was grown on double side, polished silicon or SOI wafer, shown in Figure 2-25 a); a silicon nitride layer with a thickness of 200 nm then was deposited as wet etch mask of backside silicon (Si); after that, a lower temperature oxide (LTO) layer with a thickness of 350 nm was deposited to enhance the reliability and heat resistance of the bottom electrode; a Ti/Pt layer, 200-300 nm thick, was sputtered and patterned by using lift-off as a bottom electrode. The thick PZT layers with required thickness then were deposited by using the composite technique. After a wet etching of the PZT layer, a polyimide layer was spin-coated and patterned as an insulation layer to minimize a parasitic capacitance induced by patterned electrode wiring. The top electrode also was patterned by lift-off. And, the backside silicon was etched off by KOH or DRIE until the required

thickness, usually within the range of 0 to 20 μm , depending on each other with the thickness of the PZT layer. In the example shown in Figure 2-25c), the PZT layer is about 3.5 μm in thickness, the backside silicon was completely etched out and only silicon oxide (SiO_2) layer with a thickness of about 2 μm was left, the SiN/LTO is invisible because their thickness is too thin to be observed in this magnification. If a SOI wafer with 20 μm thick top silicon layer is used, the thickness of the PZT layer should be about 10 μm , or about half of the silicon layer thickness.

Electroacoustical measurements of silicon microphones on wafer scale[90]

A schematic view of the piezoelectric microphone is shown in Figure 2-26. The sensor consists of an SiN/Al membrane (the aluminum metallization acts as one single bottom electrode), covered with a thin polymer layer of (PVDF/ TrFE) and a top electrode split into two separate parts. In case of a deflection of the membrane an electrical voltage between the top and the bottom electrode is generated due to the transversal piezoelectric effect of the corona poled polymer. The voltages, which are generated at the inner and outer part of the top electrode, are connected in series by the bottom electrode, increasing the sensitivity of the microphone. The area of the membrane is about 1 mm^2 and the source impedance amounts to 10-20 pF, depending on the thickness of the polymer layer.



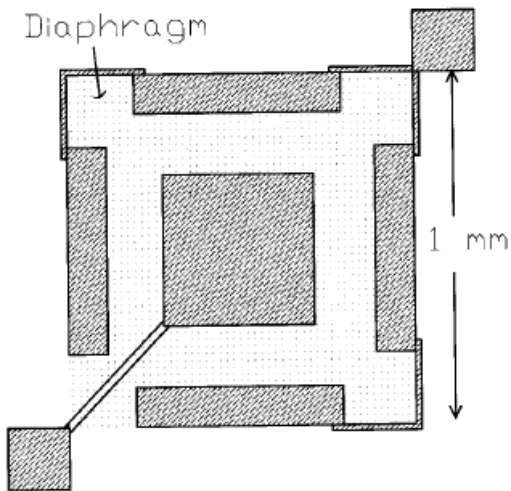


Figure 2-26 A silicon microphone with a piezoelectric polymer layer.

A measured open-circuit frequency response of a piezoelectric microphone (polymer thickness: 4.3 mm, membrane thickness: approximately 300 nm, polarization field about 150 MV/m), is shown in Figure 2-27. The measured frequency response is flat within 61 dB between 100 Hz and 10 kHz with a slight increase of 3 dB between 10 and 15 kHz. This increase may be due to a resonance of the microphone above 20 kHz. The measured sensitivity to airborne sound at 1 kHz is 0.21 mV/Pa (73.6 dB *re*: 1 V/Pa) and the loading amounts to -11 dB. Using these two values, an open-circuit sensitivity of 0.74 mV/Pa (-62.6 dB *re*: 1 V/Pa) is measured.

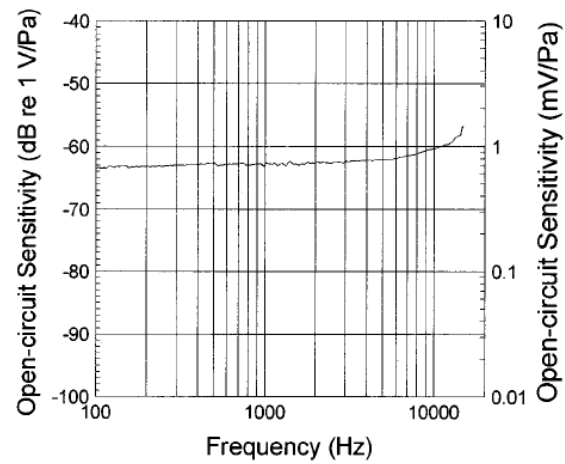


Figure 2-27 Measured open-circuit frequency response of a piezoelectric microphone.

Microphone based on Polyvinylidene Fluoride (PVDF) micro-pillars and patterned electrodes[91]

A sensor design consisting of micron-sized Polyvinylidene Fluoride (PVDF) pillars which generate a charge when subjected to normal stresses associated with acoustic waves. A rigid membrane placed between the micro-pillars and the acoustic medium ensures high mechanical coupling. The electrode covering the micro-pillars is patterned to decrease the capacitance, and hence increase the sensitivity of the sensor.

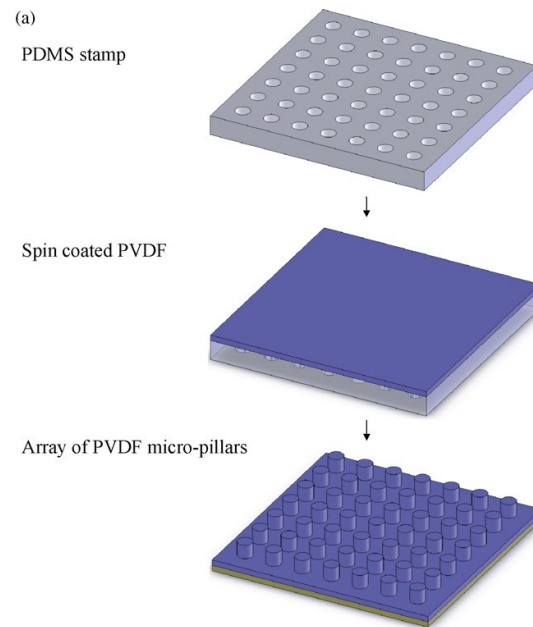


Figure 2-28 Schematic of PVDF microphone process

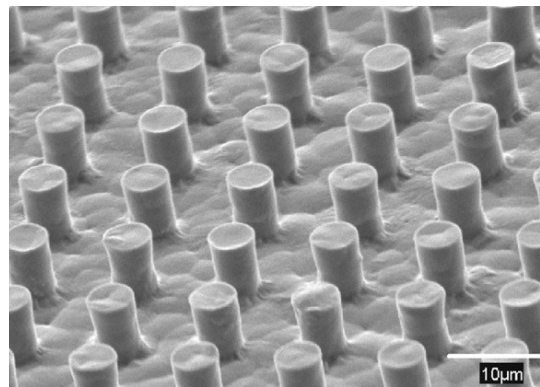


Figure 2-29 Pillar structure formed from PVDF and corresponding electrodes

PVDF micro-structures were fabricated using a procedure which is described in detail elsewhere[92]. Previously patterned PDMS (polydimethylsiloxane) stamps molded from

photolithographically fabricated masters were used to obtain arrays of PVDF micro-pillars with designed dimensions (Figure 2-30).

A 10% PVDF solution in dimethylacetamide/acetone was spin coated on the PDMS stamps at 1000-2000 rpm for 1 min. The stamps were placed on a hot plate at 100 °C for 5 min in order to drive off residual solvent and anneal the PVDF. The spin coated PVDF film was then transferred onto the adhesive side of copper tape using slight pressure. Figure 2-29 shows scanning electron micrographs of PVDF pillars.

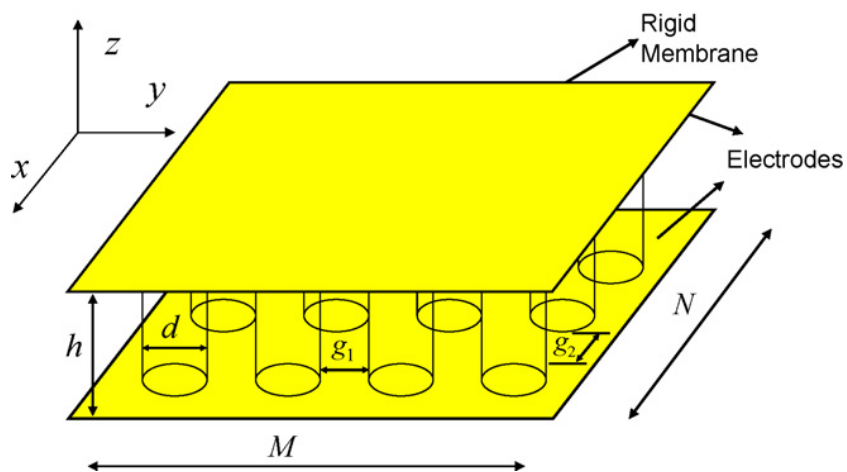


Figure 2-30 Schematic diagram of PVDF micro-pillar sensor with full electrodes.

Preliminary experiments were conducted with the goal to characterize the piezoelectric response of the PVDF micro-pillars. These proof-of-concept experiments were conducted on a non-optimal micro-pillar array ($d = 5 \mu\text{m}$, $g = 5 \mu\text{m}$, $h = 6 \mu\text{m}$, $N = M = 1000$). A gold-coated glass slide was placed on top of the micro-pillars (top electrode), and an electric field of $\sim 120\text{MV/m}$ was applied across the electrodes (top positive and bottom negative) at 160 °C for 3 h, and then at room temperature for an additional hour to pole the PVDF micro-structures.

Piezoelectric Polyimide MEMS Device[13]

The temperature stability of the piezoelectric properties of PVDF are maintained is limited to less than 80 °C. In this research, a surface-micromachined process for fabricating the structural components for polyimide-based MEMS with high-temperature stability is presented. The high temperature performance of these modified polyimide films allows these films to maintain their piezoelectric properties at temperatures up to 150 °C, twice that of PVDF[10–12], see the graph in Figure 2-31.

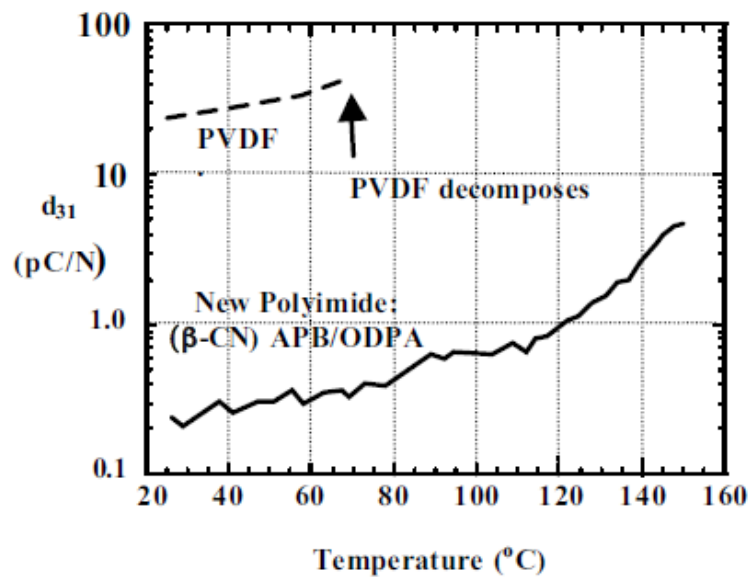


Figure 2-31 The piezoelectric strain coefficient (actuator response) of polyimides vs. PVDF.

Polyimide polymers have exceptional thermal, mechanical, and dielectric properties, polyimides are already widely utilized as matrix materials in aircraft and as dielectrics in the microelectronics industry. Recently, amorphous polyimides containing polar functional groups have been synthesized and investigated at VCU and NASA LaRC for potential use as high temperature piezoelectric sensors.[15][14]

One special step of this device is, in order to keep the polyimide film preparation temperatures low (to keep the underlying sacrificial photoresist intact), they used a chemically pre-imidized polyimide solution for this process. In this case, to form the polyimide film, the solvents are completely driven out using a 24-hour bake at 90 °C. Differential Scanning Calorimetry (DSC) measurements are underway to verify that the films are completely cured.

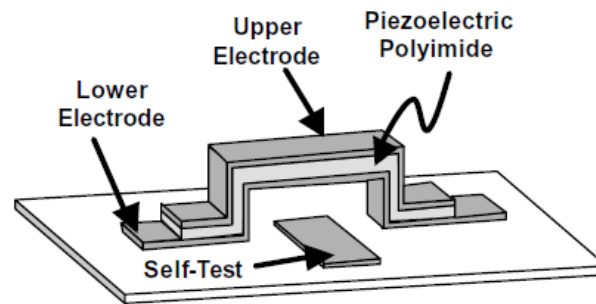


Figure 2-32 Piezoelectric polyimide sensor structure.

To ensure that the suspended components do not contact with the substrate by capillary action during drying, becoming permanently adhered by van der Waals forces. This is prevented in the release process by replacing the acetone with methanol, which is then replaced with pentane and finally, hexane. The wafer can then be dried in air at room temperature.

After the fabrication steps, poling step to orient the dipoles and give the polyimide film its piezoelectric properties is accomplished by applying a voltage across the structure at an elevated temperature ($T > T_g$). In this step, 100V is applied (applied between the upper and lower electrodes) for 1.3 μm and 2.15 μm thick polyimide bridge structures (77 MV/m and 47 MV/m respectively) at temperatures of 170 °C and 200 °C.

MEMS Condenser Microphone

A condenser microphone has a high sensitivity and a wider bandwidth among the current microphone technologies. Consequently, numerous researches have been accomplished to build a MEMS condenser (electret) microphone.

In 1986, Hohm presented a MEMS condenser microphone [20, 21]. The microphone consisted of two chips, one carrying the $150 \text{ nm} \times 0.8 \text{ mm} \times 0.8 \text{ mm}$ LPCVD silicon nitride diaphragm, and the other the silicon backplate and air gap spacer (Figure 2-33). Both chips were manufactured by bulk-micromachining and glued together to form the microphone structure (measuring $1.7 \text{ mm} \times 2 \text{ mm} \times 0.6 \text{ mm}$). The capacitance was 1.4 pF . To increase the sensitivity, nitrogen ions were implanted into the nitride diaphragm to reduce the tensile stress. For a bias voltage of 28 V , the open-circuit sensitivity was as high as 4.3 mV/Pa for frequencies up to 2 kHz . This microphone was an improvement on the above electret microphone in terms of using reproducible MEMS fabrication techniques, but the lack of acoustic holes in the backplate severely limited the frequency bandwidth.

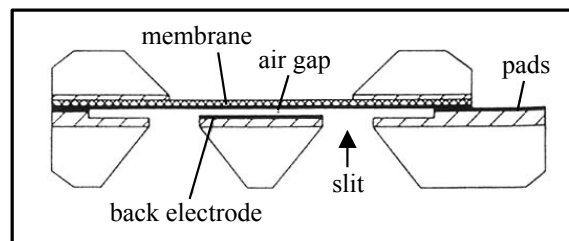


Figure 2-33 Silicon condenser microphone of Hohm and Hess (1986) [93].

SUMMARY

As we have reviewed piezoelectric transducers including microphones, the piezoelectric device has the advantage over the condenser microphones, even though its low sensitivity: no required input power and a wide dynamic range. A passive acoustic sensor is ideal for the low cost in situations not necessarily governed by sensor sensitivity.

Since the discovery of the piezoelectric effect, extensive results have been accomplished in inorganic or organic materials. Comparing to inorganic ceramic piezoelectric material being brittle, heavy and toxic [4], the polymer piezoelectric material has its advantages; flexible, lightweight, low acoustic and mechanical impedances.

Since the invention of PVDF with an acceptable level of piezoelectric coefficient due to its low mechanical modulus, polymer piezoelectric devices have been widely researched in a variety of fields and materials. However, even though the overwhelming piezoelectric properties of PVDF over other piezoelectric polymers, it is lack of the temperature stability of the piezoelectric property. It is limited to less than 80 °C. For the niche, polyimide-based MEMS devices with high-temperature stability are presented [9–15].

However, polyimide has hydrophilicity, which induces lower stability over high-humidity environment. These films are cured in convection or diffusion ovens at high enough temperatures (350-400°C) [16] to assure adequate mechanical and electrical properties. These high temperatures can change the electrical properties of the devices. If the cure temperature of these films are lowered there could be a reduction in the film (and wafer) stress as well as a lower thermal budget for the devices. However, curing polyimide films at temperatures lower than 250°C has not been found to provide the mechanical, chemical, and dielectric properties required for the final device operation parameters or mechanical and dielectric protection[17].

As we reviewed briefly, still are there lack of proper piezoelectric polymer material, which has acceptable piezoelectricity; high temperature stability; integrating ability to conventional MEMS process; and environmental safety.

Chapter 3

PIEZOELECTRICITY OF PARYLENE-C

Parylene-C

Parylene development started in 1947, when Michael Szwarc discovered the polymer as one of the thermal decomposition products of a common solvent p-xylene at temperatures exceeding 1000 °C. Szwarc first postulated the monomer to be para-xylylene which he confirmed by reacting the vapors with iodine and observing the para-xylylene di-iodide as the only product. The reaction yield was only a few percent, and a more efficient route was developed in the 1950s by William F. Gorham and was commercialized in 1965 by the Union Carbide Corporation [18]. Parylene (poly-para-xylylene) is a polymer produced from the starting dimer para-xylylene (di-para-xylylene). It is deposited from vapor phase at room temperature under medium vacuum.

He deposited parylene films by the thermal decomposition of [2.2] paracyclophane at temperatures exceeding 550 °C and in vacuum below 1 Torr. This process did not require a solvent and resulted in chemically resistant films free from pinholes[19], [20]. Since the coating process takes place at ambient temperature in mild vacuum, and because of parylene's conformal properties, it has a wide variety of applications. Union Carbide commercialized a parylene coating system in 1965. Union Carbide went on to undertake research into the synthesis of numerous parylene precursors, including parylene AF-4 (also called Parylene-HT), throughout the 1960s into the early 1970s. Various types of Parylene films have been extensively studied for numerous applications due to its mechanical and electrical properties and chemical resistance [20].

Among the Parylene variants, Parylene-N and -C are currently approved by FDA as a USP class VI polymer[21], which allows them to be used in biomedical devices. PA-C has higher thermal stability and chemical/moisture resistance than Parylene N, and thus was commonly chosen as an encapsulation material for biomedical devices and for variety of anticorrosion applications. Some applications have included stents, pacemakers, neural probes, and solder joints encapsulation [22], [23].

A Parylene D monomer has two aromatic hydrogens replaced by chlorine atoms. It is similar to Parylene C, but has better thermal stability at high temperatures. Table 3-1 lists some properties of Parylene N, C and D.

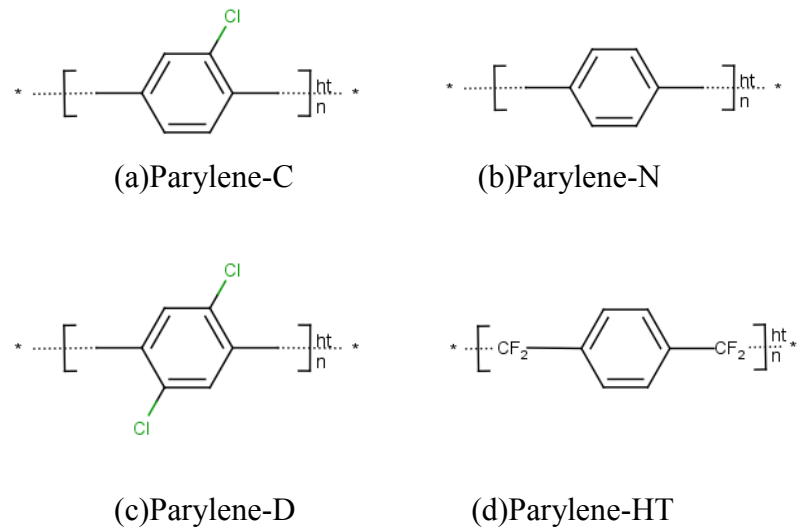


Figure 3-1 Chemical structures of Parylene N, C and D [1].

	Parylene N	Parylene C	Parylene D
Typical Physical & Mechanical Properties			
Tensile strength, MPa	45	69	76
Yield strength, GPa	2.4	3.2	2.8
Elongation at break, %	40	200	10
Density, g/cm ³	1.11	1.289	1.418
Water absorption, % (24 hr)	0.01 (0.019")	0.06 (0.029")	<0.1
Index of refraction, n _D ²³	1.661	1.639	1.669
Typical Electrical Properties			
Dielectric strength, short time (MV/m)	280	272	220
Volume resistivity, 23 °C, 50% RH (Ohm-cm)	1x10 ¹⁷	6x10 ¹⁶	2x10 ¹⁶

Surface resistivity, 23 °C, 50% RH (Ohm-cm)	1×10^{15}	1×10^{15}	5×10^{16}
Dielectric constant			
60 Hz	2.65	3.15	2.84
1k Hz	2.65	3.1	2.82
1M Hz	2.65	2.95	2.8
Gas Permeability **			
Nitrogen	7.7	0.95	4.5
Oxygen	30	7.1	32
Carbon dioxide	214	7.7	13
Chlorine	74	0.35	0.55
Moisture Vapor Transmission***	1.5	0.14	0.25
Thermal Properties			
Melting Temperature, (°C)	410	290	380
Glass Transition (°C)	>300	240	240
Linear coefficient of expansion, (ppm / °C)	69	35	38
Thermal conductivity, 10 ⁻⁴ (cal/sec)/(cm ² °C/cm)	3	2	-

Table 3-1 Properties of Parylene N, C and D [1].

* at 25um, at R.T)

** cm³-mil/100 in²-24hr-atm (23°C)*** g-mil/100 in²-24hr, 37°C, 90% RH 1 mil = = 25.4 microns

Furthermore, due to the unique CVD deposition process, Parylene is favorable for use in the fabrication of MEMS process. Conformal, uniform and pinhole free films that can range in thickness from a few hundred nanometers to a few tens of microns. Figure 3-2 shows a schematic of the Parylene deposition system. The deposition process consists of three main steps. The first step involves vaporizing Parylene from its solid dimer form at temperatures between 140 and 170°C under vacuum. The second step is pyrolysis at temperatures above 690°C, where gaseous Parylene dimers are split into monomers. The third step is that monomers enter the room temperature

deposition chamber where they simultaneously adsorb and polymerize on the surface of a substrate. The substrate temperature never rises more than a few degrees above ambient. Thus, this room temperature deposition makes it possible to have a low stress film and avoid heating problems which can be observed in the curing process of other polymers. A necessary fourth component in this system is the mechanical vacuum pump and associated protective cold traps filled with liquid nitrogen.

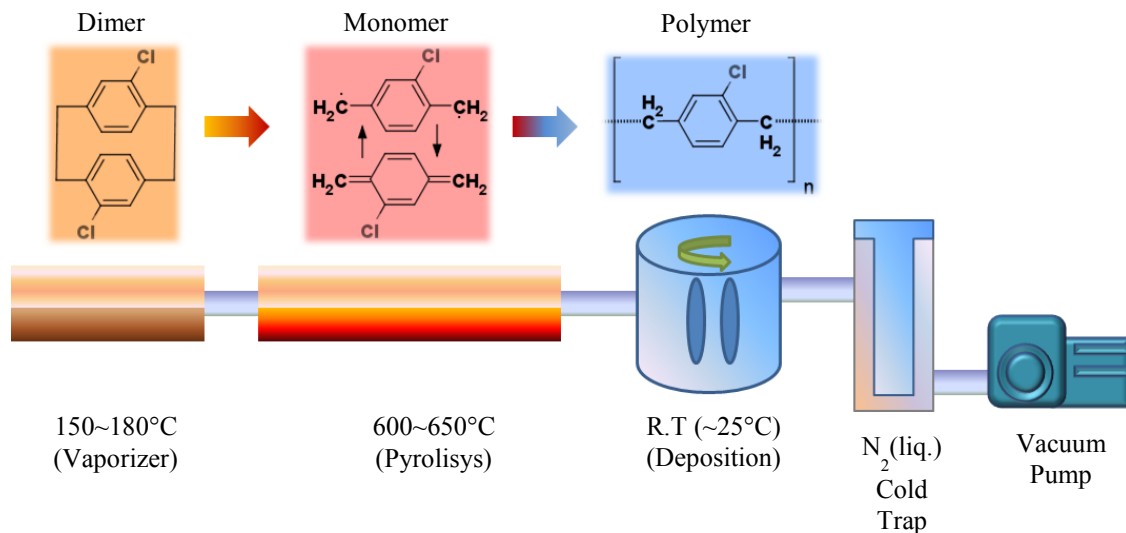


Figure 3-2 Parylene deposition system and the involved chemical processes

Parylene can be rapidly etched and patterned by oxygen plasma with photoresist or thin metal (Al, Ti, etc.) as a protective mask which can be patterned using standard lithographic or metal lift-off processes. It is highly resistant to chemical attacks at room temperature and is insoluble in all organic solvents up to 175°C. It has good compatibility with typical MEMS processes. Even it can be used as a masking material for Si bulk etching using corrosive KOH solution. For the MEMS piezoelectric microphone presented in this chapter, Parylene C will be used as the diaphragm material and at the same time as a piezoelectric material. All Parylene C depositions were carried out in a PDS 2010 LABCOTER 1 from Specialty Coating Systems Inc.

The breakdown DC voltages of both Parylene C and N films have been determined as a function of polymer thickness, a plot of which is shown in Figure 3-3. Parylene C is superior to N in this respect for films thinner than 5 μ m. These data show that both types of Parylene have excellent dielectric withstanding voltages even below the 1 micrometer thickness range, and the voltage breakdown per unit thickness generally increases with decreasing thickness.

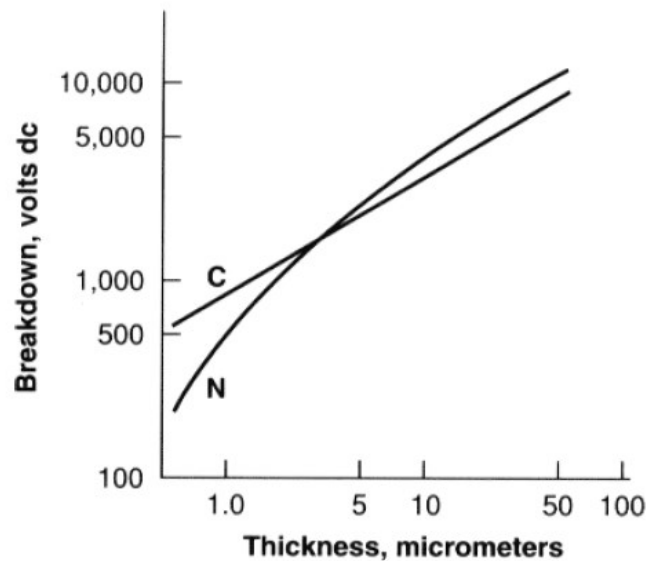


Figure 3-3 Parylene Conformal Coating Specifications & Properties

Piezoelectricity of PA-C film

There's a long-time interest to use thin-film piezoelectric materials, e.g., PZT, ZnO and PVDF [94–96] for MEMS applications such as for microphones and actuators. However, these well-known materials all have different degrees of technology difficulties when integrated into MEMS. For examples, sol-gel PZT method requires relatively high temperature (500~700°C) and PVDF film, after stretch-poling, needs to be bonded to substrate for further fabrication. In comparison, PA-C is a promising piezoelectric material for its integration into/with MEMS because it can be deposited at room temperature and electrically poled below 200°C [97].

The origin of polymer piezoelectricity comes from the molecular polar asymmetry in the unit polymer molecule. For examples, this can be found in PVDF, which is known to enable PVDF piezoelectricity if properly poled [94], [97]. Similarly, other polymer, such as PVC [95] and polyimide [96], [98] also have polar groups and, therefore, have been shown to have piezoelectricity after proper poling [94]

PA-C is well known for its mechanical properties and chemical inertness for bioMEMS applications. PA-C, like many piezoelectric materials, also has a single chlorinated benzene ring in its monomer structure, which gives an asymmetry and, hence, renders PA-C a potential piezoelectric material Figure 1-2. Interestingly, PA-C was reported as a pyroelectric sensor material (United States Patent 4147562) but it has never been reported as a piezoelectric material and this work is the first time to study methods of poling PA-C and validate that PA-C can be a piezoelectric material.

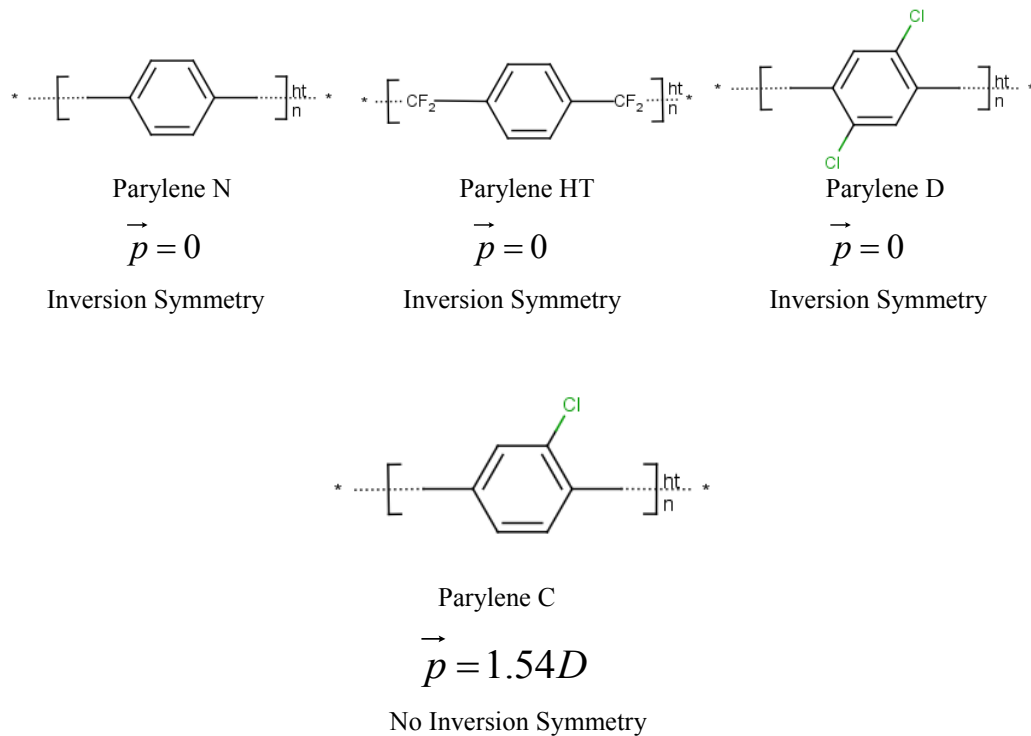


Figure 3-4 Molecular structures of various type of Parylene. Note that only PA-C has an asymmetric structure.

Piezoelectric film preparation

A 50 μ m thick PA-C film was first deposited and peeled off of a substrate. The deposition process consists of three main steps. The first step involves vaporizing Parylene solid dimer at the temperatures between 140 and 170°C under medium vacuum, with the pressure in the vicinity of 20mTorr. The second step is pyrolysis at the temperature of 690°C, where gaseous Parylene dimers are split into monomers, which is a form of conjugated di-radical. The last step is the room temperature polymerization of gaseous monomers into thin film Parylene on a substrate. For the easy delamination of the film, before deposition soap solution of 2% concentration was applied on the substrate, a 25cm x 25cm x 3mm polyethylene plate, and dried in the dust free environment at room temperature.

The film was then cut into 50 mm x 20 mm rectangular shapes. Conductive silver paint (from GC Electronics®) was applied on one side of film and dried in room temperature to form an electrode, and after one side is fully dried, on the other side is an electrode also formed with the method mentioned above. The electrodes are each 35 mm x 10 mm, finally on both sides of film Figure 3-5. To prevent the arcing at the edge of electrode, we keep a distance of 5mm between the edge of electrode and the edge of film. At the elevated temperature, a gap of 5 mm is safe to inhibit an arcing below 2~3kV, but when 10kV is reached, at least a distance of 15 mm is required. To reduce the breakdown, we applied polyimide film on the ground electrode plate (Figure 3-6).

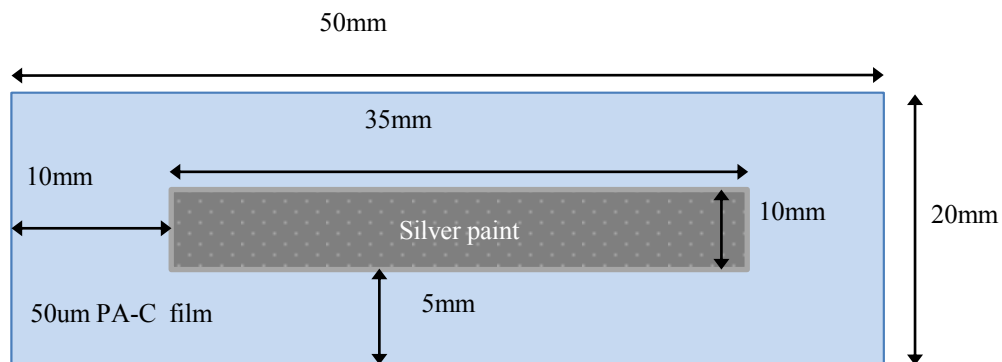
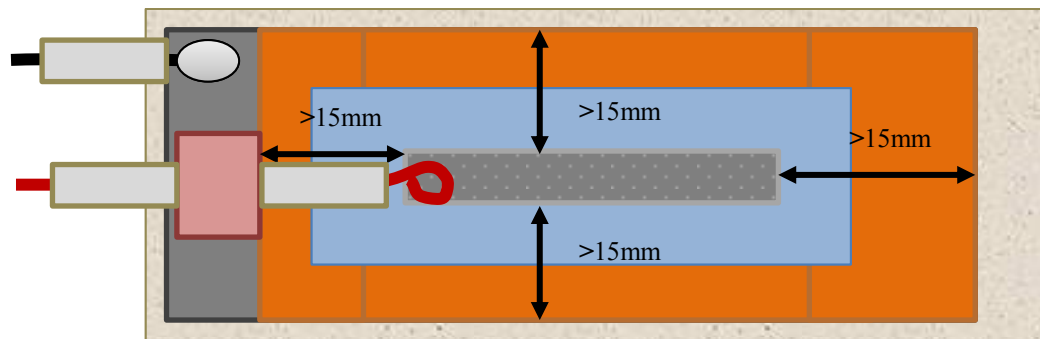


Figure 3-5 Dimensions of the sample of the PA-C film.

These electrodes are used to apply electrical field during the poling process and later to detect the piezoelectric signal induced by the applied mechanical stress. After the electrodes are formed, it is mounted on the poling jig, which is composed of a 0.5mm thick aluminum plate as a ground plate and mica film for the insulation. The bias is applied through a rounded metal wire, and except the contact point the wire is covered with PFA (fluoro polymer) jacket. However, PFA is not thick enough to prevent the arcing beyond 10KV, we add extra jacket, which is 1.65mm-thick silicone rubber tubing (Figure 3-8).

To ensure the proper mounting of the sample in the poling jig, we use an impedance meter to check the capacitance and resistance between two electrodes. A good contact between the film sample and poling jig can be judged by if it shows capacitance. By the calculation the capacitance should be in the vicinity of 100pF, if the contact is good. Also, if there is a leak through the film, low resistance will be measured. Because the PA-C film is a good insulating material, without puncture through the film, the resistance is typically over the limit of the impedance measuring instrument.



b) Top View

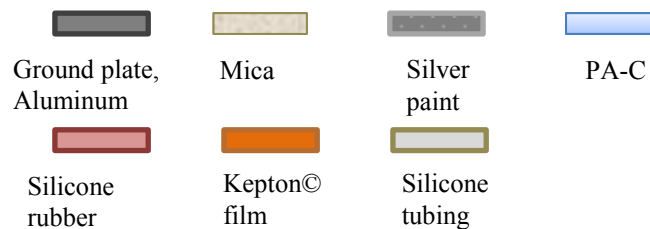


Figure 3-6 Distances from the edges of electrodes of film sample to the edge of bottom ground plate.

To pole the film, an electric field is applied at the room temperature with slow ramping (< 1kV/2sec.) to the wanted value. After the potential had reached the value that we want, the sample was moved to a hot plate and covered with mica film while still the bias is applied. During the poling, the film was sandwiched between two insulating mica sheets. The top mica sheet was used as a heat insulation to reduce nitrogen cooling during the poling process. The bottom mica sheet was to provide electrical insulation between the ground electrode of the film and the hot plate.

After the poling time passed, the poling process was finished by quenching the poled samples with the electrical field still on. During the quenching step, the top heat insulation mica film was removed first. Then the film sample, together with poling jig, was moved to a 6mm thick glass with 12.5cm in diameter at room temperature quickly. The poling process is achieved in N₂ globe box with 20sccf of N₂ purging to avoid the oxidation of PA-C film at elevated temperature. The pressure of the globe box is maintained at 3psi higher than atmospheric pressure.

The electrical field is provided by a high voltage source (Gamma High Voltage Research Inc.). A 3W, 10 MOhm resistor box is positioned in series with the film and High voltage source to limit the current to prevent the sudden film breakdown under high voltage. The poling electrical fields ranged from -5 MV/m to -40 MV/m and the poling temperatures from room temperature to 280°C.

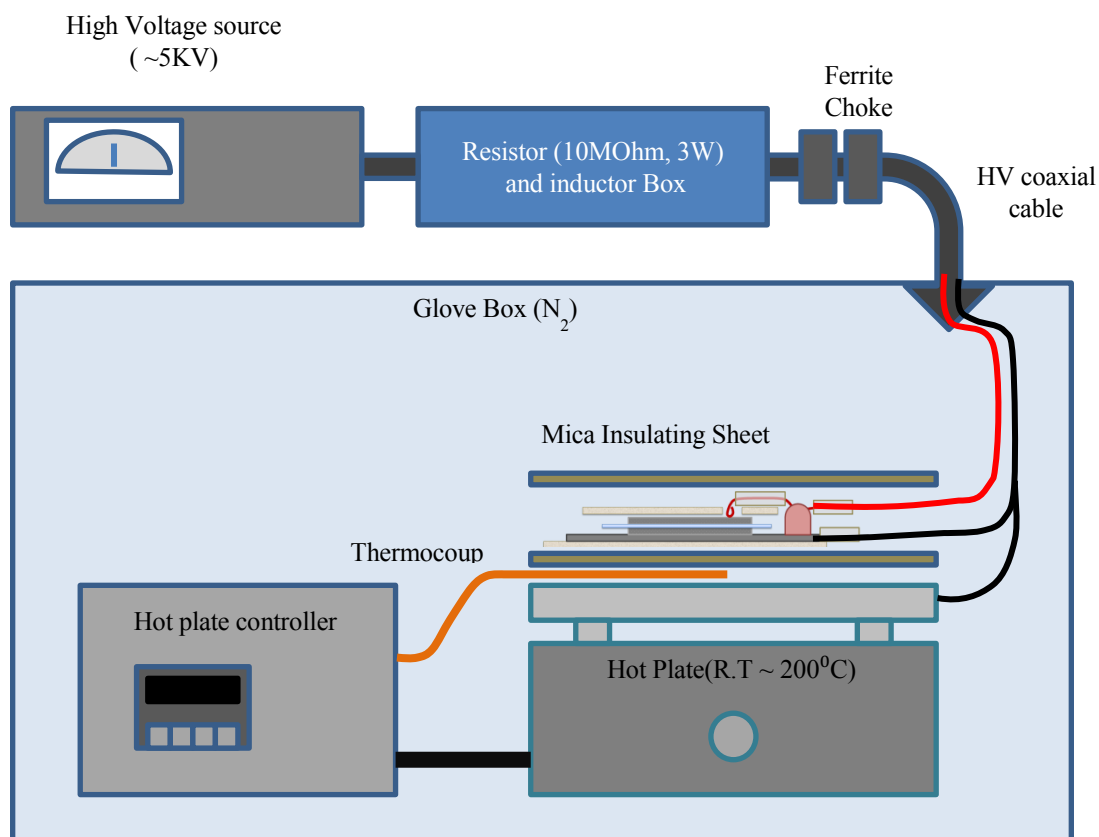
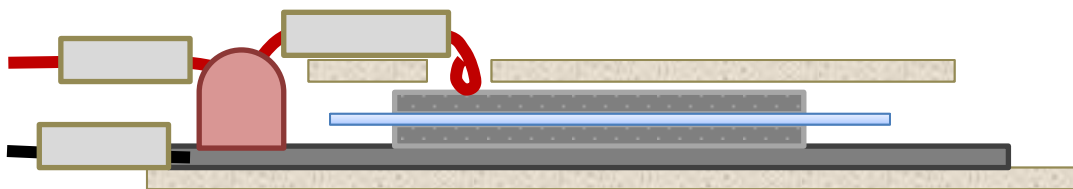


Figure 3-7 Experimental setup for PA-C poling. To avoid the oxidation of PA-C, the poling process was performed in a nitrogen-filled glove box. A thermocouple is located underneath the bottom mica insulation sheet to control the hot plate. The pressure of the globe box is maintained at 3psi higher than the atmospheric pressure.



a) Side View

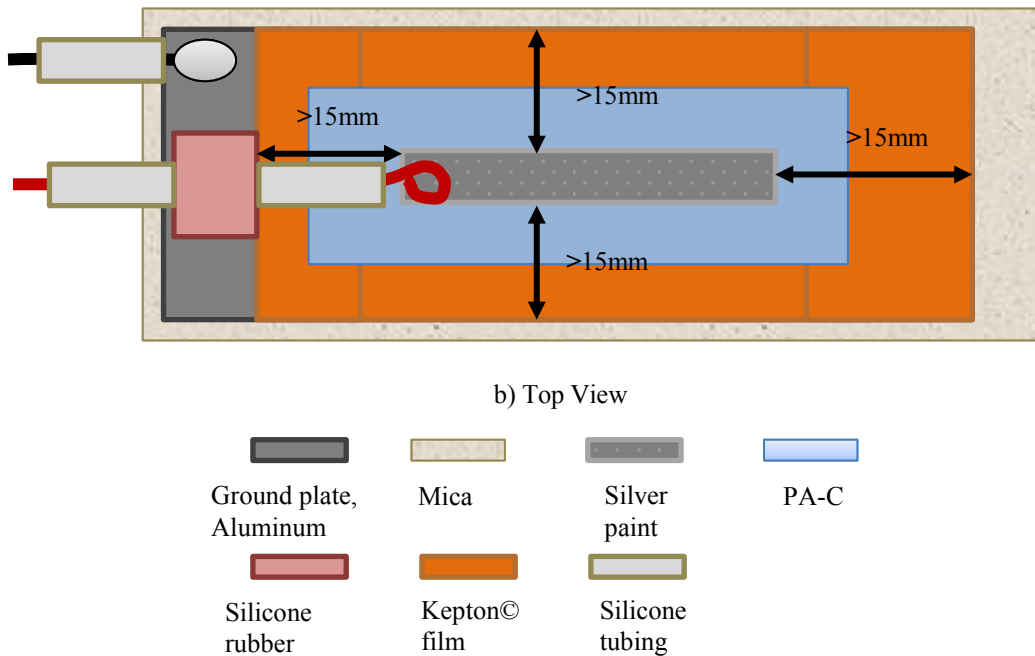


Figure 3-8 Detailed figure of poling jig

Measuring System

The piezoelectric coefficient of a film can be measured by monitoring the net charge change when a mechanical stress is applied on the film. To ensure an evenly distributed mechanical stress, we mounted the PA-C device on an aluminum chamber wall and applied a step-wise pneumatic pressure by a pressurized nitrogen gas [99].

The pneumatic system is shown in Figure 3-9 including a regulator, a gas reservoir, a 3-way solenoid valve and a gas chamber. The gas reservoir (450cm³) served to reduce pressure fluctuation when the solenoid valve was opened or closed. To minimize the filling and venting time, the solenoid valve was attached right above the lid of the chamber. Because the commercialized one doesn't meet our need of fast speed and big flow rate, we made a modification to enlarge the internal structure. When the pressuring gas is release through the solenoid valve, it generates recoil and it appears in the signal measurement. So, we add a "T" branching tubing to cancel the recoil by

ejecting the gas to opposite direction. The chamber was made out of aluminum and grounded for EMI shielding. The chamber is designed to stand up to 100psi safely.

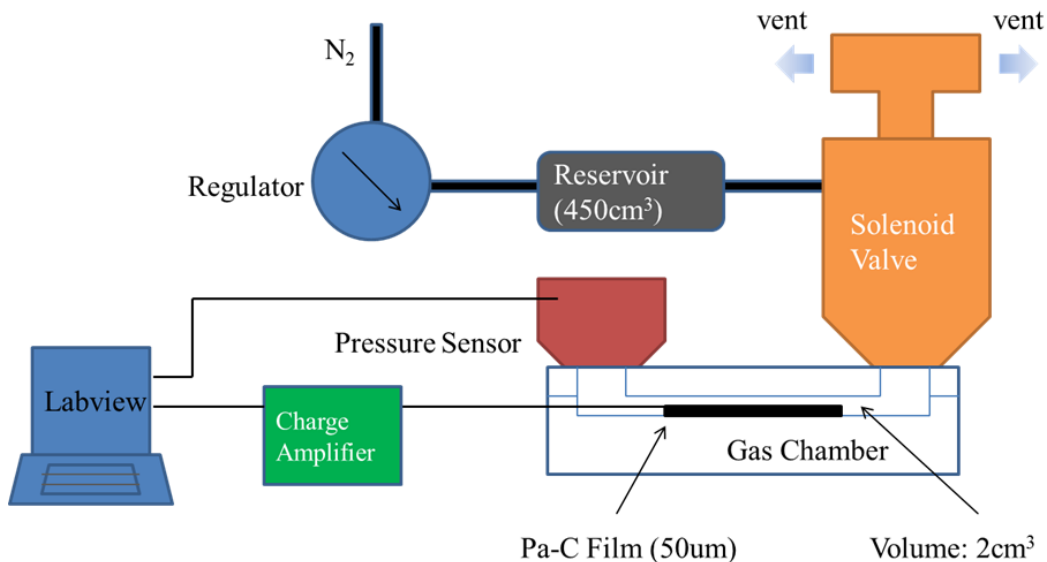


Figure 3-9 The schematic of the pneumatic testing system. The voltage (from the charge amplifier) and the pressure signals are gathered and analyzed by a control PC through NI DAQ USB-6281. The solenoid valve is also controlled by the same PC.

The interior gas chamber wall is insulated with Scotch Magic Tape™ from 3M® because it has smallest charge generation when it is pressed. On the scotch tape insulation, a 0.1mm thick brass plate is positioned as a ground of the poled PA-C sample film. And on top of the PA-C sample, a mesh electrode is placed, which is made from EMI shield gasket. It ensure good electrical contact and but due to its porous nature, it doesn't interfere with the pressuring of the film.

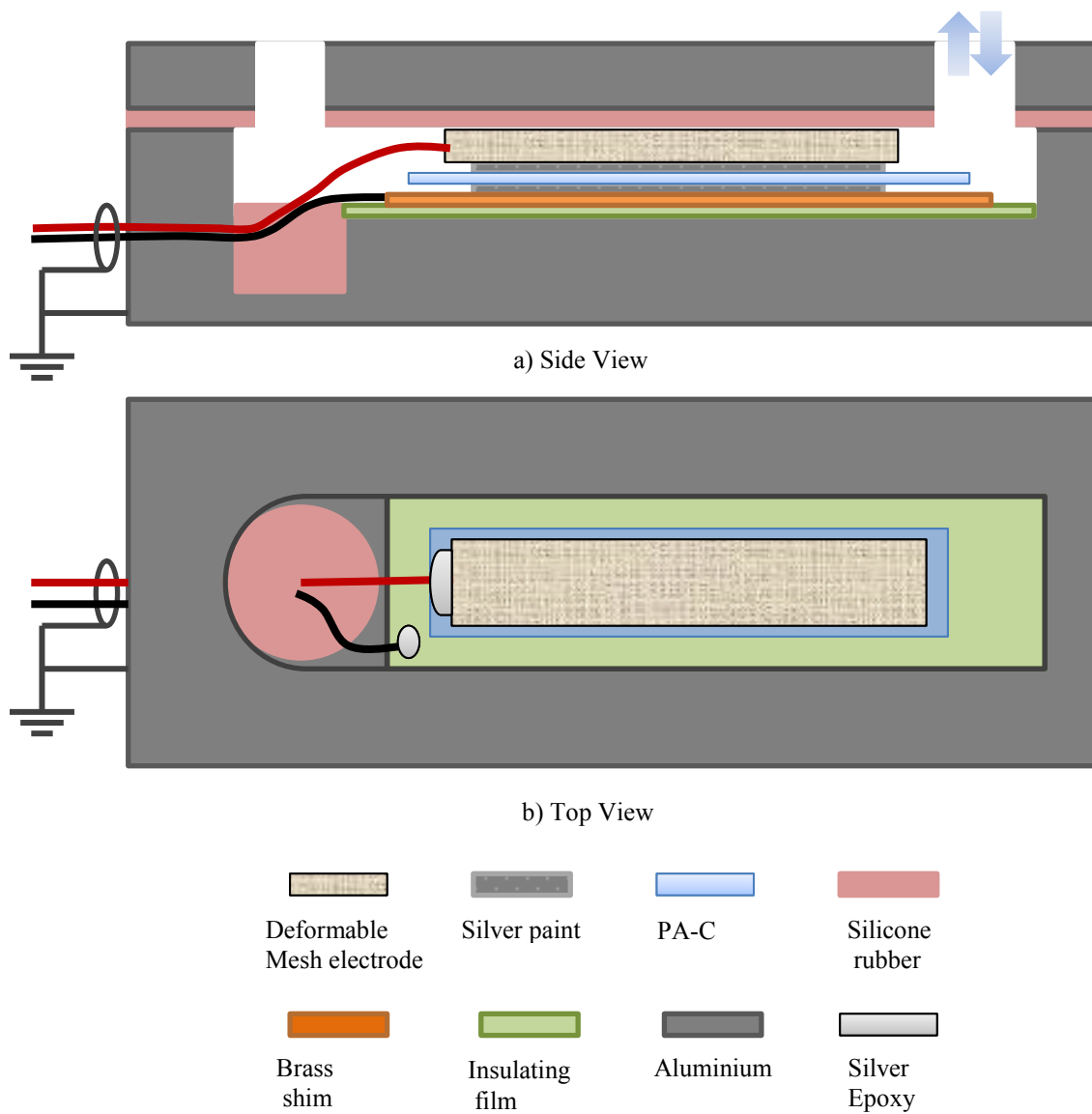


Figure 3-10 Detailed figure of pressurizing chamber. a) cross section of the chamber. b) top cover is removed. The deformable mesh electrode is translucent to show the relative position to the piezoelectric PA-C film.

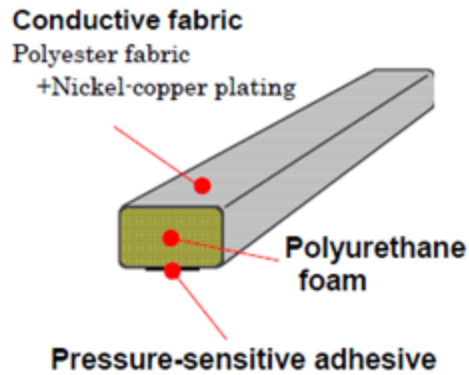


Figure 3-11 EMI (Electric Magnetic Interference) shielding gasket.

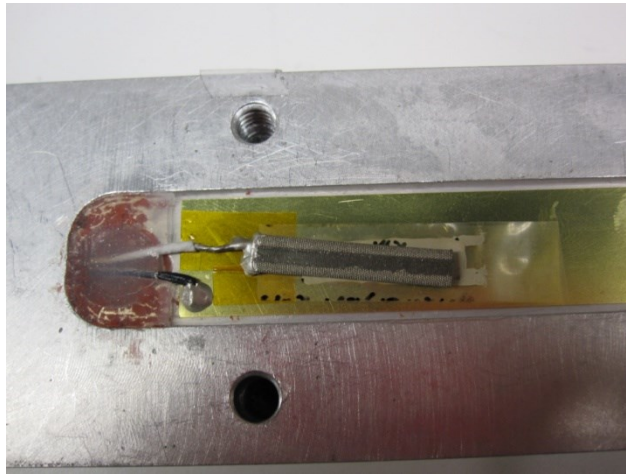


Figure 3-12 Picture of the pressuring chamber.

The piezoelectric film sensor is modeled as a charge source with a shunt capacitor and resistor, or as a voltage source with a series capacitor and resistor. These models are shown in Figure 3-13 along with a typical schematic symbol. The charge produced depends on the piezoelectric constant of the device. The capacitance is determined by the area, the width, and the dielectric constant of the material, PA-C.

However, Piezoelectric sensors are not suited for static or dc applications because the electrical charge produced decays with time due to the internal impedance of the sensor and the input impedance of the signal conditioning circuits.[100] Nevertheless, when a quasi-static force is applied to the piezoelectric film sensor, the electrical charges developed by piezoelectric materials decay with a finite time constant. Utilizing a charge integrator, the charge decay on the piezoelectric cantilevers can be monitored.[101]

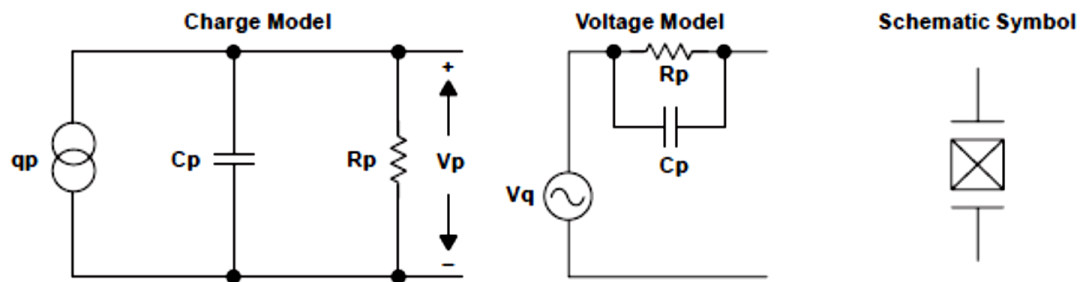


Figure 3-13 Charge model of Piezoelectric PA-C film

The charge integration technique was originally introduced for piezoelectric force transducers, which improved the response of piezoelectric transducers in low-frequency force measurements[102]. Later, it was extensively applied to the determination of the piezoelectric coefficient of piezoelectric thin films [103–106], low-level current sensor measurements [107] and pressure sensors[108].

In Figure 3-14 the bottom electrode, which was connected to the ground earlier during the poling, was connected to the ground of the charge integrator. We used the LMC662 CMOS operational amplifier because it has thousand times smaller input bias current than the former trans-impedance amplifier IVC 102. However, LMC662 doesn't have an integrated feedback capacitor reset switch and we have not been able to find a switch with smaller parasitic capacitance and larger input impedance than LM662's, respectively. Instead of using switch we leave it open and connected with a wire when we need to reset the feedback capacitance. The charge output from the PA-C piezoelectric film was connected to the capacitor [109].

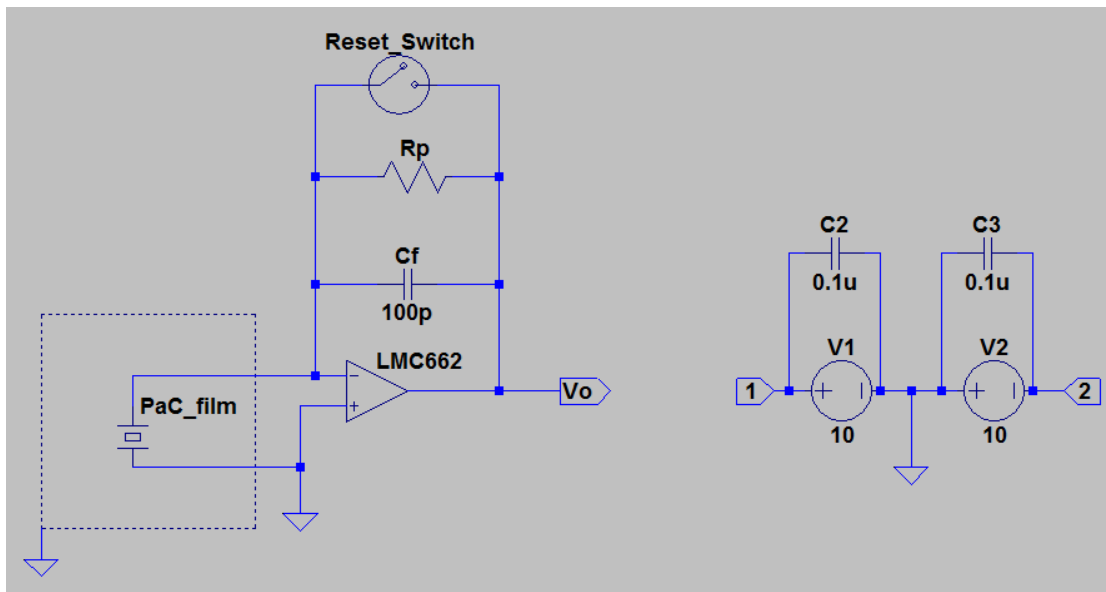


Figure 3-14 The charge integrator circuit

The amount of the charge generated by the pressure of nitrogen gas is pulled into the inverting input of op amplifier. The charge integrator will balance the charge injected into the negative input by charging feedback capacitor with $C_f = 100\text{pF}$ [110]. Resistor R_p represents the parasitic resistance in the measuring circuit. Normally, the surface leakage resistance is around $\sim 10^9$ ohm range, and the input impedance of LMC662 is $>10^{12}$ ohm.[111]

If the charge generated on the film sensor is Q_{film} , the output voltage of can be described as

$$V_{out} = \frac{Q_{film}}{C_f}$$

, then the charge is

$$Q_{film} = C_f \times V_{out}$$

Because we fix the value of C_f as 100pF, Charge generated in the film can be calculated as,

$$Q_{film} = 100 pF \times V_{out}$$

However, the operational amplifier is of inverting configuration ($V_{out} < 0$), and the actual charge is positive ($C_{film} > 0$). We applied a negative potential for the poling ($V_{bias} < 0$), and by the definition of the piezoelectric constant, the piezoelectric constant will be negative ($d_{33} < 0$).

Long Time Constant Charge Integration Amplifier

It was first found that non-optimal pneumatic switching can caused huge pressure fluctuation. Therefore, we used gas reservoir and attached the solenoid valve right on top of chamber to reduce the pressure fluctuation and transient time during pressurization and depressurization. Figure 3-15 then clearly shows our experimental data, although some fluctuation is still there.

In Figure 3-15(a), the pressure fluctuation takes about 100ms to stabilize after the solenoid valve is open. Pressurization of the chamber also induces temperature changes in the chamber. For example, Figure 3-15 (b) shows that the temperature of the film increases by applying the pressure due to an adiabatic compression and decreases by releasing the pressure due to an adiabatic expansion. For the thermal effects, it takes about 2.5 sec to return to room temperature.

From the data sheet of LMC662, its input impedance is at order of $10^{12}\Omega$. And by the geometry of piezoelectric PA-C film, the area of electrode is $35 \times 10 \text{ mm}^2$ and the thickness of the film sensor is 54um. We chose the dielectric coefficient as 3.15.

$$C = \epsilon \epsilon_0 \frac{A}{h}$$

Vacuum permittivity, here, is

$$\epsilon_0 = 8.85418 \times 10^{-12} \frac{F}{m}$$

$$C = 3.15 \cdot 8.85418 \times 10^{-12} \frac{350 \times 10^{-6}}{54 \times 10^{-6}}$$

$$C = 180 \text{ pF}$$

Also, the average of measured value is 173pF

For the low cutoff frequency,

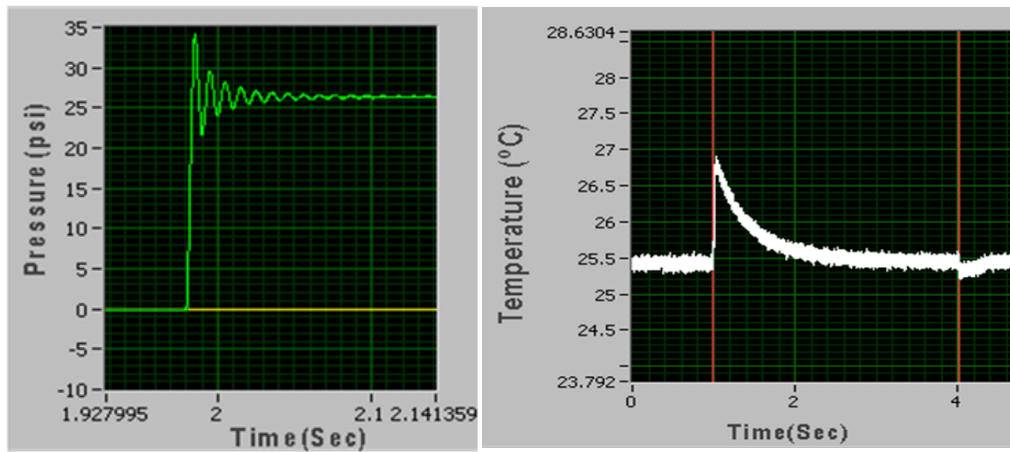
$$f_{low} = \frac{1}{2\pi C_f R_p}$$

$$f_{low} = \frac{1}{2\pi \cdot 180 \text{ pF} \cdot 10^{12}} = 8.8 \times 10^{-4}$$

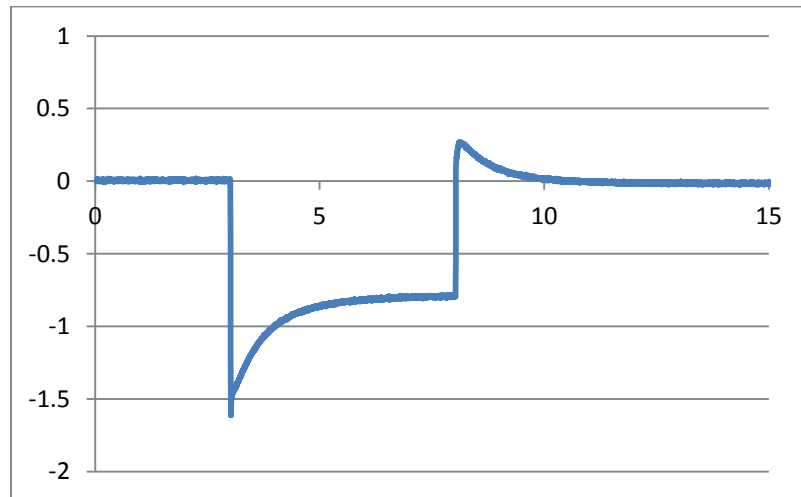
Its low cutoff frequency is 0.88mHz, i.e. its time constant is 1100 seconds and long enough to measure ~10 of seconds effect.

Setting the integration time longer than these fluctuation times allowed us to reduce interferences from both the pressure fluctuation and, hence, induced thermal effects. For example, the adiabatic compression effect is shown in Figure 3-15 a,b). the solenoid valve is turned on for 3 seconds and there is a damped pressure fluctuation (green) during 0.1 second. During the fluctuation of the pressure, the temperature inside the chamber abruptly increases and then decays with time constant of 0.5seconds and reaches to the original temperature in 2 seconds.

The voltage (red) gotten by charge integrator at 3 second increased to 0.05V due to temperature rise and then decayed to -0.0635V after 6 second. At 13 seconds the solenoid valve was open to release the pressure and the pressure dropped to atmospheric pressure. Clearly at 13 second, the voltage dropped to -0.1 volt and then returned to 0 volt because the releasing pressure generated the same amount of opposite charge at the film sensor.



(a) Pressure fluctuation (b) Temperature fluctuation



(c) The output voltage from the charge integrator.

Figure 3-15 The recorded temperature, pressure and voltage for one cycle of pneumatic stressing of the piezoelectric PA-C sample. For the pressure (green) curve, the vertical axis is the pressure difference from atmospheric pressure.

piezoelectric coefficient is defined by generated charge density over applied force per unit area, for the case at Figure 3-15 c),

, where

ΔF = Applied force on the film

ΔP = Pressure difference

A = Area of the film, 350mm^2

ΔQ_{piezo} = Charge generated

ΔV_{out} = Voltage Change

C_f = Capacitance of Integrating Capacitor

$$d_{33} = \frac{\Delta Q_{\text{piezo}}}{\Delta F} = \frac{\Delta V_{\text{out}} \times C_f}{\Delta P \times A} = \frac{-0.2V \times 171pF}{0.205MPa \times 350mm^2} ?$$

$$= 0.477pC/N$$

, where 30 psi is 0.205Mpa.

d_{33} Dependence on Poling Condition

To optimize the poling process, we studied the temperature, the poling electrical field strength and the poling time as optimizing parameters. Each point in graphs is average of 5 samples which poled with identical parameter.

piezoelectric coefficient over an electrical field

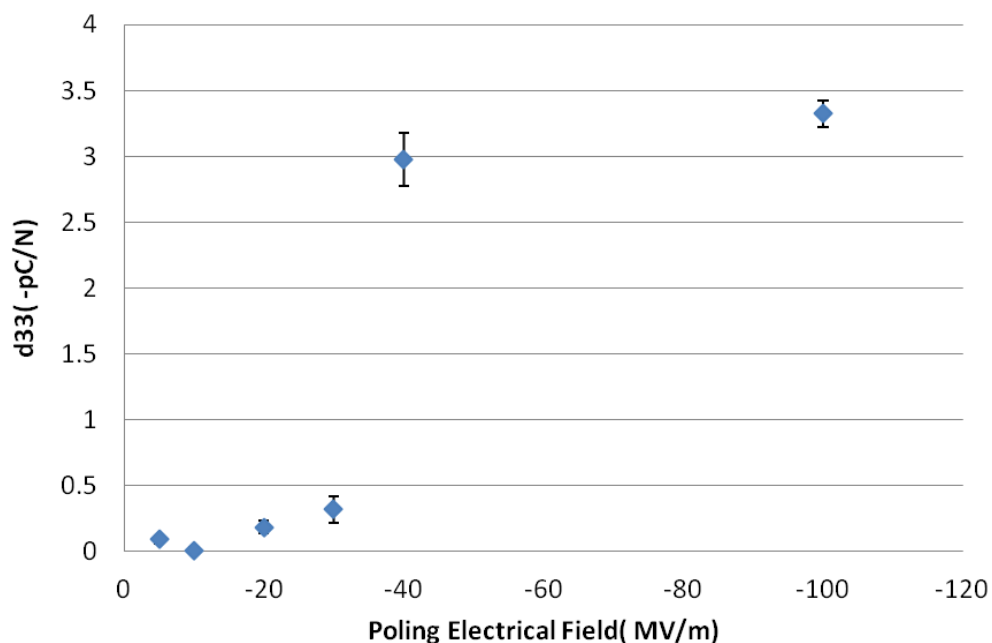


Figure 3-16 d_{33} vs. applied electrical field (poled at 200°C for 2hrs). This shows that d_{33} increases with the E-field although the significant increase occurs above -40MV/m.

In Figure 3-16, for as deposited 50um of PA-C film, when the temperature(200°C) and the poling time (2 hours, except -100MV/m sample, it is hold 5minutes) are fixed, stronger electric field produces higher d_{33} values up to -3.32pC/N at 200C, - 100MV/m. However, because of the limit due to electrical breakdown, the electric field is limited to the value of -100MV/m.

Piezoelectric coefficient over temperature

In Figure 3-17, for as deposited 50um PA-C film, when the electric field (-100MV/m) and the poling time (5 minutes) are fixed, the poling temperature is increased from the room temperature to 280°C with 40°C of step from 40°C. We can find the maximum d_{33} appears between 160°C and 200°C. At higher temperature beyond 200°C, the decrease of d_{33} is observed. In the research about PVDF by Kaura, the drop in piezoelectric coefficient may be due to an increase in electrical conductivity by elevated temperature of the sample, which would reduce the effective poling field. Even though for PA-C, the electrical conductivity has not been measured by temperature, yet, considering generally the fluoropolyme has higher electrical resistivity, this conductivity reduction over temperature maybe important factor to explain this phenomena. Also, not only the conductivity reduction, we assume it is related to the glass transition temperature of as deposited PA-C, which is known as 30~50°C [112]. Below the glass transition temperature, aligning of crystalline in an electrical field may be restricted by surrounding amorphous polymer chains and it has a small piezoelectric value. Also, at the temperature beyond 200°C, due to the high thermal energy, the tendency of randomization of the orientation of polarity may be increased, too.

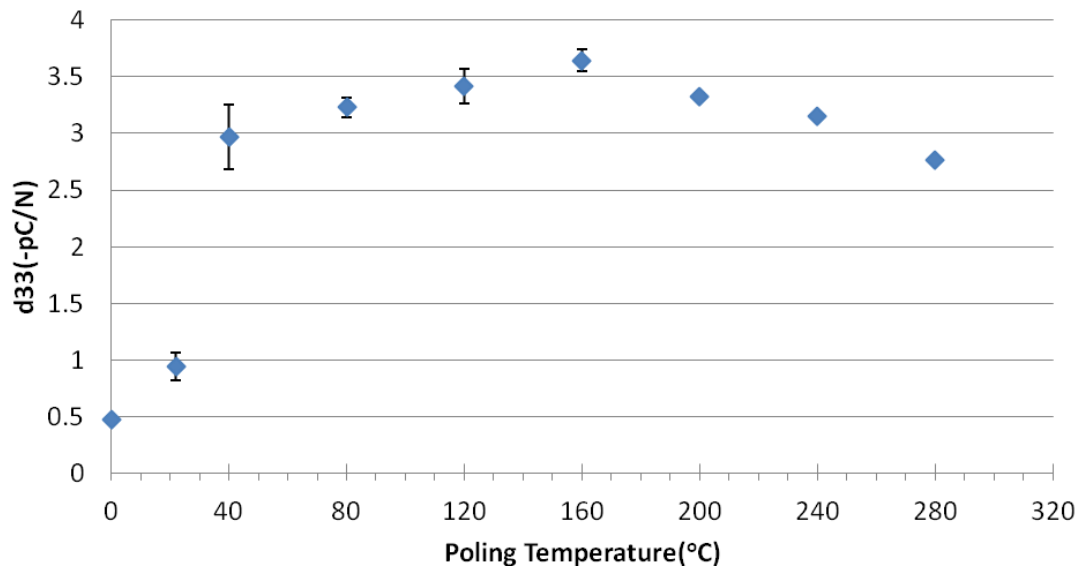


Figure 3-17 d_{33} vs. poling temperature (for 50um thick PA-C film, poled for 5 minutes with -5.0kVm, i.e. -100MV/m). This shows that d_{33} peaks at 160°C.

Piezoelectric coefficient over poling time

In Figure 3-18, for as deposited 50um of PA-C film however, it shows that there is a dramatic change of d_{33} between 30 seconds to 1 minute. This implies that, at proper poling temperature, the poling of PA-C is a fast process. Also, recently, Jeffrey found crystallization and densification of PA-C accomplished within a minutes, which may explain why the poling process is also a fast process.[113] For a long time of poling, we cannot find any meaningful trend of piezoelectricity depending on the poling time. Practically, we can estimate minimum required poling time as 5 minutes.

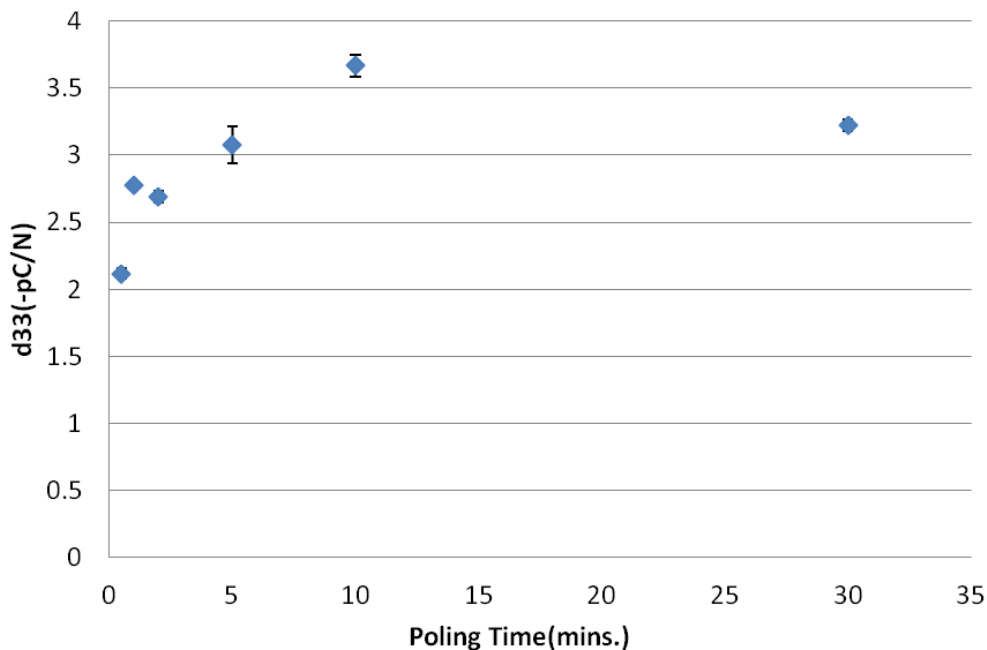


Figure 3-18 Poling process is finished within 5 minutes.

Ageing effect on Piezoelectric coefficient

As a piezoelectric polymer, PVDF has the highest piezoelectrical value(d_{33} , -33pC/N without stretching, -60pC/N with stretching [64]), however because of its low glass transition temperature,

it is lack of temperature stability. For the simultaneous stretched PVDF, it loose 12% of d_{31} at 60°C and 30% of d_{31} value at 110°C within a week. Non-stretched PVDF beacomes non piezoelectric before 2 weeks at 110°C . It is one of limiting factor of PVDF application[64]. Consequently, other polymer system which is developed to achieve thermal stability, such as polyimide, requires high temperature for curing of polyimide and it has low piezoelectric coefficient(d_{31} , 0.12pC/N)[14], [15], [114] as we see in Figure 3-20.

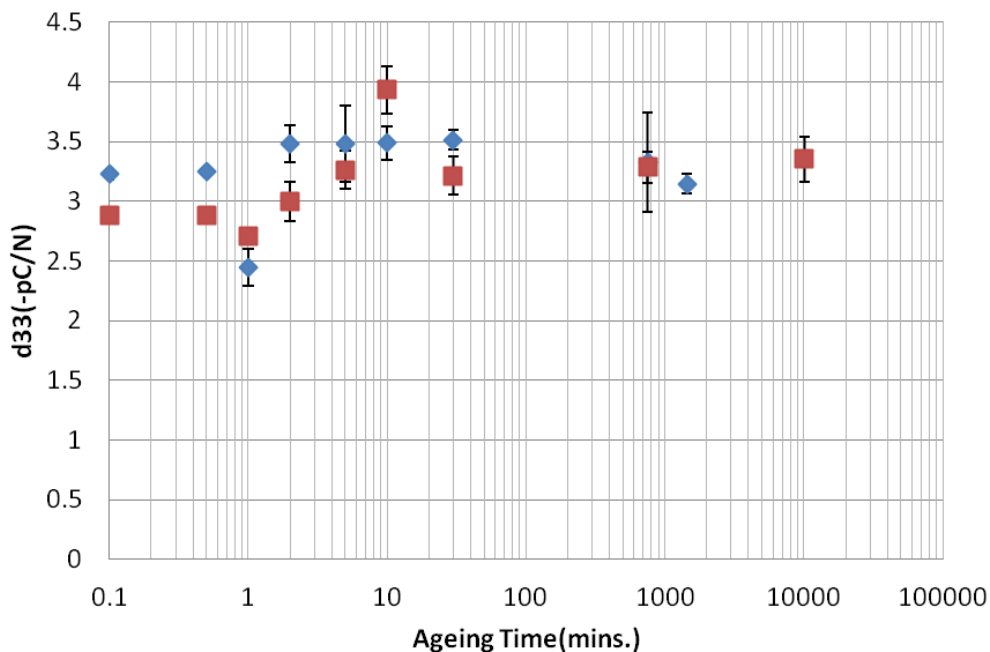


Figure 3-19 Ageing effect on Piezoelectric PA-C film

Thus, we have checked the temperature stability of piezoelectric PA-C. It is poled at 200°C , with -100MV/m of bias in 5 minutes. Comparing with the two, piezoelectric PA-C has a relatively high d_{33} (-3.55pC/N) and can maintain it in a week without decaying even at 80°C . Rather d_{33} is 30% increase at first 10 minutes of annealing, finally 10% of increase after a week. This may imply the annealing of PVDF after a poling process. At 160°C , PA-C maintain its value without decaying for 12hours, comparing that of PVDF, decayning 6% in 12 hours[64].

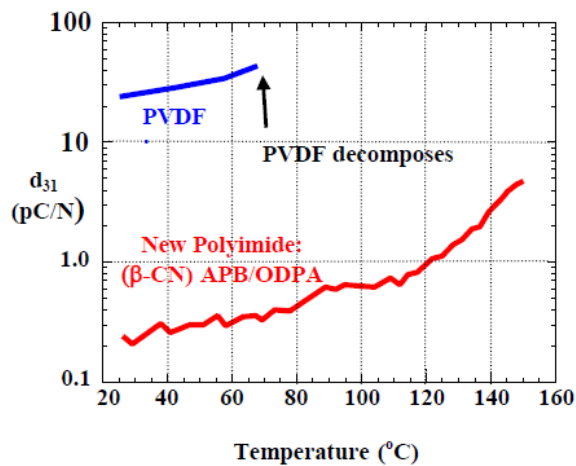


Figure 3-20 Lack of temperature stability of PVDF; polyimide with low d_{31} value

Piezoelectric coefficient over pre-annealing time

Before the poling process started, we pre-annealed the film at 200°C with different time. Because recently, Jeffrey found crystallization and densification of PA-C accomplished within a minute [26], this phenomena is also shown in Figure 3-21.

With an increase of pre-annealing time at 200°C, the final piezoelectric coefficient, d_{33} , is decreased from -3.3pC/N to -1.6pC/N. This may be explained by the decrease of the portion of uncrystallized, which can be aligned to the external electrical field during the poling process.

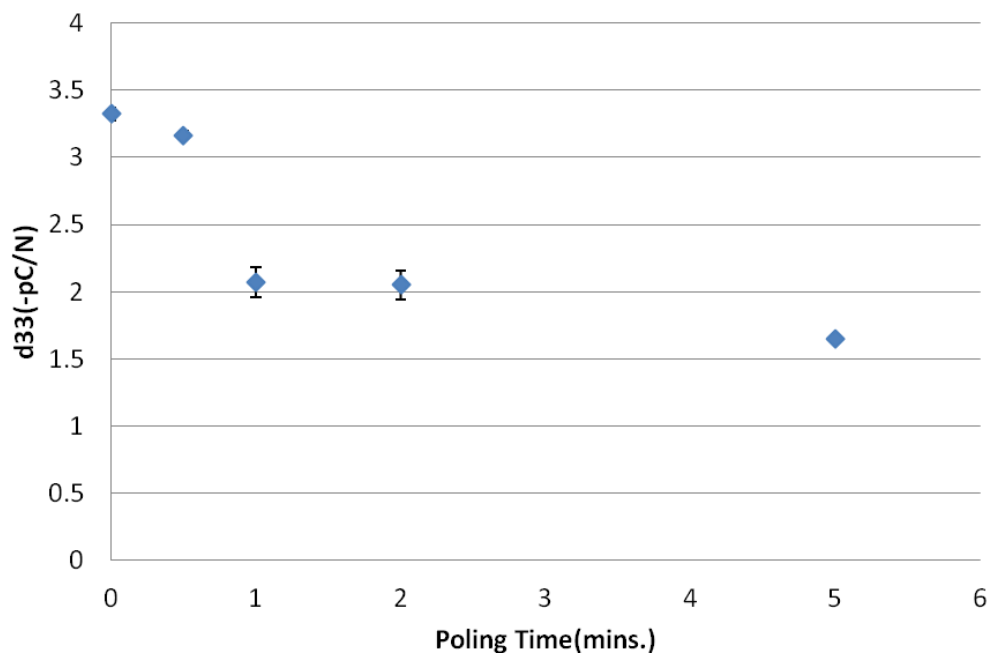


Figure 3-21 Pre-annealing can decrease the piezoelectric coefficient.

Simultaneous Poling and Stretching to Piezoelectric coefficient

For well known piezoelectric polymer, PVDF (Polyvinylidene fluoride) is known to possess the highest values of piezo- and pyroelectric constants over any polymer. PVDF is a long-chain, semicrystalline polymer having the repeat unit ($\text{CH}_2\text{-CF}_2$). It is approximately 55% crystalline and has a molecular weight of typically 4×10^5 . Four crystalline forms are known [115] and are designated phases I and II, III and IIp or β , α , γ and p, respectively. The most common forms are the polar form I (β , orthorhombic, $a = 8.58 \text{ \AA}$, $b = 4.91 \text{ \AA}$, $c = 2.56 \text{ \AA}$) and the electrically inactive form II (α , C_{2h}^5 , monoclinic, P21/c; $a = 4.96 \text{ \AA}$, $b = 9.64 \text{ \AA}$, $c = 4.62 \text{ \AA}$, $\beta = 90^\circ$) [116]. Commercial bulk polymer consists of form II material. For high degrees of piezoelectric activity, a significant amount of oriented polar form I crystalline material is needed. The polymer chain of phase I (β) material has a planar, zigzag, all trans- conformation. The dipoles are oriented normal to the polymer chain axis

and are parallel to each other. This form is not centrosymmetric and is thus intrinsically piezoelectric (Figure 3-22 (β)). By contrast, phase II(α) has a trans-gauche-trans-gauche '(TGTG)' structure and, although it has a dipole moment normal to the chain axis, the molecular chains pack such that their dipoles are in an antiparallel array, therefore a non-polar, centrosymmetric unit cell results (Figure 3-22 (α)). [117]

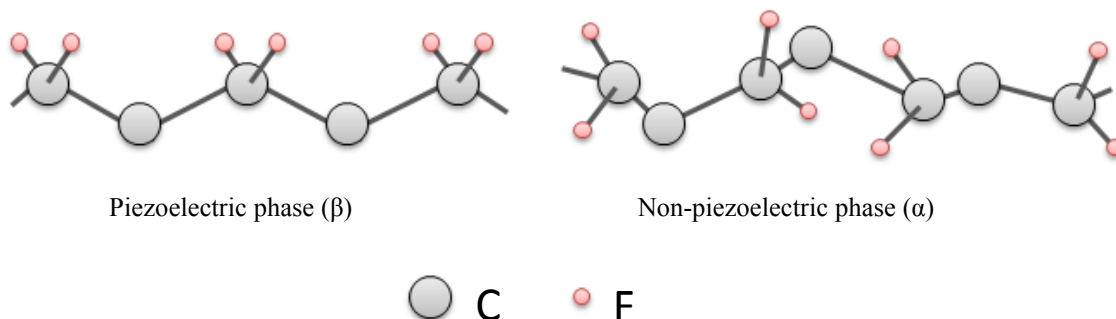


Figure 3-22 Molecular structures of PVDF. Hydrogen atoms are omitted.

The degrees of piezoelectricity of sample depend on the degree to which the dipoles can be made parallel one another. The only commonly used way of doing this is to produce oriented sheet material and apply a high potential across it with proper heating. However, the maximum values of piezoelectric constants from simultaneous stretching and corona poling are 60 pC/N by T. Kaura and et al. [64]

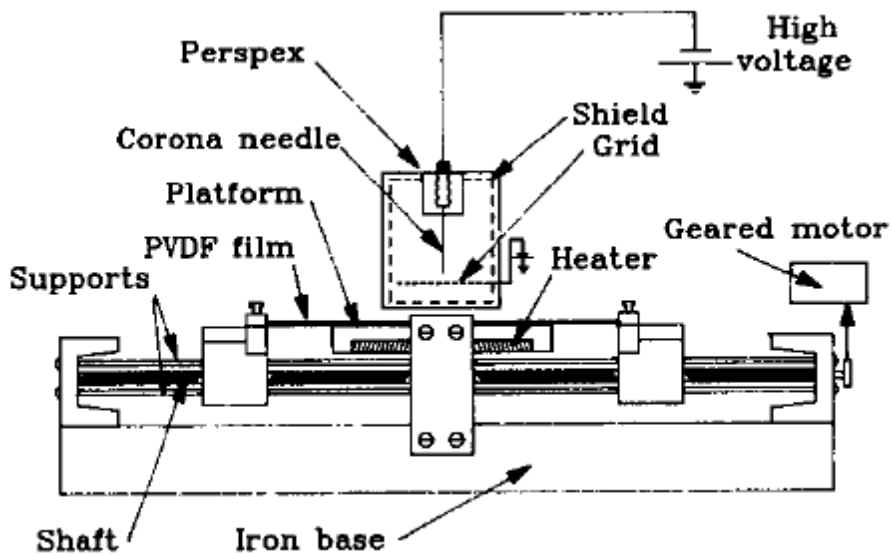


Figure 3-23 Simultaneous Stretching and Corona poling device.

Also, for mass production which needs continuous stretching and poling, continuous rolling stretching device is invented[118]

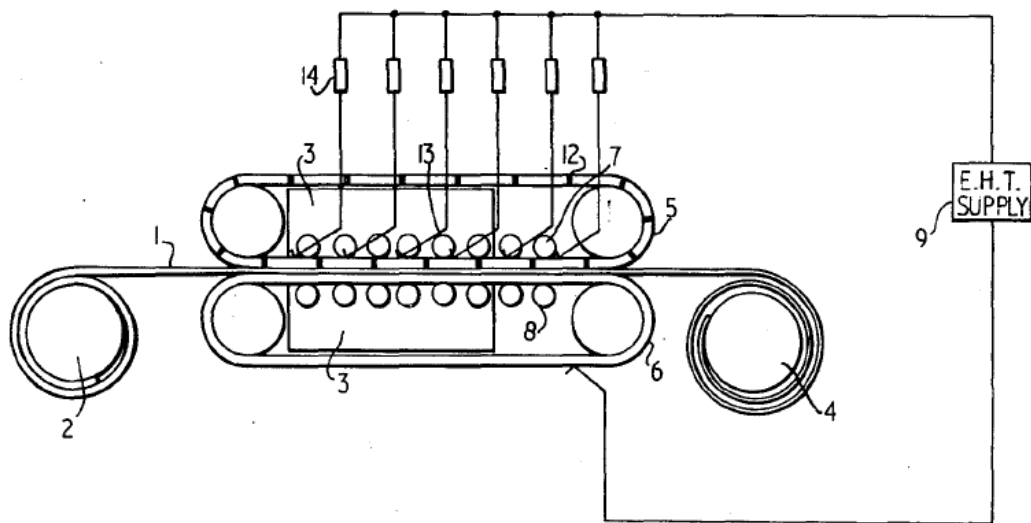


Figure 3-24 Continuous rolling stretching device

For the stretching, because it is not able to use a direct contact method with ready built electrodes, we adapted a corona charge to applied bias on the film.

When there is stretching with heating for PVDF film, increasing of piezoelectric coefficient is observed on PVDF simultaneous stretching and poling. The maximum was found at 4.5 times of stretching (350% strain) [64]

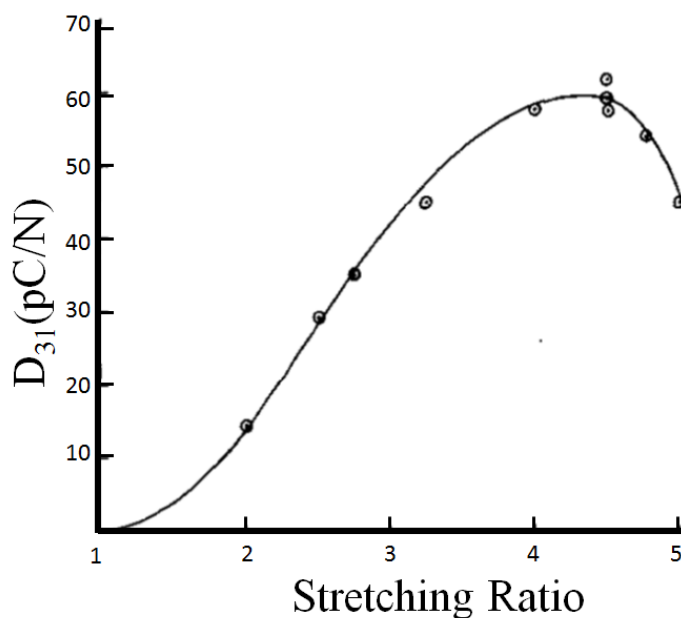


Figure 3-25 Simultaneous Stretching and poling, the maximum d_{31} is at 4.5x

There have been intensive studies for stretching of PVDF[64], [119–123]. And it is accepted as β -phase formation is more evident in stretched films by a transformation mechanism of α to β -phase via the formation of a necking region during stretching. By using FTIR techniques, a maximum content of 74% for β -phase was calculated. This was achieved during stretching at 90 °C and for a stretch ratio between 4.5 and 5[122]. This observation well matches with experimental result from Simultaneous Stretching and poling[64].

Also, Parylene-N, poly (p-xylylene), a member of the parylene family, has an α -form crystal structure when polymerized at room temperature. Upon heating, the α -form transforms to the high temperature phase (β_2 -form) and melts.[124] For PA-C, the increase of crystallinity is observed by heating[125] and by stretching[124], too.

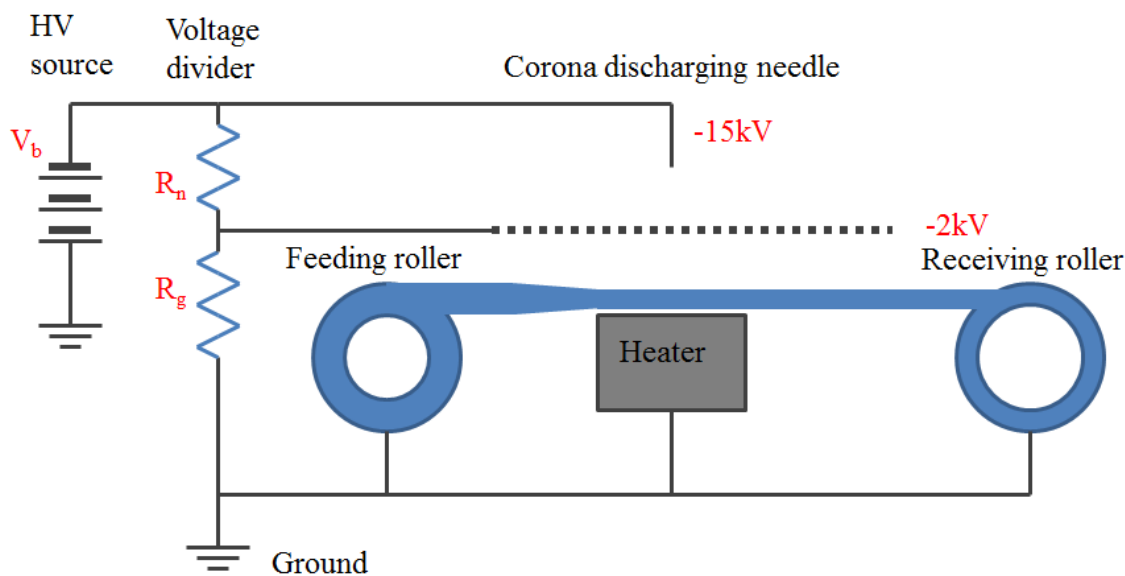


Figure 3-26 Schematics of stretching setup.

Schematic of simultaneous stretching and corona poling setup is explained in Figure 3-26. Voltage divider is a box with series of 15 of 0.5W, 10Mohm resistors. We can choose a voltage by selecting the resistor combination to achieve wanted grid potential. For example, if we choose R_n as 130 Mohm and R_g as 20Mohm, we get -2kV at the grid and it builds a 13kV difference between the discharging needle and the grid, when the bias, V_b , is -15kV.

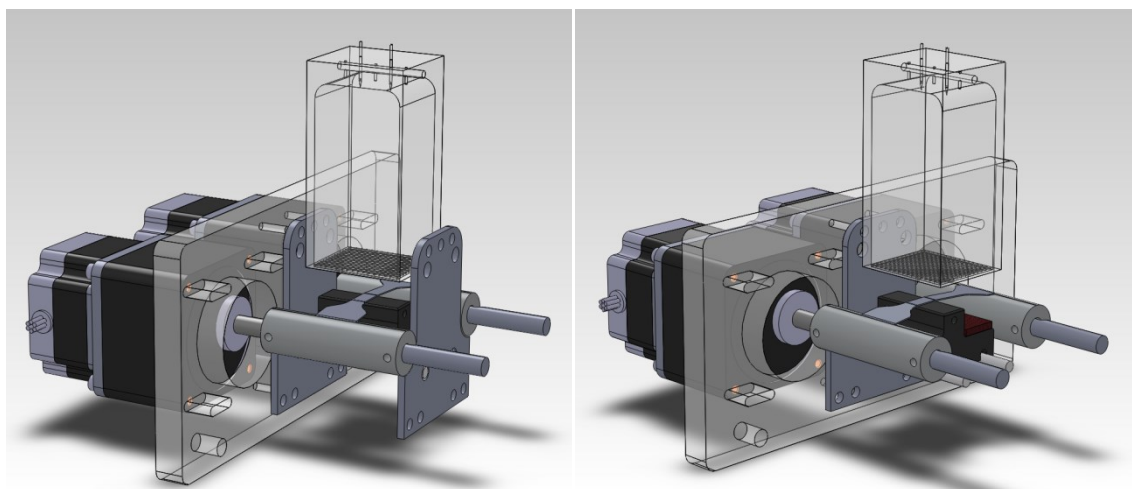


Figure 3-27 3D drawing of stretching and corona poling setup.

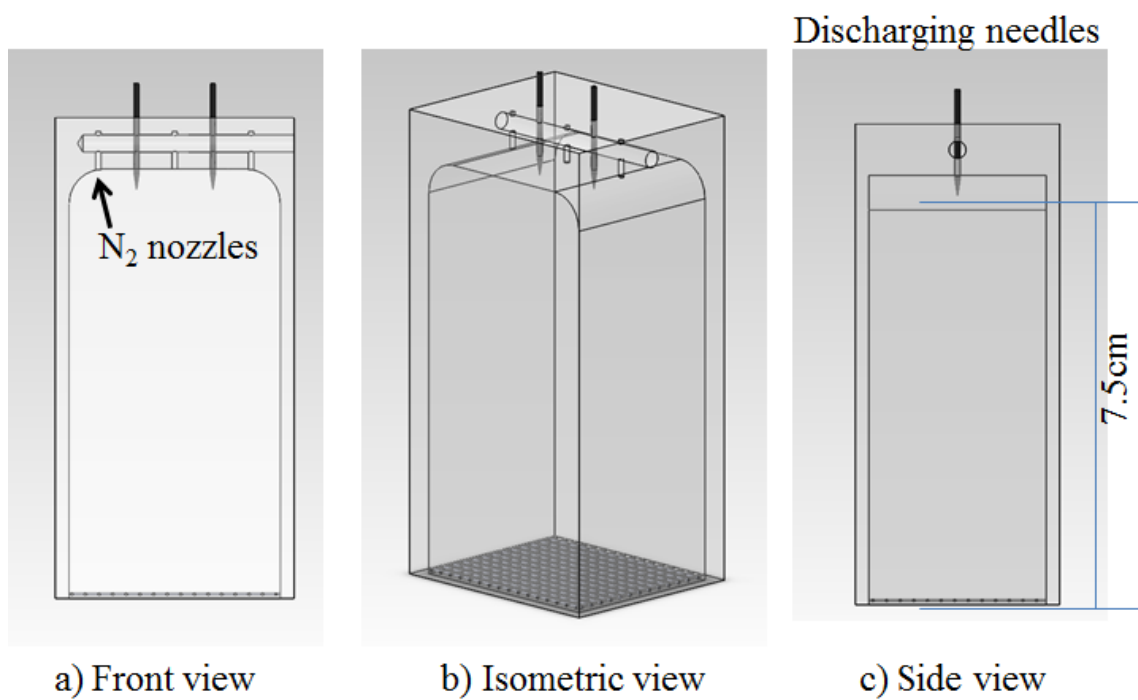


Figure 3-28 Corona charge unit.

Figure 3-28 shows the corona charge unit. Two needles have 10mm gap, Three N₂ blowing nozzles have 10mm gap, too. The distance From tip of the needle to the grid is set as 75mm. The grid is made out of #30x30 304 stainless steel mesh to reduce a local charge density fluctuation induced by shadowing from the grid.

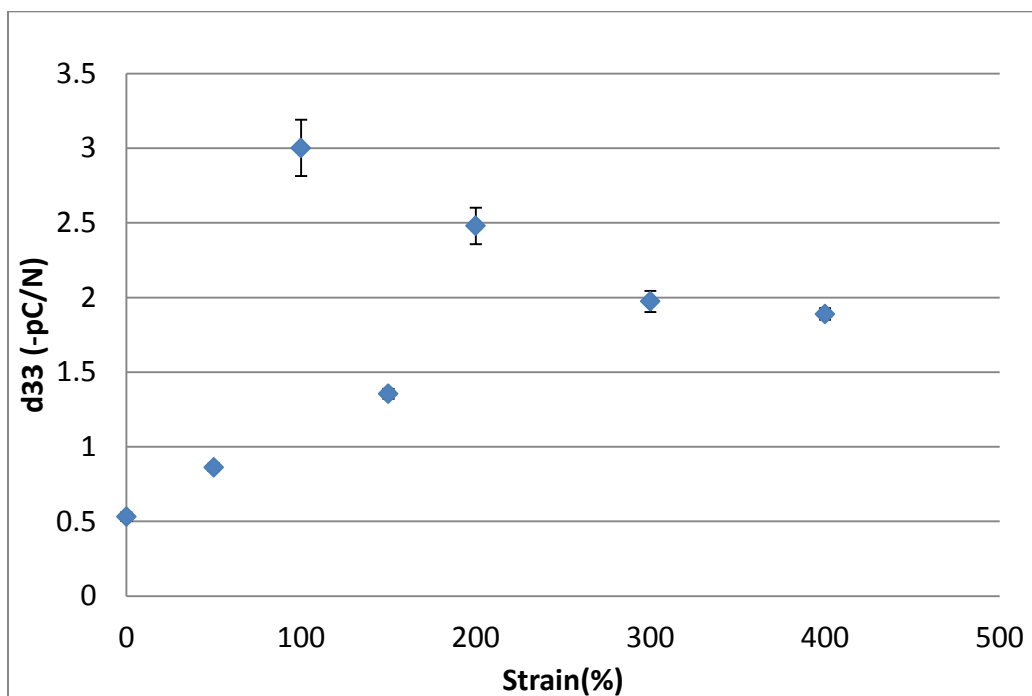


Figure 3-29 Poled at 200°C, with a speed of (2 steps/sec), with 2KV of surface static voltage, with different stretching. Stretching is shown as strain.

As shown in Figure 3-29, the d_{33} value is increasing with amount of stretching while other conditions are fixed. From the unstretched (0% strain) to 100% stretched, the d_{33} is increased - 0.5pC/N to -3.0pC/N, around 6 times. However, above 100% of stretching, it starts to decrease and saturates to -1.9pC/N.

The increase may be explained not only by the increase of crystallinity, also because, during the stretching more polymer chains are aligned along the stretching direction and more dipole of

repeating units, benzene rings with chlorine, are aligned to the normal direction of elongation. Consequently, more portion of dipole moment is pointing to the electrical field and thus the bulk polarity is increased. It is shown in Figure 3-30

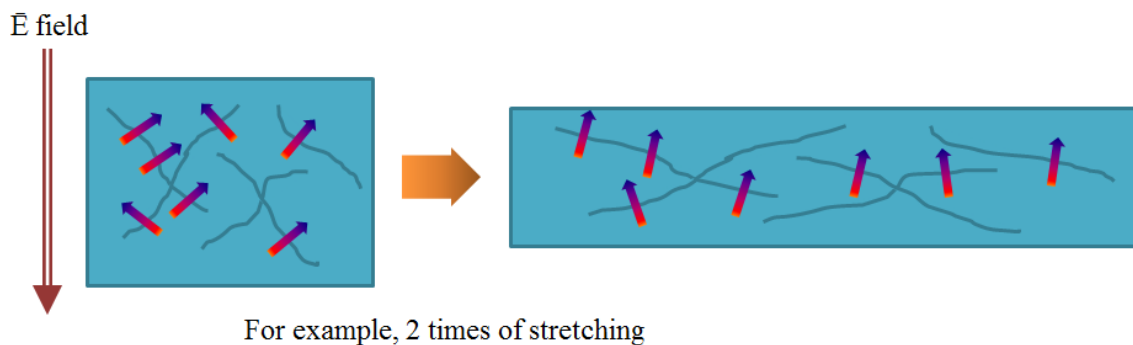


Figure 3-30 Increase of polarity of PA-C film by stretching. 2 times of stretching (100% strain)

SUMMARY

We have demonstrated for the first time that PA-C, when properly poled, can be a piezoelectric material. It shows maximum d_{33} value, -3.55pC/N , at the condition of 160°C , 100MV/m , 5 minutes and without stretching. It can reach its maximum polarity within 5 minutes and 90% of the maximum in a minute. Also, the saturation of d_{33} value is observed near 40MV/m . These facts imply that combining with its room temperature deposition, mechanical toughness, chemical inertness and biocomparability, PA-C can be a promising MEMS piezoelectric material.

Even the d_{33} is smaller than the one of PVDF, due to its high glass transition temperature, it maintains its piezoelectric coefficient even at 160°C for a week without any decaying. In contrast, the piezoelectric properties of PVDF is limited to less than 80°C due to its low β -relaxation temperature, -25°C [15], [14]. Comparing to a piezoelectric polyimide, PA-C has an advantage of larger piezoelectric coefficient, higher temperature stability and lower thermal process.

Also, it is shown that its piezoelectricity can be increased more with a simultaneous stretching and poling. At the 100% strain, it shows the maximum as 6 times larger than the one without stretching.

Chapter 4

MICROPHONE DESIGN

Design of Microphone

A diaphragm is common element of pressure sensors, which include piezoelectric, capacitive, and piezoresistive sensors[126–131]. The deflection of this diaphragm is detected either through its displacement, such as condenser microphone, or through the internal strain induced by the vibration, like piezoelectric microphone or piezoresistive sensor. The sensor bandwidth and sensitivity are related to the behavior of the diaphragm, which can be modeled by the Timoshenko's plate theory [132]. Also, membrane equations usually used to analyze the diaphragm vibrations[133] or static membrane equations have also been used in other sensor designs[134]. However, a membrane model is not always the most appropriate one. Sheplak and Dugundji [135] carried out static analysis of a clamped circular plate under initial tension and studied the transition range from plate behavior to membrane behavior in terms of the tension parameter k .

For "small and linear" deflections[136], Yu has shown that the transition from plate behavior to membrane behavior can be described in terms of the non-dimensional tension parameter k . This transition occurs over the range $1 < k < 20$, with the plate behavior dominating for $k < 1$ and the membrane behavior dominating for $k > 20$. For the term, "small and linear", if the deflection is smaller than $\leq 10\%$ diaphragm thickness, the pressure-deflection relationship will be linear. When the pressure increases, the rate of deflection decreases and the pressure-deflection relationship will produce nonlinearity. As a rule of thumb, a deflection of 12% of diaphragm thickness will produce a nonlinearity of 0.2%. [137]

Model Description and small deflection theory

Figure 4-1 shows a clamped, circular diaphragm of radius of a and thickness h . The Young's modulus of elasticity and Poisson's ratio of the diaphragm material are denoted

by Y and ν , respectively.

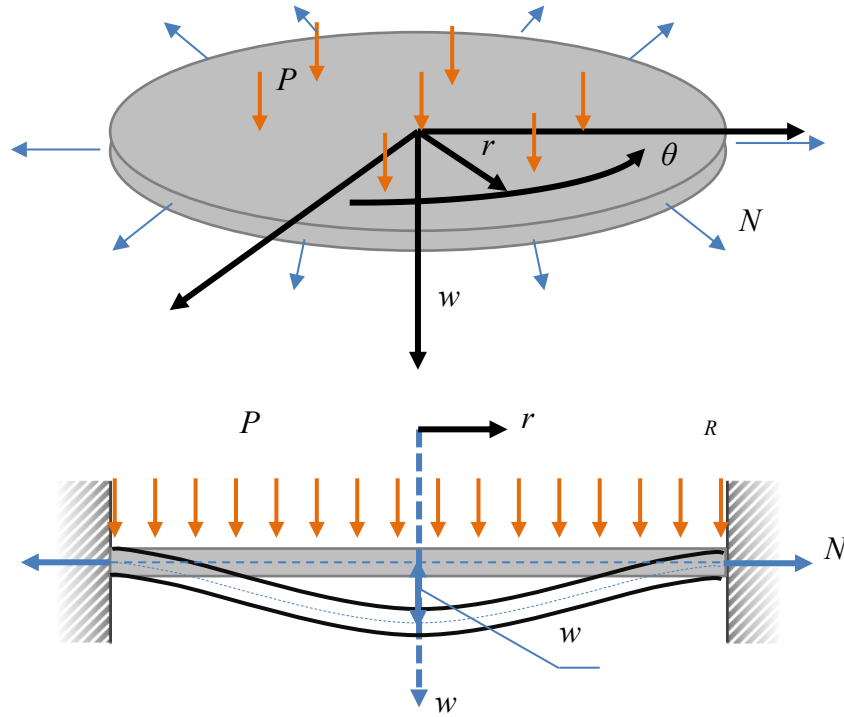


Figure 4-1 Illustration of a diaphragm clamped along its edge

Assuming the diaphragm which is homogeneous, axisymmetric, linearly elastic and perfectly clamped with zero in-plane residual stress is under the pressure P . In the small deflection theory, the transverse deflection of the diaphragm can be described as

$$w(r) = -\frac{Pa^4}{64D} \left[1 - \left(\frac{r}{a} \right)^2 \right]^2 \quad (1)$$

At the center of the diaphragm, the deflection is

$$w(0) = -\frac{Pa^4}{64D} \quad (2)$$

, where the flexural rigidity $D = Yh^3 / 12(1 - \nu^2)$ and r is the radial coordinate. The theory works as long as the deflection at the center is small enough compared to the thickness of the diaphragm ($\leq 10\%$)[137]. However, as the deflection increases, the in-plane strain increases and cannot be neglected.

Linear Model of Plate with Tension

The initial in-plane tension works to decrease the deflection of the diaphragm. Because the thermal expansion mismatch of the PA-C film and the silicon wafer during the fabrication process of the diaphragm of MEMS piezoelectric microphone, an in-plane stress tends to be built. The characteristic of the diaphragm cannot be described simply by small deflection theory as we described in (1).

Now, if we define a non-dimensional tension parameter k as

$$k = a \sqrt{\frac{N_0}{D}} = \frac{a}{h} \sqrt{\frac{12(1-\nu^2)N_0/h}{Y}} = \frac{a}{h} \sqrt{\frac{12(1-\nu^2)T}{Y}} \quad (3)$$

, where the constant $D = Yh^3 / 12(1 - \nu^2)$ and $T = N_0/h$ is the tension per unit area. N_0 is the initial tension per unit length applied to the diaphragm. In the following analysis, it is shown that the choice of a plate model or a membrane model actually depends on the tension parameter k , considering flexural strength D , not on just the initial tension per unit length N_0 applied to the diaphragm.

Starting from Love's equations[138], including damping, axial in-plane force per unit length N_r , and the transverse loading per unit area $f(r, \theta; t)$, the nonlinear partial differential equation governing a plate with initial tension can be obtained as

$$\rho h \frac{\partial^2 w}{\partial t^2} + D \nabla^4 w - N_0 \nabla^2 w = \frac{1}{r} \frac{\partial}{\partial r} \left(r N_r \frac{\partial w}{\partial r} \right) - 2\mu \frac{\partial w}{\partial t} + f(r, \theta; t) \quad (4)$$

where r is the radial distance from the center ($r = 0$), θ is the angular coordinate, $w(r, \theta; t)$ is the transverse displacement, and μ is the damping coefficient. When the displacement is small - less than 10% of diaphragm thickness - equation (4) can be reduced to the linear form by getting rid of axial in-plane force term

$$\rho h \frac{\partial^2 w}{\partial t^2} + D \nabla^4 w - N_0 \nabla^2 w = -2\mu \frac{\partial w}{\partial t} + f(r, \theta; t) \quad (5)$$

The boundary conditions along the clamped edge at $r = a$ gives

$$w(r, \theta; t)|_{r=a} = 0, \quad \frac{\partial w(r, \theta; t)}{\partial r}|_{r=a} = 0 \quad (6)$$

To fulfill the requirement of finite displacement at the center of diaphragm (i.e., $r = 0$)

$$|w(r, \theta; t)|_{r=0} < \infty \quad (7)$$

Free Oscillations of Undamped System

If we assume, there are no damping and external forcing, a solution of the form will become

$$w(r, \theta; t) = W(r, \theta) \cos \omega t \quad (8)$$

, where ω the natural angular frequency. By substituting equation (8) into equation (5), the result is

$$-\rho h \omega^2 W + D \nabla^4 W - N_0 \nabla^2 W = 0 \quad (9)$$

Then, equation (9) can be written as polynomials

$$(\nabla^2 - \alpha_1^2)(\nabla^2 - \alpha_2^2)W = 0 \quad (10)$$

where, we set new variables, α_1 and α_2

$$\alpha_1^2 = \frac{N_0 + \sqrt{N_0^2 + 4\rho h\omega^2 D}}{2D}$$

$$\alpha_2^2 = \frac{-N_0 + \sqrt{N_0^2 + 4\rho h\omega^2 D}}{2D} \quad (11)$$

with the relationship between α_1 and α_2

$$\alpha_1^2 a^2 = \alpha_2^2 a^2 + k^2 \quad (12)$$

Using equation (12) we find a relationship between α_1 and α_2 .

By expanding the transverse deflection amplitude as

$$W(r, \theta) = R(r)\Theta(\theta) \quad (13)$$

Then substituting into the spatial eigenvalue problem given by equation (10), it is determined that

$$\Theta(\theta) = A_m \cos m(\theta - \varphi_m)$$

$$R(r) = A_{1m} I_m(\alpha_1 r) + A_{2m} K_m(\alpha_1 r) + A_{3m} J_m(\alpha_2 r) + A_{4m} Y_m(\alpha_2 r) \quad (14)$$

where m is an integer that satisfies the boundary condition for the plate in the tangential direction. A_{1-4} are constants to be determined later.

The functions $I_m(\alpha_1 r)$, $K_m(\alpha_1 r)$, $J_m(\alpha_2 r)$, and $Y_m(\alpha_2 r)$ are the modified Bessel function of the first kind, the modified Bessel function of the second kind, the Bessel function of the first kind, and the Bessel function of the second kind, respectively. Each of these functions is of order m .

For the microphone, we consider the first vibrational mode and set m as 0. Thus, it simplifies equation (14) to equation (15)

$$W(r, \theta) = R(r)$$

$$R(r) = A_1 I_0(\alpha_1 r) + A_2 K_0(\alpha_1 r) + A_3 J_0(\alpha_2 r) + A_4 Y_0(\alpha_2 r) \quad (15)$$

From equations (6), (7), (8), (13), and (15), the finite displacement condition at the plate center leads to

$$A_2 = A_4 = 0 \quad (16)$$

Making use of the clamped edge boundary conditions given by equation (6,7) in equations (8), (13), and (15), the characteristic equation is determined to be

$$I_0(\alpha_1 a) J'_0(\alpha_2 a) + J_0(\alpha_2 a) I'_0(\alpha_1 a) = 0 \quad (17)$$

, where the prime indicates a derivative of related modified Bessel function. Determining the roots of equation (17)

To solve equation (17), we need to use a numerical method because for solving it requires to know k .

By using Mathematica©, we could find a values of $\alpha_2 * a$ over k . In Mathematica, because k is reserved, we use $kk1$. Also, to make it simple, instead of $\alpha_2 * a$, we use $aa2$.

$$\begin{aligned} & \text{Table}[\{10^{kk1}, aa2 /. \text{FindRoot}[-\sqrt{10^{2kk1} + aa2^2} \text{BesselI}[1, \sqrt{10^{2kk1} + aa2^2}] \text{BesselJ}[0, aa2] \\ & \quad - aa2 \text{BesselI}[0, \sqrt{10^{2kk1} + aa2^2}] \text{BesselJ}[1, aa2] = \\ & \quad = 0, \{aa2, 3\}], \{kk1, -5, 5, 1\}] \end{aligned}$$

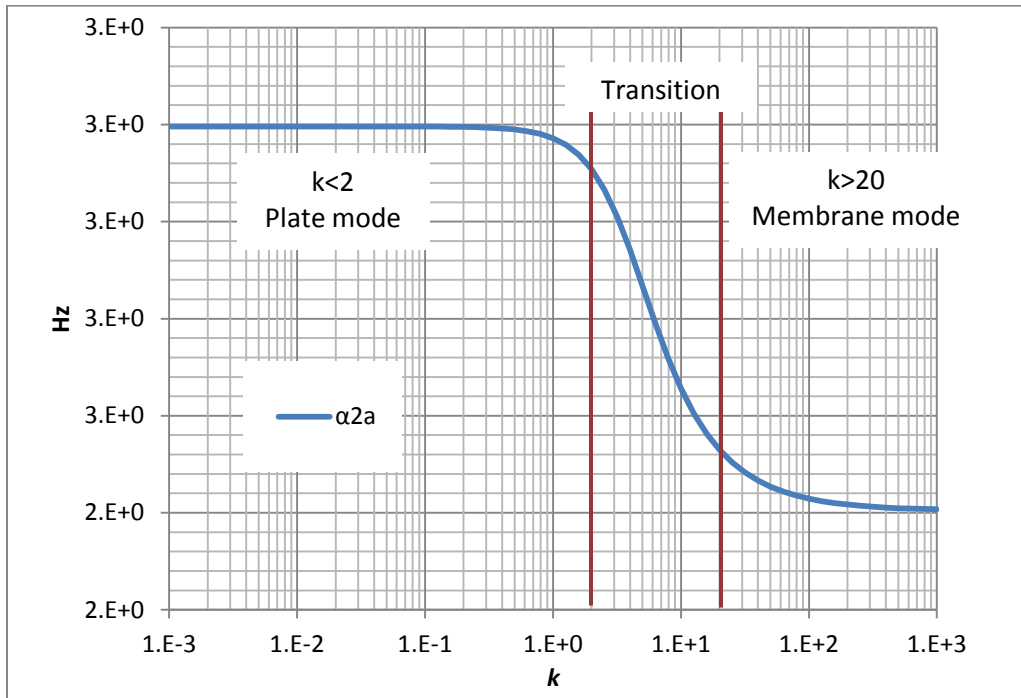


Figure 4-2 α_2*a over tension parameter k

The natural frequencies are given by

$$\omega^2 = \frac{D}{\rho h a^4} (\alpha_2 a)^2 [(\alpha_2 a)^2 + k^2] \quad (18)$$

, where k is the tension parameter introduced in equation (3). The associated mode shapes are given by

$$W(r) = R(r) = A \left[J_0(\alpha_1 r) - \frac{J_0(\alpha_2 a)}{I_0(\alpha_1 a)} I_0(\alpha_1 r) \right] \quad (19)$$

Transition of Plate-membrane Behavior and Results

The results from the former analysis are used to examine the cases of plate behavior and membrane behavior and the transition cases between them.

Plate Model ($T = 0$, i.e. $N_0 = 0$)

For this case, we can imagine a plate with thickness, flexural strength, but no initial tension built inside a diaphragm. In equation (3), when N_0 is zero, k is zero. In equation (12), α_1 becomes same as α_2 . Substituting α_1 from equations (18), and (19) further simplifies the natural frequencies and mode shapes of the associated equations. They are given by

$$f = \frac{1}{2\pi} (\alpha_2)^2 \sqrt{\frac{D}{\rho h}}$$

$$W(r) = A \left[J_0(\alpha_2 r) - \frac{J_0(\alpha_2 a)}{I_0(\alpha_2 a)} I_0(\alpha_2 r) \right] \quad (20)$$

Membrane Model ($D=0$)

For the membrane, we can assume its tension is dominant over D so that we can ignore D . Therefore using equation (3) and (12), we have $D \rightarrow 0$, $D/N_0 \rightarrow 0$, $k \rightarrow \infty$, $\alpha_1 \rightarrow \infty$. Then, from equations (18) and (19), it is found that the associated natural frequencies and the mode shapes are given by

$$f = \frac{1}{2\pi} (\alpha_2)^2 \sqrt{\frac{N_0}{\rho h}}$$

$$W(r) = A J_0(\alpha_2 r) \quad (21)$$

Plate-membrane Transition

The results shown in Figure 4-2 are applicable to any isotropic circular diaphragm whose edge is clamped. For the first vibration mode (i.e., $m = 0$), the transition behavior from plate to membrane is shown in Figure 4-2. To obtain this plot, the eigenvalue $\alpha_2 a$ is determined from equation (21) for different values of k . As k decreases and becomes less than 2, the graph of $\alpha_2 a$ is asymptotic to the plate case (i.e., $\alpha_2 a \rightarrow 3.196$). Also k increases and take over the value larger than 20, the graph is asymptotic to the membrane case (i.e., $\alpha_2 a \rightarrow 2.404$).

Between the plate and membrane behavior, there is a transition region of $2 < k < 20$. This result is similar to the obtained by Sheplak and Dugundji[135] for the static case.

For the resonance frequency of thick PA-C diaphragms with different radius as shown in Figure 4-3(30um thick PA_C diaphragm) and, Figure 4-4 (5um thick PA_C diaphragm)

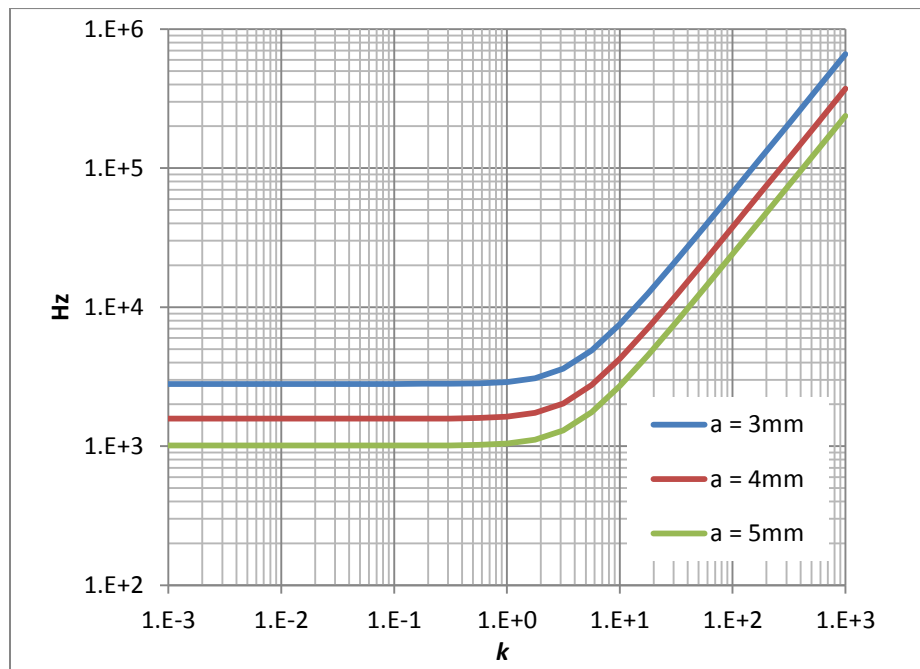


Figure 4-3 Resonance frequency dependency over different radiuses (30um thick PA-C).

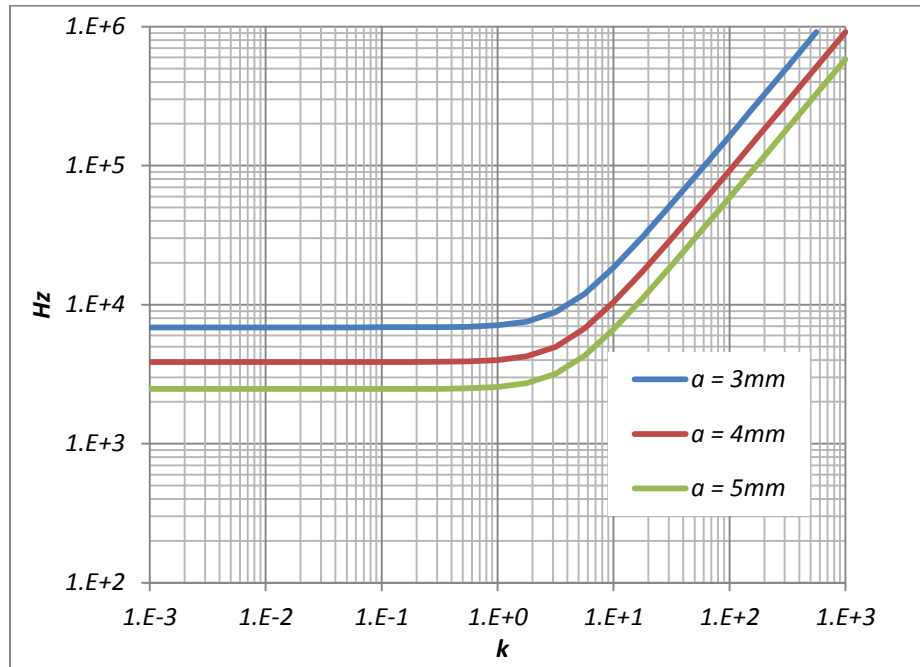


Figure 4-4 Resonance frequency dependency over different radiuses (5um thick PA-C).

For different thickness, while the radius is fixed as 3mm, we calculate the following plot (fig. 4-5).

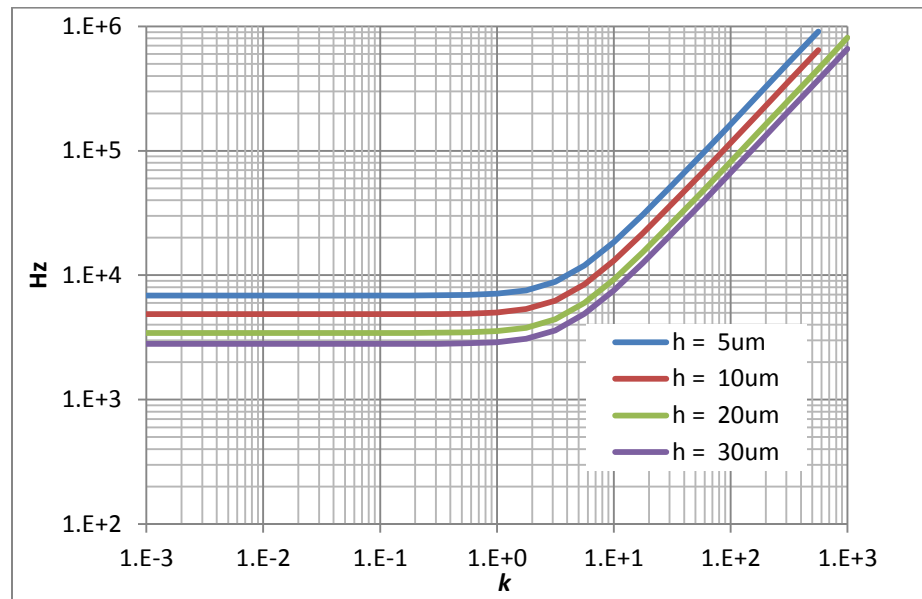


Figure 4-5 Resonance frequency dependency over different thickness (3mm in radius).

For the tension parameter dependent mode shape, we calculate Figure 4-6 for with a radius of 3mm and a thickness of 30um. However, the mode shape is independent of diameter and thickness, because we use non-dimensional tension parameter k . From the $\alpha_2 a$ over k analysis, as we have seen earlier, the transition from plate mode to membrane mode occurs over the value of $2 < k < 20$. From Figure 4-6, we see a dramatic mode change from 2 to 20 for the value of tension parameter k .

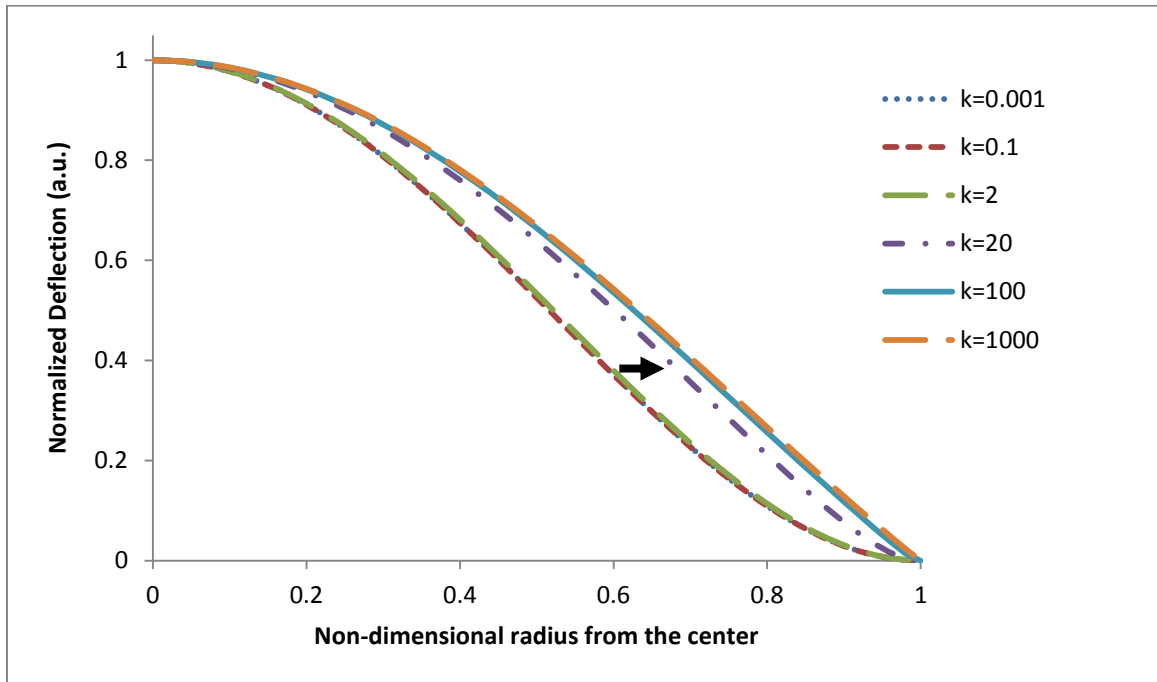


Figure 4-6 Mode shape dependency over tension parameter k

Stress distribution varies through the thickness and across the radius of the diaphragm. For instance, at the neutral plane there will be a no stress while the outer surface will be at maximum stress. In addition, at any given radius r , when the membrane is pushed up, while the upper-side experiences the tensile stress, the lower side will experience compressive stress. For the radial and tangential directions, they have their own stress components.

Since the piezoelectric microphone is a stress related charge device, we need to consider the location of the zero stress point along the non-dimensional radius.

For the top side of the membrane, when there is a static and uniform pressure, the radial stress is given as by Hooke's law.[139]

$$\sigma_r(r) = \frac{3pa^2}{h^2} \left[\frac{\nu+1}{k^2} - \frac{I_0\left(\frac{kr}{a}\right)}{kI_1(k)} - \frac{a(\nu-1)}{rk^2} \frac{I_1\left(\frac{kr}{a}\right)}{I_1(k)} \right] \quad (22)$$

If we calculate the radial stress along the radius r as shown in Figure 4-7, we find zero radial stress point is shifted from 0.64 to 0.87 in non-dimensional radius along the tension parameter k changes from 2 to 20. This radial stress zero point will be used for electrode design of chip.

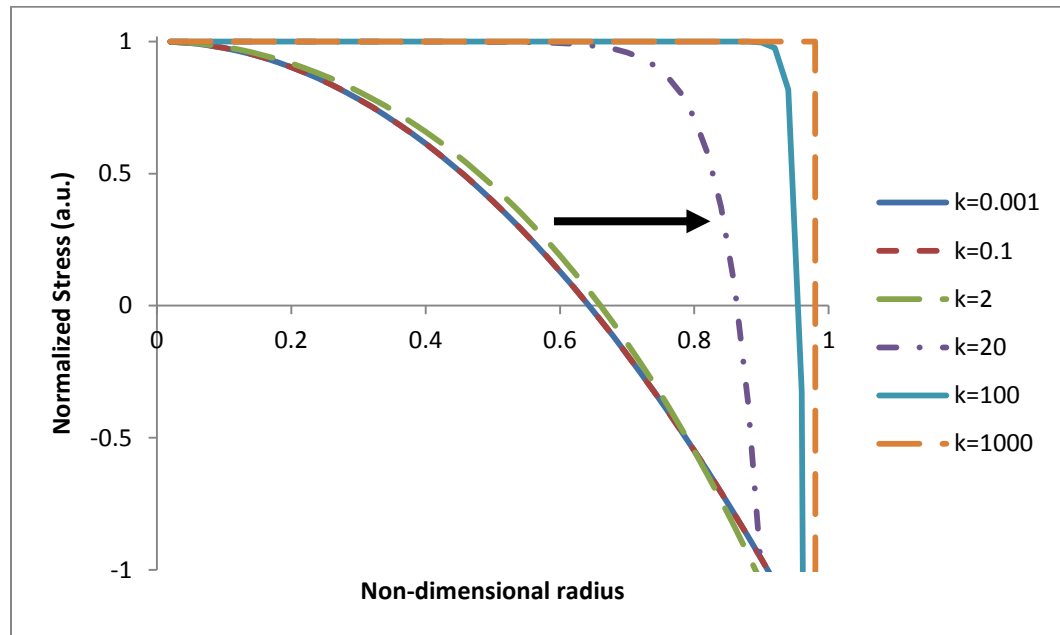


Figure 4-7 Normalized radial stress change over non-dimensional radius.

The radial stress zero point is shifting from 0.64 in non-dimensional radius to 1 along the increase of the tension parameter k . At a low k (< 1), the zeroing point is maintained at 0.64 or at a high k (> 1000), the zeroing point is kept at 1. Between two limits, by the increasing of k ($1 < k < 1000$), the zeroing point is also shifted from 0.64 to 1, as we see in Figure 4-8.

This solution is calculated in Mathematica©, with a “FindRoot” command

$$\text{FindRoot}[Qr[10^n, r] == 0, \{r, aa\}]$$

Where $Qr[k, r]$ is the equation represent the radial tension.

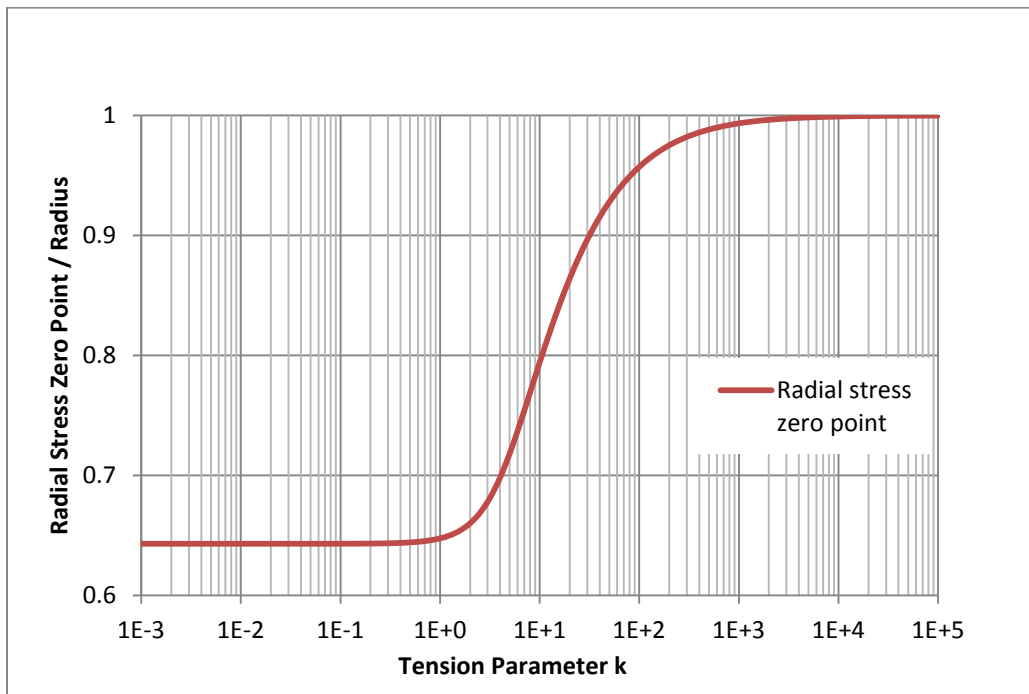


Figure 4-8 Where the radial stress becomes zero ($\sigma_r = 0$). The value is shown as fraction over radius.

For the tangential stress is, also, given as

$$\sigma_t(r) = \frac{3pa^2}{h^2} \left[\frac{\nu+1}{k^2} - \frac{\nu I_0\left(\frac{kr}{a}\right)}{kI_1(k)} + \frac{a(\nu-1)}{rk^2} \frac{I_1\left(\frac{kr}{a}\right)}{I_1(k)} \right] \quad (23)$$

And the graph from equation (23) is shown in Figure 4-8. The tangential stress's zero point is located between 0.8 and 0.87 in non-dimensional radius.

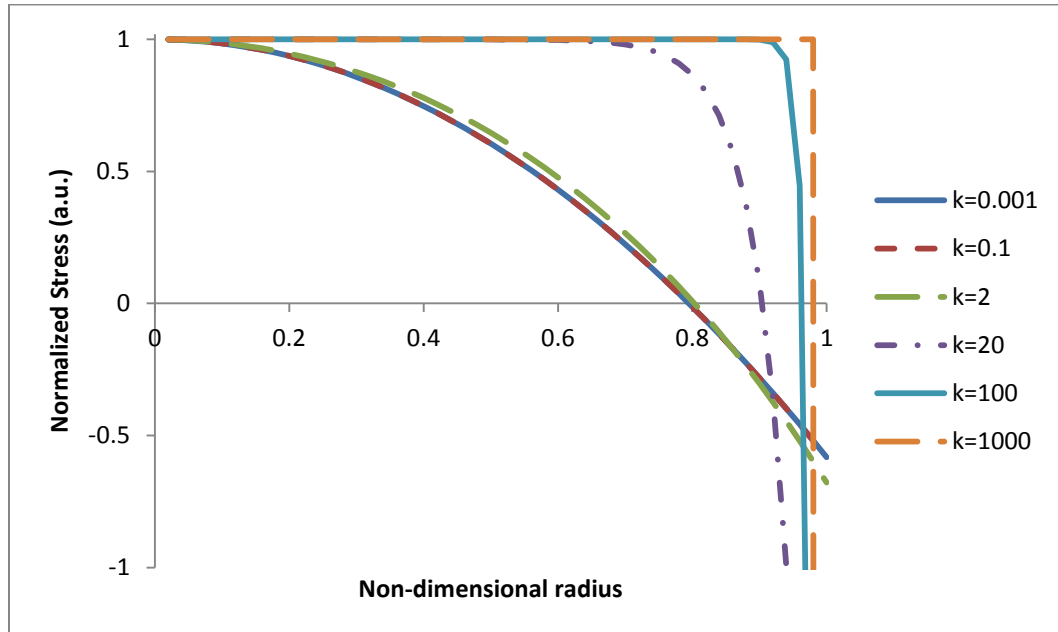


Figure 4-9 Normalized tangential stress change over non-dimensional radius.

The tangential stress zero point shifts from 0.79 in non-dimensional radius to 1 along the increase of the tension parameter k . At a low k (< 1), the zeroing point is maintained at 0.79, while at a high k (> 1000), the zeroing point is kept at 1. Between two limits, increasing k ($1 < k < 1000$) results in the zeroing point shifting from 0.79 to 1, as seen in Figure 4-10. However, this is less drastic than the radial stress zero point.

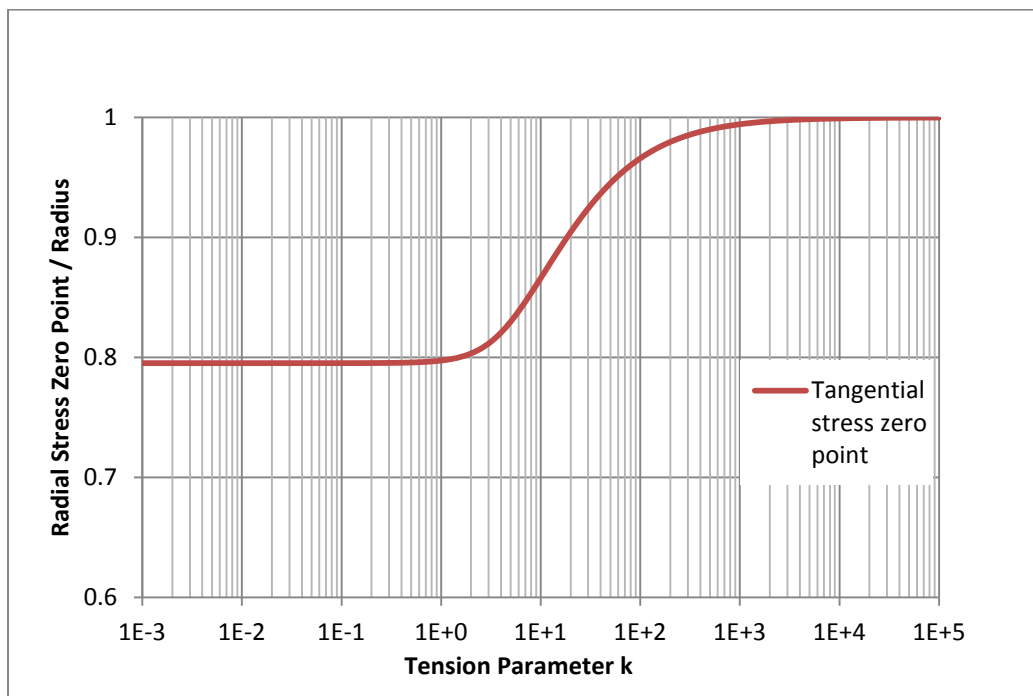


Figure 4-10 Where the Tangential stress becomes zero ($\sigma_t = 0$).
The value is shown as fraction over radius.

RESIDUAL TENSION MEASUREMENT AND TENSION PARAMETER K

Static pressure is usually present on thin films overlying a solid substrate. The static pressure is applied to the diaphragm from the back side of device, as shown in Figure 4-14. When the applied pressure is less than the critical yield point, the diaphragm bulges up without any deformation and reversible. However, when the applied pressure is larger than the yield pressure, PA-C diaphragm will be deformed and cannot be used to measure. The plastic deformation occurs in the PA-C film that causes it to bulge to a distance d that is dependent on the Young's modulus, Y (~ 3.56 GPa), Poisson's ratio, ν (~ 0.4 [140]), geometry of the diameter of the diaphragm, and thickness of the PA-C film, h .

Assuming that the deflection is small compared to the diaphragm radius, the relationship between this deflection, air pressure and the residual stress can be expressed by the following equation[141][142],

$$P = \frac{8h}{3a^4} \frac{Y}{1-\nu} d^3 + \frac{4h\sigma}{a^2} d \quad (24)$$

, where P is the differential pressure, h is the diaphragm thickness, σ is the residual stress and d is the out-of-plane displacement.

We measured residual with 3mm in radius and 30um in thickness diaphragm after whole process is finished (Figure 4-11). By the fitting data, we get 18.1Mpa for the residual tension, T , and 3.96GPa for Young's modulus, Y . Considering the difference of thermal expansion coefficient between silicon (2.6ppm) and PA-C (69ppm), the modulus of PA-C and the maximum process temperature(150°C), also, we can estimate the residual stress, $\sigma_{\text{estimation}}$ as 30.7MPa and it is within the order of range.

$$\sigma_{\text{estimation}} = (69 \text{ ppm} - 2.6 \text{ ppm}) \times (150^\circ \text{ C} - 20^\circ \text{ C}) \times 3.56 \text{ GPa} = 30.7 \text{ MPa}$$

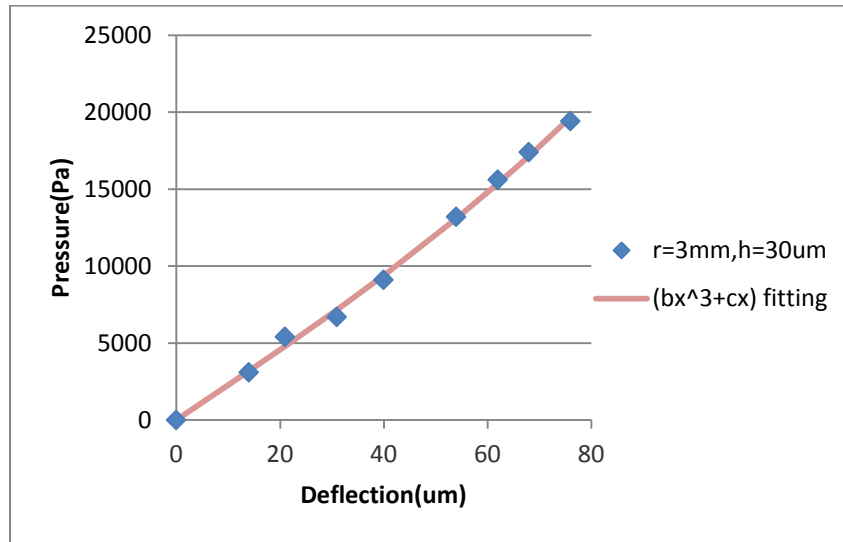


Figure 4-11 Static pressure inducing the deflection of the diaphragm, after the process

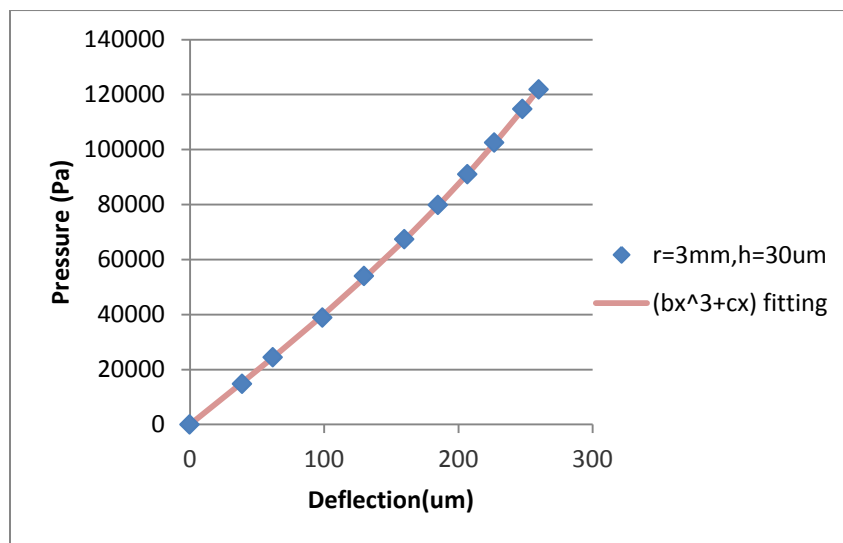


Figure 4-12 Static pressure inducing the deflection of the diaphragm, after a annealing at 160°C, 1hr

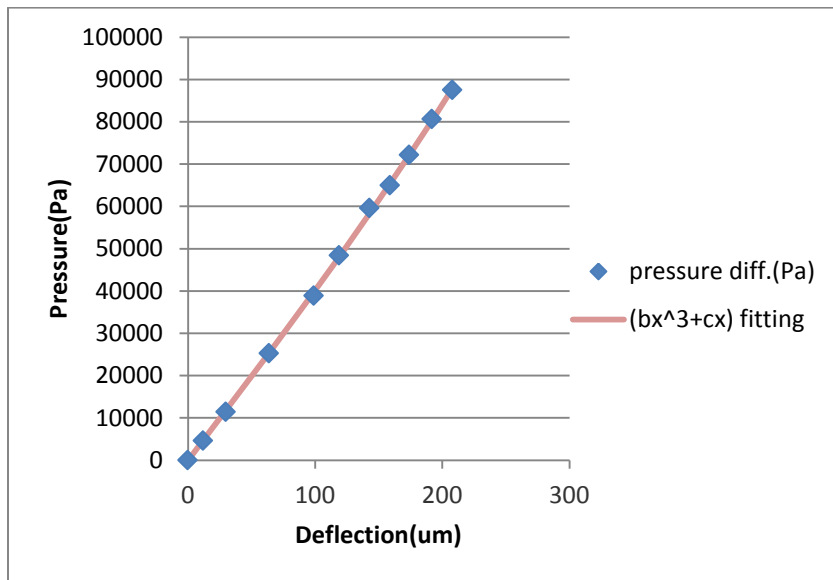


Figure 4-13 Static pressure inducing the deflection of the diaphragm, after a annealing at 200°C, 5m

	After the fabrication is done*	Annealed at 160°C, 1hr	Annealed at 200°C, 5m
Residual stress	18.1 MPa	28.8 MPa	30.7 MPa
Modulus	3.96 GPa	4.53 GPa	3.89 GPa
K	23.7	29.0	29.9
Estimated $\sigma_i=0$	87.8% of radius	89.4% of radius	89.6% of radius
Estimated $\sigma_i=0$	91.3% of radius	92.3% of radius	92.4% of radius
Estimated f_R	16.4kHz	19.9kHz	20.5kHz

Table 4-1 Measured residual tension after process and after poling process. * The maximum temperature which the device experienced during the fabrication is 150°C, 5 minutes.

From the residual tension and modulus values, tension parameter, k , will be found in Table 4-1. The value of k can be calculated by following equation (25),

$$k = \frac{a}{h} \sqrt{\frac{12(1-\nu^2)T}{Y}} \quad (25)$$

Judging by the tension parameter k , the diaphragm is in the region of membrane behavior. In this case, the radial stress zero point is >87.8% of the diaphragm radius from the center. Consequently, we choose one electrode within 90% of radius, instead of two separated electrodes in radial direction.

Static pressure deflection experimental setup

During experimentation, each die is placed in a testing jig that allows fluid (air) to apply pressure to the PA-C membrane. The jig is then connected to a fluidic setup consisting of a valve, a pressure regulator, and a pressure gauge, as shown in Figure 4-14. Figure 4-14 (a) shows the cross section view of the testing jig and Figure 4-14 (b) illustrates the overall view of the testing setup. The testing jig is placed under a microscope for observation. Pressure inside the tubing is then gradually increased by adjusting the pressure regulator. The pressure gauge reads out the current pressure inside the device.

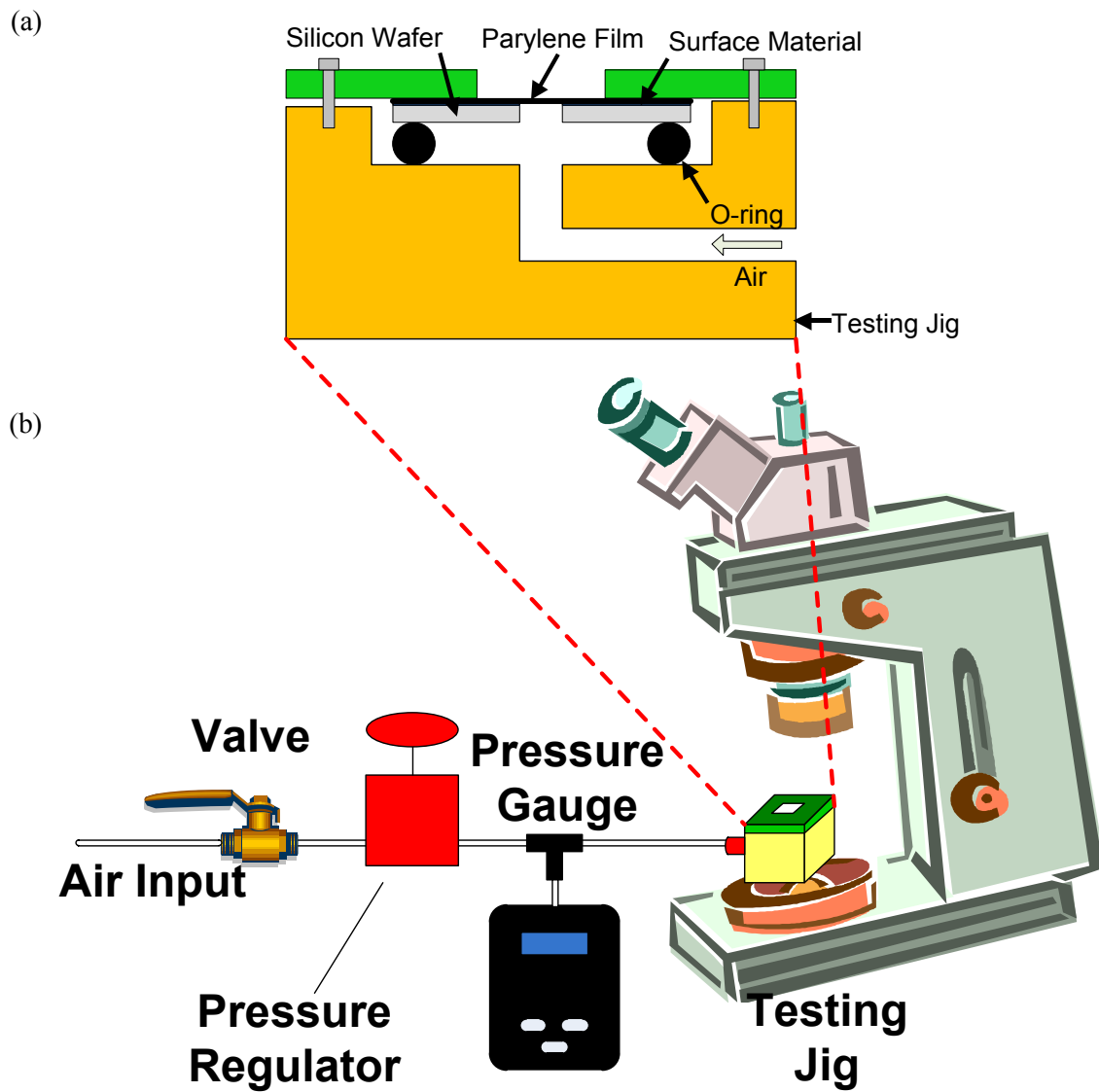


Figure 4-14: Experimental setup of the blister test: (a) the cross-section view of the test jig, and (b) schematic diagram of the testing setup

Lumped element model

The acoustic properties of the microphone structure are modeled using a lumped element model (LEM), which involves electrical, mechanical, and acoustical energy domains. In the LEM, the acoustic energy domain is assumed to be coupled to the electrical energy domain through ideal transformers. This modeling is valid as far as any length scales of the microphone are less than 10% of the acoustic wavelength. As a result, the distributed energy is lumped at a chosen spatial location. This assumption is easily met for MEMS devices in many applications due to the typically small dimensions relative to the signal wavelengths of interest. For example, if our target frequency is 5kHz and the largest dimension of the microphones is 6mm in diameter of a diaphragm, the system satisfies the lumped model condition at 5kHz ($\approx 68\text{mm}$).

In LEM, the coupling between the various energy domains is realized via equivalent models of the physical system.[143–145] An equivalent circuit model is built by lumping the distributed energy storage and dissipation into ideal circuit elements. In an electroacoustic system, differential pressure and voltage are effort variables. And volumetric flow rate and current are flow variables.[143] Acoustic and mechanical elements are modeled to be lumped elements to their electrical equivalents. Thus, the equivalent electrical circuit represents electroacoustic model.

Inductors and capacitors represent storage of kinetic and potential energy in the electrical domain, respectively, while mass and compliance (inverse of stiffness) represents kinetic and potential energy stored in the mechanical domain. Similarly, dissipation of energy is represented by a resistor in the electrical domain and damping effect in the electrical domain. Thereby a single equivalent circuit represents the dynamics of the entire system.

Also, an impedance analogy is employed, in which elements that share a common effort are connected in parallel[146], while those sharing a common flow are connected in series.[143]

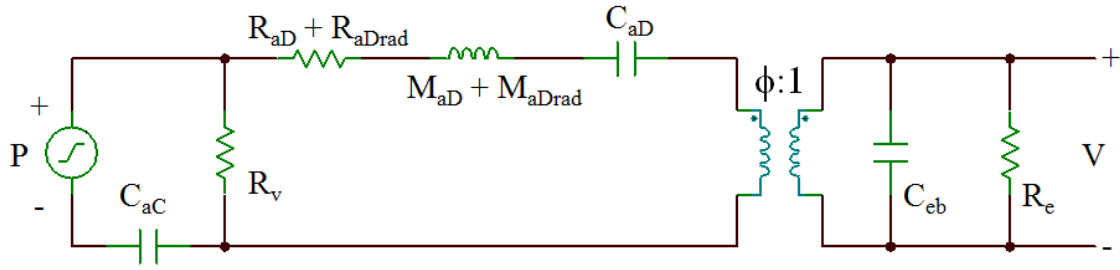


Figure 4-15 Equivalent circuit representation of a lumped-element model of a piezoelectric microphone.

Figure 4-15 shows a schematic of an equivalent circuit representation of the lumped element model.

An acoustic pressure, P , deflects the diaphragm with an angular frequency ω , which generates a voltage, V , across the piezoelectric thin film written as C_{eb} . The conversion from the acoustic domain to the electrical domain is represented by a transformer possessing a turns ratio, ϕ , also called as the electroacoustic transduction coefficient.[147].

$$\phi = \frac{-d_A}{C_{aD}} \left[\frac{Pa}{V} \right] \quad (26)$$

, where C_{aD} is the acoustic compliance of the diaphragm when an electrical circuit is short across the electrodes

$$C_{aD} = \int_0^R 2\pi r w(r) dr / P \Big|_{v=0}; \left[\frac{m^3}{Pa} \right] \quad (27)$$

and d_A is the effective acoustic piezoelectric coefficient and given as

$$d_A = \frac{\Delta V}{V} \Big|_{p \rightarrow 0} = \int_0^R w(r) \Big|_{p \rightarrow 0} 2\pi r dr / V; \left[\frac{m^3}{V} \right] \quad (28)$$

C_{eb} is the blocked electrical capacitance and

$$C_{eB} = C_{eF}(1 - \kappa^2) = \frac{\epsilon_r \epsilon_0 \pi R^2}{h_p} (1 - \kappa^2); [F] \quad (29)$$

,where ϵ_r is the relative dielectric constant of the piezoelectric material, ϵ_0 is the permittivity of free space, and κ is the electroacoustic coupling factor can be described as

$$\kappa^2 = \frac{d_a^2}{C_{eF} C_{aD}}$$

, while R_e is the dielectric loss resistance, describing one of parameters of the electrical domain.

Other components of the equivalent circuit which is describing the mechanical domain present M_{aD} , M_{aDrad} , C_{aD} , R_{ad} and R_{aDrad} as the radiation resistance, radiation mass, compliance and mass of the diaphragm, respectively[146]. A resistor R_{aD} in series with R_{aDrad} is added to describe the effect of structural damping. In addition, the cavity formed between the back of the diaphragm and the microphone package affects the dynamic response and compliance of the cavity, C_{aC} , is included in the equivalent circuit.

Finally, the resistance, R_v , represents viscous losses incurred in a vent channel that typically connects a microphone cavity to ambient pressure. In our device, a vent channel was not specifically designed into the structure; however packaging-induced leakage between the cavity and atmospheric pressure provides the same effect.

The radiation impedance is found by modeling the structure as a piston in an infinite baffle[148].

Where, M_{ad}

$$M_{aD} = \frac{2\pi}{(\Delta V)^2} \int_0^R \rho_A (w(r))^2 r dr \Big|_{v=0}; \left[\frac{kg}{m^4} \right] \quad (30)$$

,where ρ_A is the areal density of the piezoelectric PA-C diaphragm given by

$$\rho_A = \int_{Z_1}^{Z_2} \rho_i dz; \left[\frac{kg}{m^2} \right] \quad (31)$$

and ρ_i is the density of the corresponding layer.

And, M_{aDrad}

$$M_{aDrad} \approx \frac{8kR \rho c}{3\pi\omega A_{eff}}; \left[\frac{kg}{cm^4} \right] \quad (32)$$

, where A_{eff} is an effective diaphragm area to maintain continuity of volume velocity.

$$C_{aD} = \int_0^R 2\pi r w(r) dr / P \Big|_{v=0}; \left[\frac{m^3}{Pa} \right] \quad (33)$$

the acoustic compliance of the diaphragm when an electrical circuit is short across the electrodes

R_{aD} is the diaphragm resistance representing structural losses and R_{aDrad} is

$$R_{aDrad} \approx \frac{(kR)^2 \rho c}{2A_{eff}}; \left[\frac{kg}{m^4 s} \right] \quad (34)$$

It means a radiation resistance of the diaphragm

Finally, C_{aC} is the cavity compliance and

$$C_{aC} = \frac{\hat{V}}{\rho c^2}; \left[\frac{m^3}{Pa} \right] \quad (35)$$

The cavity compliance can vary easily when the chip is mounted on the stage, so that it could bring mismatch between the LEM and a measurement. [146]

R_v is the vent resistance. This cavity compliance and the vent resistance can vary easily when the chip is mounted on the stage, so that it could bring mismatch between the LEM and a measurement.

The time harmonic, two-port network equations describing the behavior of the linear reciprocal piezoelectric transducer are written in the acoustic domain as. [146]

$$\begin{bmatrix} I \\ Q \end{bmatrix} = \begin{bmatrix} j\omega C_{ef} & j\omega d_A \\ j\omega d_A & j\omega C_{aD} \end{bmatrix} \begin{bmatrix} V \\ P \end{bmatrix} \quad (36)$$

, where

$$Q = \int \frac{dw(r,t)}{dt} \cdot dS \quad (37)$$

is the volume velocity of the plate, dS is the normal projection of an infinitesimal element of area, $w(r, t)$ is the transverse deflection, and I is the electrical current.[149]

The general expression for the sensitivity of the piezoelectric microphone is written as equation (38),

$$\frac{V}{P} = \frac{\frac{R_v R_e \phi^2}{R_e s C_{eb} + 1}}{\frac{R_v}{s C_{ac}} + \left(R_v + \frac{1}{s C_{ac}} \right) \left(\frac{R_e \phi^2}{R_e s C_{eb} + 1} + s M_{aD} + \frac{1}{s C_{aD}} \right)} \quad (38)$$

, where $s = j\omega$.

The expression (38) includes the effects of cavity compliance and vent resistance in addition to the piezoelectric plate parameters. The effect of the cavity compliance, C_{ac} , should be considered to understand an overall sensitivity. The cavity must be made large enough to have a much greater compliance than the diaphragm.[146]

The distributed deflection, $w(r)$, is obtained by an analytical model was developed for the piezoelectric composite circular plate by Wang *et al.*[149]

The resulting equation also predicts any initial static deflection arising from stress in the composite structure as well as the onset of buckling. Using the lumped element model, a theoretical frequency response is computed. The predicted resonant frequency for the designed microphone geometry, using the material properties for PA-C and gold electrodes, was computed to be approximately 20.5 kHz. The theoretical response assumed a perfectly sealed cavity below the diaphragm i.e., $R_v \rightarrow \infty$. Any leakage from this cavity in the actual device leads to a low frequency roll-off in the response. Furthermore, the additional low frequency roll-off effect of the dielectric loss resistance, R_e , is not visible in this plot as the cutoff frequency is around 1 Hz.[146]

The structural parameters of the microphone are shown as follows in the Table 4-2.

	d_{33} (pC/N)	ϵ_r [150]	ρ (kg/m ³)	h (m)	Y (Gpa)	ν	σ_r (Mpa)
Top Piezo PA-C	-3	3.15	1,289[150]	1×10^{-6}	4.53	0.4	28.8
Gold electrodes	-	-	19,300[151]	200×10^{-9}	79	0.44	79,000[151]
Bottom Piezo PA-C	-3	3.15	1,289	29×10^{-6}	4.53	0.4	28.8

Table 4-2 Table of material properties

The composite plate model[152] accounts for material properties of each of the thin-film layers, as shown in Figure 4-16. These include the mechanical properties of the layers such as density, ρ , Poisson's ratio ν , Young's modulus, Y , and the in-plane tensile stress, σ_r which modifies the overall deflection and subsequently affects the dynamic behavior. The model also accounts for electrical properties including the relative permittivity constant, ϵ_r and piezoelectric coefficient d_{31} , of each layer including poled PA-C.

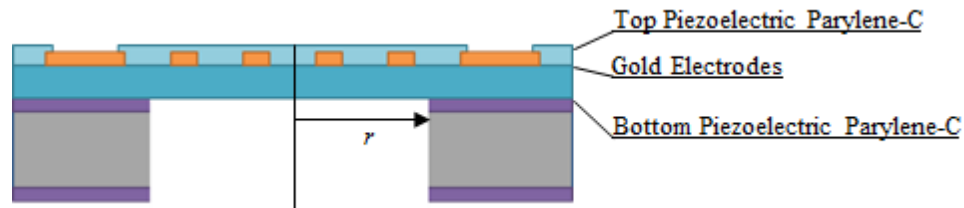


Figure 4-16 Layers of the microphone

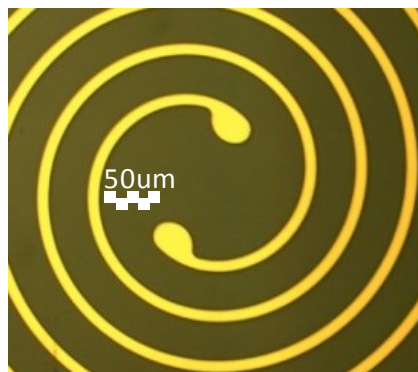


Figure 4-17 Structure of the electrodes

FREQUENCY RESPONSE

The frequency response of a near-ideal microphone (without preamplifier) is shown in Figure 4-18. Above the low frequency cut-off, f_L , and below the high frequency cut-off, f_H , the open-circuit sensitivity should be nearly flat (\pm a few dB). For measurements in the normal audio range, f_L should be less than 20 Hz and f_H should be higher than 10 kHz. The best 1/2-inch reference electret microphones by Bruel & Kjaer have flat responses (\pm 2 dB) from 6 Hz to 20 kHz [12]. The smallest hearing aid electret microphone ($3.63 \times 3.63 \times 1.76 \text{ mm}^3$) by Knowles Electronics has a relatively flat response (\pm 5 dB) between 150 Hz and 5 kHz [13]. The low and high frequency cut-offs are determined by the mechanical design of the microphone. These two frequency response limits are more closely examined in the following subsections.

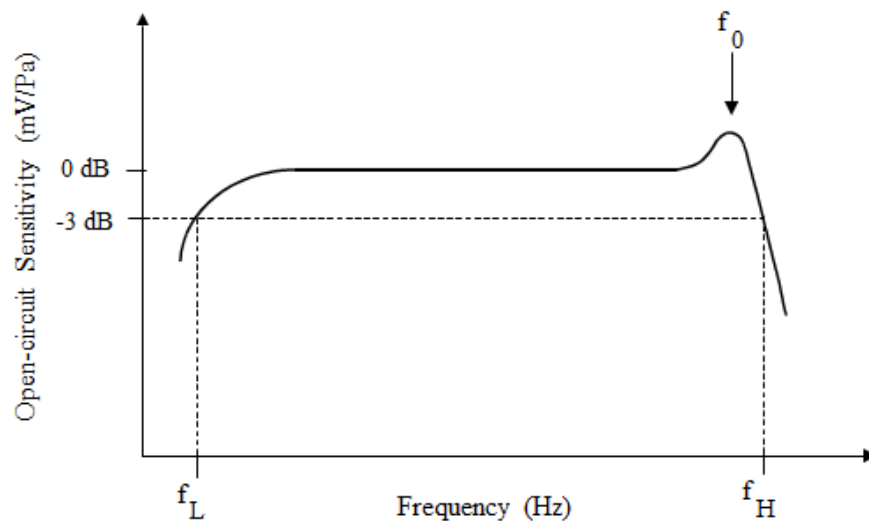


Figure 4-18 Typical frequency response of a microphone

Low-Frequency Cut-Off[153]

At low frequencies, the frequency response of a microphone (without a preamplifier) is influenced by the size and position of the static pressure equalization hole - whose purpose is to prevent the diaphragm from responding to ambient DC pressure level changes. At most frequencies in the audio range, this hole is small enough for its acoustic resistance to prevent sound waves impinging on the diaphragm from concurrently entering the back chamber and air gap. However, at lower frequencies, a small portion of the sound wave acting on the diaphragm is able to enter the back chamber and air gap through the pressure equalization hole. As a result, this low frequency sound pressure starts to oppose the motion of the diaphragm from the inside of the microphone causing the frequency response curve to tail off for lower and lower frequencies. The low frequency cut-off, f_L , is typically defined as the frequency at which the response curve has dropped 2-3 dB below the 0 dB open-circuit sensitivity reference level (Figure 4-18). At very low frequencies, the decay slope reaches a maximum of 20 dB/decade[1].

When the microphone is connected to a preamplifier, the high-pass filter lower corner frequency, $f_{e-lower}$, will also come into effect. This electrical lower cut-off frequency can be lower or higher than the mechanically controlled lower cut-off frequency, f_L . In general microphone design, it is more favorable to pick a preamplifier system such that $f_{e-lower}$ is less than f_L .

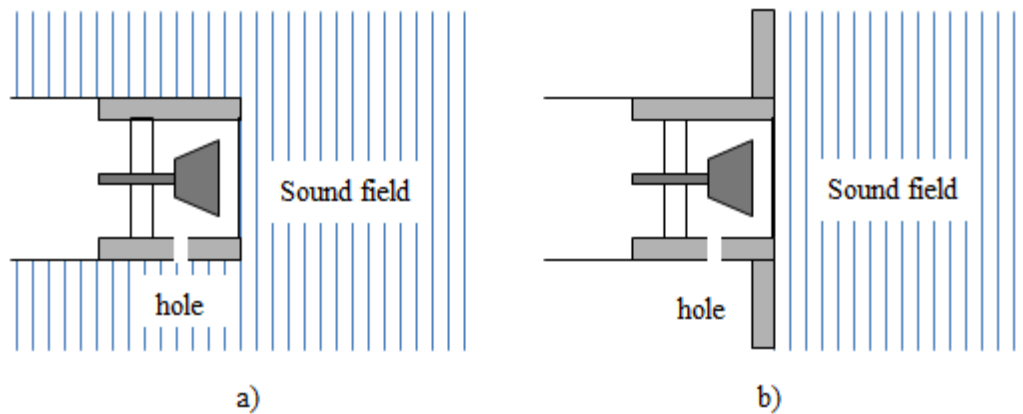


Figure 4-19 Pressure equalization hole positions. (a) Hole exposed.
(b) Hole unexposed.

In most conventional microphone structures, the pressure equalization hole is exposed to the sound field (Figure 4-19 a). Under these circumstances the hole will equalize the sound pressure in front and behind the diaphragm at low frequencies and the microphone response will drop off. However, in many MEMS microphone designs, where the entire microphone structure is encapsulated by an external package, the pressure equalization hole is sometimes not directly exposed to the sound field (Figure 4-19b). In this case, the frequency response does not fall with decreasing frequency, but rather increases (Figure 4-20). This is because the fraction of stiffness (ratio between air gap stiffness and total diaphragm system stiffness) due to the reactive pressure in the internal cavities of the microphone becomes smaller as this is equalized through the hole.

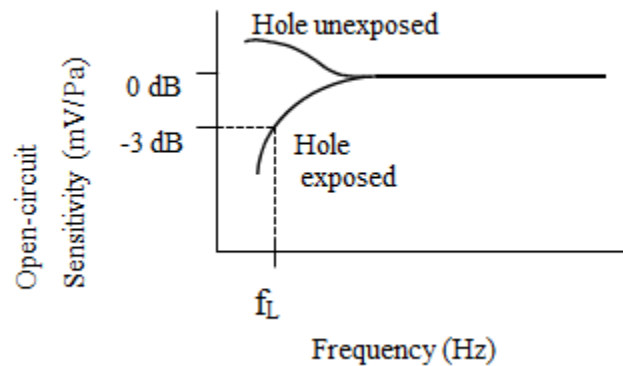


Figure 4-20 Low frequency response vs. location of pressure equalization hole.

In most MEMS microphone designs, it is difficult to predict the low frequency cut-off, f_L , before making the device because of complex packaging and assembly configuration issues. Consequently, the design, size and location of the pressure equalization hole is usually adjusted in an iterative manner based on measured experimental data.

High-Frequency Cut-Off

The high frequency cut-off of a piezoelectric microphone (without preamplifier) is mainly determined by the fundamental resonant frequency of the diaphragm. If we use the membrane model to describe the mechanical behavior of a square diaphragm (see section 2.3.1), the fundamental mechanical resonant frequency, f_0 , can be described with equation [14]:

$$f_0 = \frac{1}{2\pi} \left(\frac{D}{\rho h a^4} (\alpha_2 a)^2 [(\alpha_2 a)^2 + k^2] \right)^{1/2} \quad [\text{Hz}] \quad (39)$$

where:

D : Modulus of in the membrane [N/m]

α_2 : Solution from the characterizing equation (14) [dimensionless]

ρ : density of the membrane material [kg/m^3]

a : diameter of the circular membrane [m]

h : thickness of the circular membrane [m]

k : tension parameter [dimensionless]

The high frequency cut-off, f_H , is typically defined as the frequency after f_0 , at which the response curve has dropped 3 dB below the 0 dB open-circuit sensitivity reference level (Figure 4-21).

In MEMS microphones, the diaphragm resonant frequency is dependent on diaphragm materials as well as the processing history of the device. Since the microphone diaphragm is usually a composite structure, consisting of the piezoelectric material, metal electrode and diaphragm material, f_0 is measured experimentally after the diaphragm has been made and before the microphone is assembled. This measurement can also provide the residual tensile stress of a composite microphone diaphragm.

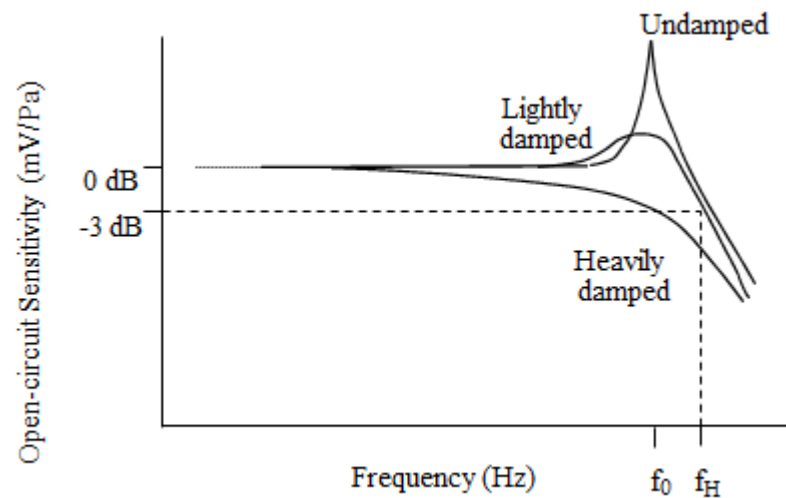


Figure 4-21 Different degrees of microphone response damping.

At the resonant frequency, the sensitivity of the microphone would peak sharply if the diaphragm is undamped. This is obviously undesirable for most cases, but is usually not a problem in actual MEMS microphones, especially with a polymer diaphragm due to its high material damping factor.

SUMMARY

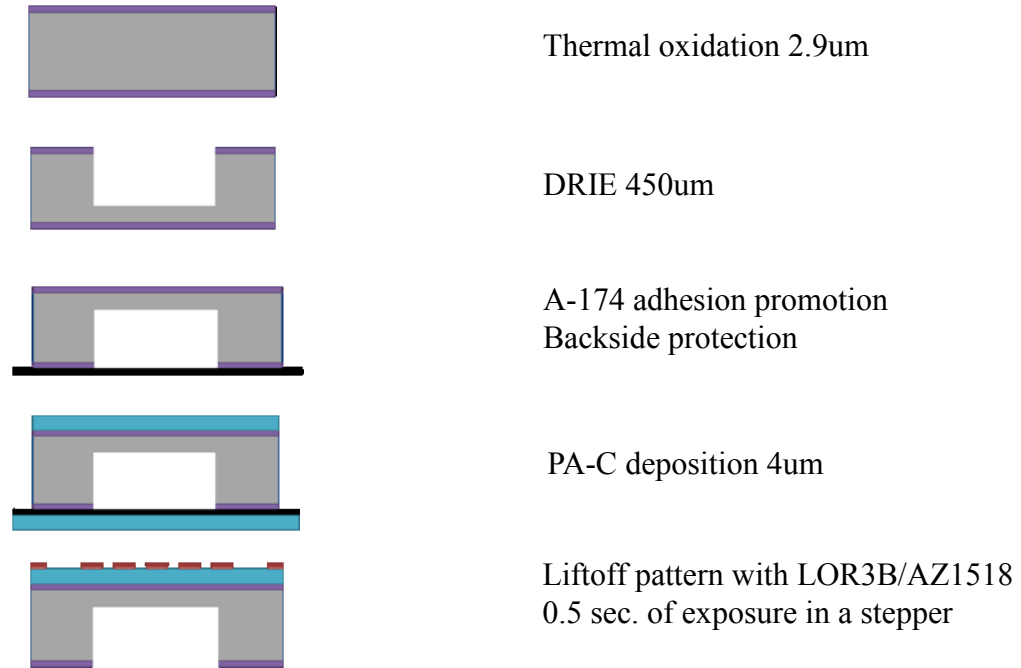
In this chapter, we have studied the theoretical calculation of a circular diaphragm. Within its linear actuation, for which the deflection is less than 10% of the thickness of the diaphragm, we have calculated its mode shape and stress zero point in order to design the electrodes and resonance frequency of the first mode. Also, by combining with the lumped element model, we have analyzed its mechanical and electrical properties and its net operation.

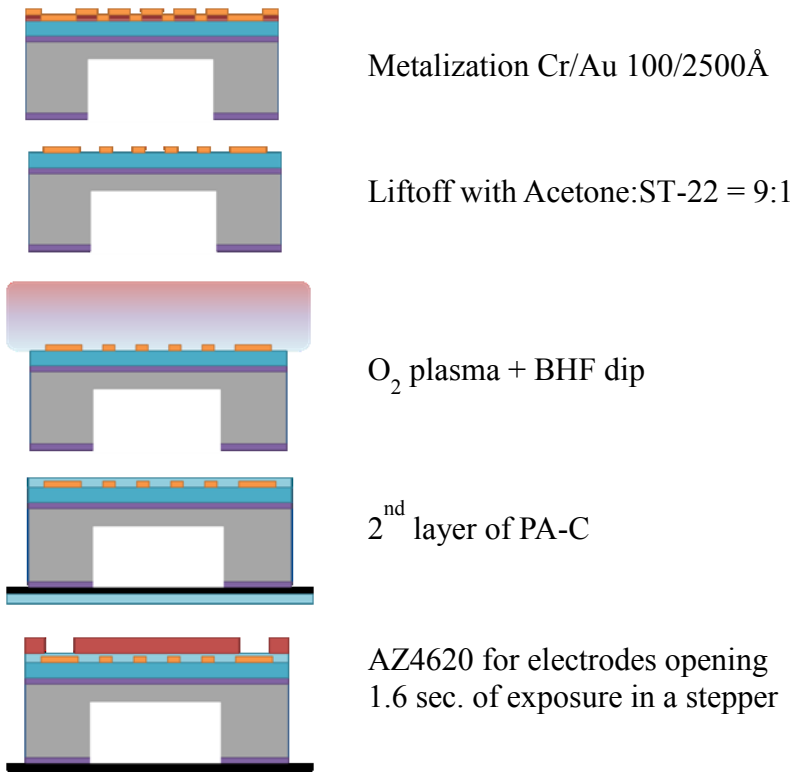
These formulas are not stand-alone models of microphone behavior, but rather, each formula closely influences the relevance and impact of the others. In almost all cases, an increase in one performance parameter will lead to a trade-off in another. During the microphone design phase, the theory provided in this chapter should only be used as a guide to microphone performance. It should not be construed as the *exact* predicted outcome since the interaction between material properties, physical dimensions and electrical parameters will undoubtedly deviate from theory. In addition, there are process variances during the fabrication process and measurement. The value of many device variables will not be able to be predicted on paper and will have to be obtained from experimental data. Often, the electro-mechanical-acoustic interactions in a MEMS microphone system are simply too complex to predict with high levels of accuracy through hand calculations. Therefore, iterative design and testing cycles are the key to microphone optimization. For the curious reader, a more mathematically rigorous analysis of condenser microphone theory can be found in [25] and [26]. However, the presented microphone theory will suffice as a practical tool for MEMS microphone design, fabrication, packaging and testing.

*Chapter 5*MEMS PIEZOELECTRIC MICROPHONES WITH PIEZOELECTRIC PARYLENE-C
DIAPHRAGMS**Preface**

There is great interest in using thin-film piezoelectric materials, e.g., PZT, ZnO and PVDF [156–158], for MEMS applications such as for microphones and actuators. However, these well-known materials all have different degrees of technological difficulties when integrated into MEMS. For examples, sol-gel PZT method requires relatively high temperature (500~700°C) and PVDF film, after stretch-poling, needs to be bonded to the substrate for further fabrication. In comparison, Parylene-C (PA-C) is a recently found piezoelectric material able to be deposited at room temperature and electrically poled at below 200°C. [159] Also, because of its chemical inertness, mechanical strength and electrical insulation, it can be easily integrated with MEMS process as well as a conformal coating material in medical, military and electronics field. By combining the piezoelectricity with the ability for MEMS integration, we could build a Piezoelectric PA-C Microphone.

PIEZOELECTRIC MICROPHONE PROCESS





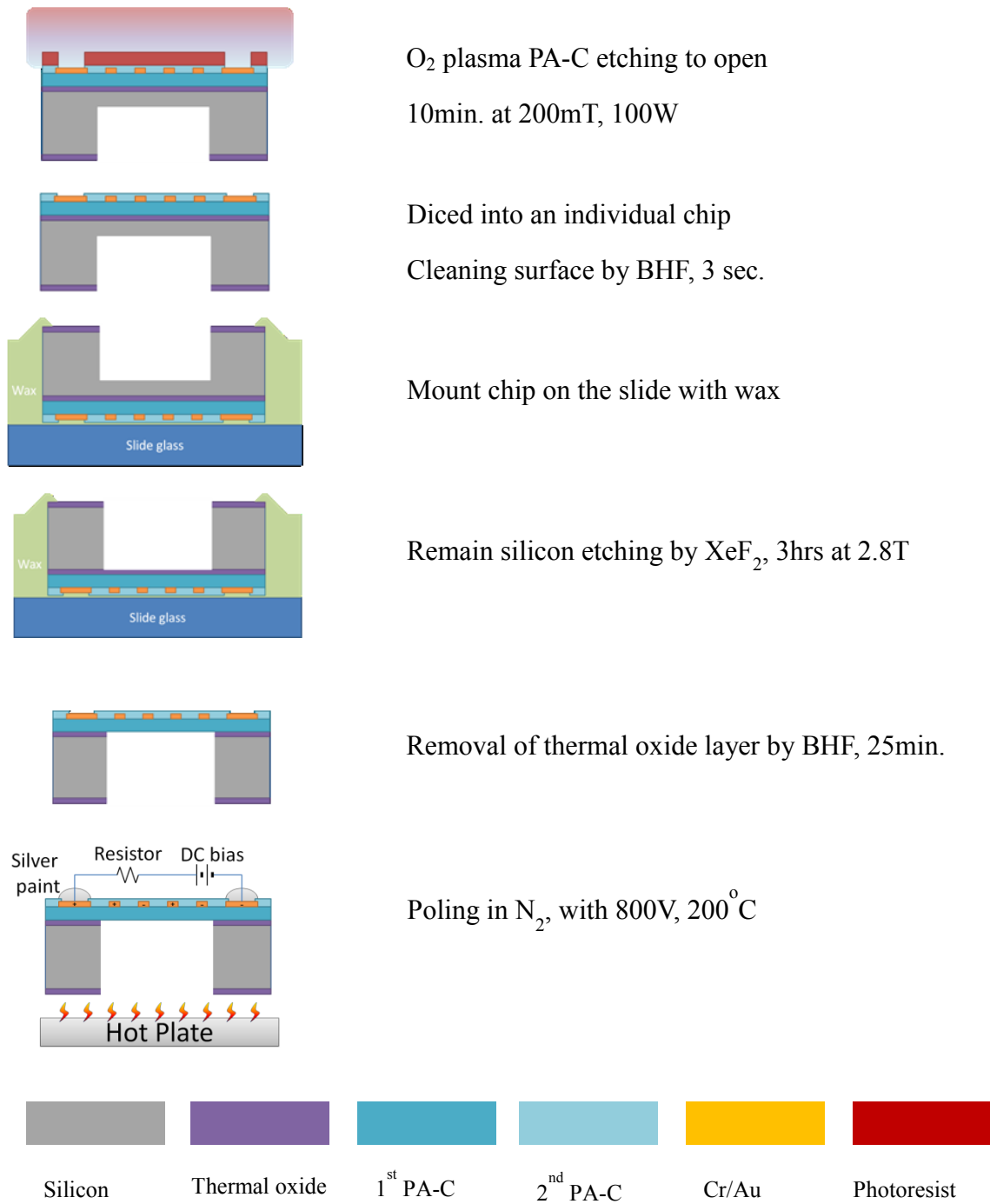


Figure 5-1 Overall processes

Thermal Oxidation

Oxidation process is the beginning for the whole process. We use wet oxidation to make a 2.9um of SiO_x layer on the both sides of a wafer. To clean the surface of the wafer and prevent cross contamination on the oxidation chamber, piranha cleaning is applied before the oxidation step. To build a 2.9um of SiO_x layer the wafer is placed inside an oxidation chamber, set as 600°C, by 1 inch per minutes of speed to prevent a thermal shock. Then the temperature inside the oxidation chamber is ramped to 1050°C and kept until 24 hours. The oxidation time is chosen by former data of oxidation.

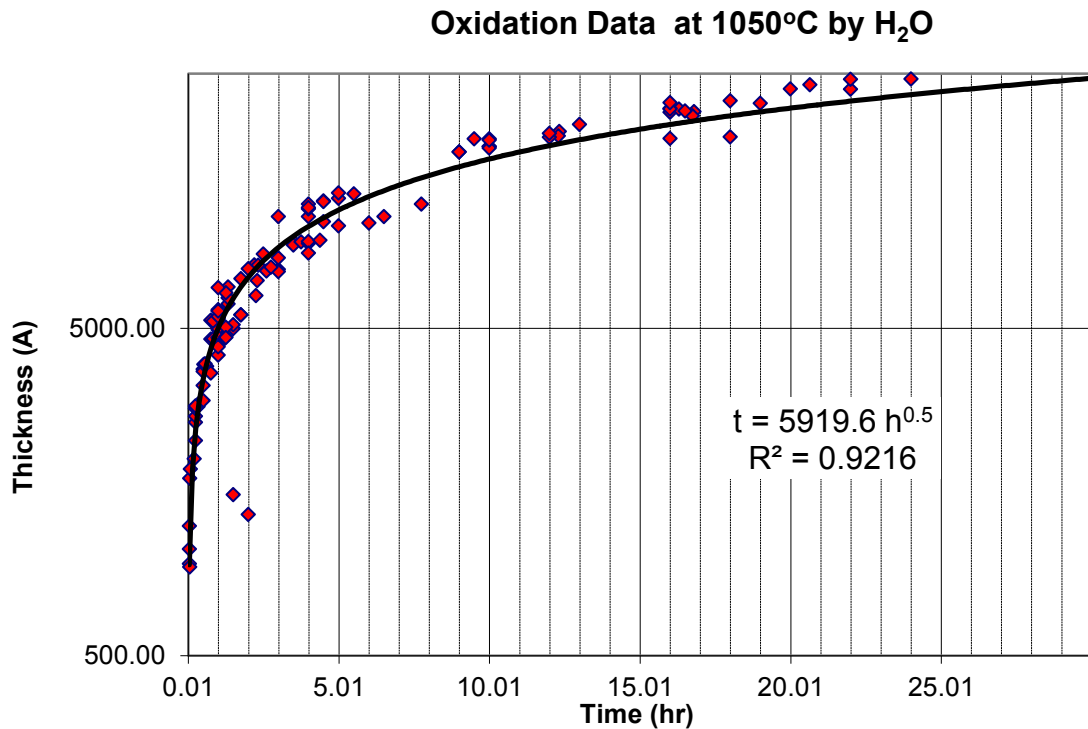


Figure 5-2 Wet thermal oxidation data

The oxidation reaction may be represented as



For a long time oxidation the estimated oxide thickness, t , by time, h , can be described as

$$t^2 = bh$$

, where b is a parabolic rate constant. [160]

$$b = 5919.6^2$$

by that equation and value of b , for 2.9um of oxide film, we can get a estimation of oxidation time as 24hours.

The oxidation process uses water as an oxygen source and the water drop rate is set as 1 drop per 10 seconds using nitrogen gas as a carrier of water vapor into the oxidation chamber. After 24 hours, the temperature of the chamber is decreased to 600°C, and the wafer is pulled out with 1 inch per minute of speed. We use a Nanospec™ to measure the thickness of the oxide layer and get 2.89um.

DRIE etching for the backside of wafer.

To make a diaphragm, we need to etch a back of silicon wafer to thin it. However, for the further process, instead of removing whole silicon under the diaphragm area, we etched 450um from 550um thick wafer to leave 100um of silicon layer strong enough to bear the stresses of the following processes. This etching is achieved by Bosch DRIE process. The Bosch is named after the German company Robert Bosch GmbH which patented the process. The Bosch Process repeats the cycle of isotropic etching followed by protection film deposition.

The etching step is nearly isotropic. The plasma contains fluorine and its derivative ions, which attack the wafer from a nearly vertical direction by the bias built up inside the chamber. In a general plasma etching, some of these ions are bounced back from the bottom and can attack the side wall to make a nearly isotropic etching. However, in the Bosch process, the side wall is protected. High fluorine ratio chemicals, such as CF₄ or SF₆ (Sulfur hexafluoride) is often used for silicon etching.

The protection of a chemically inert passivation layer follows the etching step. For this step low fluorine containing chemicals, for example, C_4F_8 (Octafluorocyclobutane), are used as source gas, which yields a substance similar to Teflon.[161]

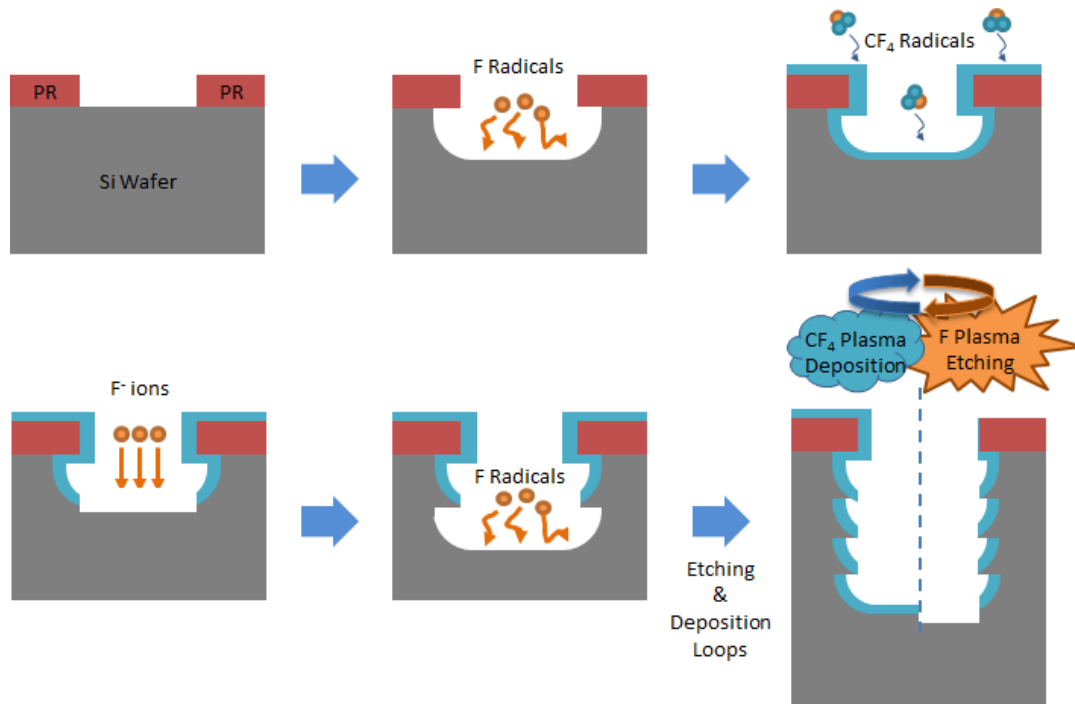


Figure 5-3 DRIE process

Each phase lasts for several seconds. The passivation layer protects the entire substrate from further chemical attack and prevents further etching. However, during the etching phase, the directional ions that bombard the substrate attack the passivation layer at the bottom of the trench (but not along the sides). They collide with it and sputter off, exposing the substrate to the chemical etching species. These etch / protect steps are repeated many times over resulting in a large number of very small isotropic etch steps taking place only at the bottom of the etched pits. To etch 450um from silicon wafer with 6mm diameter opening, 400~450 steps are needed in current Plasmatherm™ DRIE system. An etching ratio between SiO_x mask layer and Si is around 1:200. So that 2.9um of SiO_x layer is enough to etch 450 um of Si to left 100um thick Si layer under the oxide layer.

A-174 adhesion promotion for PA-C deposit.

PA-C is not favorable to make stable adhesion on the oxide layer. To improve the adhesion, A-174, γ -methacryloxypropyltrimethoxysilane(γ -MPS), Figure 5-4, from Special Coating System® is applied as 0.5 volume percent of aqueous solution[162–168]. Because A-174 is not miscible in water, 4ml of A-174 is dissolved at 400ml of isopropyl alcohol followed by 400ml of water mixing. After dipping the wafer 30 minutes at room temperature, the wafer is spin dried and wash with isopropyl alcohol, and then spin dried again.

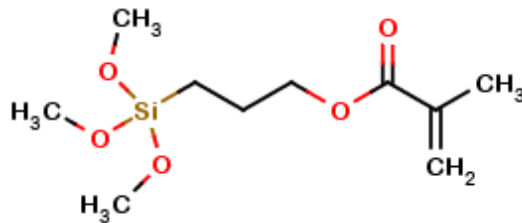


Figure 5-4. Molecular structure of A-174, γ -MPS

The process of adhesion promotion of A-174 can be described as two major steps.

The first major step is silanization of A-174 on the silicon surface[165], [166].

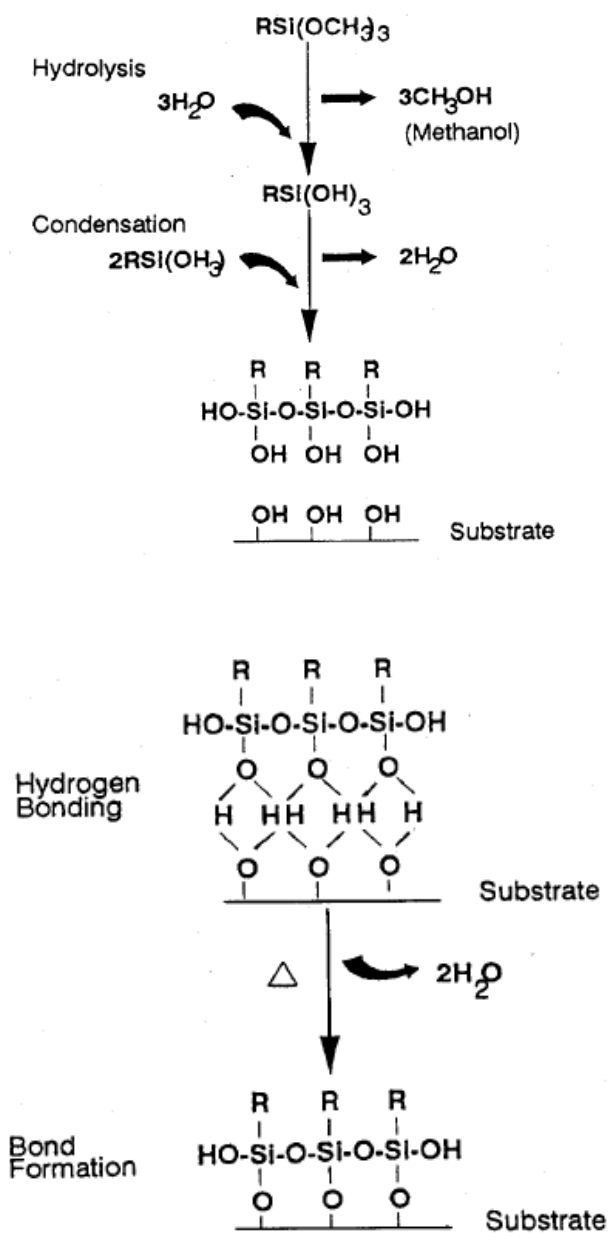


Figure 5-5. Silanization on the surface of silicon.

Reaction of these silanes involves four steps (see Figure 5-5). Initially, hydrolysis of the alkoxy (-OCH₃, here methoxy) groups occurs. In the second step, methoxy groups are hydrolyzed that condensation to oligomers follows. The silanol hydrogen is more electrophilic and much more

reactive. This is due to the larger, more electropositive, atomic structure of silicon which results in a high dipole moment for the silanol group and greater hydrogen bonding. The tendency toward self-condensation can be controlled by using fresh solutions, alcoholic solvents, dilution, and by careful selection of pH ranges. Because of self-condensation, this aqueous solution has a life time around a day at room temperature. After days we can find a solution becomes milky and oily substance on the surface. Also, to complete the hydrolysis, it requires a time about 2 hours minimum at room temperature[162][169]. At the third step, methoxy group is oriented towards, and hydrogen bonds with, hydroxy sites on the silicon substrate. Finally, during drying or curing, a covalent bond is formed with the substrate and water is liberated. At the interface, there is usually only one bond from each silicon of the organosilane to the substrate surface.[165]

Often the silane is subjected to hydrolysis prior to the surface treatment. Following hydrolysis, a reactive silanol group is formed, to form siloxane linkages on the surface of the substrate. Sufficient water for hydrolysis may be supplied from atmospheric moisture or on the substrate surface. In some cases, it may be necessary to add water to increase the degree of hydrolysis on to the A-174 and alcohol solution[165].

The second major step (in Figure 5-6) is a reaction between surface bound A-174 and monomer of PA-C. As we describe earlier, treatment of the silicon surface with the hydrolyzed organosilane generates an organosilane at the substrate surface. The PA-C (ortho-chloro-p-xylene) di-radical, which is generated by thermal cracking of dimer at 690°C, reacts with the acrylate group of the siloxane side chain quenching an PA-C radical to form a covalent bond thus aiding in adhesion. The polymerization process continues as the radicals condense and form a polymeric film. [164] [170]

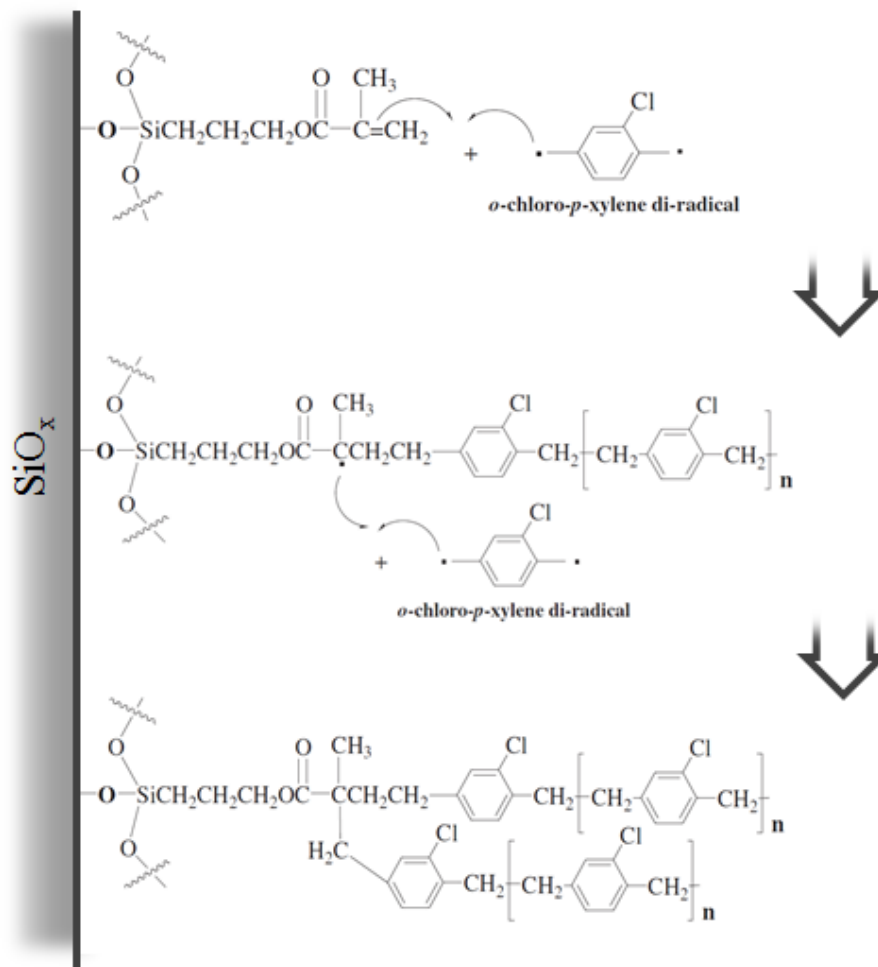


Figure 5-6. Covalent bond between PA-C and A-174

Once A-174 promotion step is accomplished, the backside of the wafer is protected by dicing tape to prevent from unwanted PA-C coating on etched surface.

PA-C deposition.

The 4 μm of PA-C layer is deposited on the surface of the wafer from 8.2gram of PA-C dimer from Special Coating System®.

The deposition process of PA-C consists of three main steps. The first step involves vaporizing PA-C from its solid dimer at temperatures between 140-170°C under vacuum. The second step is pyrolysis at temperatures above 690°C, where gaseous Parylene dimer is split into monomers. In the third step, the monomers enter the room temperature deposition chamber where they are simultaneously adsorbed and polymerized on the surface of a substrate. During the deposition, the chamber pressure is kept at 22mTorr.

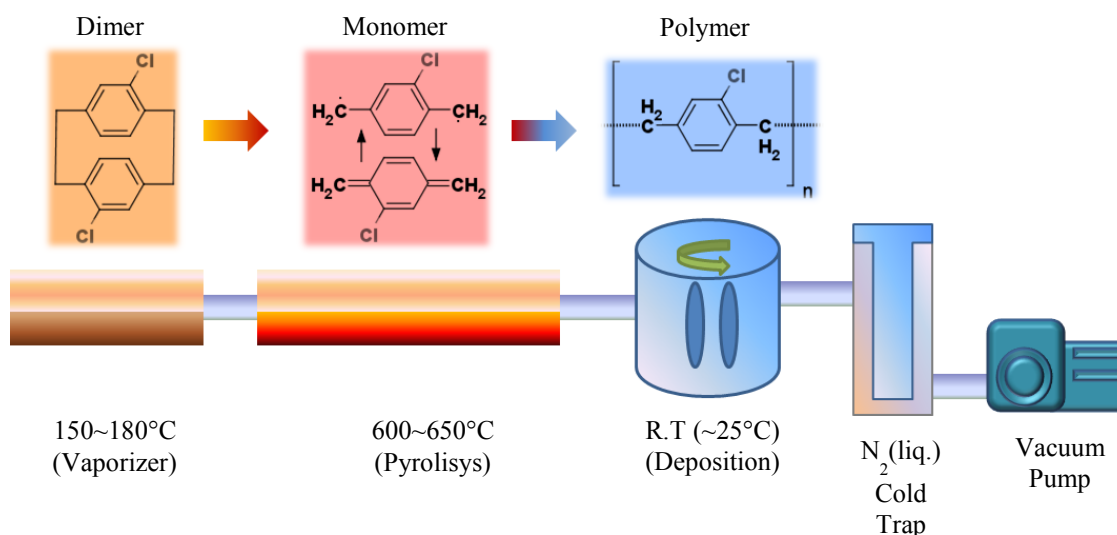


Figure 5-7. The deposition process of PA-C

Parylene deposition process is controlled by the pressure of a deposition chamber and the temperature of a vaporizer as shown in the Figure 5-8. If we take a look at the time scale for the process, after machine starts, the chamber pressure decreases to the base pressure, 10mT, by pumping out and it enters zone 1. During zone 1, the temperature of the vaporizer is increasing and the dimer of Parylene is sublimated, cracked into monomers in the pyrolysis chamber, which increases the pressure inside chamber to the set value, for example 22mT. Because this process is controlled by PID controller there is a temperature overshoot observed in zone 1. Once the pressure of chamber is stabilized at 22 mT, in zone 2, PID controller increases the temperature to compensate the decline of dimer. At the end of the zone 2, when there is not enough dimer left,

the pressure cannot be maintained and the PID controller continues increase the vaporizer temperature until to the limit of vaporizer's setting, for example, 180°C. Once the temperature reaches the limit, zone 3, the machine stops heating and lets the evaporator cool down to the room temperature, which completes the process the whole process.

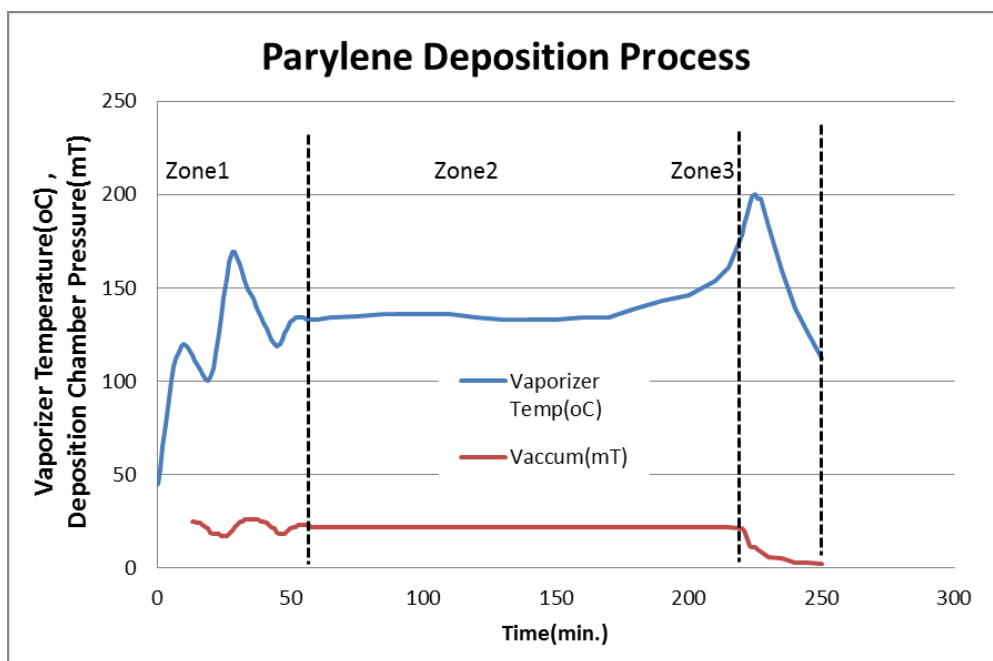


Figure 5-8. Pressure and temperature profiles of PA-C deposition process

Liftoff pattern made out of LOR3B and Az1518

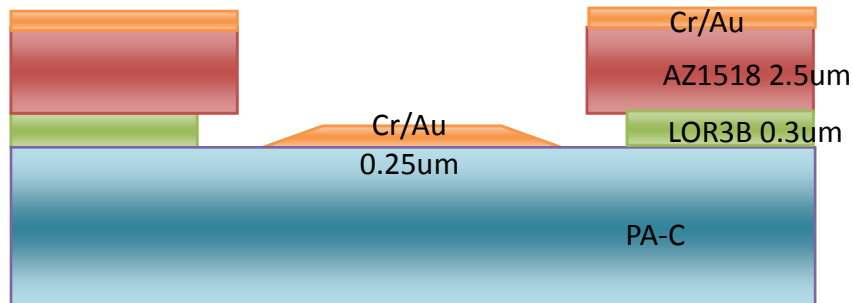


Figure 5-9 Double layer for Liftoff

To make a liftoff pattern, we use a LOR3B/AZ1518 double layer system. LOR-B series was developed by MicroChem®. It has different solvent system from other positive photoresist, so to not to dissolve when top layer is applied. Its etching rate can be adjusted by soft baking temperature and time. Also, it adheres well with most MEMS processing materials, such as gold, titanium, silicon, silicon oxide/nitride and polymer, without need of an adhesion promoter, HMDS. Furthermore, it has good high temperature stability, e.g. survives platinum e-beam deposit. Because of the aforementioned reasons, it is widely used to make a liftoff pattern, even though it requires one more photoresist spinning and baking step.

The correct LOR-B series for the clean lift off of electrodes, 0.25um thick, LOR-B layer should be 1.2~1.3 thicker than metal layer. Also, to generate maximum coating uniformity, the spin speed needs to be between 2,500 and 4,500 rpm. For simplicity, we choose a spin rate at 3krpm same as other photoresist in our lab. Following Figure 5-10, we decide LOR3B.

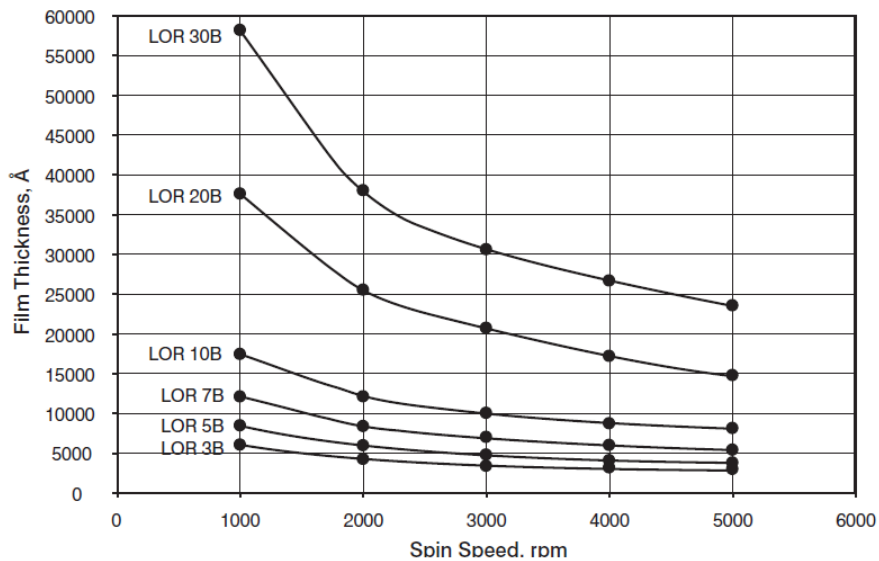


Figure 5-10. Spin speed vs thickness for LOR B series resists.

Because the recommended soft baking temperature is from 150°C to 190°C, to control the crystallization, oxidation and tension on the PA-C film, we tested a lower soft baking temperature for LOR3B. However, below 140°C, we found a delamination at the edge of the pattern, like Figure 5-11. So we decided to use 150°C as the lowest safe baking temperature. We choose 5 minutes for the baking time to minimize oxidation of PA-C and control the undercut, Table 5-1.

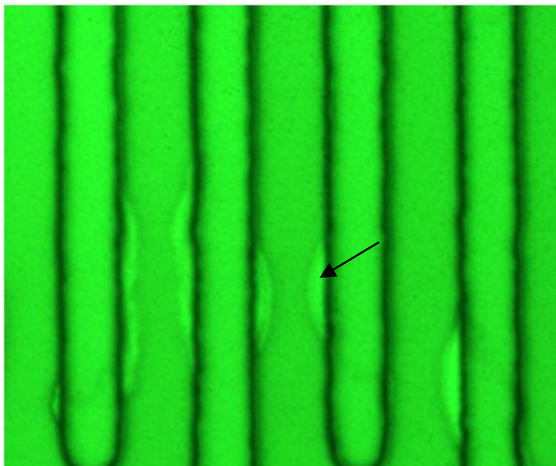


Figure 5-11 Liftoff pattern delamination from poor LOR3B adhesion, baked at 140oC, 5min.

	100°C 5min.	120°C 5min.	140°C 5min.	150°C 2min.	150°C 5min.	150°C 10min.
Delamination	severe	severe	moderate	none	none	none
Undercut @ AZ340:DI 1:4, 90sec.	>10um	>10um	~1um	~3um	~1um	<1um

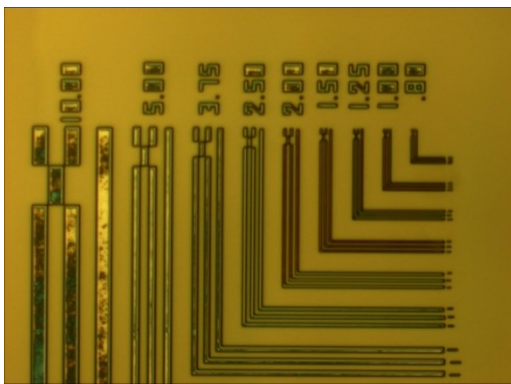
Table 5-1 LOR3B baking test (baked on a hot plate)

Due to the hot plate’s higher heat transfer rate, for the short baking, it is favorable. Finally, for LOR3B, we can decide a process condition, 0.3um at 3krpm, bake at 150°C, and 5 minutes on a hot plate.

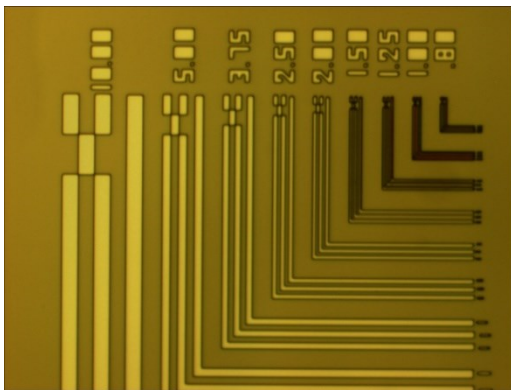
For the upper layer, AZ1518, we followed the recommended recipe from AZ-EM® and set the conditions as 2.5um at 3krpm, bake at 100°C, and 30 minutes in a convection oven.

Before placing the wafer under the stepper, we applied a dicing tape on the backside of wafer, to prevent a deflection of the diaphragm area from vacuum of the wafer stage. Even though there is 100um of silicon layer left, it can be deflected by vacuum and its deflection can induce an out focus.

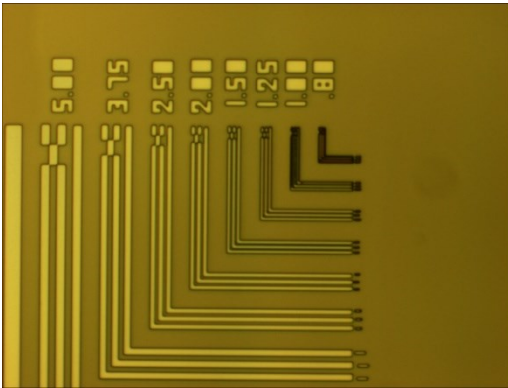
For every batch of process wafers, we use a dummy wafer to check the focus and exposure time. With the same photoresist conditions, we change the exposure time from 0.2 to 0.45 seconds, while keeping the photoresist condition and the development condition, AZ340:DI 1:4, 90seconds, Figure 5-12.



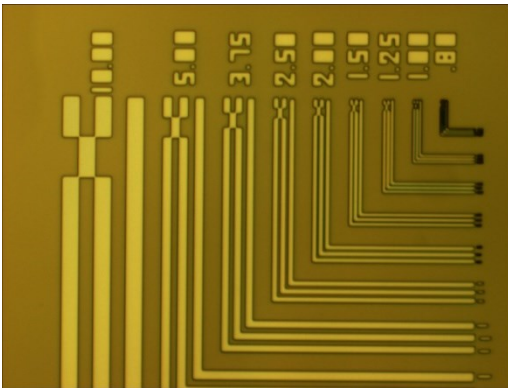
a) 0.20seconds.



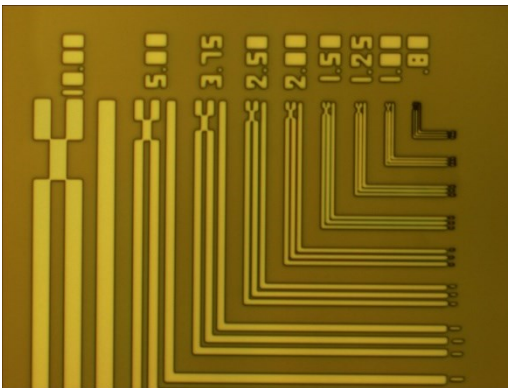
b) 0.25seconds.



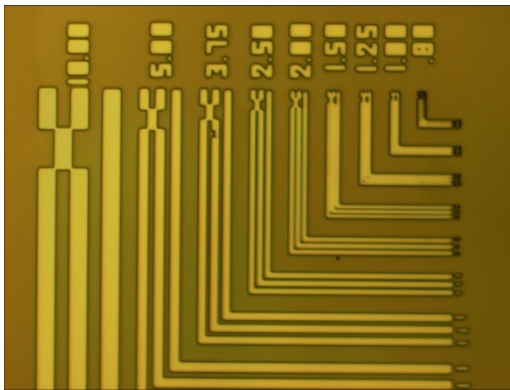
c) 0.30seconds.



d) 0.35seconds.



e) 0.40seconds.



f) 0.45seconds.

Figure 5-12 Standard pattern check with different exposure time in a stepper.

To decide a proper exposure time, we use a standard 5" reticle from DSW stepper system®, for checking three important features as Figure 5-13.

1. *Clean development.*
2. *Sharp and clear corner.*
3. *Same line width of opening and un-opening.*

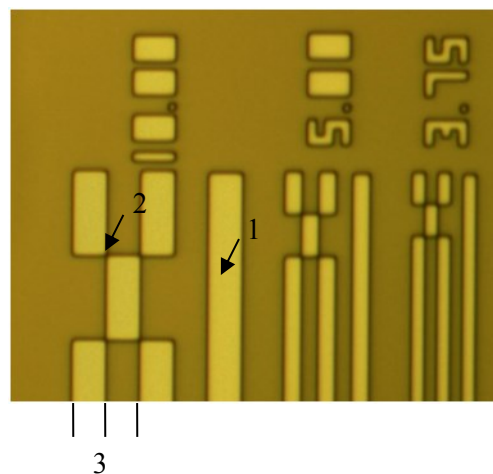


Figure 5-13 Stepper exposure check

As we see in the Figure 5-12, 0.25sec starts to make a clear development. For the exposure longer than 0.35seconds we see that the corner of pattern is rounded. However the important feature of our pattern doesn't have sharp corners. Furthermore, we want electrodes have smooth wall to avoid possible break down during the poling process. Because of the reason mentioned, we choose 0.5seconds for exposure.

For the development, we use AZ340:DI 1:4 mixture 70seconds of dipping.

Finally we could get a lift off photoresist pattern for a spiral electrode as seen in Figure 5-14.

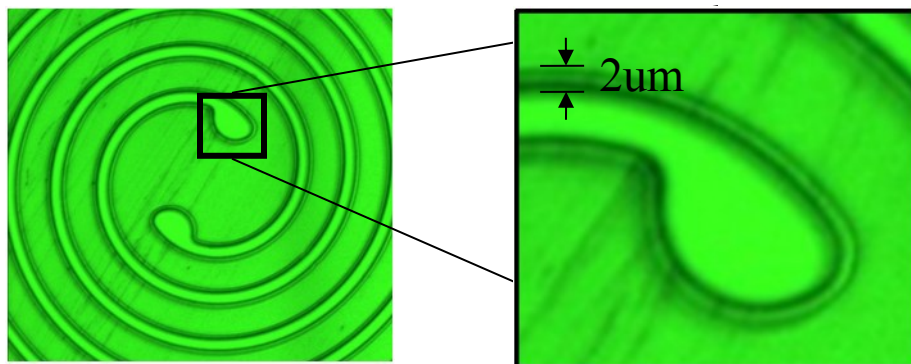


Figure 5-14. Liftoff patterns with 2um of undercut.

Metalization

Most polymer surfaces, not only the PA-C's surface, adhere poorly to metallization, because of their hydrophobic nature.[171–174]. Work by many groups have shown that this deficiency could be improved by surface treatments using plasma of reactive species, such as O_2 , NH_3 [174][175] or ion beams [176].

Burkstrand has shown that the formation of metal-oxygen-polymer complexes on oxygen-plasma treated polymer surfaces correlates with adhesion of the metal film[177]. Metals interact with hydroxyl (-OH), carbonyl (-C=O) and ester (-COOR) groups on a plasma-modified surface.

Carbonyl groups on polymer surfaces are sites for reaction with Cr during the initial steps of evaporative deposition[178], [179]. It has been suggested that charge transfer occurs from Cr atoms into the carbonyl groups of the PMDA portion of polyimide, leading to the coordination of Cr^{++} with two ligands from different monomers [180]. For the PA-C, it is reported that the adhesion of Cu/Ti is greatly improved by oxygen plasma treatment not only chemical modification, also surface roughening[181]. Both Ti and Cr have been reported as an nice adhesion layer between electrode metal(Cu, Ag, Au) and polymers(polyimide, PA-C). However, our device does not intend to implanted or deal with cells, so Ti is not necessary. Because most of metallization reported on these papers used Cr as an adhesion layer, we choose Cr/Au structure[182].

Before the metallization, oxygen plasma is applied on the PA-C layer at the condition of 200mT and 100W during 1 minute. However, the treated surface showed the tendency to rearrange itself to minimize its interfacial energy. When contacted with air (low-energy surface), polar groups were buried away from the polymer/air interface, while in contact with water (high-energy surface) polar groups remained at the polymer/water interface[183]. Gururaj, also, studied for surface contact angle changes after a plasma treatment by time. It can be seen from the Figure 5-15 that the best option would be to deposit coatings within 10 min of plasma treatment. However one can still expect considerable wettability after up to 1 hour of treatment, after which the advantage of plasma treatment may be lost[184]. Because of the reason, we placed the wafer in the thermal evaporator and started pumping within 10minutes after oxygen plasma treatment.

We use a thermal evaporation to deposit Cr/Au 100/2500Å of layers on the PA-C layer.

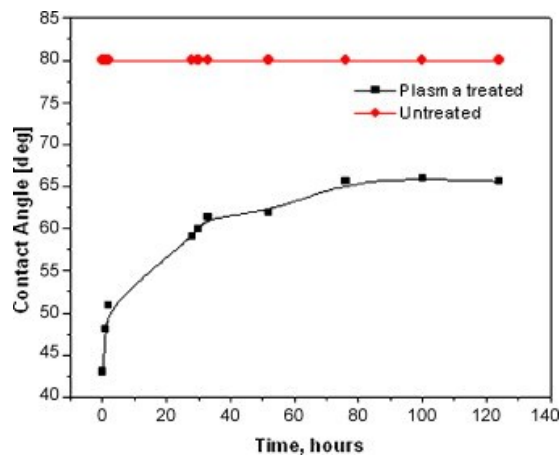


Figure 5-15. Variation of contact angle with time on polycarbonate substrate after plasma treatment.

Lift off

After metallization, liftoff of metal layer was achieved by a mixture of Acetone: ST-22(from ACSI, Inc., 510 Alder Drive, Milpitas, CA) 9:1 solution at room temperature with 300rpm of stirring. As we see in Figure 5-16, to prevent from sticking of liftoff hairy patterns on the surface of the wafer again, the wafer faces down. The stirring helps to circulate the solvent and

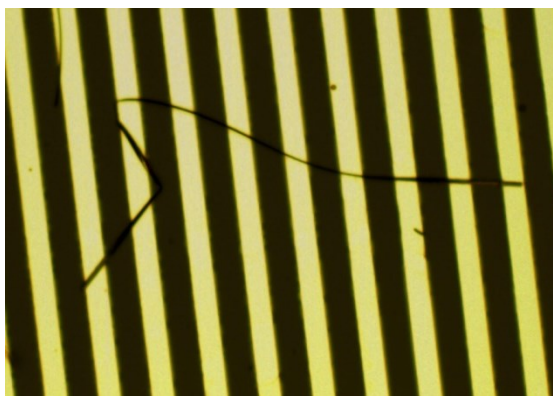


Figure 5-16. A short induced by liftoff metal pattern.

Because the liftoff photoresist pattern contains of LOR3B layer, which have different solvent system and is not be able to be stripped by acetone, we mix ST-22 to achieve a liftoff, as we see in Figure 5-17. Even though ST-22 can dissolve both of photoresist layers to accomplish the liftoff, it has a drawback in the view of a process. Because ST-22 has a higher viscosity, it cannot penetrate through the undercut easily, so it needs to be heated up to 120°C to maximize its ability as recommended by its manufacture. Because, for the parylene diaphragm, tension should be controlled during the process by keeping the process temperature as low as possible, ST-22 single system is not suitable.

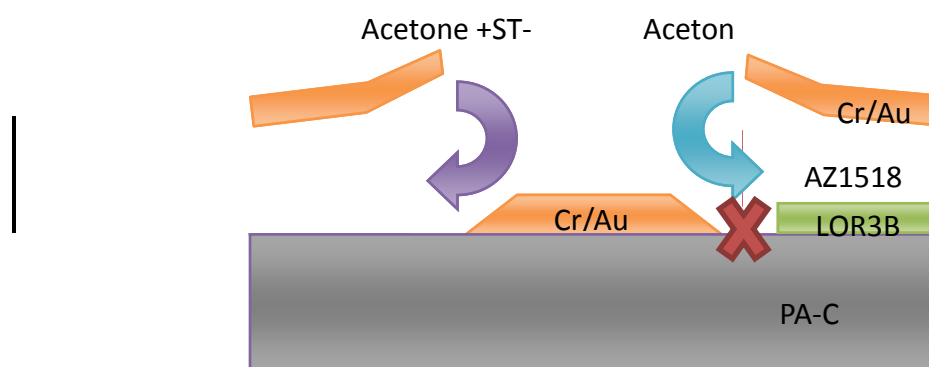


Figure 5-17 Single acetone system cannot clean all layers of LOR3B and AZ1518

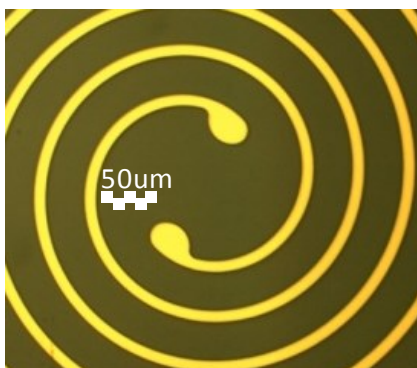


Figure 5-18. After liftoff process is completed

Parylene-Parylene adhesion improvement step

After the deposit is complete, the surface of PA-C is very stable and has low surface energy. Thus, it is found over the years that its adhesion capability to substrates may be compromised after thermal treatments, cleaning, handling, bench testing and implantations. Besides, serious delamination between PA-C and other materials is often found even during standard MEMS processes such as lift-off and sacrificial photoresist releasing. Therefore, physical and chemical surface treatments before parylene deposition that can enhance the interface adhesion between the deposited PA-C and the coated surface are highly desirable. Interestingly, the chemical structure of PA-C does suggest that PA-C deposition on a clean hydrophobic surface favors a good interface adhesion[185]. In the research about PA-C adhesion on PA-C, O₂ plasma treatment followed by HF(1%) dipping improved adhesion. O₂ plasma greatly improves the surface roughness and hydrophilicity[186], and then following HF dipping return the surface to hydrophobic PA-C proper.

For the current process, because of safety issue, we replace the diluted HF with BHF from Transene®. First we apply O₂ plasma at the condition of 200mT, 100W and 1 minute, followed by BHF 10 seconds dipping at room temperature.

2nd PA-C Layer Deposition

The backside of the wafer is protected by dicing tape again to prevent unwanted PA-C coating on etched surface to protect etched surface from depositing PA-C on the back. Additional 1.5 um of PA-C is deposited from 3g of dimmer. To ensure the adhesion, O₂ plasma + BHF treated wafer is placed in the chamber within 10 minutes.[184]

Electrodes Opening by O₂ Plasma

PA-C can be easily patterned by oxygen plasma[187–190]. To make a pattern we use a AZ4620 as an etching mask. Because the etching rate of AZ4620 is 1.2~1.3 times faster than PA-C, the

minimum thickness of AZ4620 can be decided as 2um for 1.5um of PA-C[189]. But for the safe etching we choose 10um of AZ4620 at 3krpm. Because AZ4620 is thicker than AZ1518, for the soft bake we measure solvent evaporation by baking time. Either on the hot chuck, made out of aluminum for better heat conduction, or on stack of several Tek-wipes™ in the convection oven, the weight loss stops after 30 minutes in Figure 5-19. Thus we choose 30 minutes in oven for soft baking.

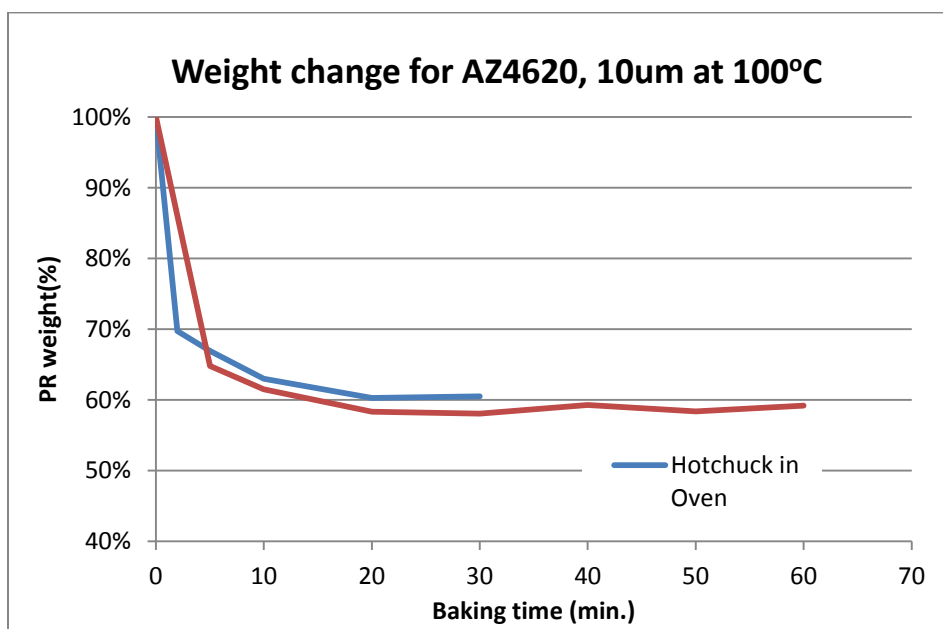


Figure 5-19 Weight decreasing of AZ4620 10um by baking time.

We expose 1.6 seconds in the stepper and then develop in az340 1:4 solution until 2 minutes. After patterning for electrodes opening, we use O₂ RIE to etch 1.5um PA-C at 200mT with 400W power until 10 minutes[187–190]. After O₂ RIE, a dicing saw is used to separate the wafer as an individual chip(Figure 5-1).

Cleaning surface with BHF and chip mounting

For the following XeF_2 etching, we apply a drop of BHF on the etched area to strip any oxide built up during 3 seconds. We then mount a chip on a slide glass PA-C side down by using, Aremco® Crystalbond 555™ wax (melting point, 55°C, washable with water). For the bonding, we place a slide glass on the hot plate set as 85°C, and then melt the wax on the slide. For the beginning of the research, we used a 10um thick photoresist to protect front face and the edges but it was found that photoresist has difficulty after long time of XeF_2 exposure. Even the front surface which was protected by 10um of photoresist and 5.5um of PA-C, was found to have bubbles initiated by localized delamination at the interface of PA-C and SiO_x , as we see in Figure 5-20.

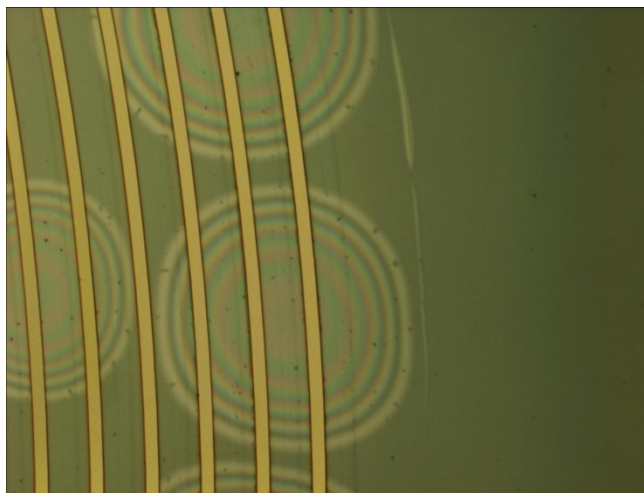


Figure 5-20 Delamination at the interface of PA-C and SiO_x after 1hr of XeF_2 etching.

XeF_2 etching

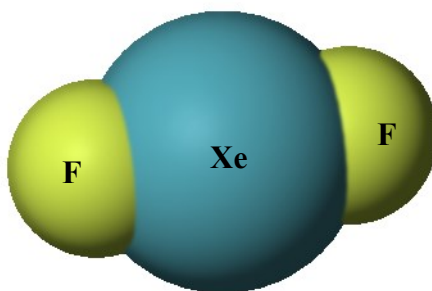
Room temperature gas phase etching has recently been focused. For the MEMS process, such as cantilever or diaphragm, wet chemical etchants yield high selectivity but has a trouble with (1) long side etching is difficult because etching rate decreases with etching time due to the diffusion effect of the solution, (2) evolution of hydrogen bubbles during etching reaction damages microstructures, (3) removal of the residuals from the etched cavity is difficult, and (4) microstructures tend to cause sticking during drying process which can induce direct mechanical damage and surface stiction of

fragile structures[192]. In addition, because the interface between the PA-C and thermal oxide layer is promoted by silanization, it is weak for catalytic hydrolysis by acid in the Si etching solution[193].

Material	What happens
Wet oxide	SiO _x :Si >500:1
Acrylic	Does not etch
Al	Does not etch
Cu	Does not etch
Mo	Etches
Ni	Does not etch
Plastics (e.g. petri dishes, wire insulation)	Becomes corroded if left in the etch chamber; may absorb Fluorine.
PolySi	Etches
Photoresist	Does not etch. Stripping resist after very long XeF ₂ etching (>1hr) is difficult.
Pt	Does not etch
Si	Etches up to 10 μm/min
Ti	Etches
low-stress nitride	100:1 (Si ₃ N ₄ :Si) selectivity or better (See section 5.1)
stoichiometric nitride	100:1 (Si ₃ N ₄ :Si) selectivity or better (See section 5.1)

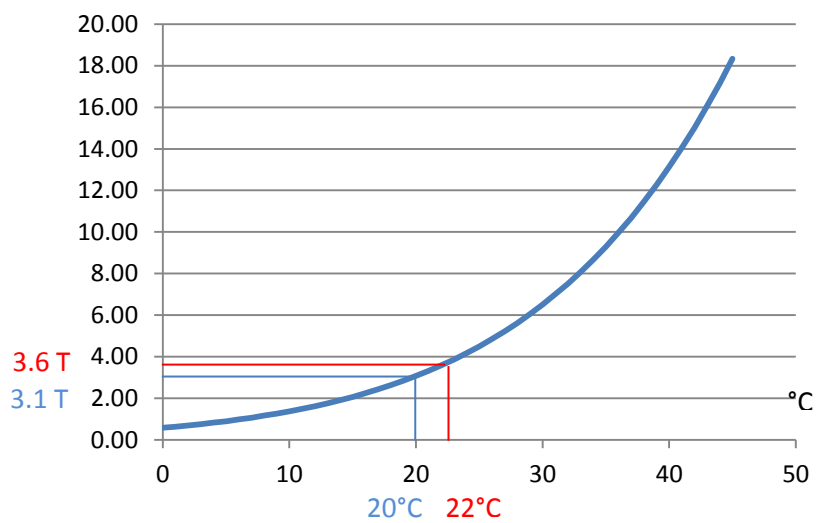
Table 5-2 XeF₂ Etching depends on Materials

Plasma reactive ion etching processes solve many of these problems with the threatening of limited selectivity over silicon dioxide and nitride, which induced by accelerated high energy ion. For these reasons, it is advantageous to have a pure gas phase silicon etchant that is low energy, selective and tension-free, see Table 5-2. It has been reported that many fluorine-containing interhalogens, such as ClF, BrF, IF, will etch silicon spontaneously in the vapor phase including xenon difluoride, XeF₂, and bromine trifluoride, BrF₃[194–196]. Even though BrF₃ has a higher etching rate, byproduct of XeF₂ is nothing but less reactive gas, Xe, SiF₆, we adopt XeF₂ etching system. Also, there is an interesting application of XeF₂, where the increased roughness of silicon surface, can be used to control the stiction of a check valve[197].

Figure 5-21 Ball model of XeF₂

For xenon difluoride, the following equation represents the experimental results between 273 and 388°K.[198]

$$\text{Log } P_{\text{mmHg}} = -\frac{3057.67}{T} - 1.23521 \text{ Log } T + 13.969736$$

Figure 5-22 XeF₂ sublimation Pressure

The diffusion limited effects by comparing the circular opening radius with the mean free path L of the XeF_2 molecules was qualitatively explained[192], [194].

When the opening radius r is close to L , the diffusion front profile can be represented by a semispherical surface with radius r shown as opening A in Figure 5-23, which has a surface area of $2\pi r^2$. If $r \gg L$, as in the case of opening B, it has a surface area of πr^2 , which means the number of etching gas molecules reach the silicon surface per unit area without any collision with other gas molecules is half of the case A. This explains why the etching depth per pulse in B is half of A as shown in Figure 5-23. In the case of opening C, after etch down a depth of d , when $d > 2r$, and $r \ll L$, the opening that allows gas molecules get into it is reduced compare to the case of r similar to d , thus reducing the etching rate.

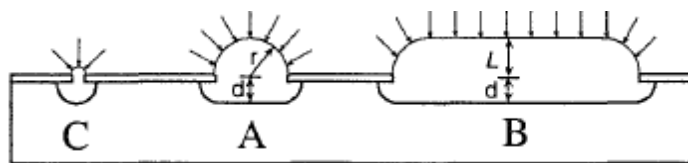


Figure 5-23 Local loading effect and Aperture opening effect

Mean free path L is

$$L = \frac{k_B T}{\sqrt{2} \pi d^2 p}$$

Where, k_B is the Boltzmann constant in J/K, T is the temperature in K, p is pressure in Pascals, and d is the diameter of the gas particles in meters.

For XeF_2 being used in room temperature,

$$k_B = 1.3806488 \times 10^{-23} \text{ J/K}$$

$$T = 300 \text{ K}$$

$$p = 2.8 \text{ Torr} = 373.3 \text{ pa}$$

$$d = 216 \text{ pm (Atomic diameter of Xe)}$$

So, we can get $L \approx 53\mu\text{m}$.

We can assume that the opening with $53\mu\text{m}$ in diameter the maximum etching rate. However, the opening diameter of our device is 6mm and so big enough to ignore the effect.

Here is a brief schematic of XeF_2 etching system. The cylinder of XeF_2 is connected to expansion chamber because the sublimation pressure at room temperature is not high enough to fill the etching chamber quickly. A rotary vein pump is connected to the output port of the etching chamber. The pressure in the system is monitored by pressure gauge. Then the device mounted on a slide glass is placed inside the etching chamber.

For the etching, instead of pulsed etching[192], we use continuous flow etching. The chamber pressure is set at 2.8T . After 3hrs, $50\sim 60\mu\text{m}$ of silicon is removed.

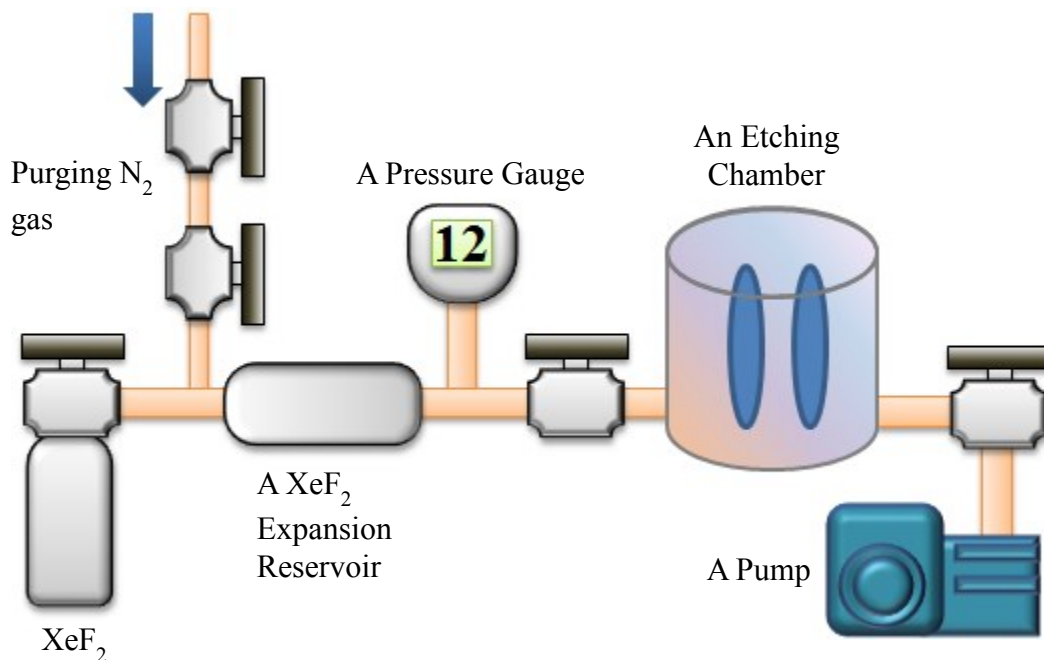


Figure 5-24 Schematics of XeF_2 etching system

Detach a chip from the slide glass.

After XeF_2 etching is done, we place devices mounted on the slide glass at a hot plated set as 85°C . When the wax becomes clear and melts, we detach the chip. This normally occurs within 5 minutes. Then, we apply 1~2 drop of BHF to the backside of a diaphragm to remove the 2.9um oxide layer during 25 minutes. To decide BHF etching time, we add 10% to the oxide removal time of 2.9um of SiO_x to BHF (Transen co.) and the total etching time is 22 minutes.

Poling

We use the same poling setup from the piezoelectric PA-C film. To avoid oxidation of PA-C, poling process was achieved in N_2 filled glove box. Thermocouple is located underneath the bottom mica insulation sheet to control the hot plate.

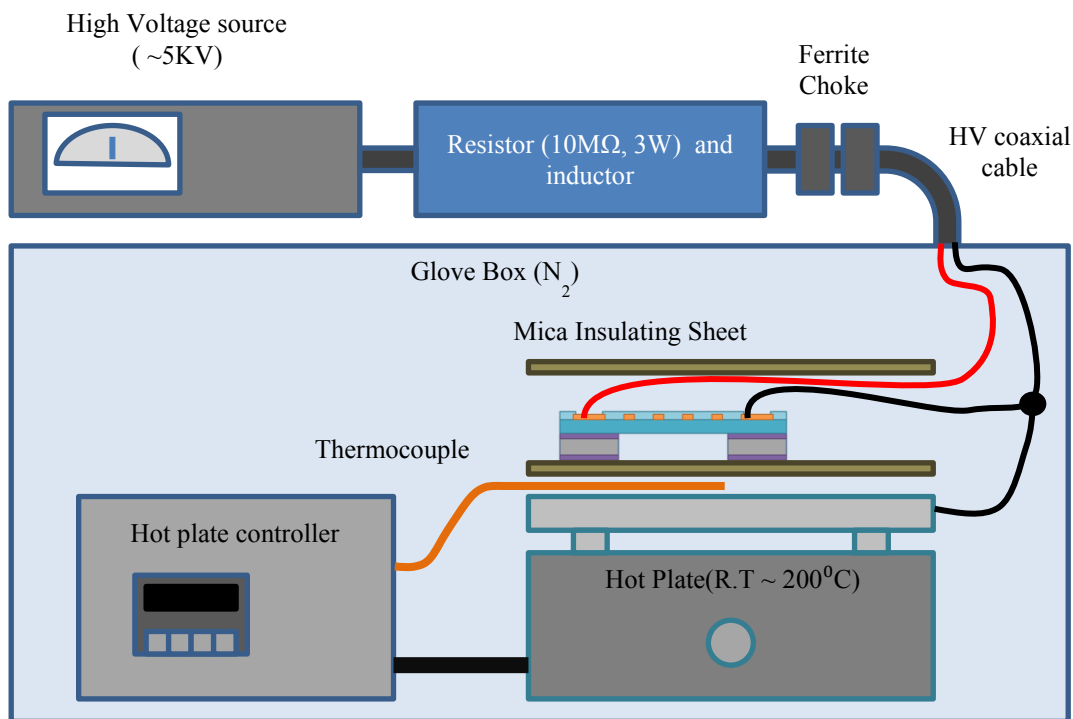


Figure 5-25 A setup for poling process.

To apply a bias on a chip, chip is mounted on poling jig made out of mica film and thin wire. To ensure a connection, we apply silver paint where a thin wire and the electrodes of a chip meet. To confirm the connection, we use an impedance meter to measure capacitance. Typically, without a microphone chip, the jig has 1.2pF but with the microphone chip it becomes 5~7pF with a good contact.

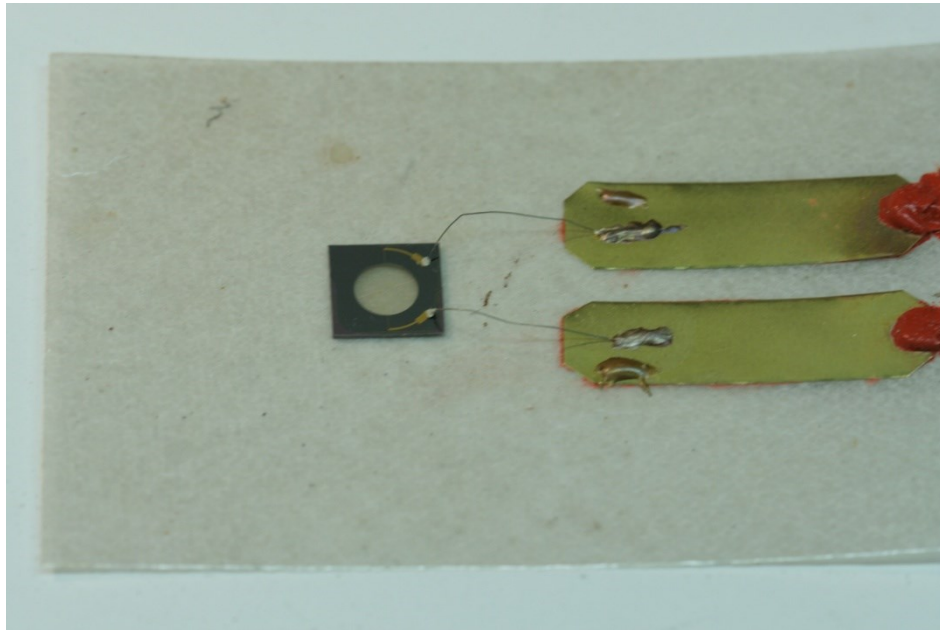


Figure 5-26 Microphone chip poling jig

We apply 800V of bias on the chip at room temperature and move the jig on the hot plate, which is heated at 200°C, and then hold 5 minutes in N₂ environment.

MICROPHONE ASSEMBLY

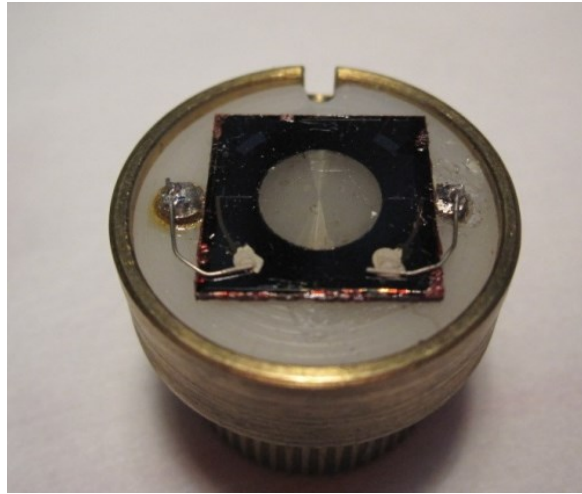


Figure 5-27 Microphone with assembly

Finally, a chip is mounted on microphone assembly as shown in Figure 5-27. Figure 5-32 shows a schematic cross-section of the assembled microphone. The chip is enclosed in a brass housing that provides electromagnetic shielding. The rear of the housing is threaded so that it will seamlessly screw onto a B&K Type 2669 preamplifier (Figure 5-29). The chip is attached with double-side taped to an electrically insulating surface inside the housing. One of the electrodes is connected to a non-grounded terminal that will be coupled to the preamplifier input, while other is connected to ground.

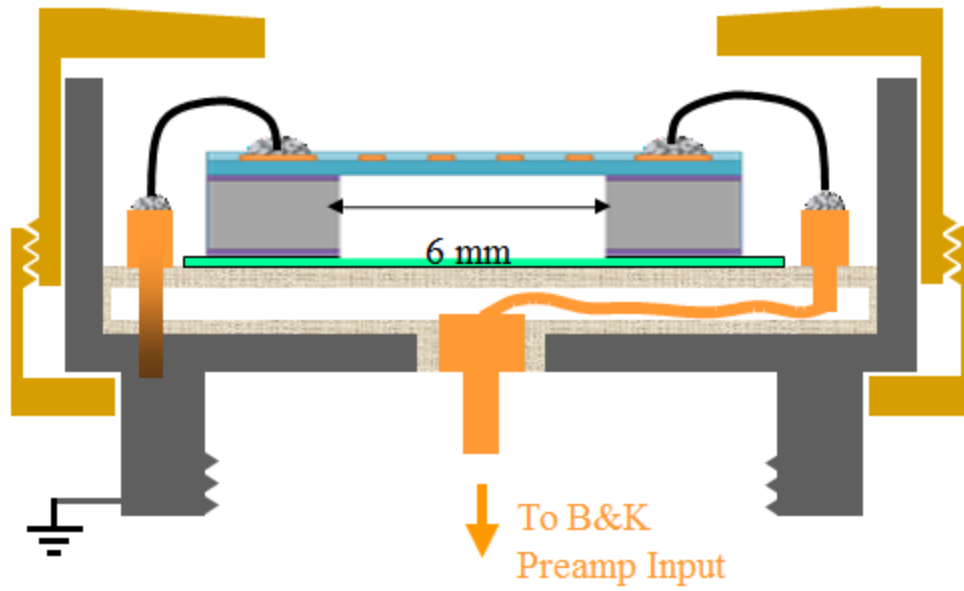


Figure 5-28 Schematic of microphone assembly



a) Brass housing



b) Connected with B&K Type 2669 Preamplifier.

Figure 5-29 a) Microphone housing, b) with preamplifier

RESONANCE FREQUENCY MEASURING SETUP

Since the first CD (compact disc) was commercialized in 1982, laser-based data acquisition technology has continuously progressed. Nowadays, the development of the optical pick-up head embedded in CD-ROM or DVD-ROM is quite mature. The well-developed optical and circuit design, as well as the focusing characteristics, is well suited for optical metrology applications at low cost and compactness. Several systems have been developed for collimators [199], profile measurements[200], [201], and confocal compact scanning optical microscopes [202].

Specifications	DVD-ROM	CD-ROM
Laser wavelength (nm)	650	780
Track distance (μm)	0.74	1.6
Pit depth (μm)	0.12	0.11
Pit length (μm)	0.4	0.834
Pit width (μm)	0.32	0.6
Numerical aperture (N.A.)	0.6	0.45
Diameter spot-size (μm)	1.32	2.11

Table 5-3 Specifications of the DVD optical pickup head white paper.

The DVD pick-up head uses a laser diode to produce optical light. Passing through a grating, the light diffracts into three beams, as shown in Figure 5-30. These beams pass through a polarized beam splitter, a quarter wave plate, and a collimator lens to transform the laser beams into a collimated beam. The collimated laser beam is then passed through a holographic Fresnel lens that has concentric circular grooves with interval spacing of tens to hundreds of micrometer.

The laser beam then focus on the reflective Aluminum layer in the CD/DVD ROM passing through its polycarbonate protecting layer. Then the beam reflects back along the original path and pass through the same collimator lens, beam splitter, and a cylindrical lens, and finally project onto the

four-quadrant photodiode (A,B,C,D), which outputs a focus error signal (FES) according to the beam spot distribution among four quadrants.

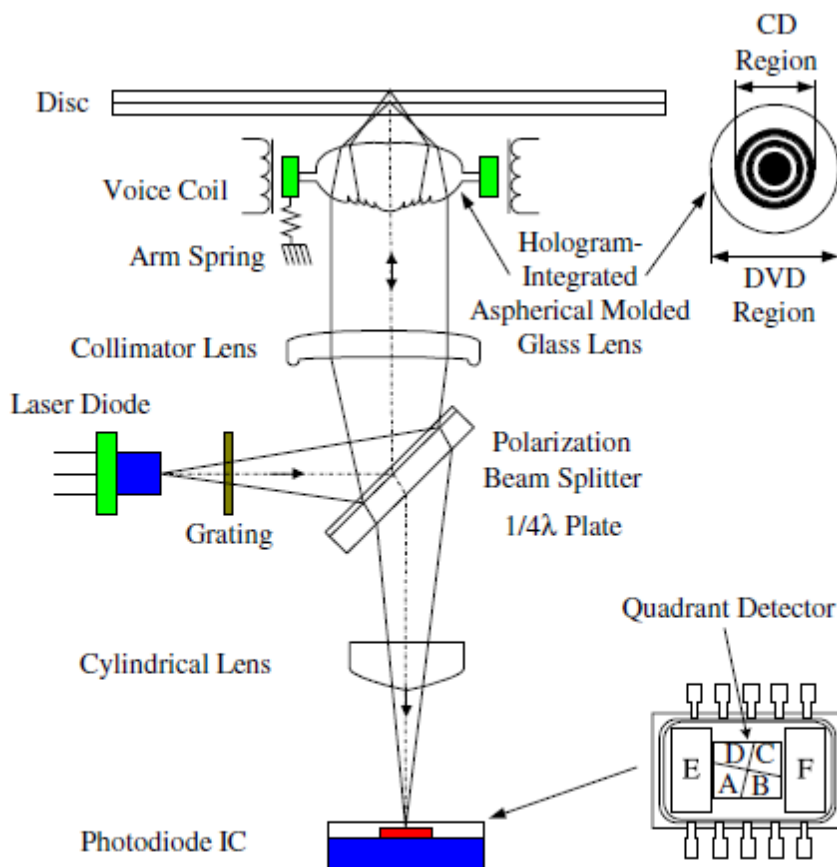


Figure 5-30 Structure of a DVD/CD pick-up head.

An astigmatic detection scheme used in most of the optical DVD pick-up heads. A laser beam emitted by a laser diode is focused onto a reflective surface through a collimator and an objective lens with a voice coil motor mounted. The laser beam is not exactly circular shape rather it is elliptical shape (along to the Y axis) because of the waveguide in the laser diode is normally thin and wide. The laser beam is reflected from the surface, passes through a beam splitter plate, and then imaged onto a photo diode integrated chip (PDIC). The PDIC is composed of four quadrant photosensors (A, B, C, D) with a current preamplifier assigned to each of them. The output signal of

the PDIC has a bandwidth of several tens of MHz (-3 dB) to meet with the specification of DVD player, which can be defined as A_{PD} , B_{PD} , C_{PD} and D_{PD} . Along the optical path, the laser diode and the PDIC are placed in 45 degree tilted. The reflected beam then passes through a cylindrical lens and distorted and elongated to 90 degree of the original beam. At the right focal distance the original beam shape is compensated to become a circular shape and it is evenly distributed on the PDIC (the red spot). The focus error signal (FES), $A_{PD} + C_{PD} - (B_{PD} + D_{PD}) = 0$, becomes zero. When the surface is lifted, the beam is less distorted and keeps original elongation (Y axis) on the PDIC (the blue spot). The FES becomes smaller than zero, $A_{PD} + C_{PD} - (B_{PD} + D_{PD}) > 0$. When the surface is lowered, the beam is more distorted to 90 degree of the original elongation (along to X axis) on the PDIC (the yellow spot). The FES becomes larger than zero, $A_{PD} + C_{PD} - (B_{PD} + D_{PD}) < 0$. See the Figure 5-31

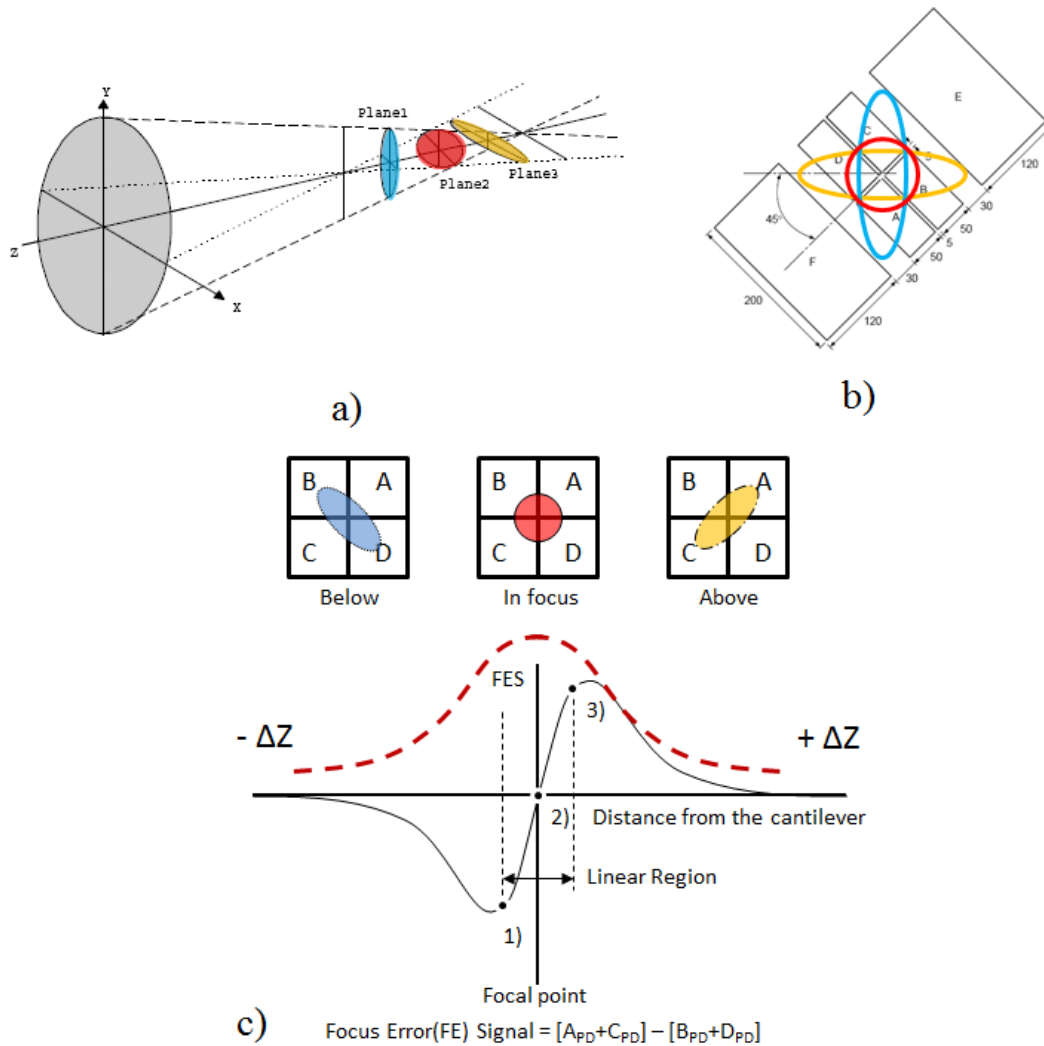


Figure 5-31 An astigmatic detection scheme. FES signal is represented as a black line. Intensity is represented as a dotted red line.

The size of the focus beam depends on the numerical aperture of the objective lens and the wavelength used in the system. For the CD/DVD pickup, it has two beam; 780nm for CD and for 650nm for DVD as we see in Table 5-3. Since the lateral resolution achievable using an optical

system is limited by diffraction effects, shorter-wavelength beam is advantageous to use. In fact, assuming that optical aberrations are negligible, the resolution d is given by

$$d = \frac{\lambda}{N.A.}$$

, where N.A. represents the numerical aperture of the front lens of the optical system and λ is the wavelength of the radiation. Clearly, DVD optical units provide superior resolution due to their higher numerical aperture and the shorter wavelength. As a further remark, it should be noted that the light beam produced by a DVD pickup is visible as red color to the human eye, thus simplifying positioning of the laser beam at the desired location (Figure 5-35).

In our measurement, the movement of the membrane is measured by a DVD pickup head [203], SF-HD62 from Sanyo Co. Ltd. Normally the data specification of DVD pickup is treated as non-disclosure information, we had to disassemble to each component and figure out electrical connections and optical configuration. Fortunately, because SF-HD62 has been widely used in consumer electronics, we could find helpful information such as pin configuration, supply voltage and operating current by searching repair or service manual for DVD players.

Pin No.	Pin Name	Functional Unit
1	F-	Actuator
2	F+	
3	T+	
4	T-	
5	C/c	Photo detector
6	D/d	
7	CD/DVD SW	
8	RF	
9	A/a	
10	B/b	

11	F	
12	GND-PD	
13	Vc(Vref)	
14	Vcc	
15	E	
16	(N.C.)	
17	VR-CD	Laser diode
18	VR-DVD	
19	CD-LD	
20	MD	
21	HFM	
22	(N.C.)	
23	DVD-LD	
24	GND-LD	

Table 5-4 Pin connection of Sanyo SF-HD62, A,B,C,D for DVD mode, a,b,c,d for CD mode are used to generate FES signal; Pin 8, RF represents intensity of light used to figure out the maximum reflecting point.

The pin connection of Sanyo SF-HD62 is shown in Table 5-4.

Detail pictures are shown in the Figure 5-30. The first criteria to choose DVD pickup is either we can get an information of it or not. The second factor is the position of half mirror as we see in Figure 5-32 b). In this configuration we could easily mount a CCD camera on top of the DVD pickup without adjusting it. For the laser diode can be easily damaged by static charge, it has a solder short between the laser diode cathode and the ground. The solder short of new DVD pickups should be removed before use.

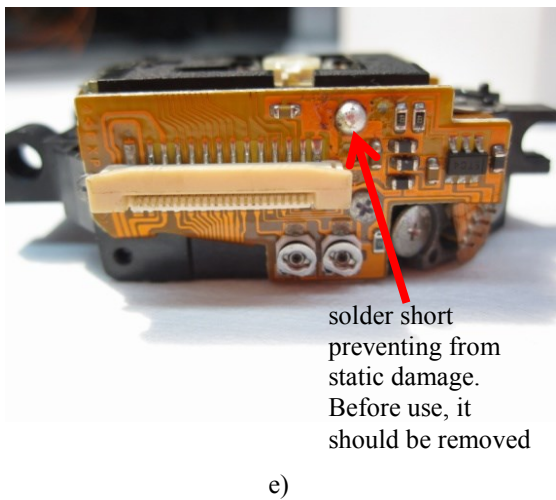
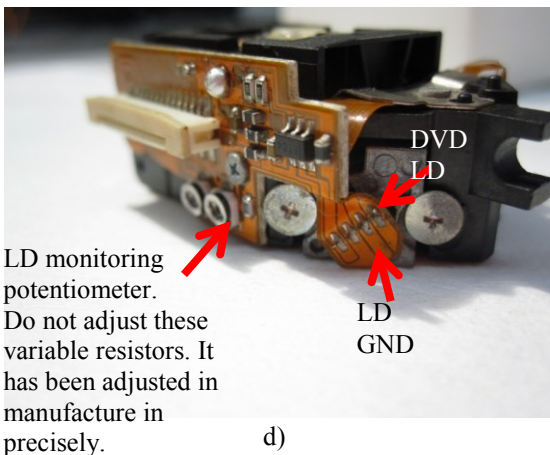
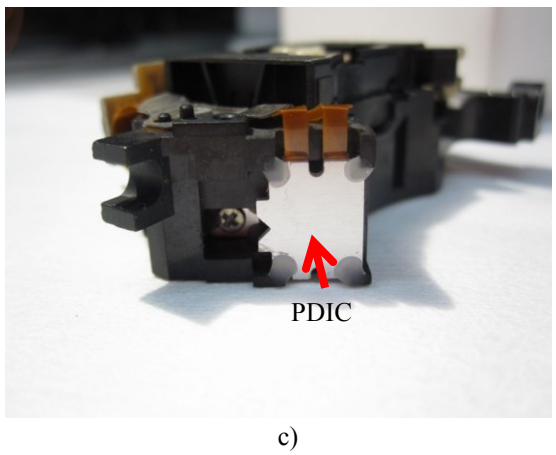
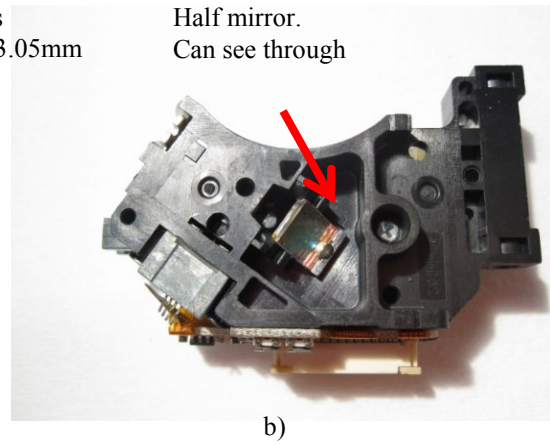
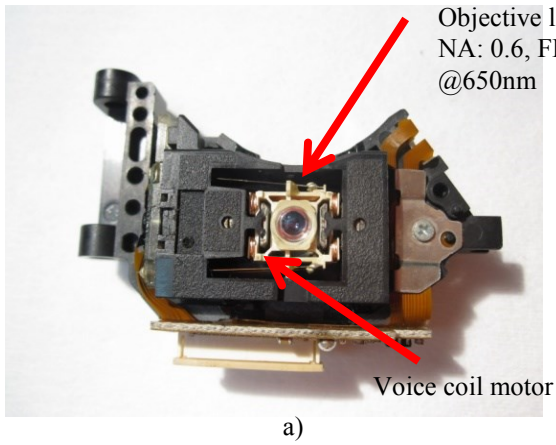
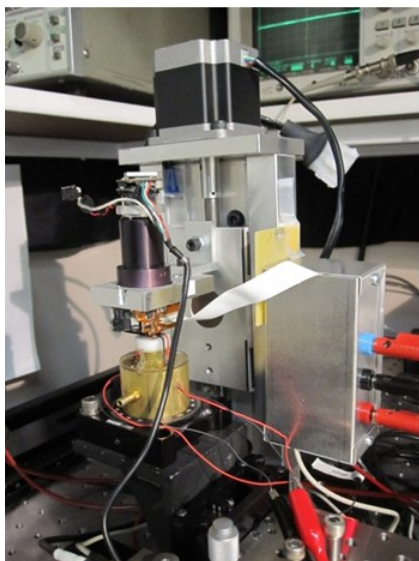
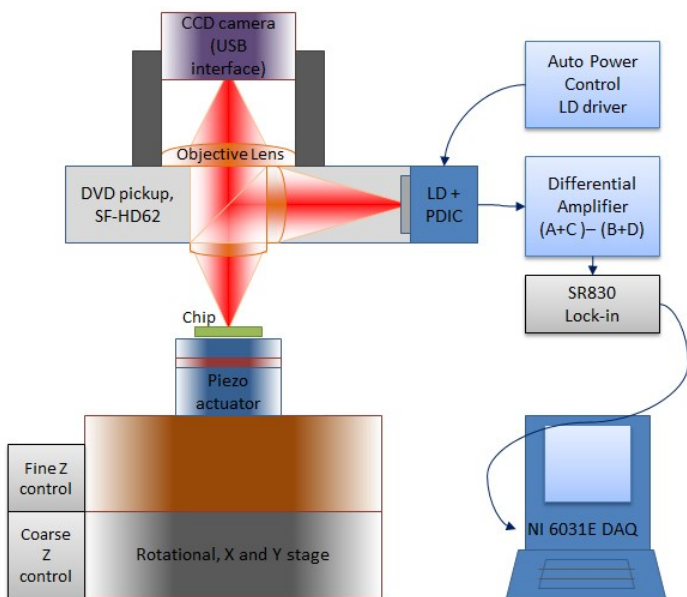


Figure 5-32 Sanyo SF-HD62

The flat flexible cable to fit the connector on the circuit board on DVD pickup is a 24 connector, 0.5mm pitch and 0.1mm with support from Digikey®. DVD pickup is pretty robust to the mechanical damage. However after removing the solder short, , it should be handle with care to prevent damage to the laser diode and PDIC.



a)



b)

Figure 5-33 Measuring setup with DVD pickup. Corse z stage is composed of a linear motorized stage form Vlemex®. For a fine z stage, piezo stack from Omega® is adopted

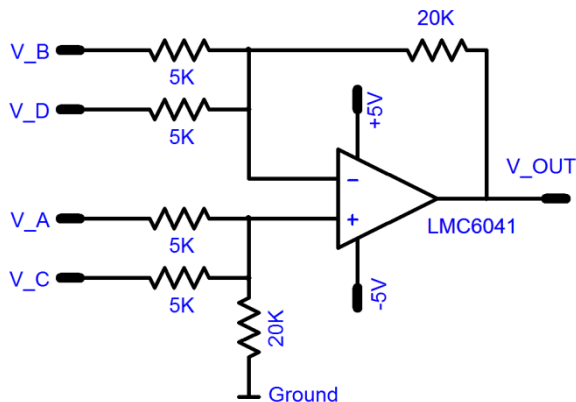


Figure 5-34 A differential amplification circuit to get FES signal

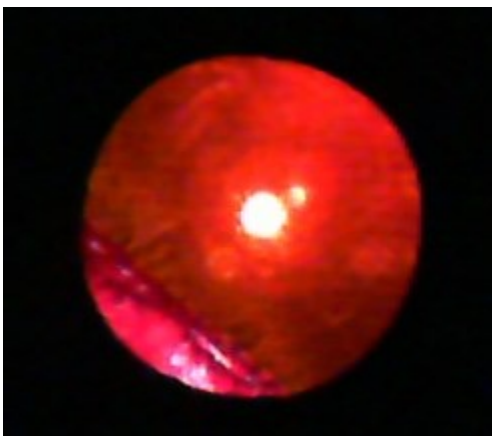


Figure 5-35 Beam, focused at the center electrode

After the laser beam was focused on the mirror at the center of the membrane (Fig.4d), the output of the PDIC was amplified by the designed circuit (Figure 5-34) and the FES ($A_{PD}+C_{PD} - [B_{PD}+D_{PD}]$) was obtained. We focused the beam on the electrode to get a maximum light reflection; first move z stage to find a coarse focus while monitoring the USB camera; after finding a coarse focus, we

move x, y stage to move a beam on the electrode; control fine z stage to get a maximum intensity of reflected light.

Then, a SR830 Lock-in amplifier was used to read the FES, which is proportional to the deflection of the membrane. Once FES was measured, the proportional constant (i.e., 9 nm/V) between the distance change and the measured voltage was calibrated as shown in Figure 5-36. In this calibration, the linear range is 2 μm in z direction and it is large enough for our diaphragm measurement. Because FES depends on surface reflectivity too, every measurement requires a calibration. To do, we use a RF signal from the DVD Pickup ($A_{\text{PD}}+C_{\text{PD}} + B_{\text{PD}}+D_{\text{PD}}$).

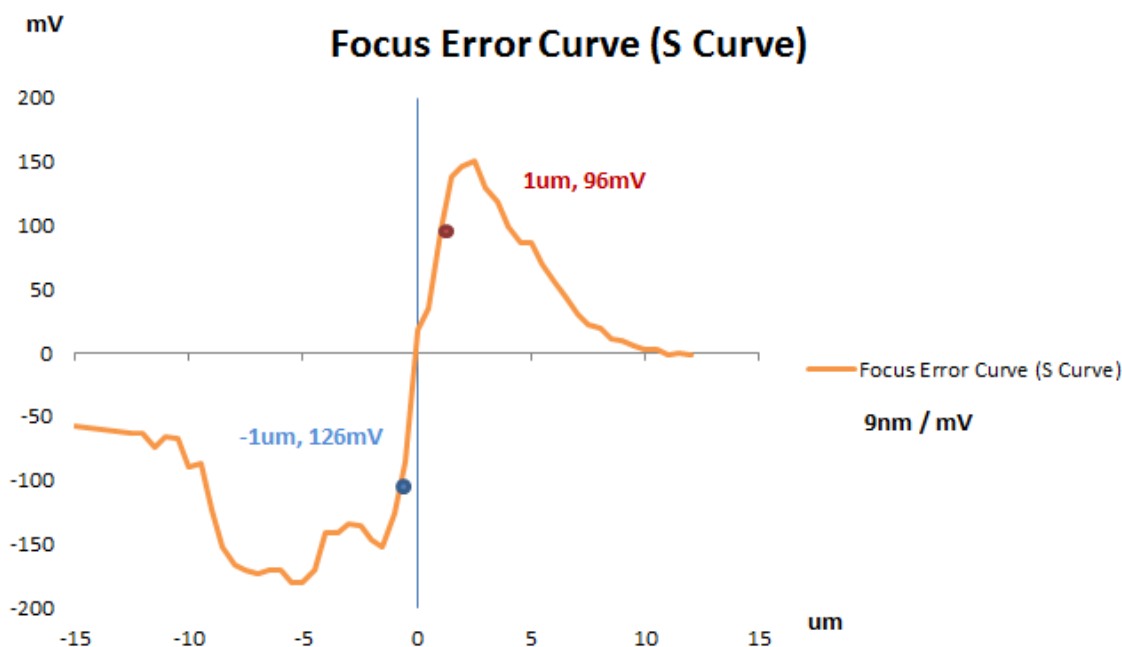


Figure 5-36 The measured F-E signal Vs distance. For this case, the proportional constant between the distance change and the measured voltage is 9×10^{-6} m/V.

An USB CCD camera, Microsoft HD 6000, and an objective lens of a microscope were mounted on the top of the pickup, right above its beam splitter (half mirror), to locate the laser beam at the sensing mirror on the cantilever (Figure 5-35).

We also adopted an automatic power control to reduce the noise from laser power fluctuation. The purpose of the automatic power control circuitry APC is to keep the LD inside the optimal operative range and to accurately stabilize the emitted optical power, despite possible changes of the environmental temperature, power supply voltage and any other disturbing factor.

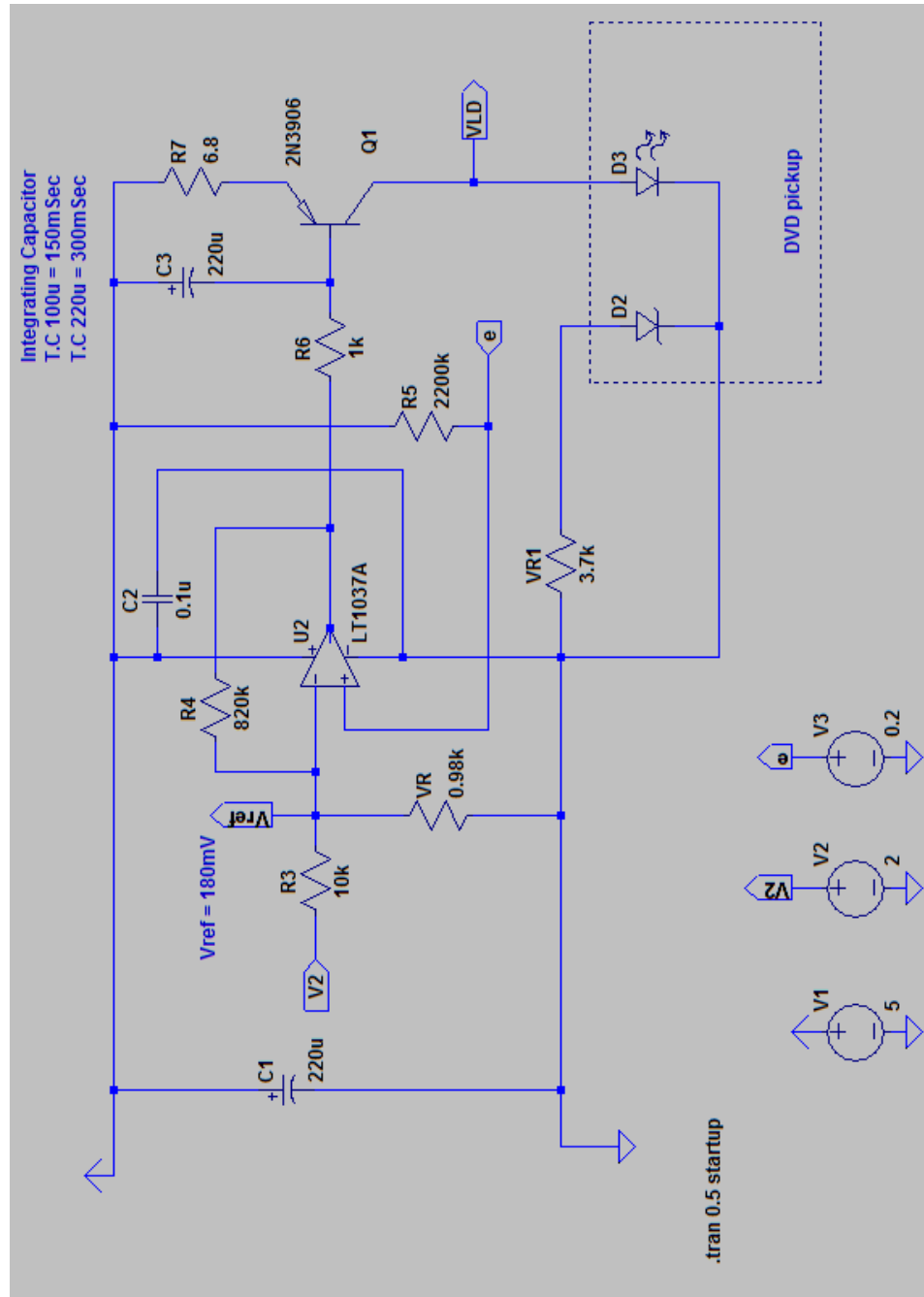


Figure 5-37 A reference Automatic Power Control circuit suggested from Sanyo®

The reference signal, maximum amplitude of 5 Vrms from the SR830, was fed into the power amplifier and then amplified 4 times and applied to the external piezo shaker to vibrate the diaphragm.

By the setup, we can find a peak at 24.22 kHz. This value does not exactly match with the calculation. The difference may be assumed to be related the thickness and the density of PA-C which are not known exactly and the diameter alteration of the diaphragm by the XeF₂ gas.

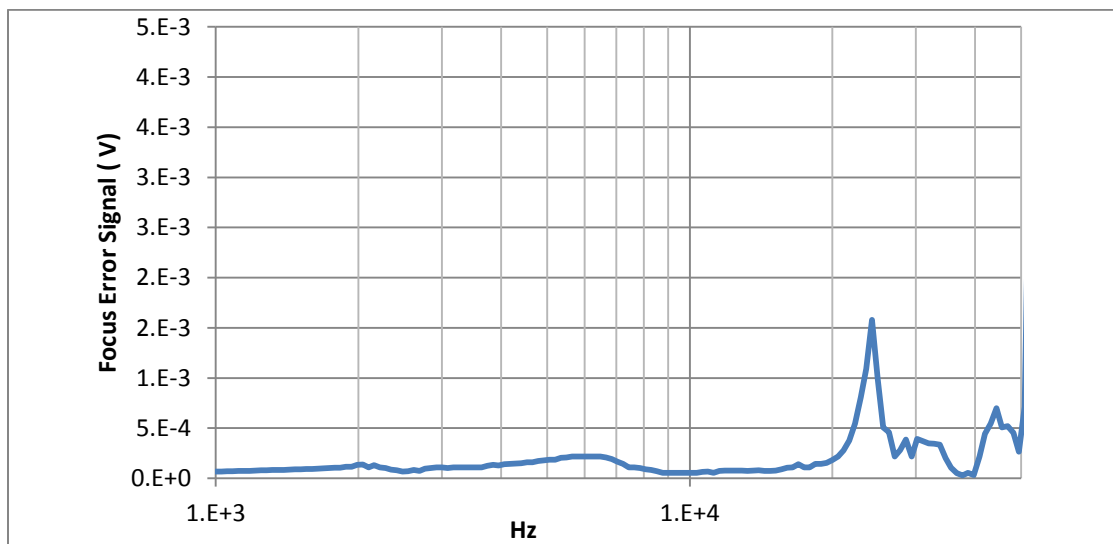


Figure 5-38 Measured data, resonance peak at 24.22kHz for 29um thickness, 6mm in diameter.

MICROPHONE MEASURING SETUP

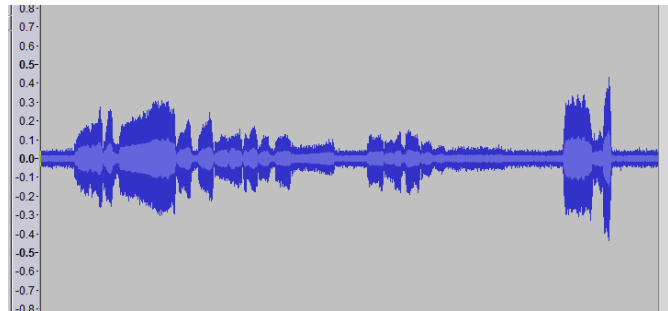
Testing

Figure 5-39 Loud human voice record.

The microphone was barely able to detect sound from a loud human voice with the use of an amplifier with 50dB of gain, when the microphone was connected to the B&K Type 2669 preamplifier and a B&K Type 5935 dual channel amplifier/power supply. When the linear amplifier PA119 is connected with SR 780 spectrum analyzer with 2kHz signal, to generate 10pa of sound pressure, the microphone generates a 80uV. The measured open-circuit sensitivity of the microphone at this frequency is about 8 $\mu\text{V}/\text{Pa}$. However, taking into account the 15 pF input capacitance of the pre-amplifier and the $\sim 20\text{pF}$ stray capacitance of the assembled microphone, and comparing to the capacitance of microphone itself, 5.6pF, this is quite obvious.

Performance testing

The piezoelectric PA-C microphone was tested in a B&K Type 4232 anechoic test chamber (Figure 5-40). An integrated speaker in the test chamber served as the acoustic source. A B&K Type 4189 1/2-inch reference microphone was used to measure the sound pressure level at the test position. The reference microphone was connected to a B&K Type 2669 preamplifier and a B&K Type 5935 dual channel amplifier/power supply. The piezoelectric microphone under test was also connected to a B&K Type 2669 preamplifier and it shared the same B&K dual channel amplifier/power supply

with the reference microphone. This ensured that the only variable in the entire test system was the MEMS piezoelectric microphone and that the other components were kept constant.

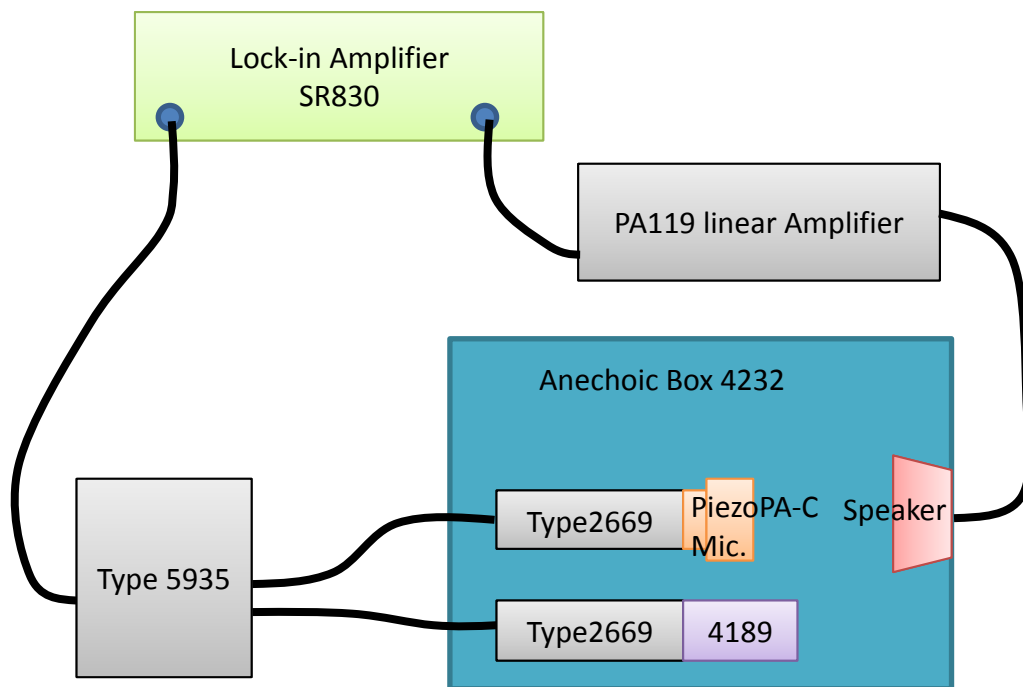


Figure 5-40 Measuring setup.

Using a Stanford Research Systems Model SR830 Lock-in Amplifier to apply an input sinusoidal signal of known sound pressure from 1 kHz to 10 kHz (Figure 5-13), the frequency response of the piezoelectric microphone was obtained. Sound pressure levels with higher frequencies were not used because the output of the built-in speaker in the anechoic sound chamber is attenuated above 10 kHz.

Sound pressure Level

Sound pressure level (SPL) or sound level is a logarithmic measure of the effective sound pressure of a sound relative to a reference value. It is measured in decibels (dB) above a standard reference

level. The commonly used "zero" reference sound pressure in air is 20 uPa RMS, which is usually considered the threshold of human hearing at 1 kHz (roughly the sound of a mosquito flying 3 m away). Most sound level measurements will be made relative to this level, meaning 1 Pa will equal SPL of 94 dB. In other media, such as underwater, a reference level of 1 μPa is more often used.[204] These references are defined in ANSI S1.1-1994.

$$L_p = 10 \text{Log}_{10} \left(\frac{P_{rms}^2}{P_{ref}^2} \right) = 20 \text{Log}_{10} \left(\frac{P_{rms}}{P_{ref}} \right) \text{ [dB SPL]}$$

where P_{ref} is the reference sound pressure and P_{rms} is the rms sound pressure being measured [205]. Sometimes variants are used such as dB (SPL), dB_{SPL}, or dB_{SPL}, which are not recognized as SI units.[206]. Sometimes Abbreviation “dB” of dB(SPL) can give a confusion that a dB is an absolute unit by itself.

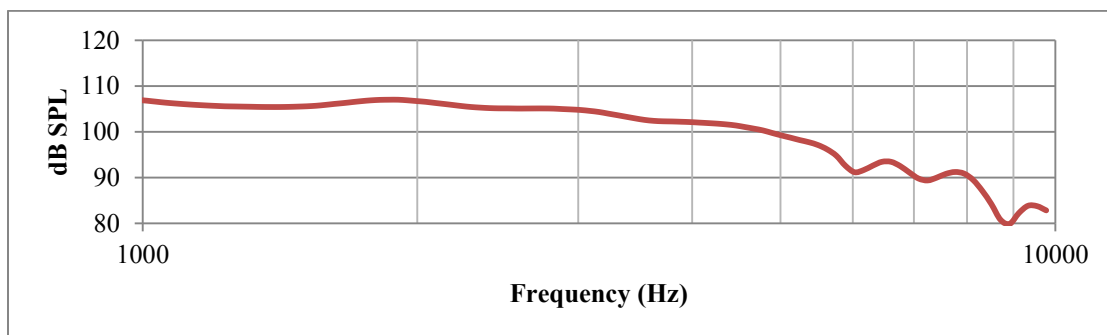


Figure 5-41 Input sound pressure level for frequency response measurements

As we see in the Figure 5-41, sound pressure level quickly drops beyond 10 kHz, due to the driving unit of the B&K Type 4232 anechoic test chamber.

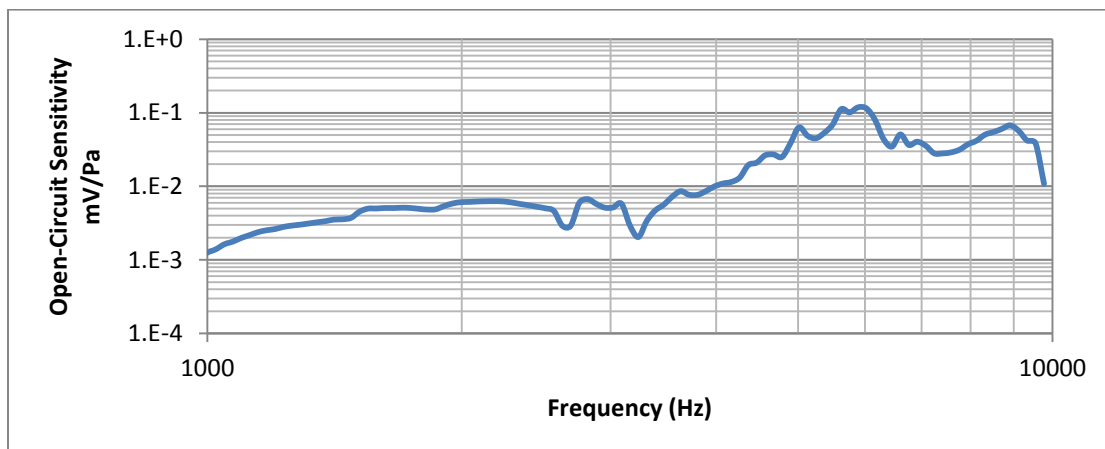


Figure 5-42 Frequency response of MEMS piezoelectric microphone.

In Figure 5-42, it shows the frequency response of 5.5um thick, 200C, 800V, 5 minutes poled PA-C diaphragm microphone, with 6mm in diameter. Since the microphone doesn't have a thin air gap observed in a MEMS electret microphones, it doesn't show an acoustic resonance at low frequency near ~600Hz. The peaks in the frequency response between 5 - 8 kHz are most likely due to the squeezed-film damping in the air gap.

The distortion limit of the MEMS microphone was found to be above 110 dB SPL (the maximum output of the anechoic sound chamber speaker). This test was conducted at 1 kHz and the measured Total Harmonic Distortion was less than 1% at 110 dB SPL. Given that the lowest detectable sound pressure level is 60 dB SPL, this translates into a microphone dynamic range that is greater than 50 dB SPL.

SUMMARY

This chapter has described the first successful use of piezoelectric PA-C diaphragms in MEMS piezoelectric microphones. The promising results presented here open up new possibilities of using Parylene as a piezoelectric material and structural material for the surface of microphones integrated with microelectronics. The room temperature deposition of Parylene would allow such a device to be fabricated in a post-IC process. If successfully developed, this miniature, self-generating, low-cost, microelectronics-compatible condenser microphone would revolutionize the entire acoustic sensor industry.

Chapter 6

CONCLUSION

This thesis describes the development of miniature thin film piezoelectric microphones that are fabricated from piezoelectric Parylene-C (PA-C) using Micro Electro Mechanical Systems (MEMS) technology and poling technology. Device issues such as material selection, design, modeling, fabrication, packaging, testing and performance were studied.

First, a poling process is determined, which can be varied by temperature, bias and time. Also stretching is studied to optimize parameters. Piezoelectric PA-C, with its ability to be deposited at room temperature and characteristics, chemical inertness, mechanical property, high temperature endurance, bio-compatibility and electric insulation, it can be easily integrated to conventional MEMS process with moderate condition of poling, $<200^{\circ}\text{C}$, 800V and 5minutes. Its piezoelectricity is stable even at 160°C for a week with -3.2pC/N of d_{33} value.

Using this new thin film piezoelectric PA-C technology, the fabrication, packaging and testing of MEMS piezoelectric microphone designs were investigated. The microphone was fabricated using bulk-micromachining techniques, such as DRIE and XeF_2 etching. The microphone was manufactured as a single layer diaphragm structure. This gives design simplicity and tolerance in process.

Overall, the dynamic range of the microphone was from less than 30 dB to above 110 dB SPL and the open-circuit sensitivities obtained range from 0.001 – 0.11 mV/Pa over the frequency range 1 kHz - 10 kHz. The total harmonic distortion of the device was less than 20% at 110 dB SPL, 1 kHz

In the work of the thesis as an acoustic device only MEMS microphone is introduced and investigated. However, considering the outstanding properties of PA-C could be a choice for the area requires gas phase conformal coating, high temperature operation and bio-medical compatibility. The work presented in this thesis was meant to serve as a foundation for the development of these types of integrated acoustic and vibration sensing solutions.

BIBLIOGRAPHY

- [1] "A. C. Becquerel, Bulletin des Sciences, par la Societe Philomatique de Paris, France, vol. 7, pp. 149-155; March, 1820."
- [2] "J. and P. Curie, Bulletin de la Societe Mineralogique de France, vol. 3, pp. 90-93; April, 1880."
- [3] "C. B. Sawyer, 'The use of Rochelle Salt crystals for electrical reproducers and microphones,' PROC. IRE, vol. 19, pp. 2020-2029; November, 1931."
- [4] "Grey, U. S. Patenit No. 2,486,560; 1949."
- [5] "Jaffe, U. S. Patent No. 2,708,244; 1955."
- [6] J. S. Harrison and N. Langley, "Piezoelectric Polymers," 2001.
- [7] G.T. DAVIS, *Piezoelectric and Pyroelectric Polymers. In Polymers for Electronic and Photonic Applications*. Boston, MA: Academic Press, Inc, 1993, p. 435.
- [8] M. Specialties, "Piezo Film Sensors Technical Manual."
- [9] B. Gonzalo, T. Breczewski, J. L. Vilas, M. A. Perez-Jubindo, M. R. De La Fuente, J. R. Dios, and L. M. León, "Dielectric Properties of Piezoelectric Polyimides," *Ferroelectrics*, vol. 370, no. 1, pp. 3–10, 2008.
- [10] G. M. Atkinson, R. E. Pearson, Z. Ounaies, C. Park, J. S. Harrison, S. Dogan, and J. a. Midkiff, "Novel piezoelectric polyimide MEMS," *TRANSDUCERS '03. 12th International Conference on Solid-State Sensors, Actuators and Microsystems. Digest of Technical Papers (Cat. No.03TH8664)*, vol. 1, pp. 782–785, 2003.
- [11] G. M. Atkinson, R. E. Pearson, Z. Ounaies, C. Park, J. S. Harrison, and W. C. Wilson, "Piezoelectric Polyimide MEMS Process," no. 1, pp. 1–6.
- [12] G. M. Atkinson, R. E. Pearson, Z. Ounaies, C. Park, J. S. Harrison, and W. C. Wilson, "Piezoelectric Polyimide MEMS Process," no. 1, pp. 1–6.
- [13] G. M. Atkinson, R. E. Pearson, Z. Ounaies, C. Park, J. S. Harrison, and J. a. Midkiff, "Piezoelectric polyimide tactile sensors," *Proceedings of the 15th Biennial University/Government/ Industry Microelectronics Symposium (Cat. No.03CH37488)*, no. 1, pp. 308–311.
- [14] "Z. Ounaies and J.S. Harrison, 'An Investigation of Piezoelectricity of a Nitrile -Substituted Polyimide', accepted Journal of Polymer Science: Polymer Physics, August, (2002)."
- [15] "C. Park, Z. Ounaies, J. Su, J.G. Smith Jr., J.S. Harrison, 'Polarization Stability of Amorphous Piezoelectric Polyimides', Materials Research Society Meeting Proceedings: Symposium FF, December, (1999)."
- [16] "http://hdmicrosystems.com/HDMicroSystems/en_US/index.html." [Online]. Available: http://hdmicrosystems.com/HDMicroSystems/en_US/index.html.

- [17] R. L. Hubbard, Z. Fathi, I. Ahmad, H. Matsutani, and T. Hattori, "Low temperature curing of polyimide wafer coatings," *IEEE/CPMT/SEMI 29th International Electronics Manufacturing Technology Symposium (IEEE Cat. No.04CH37585)*, pp. 149–151.
- [18] "E. M. Maynard, C. T. Nordhausen, and R. A. Normann, *Electroencephalogr Clin Neurophysiol*, vol. 102 (1997) 228-39."
- [19] "Jeffrey B. Fortin, Toh-Ming Lu (2003). *Chemical vapor deposition polymerization: the growth and properties of parylene thin films*. Springer. pp. 4–7. ISBN 978-1-4020-7688-6."
- [20] "Mattox, D. M. *The foundations of vacuum coating technology*, Springer, 2003 ISBN 978-3-540-20410-7 Google books."
- [21] "<http://www.scscoatings.com/about/history.aspx>."
- [22] "P. A. Stupar and A. P. Pisano, *The 11th international conference on solid-state sensors and actuators*, Munich, Germany, 2001."
- [23] "H.-M. Tong, L. S. Mok, K. R. Grebe, H. L. Yeh, K. K. Srivastava, and J. T. Coffin, *IEEE Transactions on component, hybrids, and manufacturing technology*, vol. 16 (1993) 571-576."
- [24] "Fairchild Semiconductor Corp, <http://www.Fairchildsemi.com/company/history.html>."
- [25] "Texas Instruments Inc., <http://www.ti.com/corp/docs/kilbyctr/jackbuilt.shtml>."
- [26] "K.E. Petersen, 'Silicon as a Mechanical Material,' *Proceedings of the IEEE*, Vol. 70 (5), pp. 420-457, May 1982."
- [27] "'Special Issue: Integrated Sensors, Microactuators and Microsystems (MEMS),' *Proceedings of the IEEE*, August 1998."
- [28] "G.T.A. Kovacs, N.I. Maluf and K.E. Petersen, 'Bulk Micromachining of Silicon,' *Proceedings of the IEEE*, Vol. 86, No. 8, August 1998."
- [29] "J.M. Bustillo, R.T. Howe and R.S. Muller, 'Surface Micromachining for Microelectromechanical Systems,' *Proceedings of the IEEE*, Vol. 86, No. 8, August 1998."
- [30] "W.H. Hsieh, M. Lucas, C.R. Marsh, S. Wu, C.I. Grosjean and Y.C. Tai, 'A Novel Silicon Holder for Three-Point Bending of Micro Silicon Beams,' 1996 ASME Mechanics and Materials Conference."
- [31] "M. Madou, 'Fundamentals of Microfabrication,' CRC Press, Boca Raton, 1997."
- [32] "E.B. Arkilic, M.A. Schmidt and K.S. Breuer, 'Gaseous Slip-Flow in Long Microchannels,' *Journal of Microelectromechanical Systems*, Vol 6 (2), pp. 167-178, 1997."
- [33] "W.H. Hsieh, T.Y. Hsu and Y.C. Tai, 'A Micromachined Thin Film Teflon Electret Microphone,' *Technical Digest 9th International Conference on Solid State Sensors and Actuators (Transducers '97)*, Vol. 2, pp. 425-428, Chicago, USA, June 1997."
- [34] "S. Wu, J. Mai, Y.C. Tai and C.M. Ho, 'Micro Heat Exchanger Using MEMS Impinging Jets,' *Proc. 12th Annual International Workshop on Micro Electro Mechanical Systems*, pp. 171-176, Orlando, USA, January 1999."

- [35] “A. Rogner, W. Ehrfeld, D. Munchmeyer, P. Bley, C. Burbaum and J. Mohr, ‘LIGA-Based Flexible Microstructures for Fiber-Chip Coupling,’ *Journal of Micromechanics and Microengineering*, Vol. 1 (3), pp. 167-170, 1991.”
- [36] “R.C. Anderson, G.J. Bogdan and R.J. Lipshutz, ‘Miniaturized Genetic-Analysis System,’ *Technical Digest, IEEE Solid-State Sensors and Actuators Workshop*, pp. 258-261, Hilton Head Island, South Carolina, USA, June 1996.”
- [37] “K. Ikuta and K. Hirowatari, ‘Real Three-Dimensional Micro Fabrication Using Stereo Lithography,’ *Proceedings of IEEE Workshop on Micro Electro Mechanical Systems, MEMS ’93*, pp. 42-47, Fort Lauderdale, USA, 1993.”
- [38] “T.R. Anthony, ‘Diodes Formed by Laser Drilling and Diffusion,’ *Journal of Applied Physics*, Vol. 53, No. 12, pp. 9154-9164, December 1982.”
- [39] “T. Masaki, K. Kawata and T. Masuzawa, ‘Micro Electro-Discharge Machining and Its Applications,’ *Proceedings of IEEE Workshop on Micro Electro Mechanical Systems, MEMS ’90*, pp. 21-26, Napa Valley, USA, 1990.”
- [40] “A.J. Fleischman, S. Roy, C.A. Zorman and M. Mehregany, ‘Polycrystalline Silicon Carbide for Surface Micromachining,’ *Proceedings of IEEE Workshop on Micro Electro Mechanical Systems, MEMS ’96*, pp. 234-238, San Diego, USA, 1996.”
- [41] “X.Q. Wang, ‘Integrated Parylene Micro Electro Mechanical Systems (MEMS),’ Ph.D. Thesis, Caltech, 2000.”
- [42] “L. Spangler and C.J. Kemp, ‘ISAAC - Integrated Silicon Automotive Accelerometer,’ *Technical Digest 8th International Conference on Solid State Sensors and Actuators (Transducers ’95)*, pp. 585-588, Stockholm, Sweden, June 1995.”
- [43] “S. Sugiyama, T. Suzuki, K. Kawahata, K. Shimaoka, M. Takigawa and I. Igarashi, ‘Micro-Diaphragm Pressure Sensor,’ *Proceedings of IEEE International Electron Devices Meeting*, pp. 184-187, Los Angeles, USA, December 1986.”
- [44] “A. Manz, N. Graber, H.M. Widmer, ‘Miniaturized Total Chemical Analysis Systems; A Novel Concept for Chemical Sensing,’ *Sensors and Actuators, B1*, pp. 244-248, 1990.”
- [45] “P. Heywood, ‘The Optical Future: Optical Switching Fabric,’ *Light Reading Online*, www.lightreading.com/document.asp?doc_id=355&page_number=9, March 29, 2000.”
- [46] “Harper, Douglas. ‘piezoelectric’. *Online Etymology Dictionary*.”
- [47] A. Safari and E. K. Akdoğan, *Piezoelectric and Acoustic Materials for Transducer Applications (Google eBook)*. Springer, 2008, p. 481.
- [48] T. Bein, “APPLICATION OF PIEZOELECTRIC MATERIALS IN,” no. October, 2006.
- [49] R. Lin, S. Member, and H. Shih, “Piezoelectric Transformer Based Current-Source Electronic Ballast,” vol. 23, no. 3, pp. 1391–1400, 2008.
- [50] P. I. (PI) G. & C. KG, *Piezoelectrics in Positioning Tutorial on Piezotechnology in Nanopositioning Applications*. Physik Instrumente (PI) GmbH & Co. KG, 2008.

- [51] Marvell Nanofabrication laboratory and M. L. Berkeley, "Xenon Difluoride Etching System Manual," pp. 2–5.
- [52] Y. Higashihata, J. Sako, and T. Yagi, "Piezoelectricity of vinylidene fluoride-trifluoroethylene copolymers," *Ferroelectrics*, vol. 32, no. 1, pp. 85–92, 1981.
- [53] U. S. D. O. H. A. H. SERVICES, "DRAFT NTP MONOGRAPH ON HEALTH EFFECTS OF LOW-LEVEL LEAD," 2011.
- [54] in E. M.G. BROADHURST AND G.T. DAVIS, *lectrets*, G.M. Sessler. New York, NY: Springer-Verlag, 1980, p. vol. 33, p. 283.
- [55] W. L. Bongiani, "Effect of crystallization and anneal on thin films of vinylidene fluoride/trifluorethylene (VR2/F3E) copolymers," *Ferroelectrics*, vol. 103, no. 1, pp. 57–65, 1990.
- [56] J. Kulek, B. Hilczer, S. Kamba, and J. Petzelt, "Effect of crystallization, poling and ageing conditions on the FIR, dielectric and pyroelectric properties of hot-pressed PVDF and P(VDF/TFE)-(0.98/0.02)," *Acta Polymerica*, vol. 46, no. 2, pp. 152–155, 1995.
- [57] N. JAITANONG and A. CHAIPANICH, "Effect of Poling Temperature on Piezoelectric Properties of 0-3 PZT-Portland Cement Composites," *Ferroelectrics Letters Section*, vol. 35, no. 1–2, pp. 17–23, 2008.
- [58] J. Kulek, B. Hilczer, and A. Szlaferek, "Effect of the poling temperature on the dielectric properties of oriented PVDF film," *Ferroelectrics*, vol. 81, no. 1, pp. 365–368, 1988.
- [59] S. S. Visher, "LAWS OF TEMPERATURE," *Annals of the Association of American Geographers*, vol. 13, no. 1, pp. 15–40, 1923.
- [60] H. Lefebvre, F. Bauer, and L. Eyraud, "Optimization and characterization of piezoelectric and electroacoustic properties of PVDF- β induced by high pressure and high temperature crystallization," *Ferroelectrics*, vol. 171, no. 1, pp. 259–269, 1995.
- [61] Y. U. N. YE, Y. JIANG, Z. WU, and H. ZENG, "PHASE TRANSITIONS OF POLY(VINYLLIDENE FLUORIDE) UNDER ELECTRIC FIELDS," *Integrated Ferroelectrics*, vol. 80, no. 1, pp. 245–251, 2006.
- [62] D. K. D.-G. and K. Doughty, "Piezo- and pyroelectric behaviour of corona-charged polyvinylidene fluoride," *J. Phys. D: Appl. Phys.*, vol. 11, p. 2415, 1978.
- [63] J. a. Giacometti and O. N. Oliveira, "Corona charging of polymers," *IEEE Transactions on Electrical Insulation*, vol. 27, no. 5, pp. 924–943, 1992.
- [64] R. N. and M. M. P. T Kaura, "Simultaneous stretching and corona poling of PVDF films," *J. Phys. D: Appl. Phys.*, vol. 24, p. 1848, 1991.
- [65] H. KAWAI, "The Piezoelectricity of Poly(vinylidene fluoride)," *Jpn. J. Appl. Phys.*, vol. 8, p. p. 975., 1969.
- [66] Lovinger AJ., "Science," vol. 220, p. 1115, 1983.
- [67] Humphrey JS, *Vinylidene fluoride polymers*. New York: Wiley.
- [68] Lovinger AJ., *Developments in crystalline polymers*. Englewood, NJ: Applied Science Publishers Ltd;

- [69] K. F. J. Briber RM, "Polym Sci, Polym Phys," vol. 31, p. 1253., 1993.
- [70] A. M. K. K. TASHIRO, H. TADOKORO, "Structure and Piezoelectricity of Poly(vinylidene fluoride)," *Ferroelectrics*, vol. 32, p. 167, 1981.
- [71] T. FURUKAWA, "Piezoelectricity in Polymers," *IEEE Trans. Electr. Insul.*, vol. 24, pp. 375–393, 1989.
- [72] R. G. Polcawich, "A Piezoelectric MEMS Microphone Based on Lead Zirconate Titanate (PZT) Thin Films," no. November, 2004.
- [73] "Budd, K. D.; Dey, S. K.; Payne, D. A. Sol-Gel Processing of PbTiO₃, PbZrO₃, PZT, and PLZT Thin Films. *Brit. Cer. Proc.* 1985, 36, 107-21."
- [74] M. D. Williams, B. A. Griffin, T. N. Reagan, J. R. Underbrink, and M. Sheplak, "An AlN MEMS Piezoelectric Microphone for Aeroacoustic Applications," *Microelectromechanical Systems, Journal of*, vol. 21, no. 2. pp. 270–283, 2012.
- [75] "R. S. Fazzio, T. Lamers, O. Buccafusca, A. Goel, and W. Dauksher, 'Design and performance of aluminum nitride piezoelectric microphones,' in Proc. 14th Int. Conf. Micro-Sens., Actuators Microsyst., Lyon, France, Jun. 10–14, 2007, pp. 1255–1258."
- [76] "R. J. Littrell, 'High performance piezoelectric MEMS microphones,' Ph.D. dissertation, Univ. Michigan, Ann Arbor, MI, 2010."
- [77] "M. Williams, B. Griffin, A. Ecker, J. Meloy, and M. Sheplak, 'An aluminum nitride piezoelectric microphone for aeroacoustics applications,' in Proc. Solid-State Sens., Actuators, Microsyst. Workshop, Hilton Head, SC, Jun. 6–10, 2010, pp. 1–4."
- [78] "S. Trolier-McKinstry and P. Muralt (2004, Jan.). Thin film piezoelectrics for MEMS. *J. Electroceram.* [Online]. 12(1/2), pp. 7–17."
- [79] "No Title T. L. Lamers and R. S. Fazzio, 'Accelerating development of a mems piezoelectric microphone,' presented at the ASME Int. Design Engineering Technical Conf. Computers Information in Engineering Conf., Las Vegas, NV, Sep. 4–7, 2007, pp. 593–601, Pap."
- [80] "S. Franssila, *Introduction to Microfabrication*. Boulder, CO: Wiley, 2004, p. 401."
- [81] M. G. M. Royer, J.O. Holmen, M.A. Wurm, O.S. Aadland, "ZnO on Si integrated acoustic sensor," *Sensors and Actuators*, vol. 4, pp. 357 – 362, 1983.
- [82] "J Conragan and R S Muller, Piezoelectric held-effect transistor stram transducers, Proc IEEE Solrd State Sensors Symp , Mmneapolis, Mmn , USA, June 1970, pp 52 - 55."
- [83] "P L Chen, R S Muller, R M White and R Jolly, Thin Film ZnO-MOS transducer with virtually d c response, Proc IEEE US Symp , Boston, Mass, USA, Nov 1980."
- [84] "M Royer, Integrated ZnO/Si pressure sensor, US Patent pendmg, 1009211-US, March 198X."
- [85] "S Tlmoshenko and S Womowsky-Krleger, *Tehory ofPlates and Shells*, McGraw Hill, New York, 2nd Edn ,1959."
- [86] "T Shlosakl, High speed fabrication of high quahty sputtered ZnO thin fdms for bulk and surface wave apphcatlons, Proc IEEE US Symp , CH 1344 (1978) 100 – 110."

- [87] “Fabrication and Characterization of Piezoelectric Micromachined Ultrasonic Transducers with Thick Composite PZT Films Zhihong Wang, Weiguang Zhu, Member, IEEE, Hong Zhu, Jianmin Miao, Member, IEEE, Chen Chao, Changlei Zhao, and Ooi Kiang Tan, Senior Membe.”
- [88] “W. Zhu, Z. Wang, C. Zhao, O. Tan, and H. Hng, ‘Low temperature sintering of piezoelectric thick films derived from a novel sol-gel route,’ *Jpn. J. Appl. Phys.*, vol. 41, no. 11B, pp. 6969–6975, 2002.”
- [89] “Z. Wang, W. Zhu, C. Zhao, and O. K. Tan, ‘Dense PZT thick films derived from sol-gel based nanocomposite process,’ *Mater. Sci. Eng.*, vol. B99, no. 1–3, pp. 56–62, 2003.”
- [90] M. Pedersen, R. Schellin, W. Olthuis, and P. Bergveld, “Electroacoustical measurements of silicon microphones on wafer scale,” vol. 101, no. 4, pp. 2122–2128, 1997.
- [91] D. H. J. Xua, M.J. Dapino, D. Gallego-Perezb, “Microphone based on Polyvinylidene Fluoride (PVDF) micro-pillars and patterned electrodes,” *Sensors and Actuators A*, vol. 153, pp. 24–32, 2009.
- [92] “D. Gallego-Perez, N. Ferrell, N. Higuaita, D. Hansford, Versatile methods for the fabrication of polyvinylidene fluoride microstructures, *Macro. Rapid. Commun.*, in review.”
- [93] “D. Hohm and G. Hess, ‘A Subminiature Condenser Microphone with Silicon Nitride Membrane and Silicon Backplate,’ *J. Acoust. Soc. Am.*, 85 (1), pp. 476-480, January 1989.”
- [94] “Lee, C. et al., ‘Sol-gel derived PZT force sensor for scanning force microscopy,’ *Mater. Chem. Phys.*, Vol. 44, pp. 25-29, 1996.”
- [95] “Jae Bin Lee, et al, “Deposition of ZnO thin films by magnetron sputtering for a film bulk acoustic resonator“, *Thin Solid Film*, Vol. 435, pp. 179–185, 2003.”
- [96] “Yang Xin, et al,” Piezoelectric diaphragm as a high performance biosensor platform”, *Appl. Phys. Lett.*, Vol. 89, 223508(3pp.), 2006.”
- [97] “Kim, J.Y.-H. et al, ‘Parylene-C as a Piezoelectric Material’, *MEMS 2011*, Cancun, Mexico, pp. 473-476, 2011.”
- [98] “E Dayss, et al, “Surface modification for improved adhesion of a polymer–metal compound “, *Surface and Coatings Technology*, Vol. 116-119, pp. 986-990, 1999.”
- [99] “F. Xu, F. Chu, and S. Trolier-McKinstry, ‘Longitudinal piezoelectric coefficient measurement for bulk ceramics and thin films using pneumatic pressure rig’, *Journal of Applied Physics*, Volume 86, Number 1. pp 588-594.”
- [100] J. Karki, “Signal Conditioning Piezoelectric Sensors,” *Texas Instruments, Application Report*, no. September, pp. 1–6, 2000.
- [101] D. Isarakorn, M. Linder, D. Briand, and N. F. de Rooij, “Evaluation of static measurement in piezoelectric cantilever sensors using a charge integration technique for chemical and biological detection,” *Measurement Science and Technology*, vol. 21, no. 7, p. 075801, Jul. 2010.
- [102] J. F. S. Jr., P. J. Moses, and S. Trolier-McKinstry, “The wafer flexure technique for the determination of the transverse piezoelectric coefficient (d_{31}) of PZT thin films,” *Sensors and Actuators A: Physical*, vol. 71, no. 1–2, pp. 133–138, 1998.

- [103] J. F. Shepard, F. Chu, I. Kanno, and S. Trolier-McKinstry, "Characterization and aging response of the $d(31)$ piezoelectric coefficient of lead zirconate titanate thin films," *JOURNAL OF APPLIED PHYSICS*, vol. 85, no. 9, pp. 6711–6716, May 1999.
- [104] J. Joseph F. Shepard, F. Chu, I. Kanno, and S. Trolier-McKinstry, "Characterization and aging response of the $d[31]$ piezoelectric coefficient of lead zirconate titanate thin films," *Journal of Applied Physics*, vol. 85, no. 9, pp. 6711–6716, 1999.
- [105] F. Xu, F. Chu, and S. Trolier-McKinstry, "Longitudinal piezoelectric coefficient measurement for bulk ceramics and thin films using pneumatic pressure rig," *Journal of Applied Physics*, vol. 86, no. 1, pp. 588–594, 1999.
- [106] F. U. Desheng, K. I. Shikawa, M. M. Inakata, and H. S. Uzuki, "Observation of Piezoelectric Relaxation in Ferroelectric Thin Films by Continuous Charge Integration (a) sample Amplifier X-Y Metallic tip Au electrode Piezoelectric film Pt-coated substrate," vol. 40, no. 9, pp. 5683–5686, 2001.
- [107] S. Salvatori, N. Masarone, G. Di Nucci, and G. Conte, "Compact front-end electronics for low-level current sensor measurements," *Electronics Letters*, vol. 42, no. 12, pp. 682–684, 2006.
- [108] A. V Shirinov and W. K. Schomburg, "Pressure sensor from a PVDF film," *Sensors and Actuators A: Physical*, vol. 142, no. 1, pp. 48–55, 2008.
- [109] "D Isarakorn et al, "Detection of Surface Stress Induced Deflections in Piezoelectric Cantilever Sensors Using a Charge Integrator", 2010 Meas. Sci. Technol. Volume 21, Number 7, pp 075801."
- [110] "IVC102 Precision switched integrator transimpedance amplifier Datasheet Burr-Brown Corporation."
- [111] G. Description, C. Diagram, T. Application, and O. Information, "LMC662 CMOS Dual Operational Amplifier CMOS Dual Operational Amplifier," no. April, 2003.
- [112] "Jay J. Senkevich*, Seshu B. Desu, 'Morphology of poly(chloro-p-xylylene) CVD thin films', *Polymer* 40 (1999) pp 5751–5759."
- [113] "Jeffrey Chun-Hui Lin, Feiqiao Yu, Yu-Chong Tai, 'Integration of Slanted Tether Check-valves for High Pressure Applications', NEMS 2011, Kaohsiung, Taiwan, Feb. 20-23, 2011, pp. 750-753."
- [114] "Z. Ounaies, J.S. Harrison, 'An Investigation of Piezoelectricity of a Nitrile-Substituted Polyimide', *Polymer Physics*, August 2002."
- [115] p. 50. Davies, G.R. "Physics of Dielectric Solids", 1980, Conf. Series No. 58, (IOP, Bristol 1980), "No Title."
- [116] M. A. Bachmann and B. Lando, "A Reexamination," pp. 40–46, 1981.
- [117] A. G. Holmes-Siedle, P. D. Wilson, and A. P. Verrall, "PVdF: An electronically-active polymer for industry," *Materials & Design*, vol. 4, no. 6, pp. 910–918, 1984.
- [118] F. Application, P. Data, and P. E. B. Lowe, "United states Patent 4,340,786," vol. 100, 1982.

- [119] L. L. Sun, B. Li, Z. G. Zhang, and W. H. Zhong, "Achieving very high fraction of β -crystal PVDF and PVDF/CNF composites and their effect on AC conductivity and microstructure through a stretching process," *European Polymer Journal*, vol. 46, no. 11, pp. 2112–2119, 2010.
- [120] A. Salimi and A. A. Yousefi, "Analysis Method: FTIR studies of β -phase crystal formation in stretched PVDF films," *Polymer Testing*, vol. 22, no. 6, pp. 699–704, 2003.
- [121] C. Du, B. Zhu, and Y. Xu, "Effects of Stretching on Crystalline Phase Structure and Morphology of Hard Elastic PVDF Fibers," no. January, 2006.
- [122] V. Sencadas, V. M. Moreira, A. S. Pouzada, R. G. Jr, W. Luis, and S. Carlos, " α - to - β Transformation on PVDF Films Obtained by Uniaxial Stretch *," pp. 3–7.
- [123] V. Sencadas, R. Gregorio Jr., and S. Lanceros-Mendez, "alpha to beta Phase Transformation and Microstructural Changes of PVDF Films Induced by Uniaxial Stretch," *JOURNAL OF MACROMOLECULAR SCIENCE PART B-PHYSICS*, vol. 48, no. 3, pp. 514–525, 2009.
- [124] W. D. Niegisch, "Crystallography of Poly-p-Xylylene," *Journal of Applied Physics*, vol. 37, no. 11, pp. 4041–4046, 1966.
- [125] J. J. Senkevich and S. B. Desu, "Morphology of poly(chloro-p-xylylene) CVD thin films," *Polymer*, vol. 40, no. 21, pp. 5751–5759, 1999.
- [126] J. Hillenbrand and G. M. Sessler, "High-sensitivity piezoelectric microphones based on stacked cellular polymer films (L)," *The Journal of the Acoustical Society of America*, vol. 116, no. 6, p. 3267, Dec. 2004.
- [127] J. Medill, "A miniature piezoelectric microphone," *Audio, Transactions of the IRE Professional Group on*, vol. 1, no. 6. pp. 7–10, 1953.
- [128] P. Murphy, "Piezoelectric polymer microphones and receivers of improved efficiency," *The Journal of the Acoustical Society of America*, vol. 72, no. S1, p. S61, Nov. 1982.
- [129] "Matsuoka, Y, Yamamoto, Y, Tanabe, M., Shimada, S., Yamada, K., Yasukawa, A., and Matsuzaka, H., 'Low-pressure Measurement Limits for Silicon Piezoresistive Circular Diaphragm Sensors,' *Journal of Micromechanics and Microengineering*, 5, 32-35 (1995)."
- [130] "Pedersen, M., Meijerink, M.G.H., Olthuis, W., and Bergveld, P, 'A Capacitive Differential Pressure Sensor with Polyimide Diaphragm,' *Journal of Micromechanics and Microengineering*, 7, 250-252 (1997)."
- [131] "Xiao, Z., Engstrffm, O., and Vidovic, N., 'Diaphragm Deflection of Silicon Interferometer Structures Used as Pressure Sensors,' *Sensors and Actuators A*, 58, 99-107 (1997)."
- [132] S. Timoshenko and S. Woinowsky-Krieger, *Theory of plates and shells*. McGraw-Hill, 1959, p. 580.
- [133] "Zuckerwar, A.J., 'Theoretical Response of Condenser Microphone,' *Journal of the Acoustical Society of America*, 64, 1278-1285 (1978)."
- [134] "Zeng, N., Shi, C., Wang, D., Zhang, M., and Liao, Y, 'Diaphragm-type Fiber-optic Interferometric Acoustic Sensor,' *Optical Engineering*, 42 (9), 2558-2562 (2003)."

- [135] “Sheplak, M. and Dugundji, J., ‘Large Deflections of Clamped Circular Plates under Initial Tension and Transitions to Membrane Behavior,’ *ASME Journal of Applied Mechanics*, 65 (1), 107-115 (1998).”
- [136] M. Yu, “Sensor Diaphragm Under Initial Tension: Linear Analysis,” *Experimental Mechanics*, vol. 45, no. 2, pp. 123–129, Apr. 2005.
- [137] S. Beeby, *Mems Mechanical Sensors*. Artech House, 2004, p. 269.
- [138] *Soedel, W., Vibrations of Shells and Plates, Marcel Dekker, New York (1993).* .
- [139] M. Sheplak and M. A. Schmidt, “A MEMS Microphone for Aeroacoustics Measurements.”
- [140] “T. A. Harder, T. J. Yao, Q. He, C. Y. Shih, and Y. C. Tai, ‘Residual stress in thin-film parylene-C,’ in Proc. of the 15th IEEE International Conference on Micro Electro Mechanical Systems, Las Vegas, NV, 2002, pp. 435–438.”
- [141] M. Olfatnia, T. Xu, L. S. Ong, J. M. Miao, and Z. H. Wang, “Investigation of residual stress and its effects on the vibrational characteristics of piezoelectric-based multilayered microdiaphragms,” *Journal of Micromechanics and Microengineering*, vol. 20, no. 1, p. 015007, Jan. 2010.
- [142] *Madou M J 2002 Fundamentals of Microfabrication (Boca Raton, FL: CRC Press).* .
- [143] S. Senturia, *Microsystems Design*. Boston: Kluwer Academic, 2001, p. Chap.5.
- [144] M. Rossi, *Acoustics and Electroacoustics*. Norwood, MA: Artech House, 1988.
- [145] J. Merhaut, *Theory of Electroacoustics*. New York: McGraw-Hill, 1981.
- [146] S. Horowitz, T. Nishida, L. Cattafesta, and M. Sheplak, “Development of a micromachined piezoelectric microphone for aeroacoustics applications.,” *The Journal of the Acoustical Society of America*, vol. 122, no. 6, pp. 3428–36, Dec. 2007.
- [147] and M. S. S. Prasad, B. V. Sankar, L. N. Cattafesta, S. Horowitz, Q. Gallas, “Two-port electroacoustic model of an axisymmetric piezoelectric composite plate,” *AIAA J.*, vol. 4, pp. 2311–2318, 2006.
- [148] B. Tuttle et al., “Ferroelectric thin film microstructure development and related property enhancement,” *Ferroelectrics*, vol. 151, pp. 11–20, 1994.
- [149] and M. S. G. Wang, B. Sankar, L. Cattafesta, “Analysis of a composite piezoelectric circular plate with initial stresses for MEMS,” in *International Mechanical Engineering Congress and Exposition, ASME, New Orleans,*, 2002.
- [150] S. Coatings, “SCS Parylene Coatings,” 2013. [Online]. Available: <http://scscoatings.com/>.
- [151] Wikipedia, “Gold,” 2013. [Online]. Available: <http://en.wikipedia.org/wiki/Gold>.
- [152] M. Sheplak and J. Dugundji, “Large deflections of clamped circular plates and transitions to membrane behavior,” *J. Appl. Mech.*, vol. 65, pp. 107–115, 1998.
- [153] W. H. Hsieh, “MEMS Thin Film Teflon Electret Condenser Microphones,” California Institute of Technology, 2001.
- [154] “G.S.K. Wong and T.F.W. Embleton, ‘AIP Handbook of Condenser Microphones: Theory, Calibration and Measurement,’ AIP Press, New York, 1995.”

- [155] “M. Gayford, ‘Microphone Engineering Handbook,’ Butterworth-Heinemann Ltd., 1994.”
- [156] “Lee, C. et al., ‘Sol-gel derived PZT force sensor for scanning force microscopy’, *Mater. Chem. Phys.*, Vol. 44, pp. 25-29, 1996.”
- [157] “Jae Bin Lee, et al, “Deposition of ZnO thin films by magnetron sputtering for a film bulk acoustic resonator“, *Thin Solid Film*, Vol. 435, pp. 179–185, 2003.”
- [158] “Yang Xin, et al,” Piezoelectric diaphragm as a high performance biosensor platform”, *Appl. Phys. Lett.*, Vol. 89, 223508(3pp.), 2006.”
- [159] “Kim, J.Y.-H. et al, ‘Parylene-C as a Piezoelectric Material’, MEMS 2011, Cancun, Mexico, pp. 473-476, 2011.”
- [160] “B. E. Deal in *Semiconductor materials and process technology handbook : for very large scale integration (VLSI) and ultra large scale integration (ULSI) / edited by Gary E. McGuire.* (pp. 48-57).”
- [161] “Laermer, Franz, Schilp, Andrea, Method of anisotropic etching of silicon United States Patent 6531068.”
- [162] T. M. Chen and G. M. Brauer, “Solvent Effects on Bonding Organo-silane to Silica Surfaces,” *Journal of Dental Research*, vol. 61, no. 12, pp. 1439–1443, Dec. 1982.
- [163] G.-R. Y. & J. J. S. Christopher J. Mitchell, “Adhesion aspects of poly(p-xylylene) to SiO₂ surfaces using γ -methacryloxypropyltrimethoxysilane as an adhesion promoter,” *Journal of Adhesion Science and Technology*, vol. 20, no. 14, pp. 1637–1647, 2006.
- [164] T. Tan, J. Meng, N. Rahbar, H. Li, G. Papandreou, C. A. Maryanoff, and W. O. Soboyejo, “Effects of silane on the interfacial fracture of a parylene film over a stainless steel substrate,” *Materials Science and Engineering: C*, vol. 32, no. 3, pp. 550–557, 2012.
- [165] G. L. Witucki, “BACK TO BASICS A Silane Primer : Chemistry and Applications of Alkoxy Silanes,” 1992.
- [166] J. M. Antonucci, S. H. Dickens, and B. O. Fowler, “Chemistry of Silanes : Interfaces in Dental,” vol. 110, no. 5, pp. 541–558, 2005.
- [167] Y. Rong, H.-Z. Chen, H.-Y. Li, and M. Wang, “Encapsulation of titanium dioxide particles by polystyrene via radical polymerization,” *Colloids and Surfaces A: Physicochemical and Engineering Aspects*, vol. 253, no. 1–3, pp. 193–197, 2005.
- [168] D. Corning, “Silane Lab Notes The Use of Mixed Silane Coupling Agents.”
- [169] D. Corning, “Organofunctional Silanes Dow Corning Z-6030 Silane.”
- [170] “D.D. Stewart. US patent 3,600,216, 1971.”
- [171] M. Alami, M. Charbonnier, and M. Romand, “Interest of NH₃ and N₂ plasmas for polymer surface treatment before ‘electroless’ metallization,” *Plasmas and Polymers*, vol. 1, no. 2, pp. 113–126, 1996.
- [172] S. H. Kim, S. W. Na, N.-E. Lee, Y. W. Nam, and Y.-H. Kim, “Effect of surface roughness on the adhesion properties of Cu/Cr films on polyimide substrate treated by inductively coupled oxygen plasma,” *Surface and Coatings Technology*, vol. 200, no. 7, pp. 2072–2079, 2005.

- [173] Y. T. M. D. Ringenbach, A; Jugnet, "Interfacial chemistry in Al and Cu metallization of untreated and plasma treated polyethylene and polyethyleneterephthalate," *Journal of Adhesion Science and Technology, Volume 9, Number 9, 1995* , pp. 1209-1228(20).
- [174] F. D. Egitto and L. J. Matienzo, "Plasma modification of polymer surfaces for adhesion improvement," *IBM Journal of Research and Development*, vol. 38, no. 4, pp. 423–439, Jul. 1994.
- [175] "Yu, Q., J. Deffeyes, H. Yasuda, 'Engineering the surface and interface of parylene C coatings by low-temperature plasmas', *Progress in Organic Coatings*, Vol. 41, pp. 247-253, 2001."
- [176] "Seong, J.W., K.W. Kim, Y.W. Beag, S.K. Koh, K.H. Yoon, J.H. Lee, 'Effects of ion bombardment with reactive gas environment on adhesion of Au films to parylene C film', *Thin Solid Films*, Vol.476, pp. 386-390, 2005."
- [177] "J. M. Burkstrand, 'Substrate Effects on the Electronic Structure of Metal Overlayers—An XPS Study of Polymer-Metal Interfaces,' *Phys. Rev. B*. 20, No. 12, 4853 (1979)."
- [178] "N. J. Chou, D. W. Dong, J. Kim, and A. C. Liu, 'An XPS and TEM Study of Intrinsic Adhesion Between Polyimide and Cr Films,' / *Electrochem. Soc.* 131, No. 10, 2335 (1984)."
- [179] "J. L. Jordan, C. A. Kovac, J. F. Morar, and R. A. PoUak, 'High Resolution Photoemission Study of the Interfacial Reaction of Cr with Polyimide and Model Polymers,' *Phys. Rev. B*. 36, 1369 (1987)."
- [180] "M. J. Goldberg, J. G. Clabes, A. Viehbeck, and C. A. Kovac, 'Charge Transfer Reactions Between Metals and Polyimides,' *Pofym. Mater. Sci. Eng.* 59, 199 (1987)."
- [181] "Metallization of Cu on Parylene-C Film Micro-patterned by Hot-embossing Sung-Won Youn *, Akihisa Ueno , Masaharu Takahashi and Ryutaro Maeda Advanced Manufacturing Research Institute (AMRI), National Institute of Advanced Industrial Science and Technolo," pp. 1–2, 2007.
- [182] "E Dayss, et al, "Surface modification for improved adhesion of a polymer–metal compound “, *Surface and Coatings Technology*, Vol. 116-119, pp. 986-990, 1999."
- [183] E. Occhiello, M. Morra, G. Morini, F. Garbassi, and P. Humphrey, "Oxygen-plasma-treated polypropylene interfaces with air, water, and epoxy resins: Part I. Air and water," *Journal of Applied Polymer Science*, vol. 42, no. 2, pp. 551–559, 1991.
- [184] T. Gururaj, R. Subasri, K. R. C. S. Raju, and G. Padmanabham, "Effect of plasma pretreatment on adhesion and mechanical properties of UV-curable coatings on plastics," *Applied Surface Science*, vol. 257, no. 9, pp. 4360–4364, 2011.
- [185] J. H.-C. Chang, B. Lu, and Y.-C. Tai, "Adhesion-enhancing surface treatments for parylene deposition," *Solid-State Sensors, Actuators and Microsystems Conference (TRANSDUCERS), 2011 16th International*. pp. 390–393, 2011.
- [186] B. Lu, J. C.-H. Lin, Z. Liu, Y.-K. Lee, and Y.-C. Tai, "Highly flexible, transparent and patternable parylene-C superhydrophobic films with high and low adhesion," *Micro Electro Mechanical Systems (MEMS), 2011 IEEE 24th International Conference on*. pp. 1143–1146, 2011.

- [187] R. R. a. Callahan, K. G. Pruden, G. B. Raupp, and S. P. Beaudoin, "Downstream oxygen etching characteristics of polymers from the parylene family," *Journal of Vacuum Science & Technology B: Microelectronics and Nanometer Structures*, vol. 21, no. 4, p. 1496, 2003.
- [188] E. Meng, P.-Y. Li, and Y.-C. Tai, "Plasma removal of Parylene C," *Journal of Micromechanics and Microengineering*, vol. 18, no. 4, p. 045004, Apr. 2008.
- [189] E. Meng and Y. Tai, "PARYLENE ETCHING TECHNIQUES FOR MICROFLUIDICS AND BIOMEMS."
- [190] E. Zakar and M. D. Grapes, "Patterning of Thick Parylene Films by Oxygen Plasma for Application as Exploding Foil Initiator Flyer Material," no. September, 2009.
- [191] *Fomblin Y HVAC MSDS Sheet*. SOLVAY SOLEXIS S.p.A., 2006.
- [192] K. Su and O. Tabata, "Effects of aperture size and pressure on XeF₂ etching of silicon," *Microsystem Technologies*, vol. 9, no. 1–2, pp. 11–16, Nov. 2002.
- [193] C. J. Brinker, "Hydrolysis and condensation of silicates: Effects on structure," *Journal of Non-Crystalline Solids*, vol. 100, no. 1–3, pp. 31–50, 1988.
- [194] X. Wang, X. Yang, K. Walsh, and Y. Tai, "Gas-Phase Silicon Etching with Bromine Trifluoride," *TRANSDUCERS '97*, pp. 1505–1508, 1997.
- [195] F. I. C. R. Y. G. L. P. B. C. E. G. H. E. J. K. K. S. J. P. M. H. Hecht, "Gas-phase silicon micromachining with xenon difluoride (Proceedings Paper)," *Proceedings*, vol. 2641, pp. 117–128, 1995.
- [196] H. F. Winters and J. W. Coburn, "The etching of silicon with XeF₂ vapor," *Applied Physics Letters*, vol. 34, no. 1, pp. 70–73, 1979.
- [197] F. Yu, J. C.-H. Lin, P.-J. Chen, and Y.-C. Tai, "Parylene stiction," *Micro Electro Mechanical Systems (MEMS), 2010 IEEE 23rd International Conference on*. pp. 408–411, 2010.
- [198] G. McDonald, F. Schreiner, G. N. McDonald, and C. L. Chernick, "The Vapor Pressure and Melting Points of Xenon Difluoride," vol. 814, no. 5, pp. 1162–1166, 1967.
- [199] "Armstrong T R and Fitzgerald M P 1992 An autocollimator based on the laser head of a compact disc player Meas. Sci. Technol. 3 1072–6."
- [200] "Fan K C, Lin C Y and Shyu L H 2000 Development of a low-cost focusing probe for profile measurement Meas. Sci. Technol. 11 1–7."
- [201] "Fan K C, Chu C L and Mou J I 2001 Development of a low-cost autofocusing probe for profile measurement Meas. Sci. Technol. 12 2137–46."
- [202] "Benschop J and Rosmalen G V 1991 Confocal compact scanning optical microscope based on compact disc technology Appl. Opt. 30 1179–84."
- [203] "E-T Hwu, et al, "A hybrid scanning probe microscope (SPM) module based on a DVD optical head", Meas. Sci. Technol., Vol. 20, 084005(8pp.), 2009."
- [204] "C. L. Morfey, Dictionary of Acoustics (Academic Press, San Diego, 2001)."
- [205] "Bies, David A., and Hansen, Colin. (2003). Engineering Noise Control."

- [206] “Taylor 1995, Guide for the Use of the International System of Units (SI), NIST Special Publication SP811.”